

# A DIPOLE MODEL FOR HIGH ENERGY QCD

*Christoffer Flensburg*

Department of Theoretical Physics  
Lund University

**Thesis for the degree of Doctor of Philosophy**

Thesis Advisor: *Leif Lönnblad*

Faculty Opponent: *Raju Venugopalan*

To be presented, with the permission of the Faculty of Science of Lund University, for public criticism in lecture hall F of the Department of Physics on Friday, the 29th of April 2011, at 10.15.

Organization <b>LUND UNIVERSITY</b> Department of Theoretical Physics Sölvegatan 14A SE-223 62 LUND Sweden		Document name <b>DOCTORAL DISSERTATION</b>	
Author(s) <b>Christoffer Flensburg</b>		Date of issue <b>March 2011</b>	
		Sponsoring organization	
Title and subtitle <b>A Dipole Model for High Energy QCD</b>			
Abstract <p>This thesis considers a model of high energy particle collisions. The model is based on the so called BFKL formalism which is valid only at low <math>x</math>, that is collisions at very high energies, such as at the LHC. The initial state of the incoming particles are simulated by colour dipoles in transverse space evolved through rapidity. With this approach, all fluctuations are dynamically described, allowing for a large set of observables to be calculated.</p> <p>The first paper compares the model to experimental results and the model is found to describe a large set of experiments with <math>pp</math> and <math>\gamma^*p</math> accurately with just four tunable parameters. The second paper studies the fluctuations in the interaction probability, and how this affects the cross section for diffractive excitation in <math>pp</math> and <math>\gamma^*p</math>. The model is further compared to a different approach, and many similarities are noted. The third paper studies the correlations between multiple hard subscatterings in <math>pp</math> which are important for finding new physics at LHC.</p> <p>The fourth paper is the largest project, and introduces a full event generator based on the dipole model. Here the dipoles are not only tracked in the initial evolution, but also all the particles coming out from the collision are calculated. It is found to provide a competitive description of all minimum bias data, something that has never been done in the BFKL formalism before. This provides a good comparison for other event generators that normally use a different approach.</p>			
Key words: <b>QCD, Phenomenology, Dipole Model, low <math>x</math></b>			
Classification system and/or index terms (if any):			
Supplementary bibliographical information:		Language <b>English</b>	
ISSN and key title:		ISBN <b>978-91-7473-112-5</b>	
Recipient's notes		Number of pages <b>190</b>	Price
		Security classification	

Distributor

Christoffer Flensburg

Department of Theoretical Physics, Sölvegatan 14A, SE-223 62 Lund, Sweden

I, the undersigned, being the copyright owner of the abstract of the above-mentioned dissertation, hereby grant to all reference sources the permission to publish and disseminate the abstract of the above-mentioned dissertation.

Signature \_\_\_\_\_

Date 2011-03-24

# A DIPOLE MODEL FOR HIGH ENERGY QCD

*Christoffer Flensburg*

Department of Theoretical Physics  
Lund University

Copyright © Christoffer Flensburg

Department of Theoretical Physics, Lund University  
ISBN 978-91-7473-112-5

Printed in Sweden by Media-Tryck, Lund University  
Lund 2011

## Sammanfattning

Fysiker försöker beskriva verkligheten. Idag finns det en beskrivning som förklarar i stor utsträckning det vi ser omkring oss, från solens energikälla och himlens färg, till atomers uppbyggnad och universums minsta beståndsdelar. Beskrivningen kan sammanfattas i en ekvation på ett par rader, och kallas för Standardmodellen, och inkluderas här huvudsakligen av estetiska skäl:

$$\begin{aligned}\mathcal{L} &= i\bar{\psi}\not{D}\psi + \psi_i y_{ij} \psi_j \phi + h.c. \\ &- \frac{1}{4} \mathcal{F}_{\mu\nu} \mathcal{F}^{\mu\nu} + |D_\mu \phi|^2 - V(\psi)\end{aligned}$$

Standardmodellen beskriver de minsta beståndsdelarna: materiepartiklarna, och de kraftbärande partiklarna. Den beskriver hur ett fåtal partiklar interagerar med varandra, och man kan utifrån det i princip beskriva situationer med hur många partiklar som helst. I praktiken blir dock matematiken snabbt för komplicerad om man försöker att direkt lösa standardmodellens ekvationer för många partiklar, och man kan inte längre göra exakta förutsägelser

För att avgöra om det är en bra beskrivning så behöver den jämföras med verkligheten; teorin behöver jämföras med experiment. Så för att testa standardmodellen mot så många experiment som möjligt, är det viktigt att räkna ut förutsägelser för så många scenarier som möjligt. I de flesta fall är det omöjligt att räkna ut en exakt förutsägelse, och det är nödvändigt att införa approximationer och förenklingar i beräkningarna.

För att undersöka Standardmodellen så direkt som möjligt, används ofta experiment med partikelacceleratorer, där man accelererar partiklar (som till exempel elektroner eller protoner) till hög hastighet, kolliderar dem, och ser hur de interagerar. I det fallet är det i allmänhet bara ett fåtal partiklar inblandade i kollisionen, vilket gör det möjligt att göra förutsägelser. Standardmodellen stämmer mycket väl överens med dessa experiment, vilket bekräftar att det är en bra modell.

Det är inte alltid enkelt att göra förutsägelser för partikelkollisioner; detta gäller speciellt när det är protoner som kolliderar, som är fallet vid den nybyggda acceleratoren LHC: Large Hadron Collider, i Geneve. En proton är inte en elementarpartikel, utan är uppbyggd av tre mindre partiklar som kallas kvarkar. En kvark är en av elementarpartiklarna i standardmodellen, och är en del av all materia vi har omkring oss. De



tre kvarkarna i en proton hålls ihop av en kraft som kallas "den starka kraften". Detta sker genom att de hela tiden skickar gluoner mellan varandra, där gluonerna är de kraftbärande partiklarna för den starka kraften. Detta gör att när en proton accelereras och kolliderar, så är det inte en ensam partikel som kolliderar, utan det är tre kvarkar tillsammans med en mängd gluoner. Detta gör det mer komplicerat att räkna ut vad som händer när två protoner kolliderar.

Dessutom interagerar gluonerna med varandra, vilket gör situationen ännu mer komplicerad. Även om en proton börjar som tre kvarkar, så kommer den i varje ögonblick också ha några gluoner, låt oss säga två stycken, som skickas mellan kvarkarna. Det förändrar nu situationen igen, eftersom gluonerna kan skicka ut ytterligare gluoner mellan varandra. Så de tre kvarkarna och två gluonerna kommer ha ytterligare gluoner mellan sig, som i sin tur orsakar ännu fler gluoner och så vidare. Den här självförstärkande kaskaden av gluoner är kraftigare ju mer energi protonerna kolliderar med.

Så när två protoner kolliderar är det egentligen två kaskader av kvarkar och gluoner som krashar in i varandra, och ju högre energi de krockar med, desto fler kvarkar och gluoner är det som kolliderar. Detta är mycket komplicerat att räkna ut direkt från standardmodellen. Vid kollisioner med tillräckligt hög energi finns det dock en förenkling av standardmodellen, som kallas BFKL-ekvationen, som möjliggör beräkningar av den inkommande kaskaden av kvarkar och gluoner.

Jag har i mitt doktorandarbete utgått från BFKL-ekvationen och utvecklat en model som simulerar de inkommande kaskaderna av kvarkar och gluoner, och som därmed kan beskriva mycket av det som händer i kollisioner, till exempel vid LHC.

Vår lösningsansats är att utgå från kvarkarna och sedan med hjälp av en dator simulera en gluon i taget som skickas ut från de föregående partiklarna, och i varje ny utskickad gluon ta hänsyn till så mycket detaljer som möjligt. På så sätt kan vi få en mycket mer detaljerad bild av hur de kolliderande kaskaderna ser ut än vad som har gjorts tidigare.

När de två kaskaderna kolliderar och kvarkarna och gluonerna far ut från kollisionen så gäller andra regler, och vår model kan inte användas längre. Det finns dock andra förenklingar som beskriver de utgående partiklarna väl, och vi har kombinerat vår model med andra tidigare modeller för att kunna fortsätta att beskriva vad som händer med kaskaderna även efter kollisionen. På det sättet har vi byggt upp en så kallad händelsegenerator, som simulerar hela processen från de första inkommande kvarkarna, genom kaskaden innan kollision, interaktionen med

den andra kaskaden och interaktioner på vägen ut från kollisionen, hela vägen till de partiklar som till slut kommer ut från kollisioner.

En sådan kaskad från händelsegeneratoren finns illustrerad längst ner till höger på varje uppslag, och genom att bläddra igenom hörnet på alla sidorna snabbt kan man se två protoner vid LHC röra sig mot varandra och kollidera. Protonerna beskrivs av de tre kvarkarna, sammankopplade av "dipoler" som representerar gluonerna som hela tiden skickas fram och tillbaka. Efter hand som fler och fler gluoner skickas ut kommer det fler och fler dipoler som kopplar ihop de nya gluonerna.

I till exempel LHC mäts dessa utgående partiklarna, och vi kan jämföra resultaten från våra simuleringar med experiment. Standardmodellen är inte en "Teori för Allting", utan vi vet att det måste finnas något mer, om inte annat så ingår inte gravitation. Genom att bättre förstå vad vi väntar oss från standardmodellen kan vi enklare se tecken på om något nytt behövs.



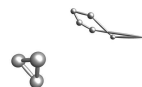
This thesis is based on the following publications:

- I Christoffer Flensburg, Gösta Gustafson and Leif Lönnblad,  
**Elastic and quasi-elastic  $pp$  and  $\gamma^*p$  scattering in the Dipole Model**  
*European Physics Journal* **C60** (2009) 233-247 e-Print:  
 [arXiv:0807.0325].
- II Christoffer Flensburg and Gösta Gustafson  
**Fluctuations, Saturation, and Diffractive Excitation in High Energy Collisions**  
*Journal of High Energy Physics* **1010** (2010) 014 e-Print:  
 [arXiv:1004.5502].
- III Christoffer Flensburg, Gösta Gustafson, Leif Lönnblad and Andras Ster,  
**Correlations in double parton distributions at small  $x$**   
**LU-TP 11-12**  
**CERN-PH-TH-2011-059**  
**MCnet-11-09**  
 e-Print: [arXiv:1103.4320].
- IV Christoffer Flensburg, Gösta Gustafson and Leif Lönnblad,  
**Inclusive and Exclusive observables from dipoles in high energy collisions**  
**LU-TP 11-13**  
**CERN-PH-TH-2011-058**  
**MCnet-11-08**  
 e-Print: [arXiv:1103.4321].



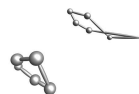
# Contents

<b><i>i</i></b>	<b>Introduction</b>	<b>1</b>
<i>i.1</i>	Particle Physics: history up to today . . . . .	1
<i>i.1.1</i>	The atom . . . . .	2
<i>i.1.2</i>	The atom as electrons and nucleus . . . . .	3
<i>i.1.3</i>	The nucleus as protons and neutrons . . . . .	4
<i>i.1.4</i>	The protons and neutrons as quarks . . . . .	6
<i>i.1.5</i>	The properties of the forces . . . . .	8
<i>i.1.6</i>	The standard model . . . . .	9
<i>i.1.7</i>	The strong force at hadron colliders . . . . .	10
<i>i.2</i>	Mathematical foundation . . . . .	12
<i>i.2.1</i>	The observables . . . . .	12
<i>i.2.2</i>	Feynman diagrams, and calculating a cross section . . . . .	13
<i>i.2.3</i>	QCD, not so simple . . . . .	14
<i>i.2.4</i>	BFKL: a high energy approximation . . . . .	16
<i>i.3</i>	The Lund Dipole Model: my contribution . . . . .	17
<i>i.3.1</i>	Our model . . . . .	18
<i>i.3.2</i>	Further applications . . . . .	21
<i>i.3.3</i>	Future development . . . . .	23
<i>i.4</i>	Introduction to papers . . . . .	24
<i>i.4.1</i>	Paper I: Elastic and quasi-elastic $pp$ and $\gamma^*p$ scattering in the Dipole Model . . . . .	24
<i>i.4.2</i>	Paper II: Fluctuations, Saturation, and Diffractive Excitation in High Energy Collisions . . . . .	25
<i>i.4.3</i>	Paper III: Correlations in double parton distributions at small $x$ . . . . .	25
<i>i.4.4</i>	Paper IV: Inclusive and Exclusive observables from dipoles in high energy collisions . . . . .	26
<i>i.4.5</i>	List of contributions . . . . .	26
<i>i.5</i>	A PhD defence for a non-physicist . . . . .	27
<i>i.5.1</i>	The schedule . . . . .	27
<i>i.5.2</i>	What to do during the defence? . . . . .	28



	Acknowledgments . . . . .	29
	References . . . . .	30
<b>I</b>	<b>Elastic and quasi-elastic <math>pp</math> and <math>\gamma^*p</math> scattering in the Dipole Model</b>	<b>33</b>
I.1	Introduction . . . . .	34
I.2	Formalism . . . . .	36
I.2.1	The dipole cascade model and the eikonal approximation . . . . .	36
I.2.2	DVCS and exclusive vector meson production in $\gamma^*p$ collisions . . . . .	37
I.2.3	Differential cross sections . . . . .	38
I.3	The improved dipole cascade . . . . .	39
I.3.1	Non-leading perturbative effects . . . . .	39
I.3.2	Saturation within the cascades . . . . .	40
I.3.3	Confinement effects . . . . .	41
I.4	Initial wave functions . . . . .	42
I.4.1	Proton wave function . . . . .	42
I.4.2	Photon wavefunction . . . . .	44
I.4.3	Meson wavefunctions . . . . .	46
I.5	Tuning of parameters and the differential $pp$ cross section	49
I.5.1	The total and elastic $pp$ cross section . . . . .	49
I.5.2	The differential elastic $pp$ cross section . . . . .	52
I.5.3	The total $\gamma^*p$ cross section and tuning the photon wave function . . . . .	53
I.6	Results for quasi-elastic $\gamma^*p$ collisions . . . . .	55
I.6.1	Deeply Virtual Compton Scattering . . . . .	55
I.6.2	Exclusive Production of Light vector Mesons . . . . .	56
I.6.3	Exclusive $\psi$ Production . . . . .	60
I.7	Conclusions and Outlook . . . . .	61
	References . . . . .	64
<b>II</b>	<b>Fluctuations, Saturation, and Diffractive Excitation in High Energy Collisions</b>	<b>69</b>
II.1	Introduction . . . . .	70
II.2	The eikonal approximation and the Good–Walker formalism . . . . .	72
II.2.1	Eikonal approximation . . . . .	72
II.2.2	Good–Walker formalism . . . . .	73
II.2.3	What are the diffractive eigenstates? . . . . .	74

II.3	The dipole cascade model . . . . .	74
II.3.1	Mueller's dipole model . . . . .	74
II.3.2	The Lund dipole cascade model . . . . .	76
II.3.3	Application to diffraction . . . . .	79
II.4	The nature of the fluctuations and effects of saturation . . . . .	82
II.4.1	$\gamma^*p$ scattering . . . . .	82
II.4.2	$pp$ scattering . . . . .	84
II.5	Impact parameter profile and $t$ -dependence in $pp$ -collisions . . . . .	86
II.6	Relation Good-Walker – Triple-Regge . . . . .	88
II.7	Conclusions . . . . .	93
II.8	Acknowledgements . . . . .	94
	References . . . . .	95
<b>III</b>	<b>Correlations in double parton distributions at small <math>x</math></b>	<b>99</b>
III.1	Introduction . . . . .	100
III.2	Double Parton Scattering and Double Parton Distributions . . . . .	102
III.2.1	Experimental results . . . . .	102
III.2.2	Formalism . . . . .	103
III.2.3	Correlations . . . . .	104
III.3	The Lund Dipole Cascade Model . . . . .	107
III.3.1	Mueller's dipole cascade . . . . .	107
III.3.2	The Lund dipole cascade model . . . . .	108
III.4	Application to double parton distributions . . . . .	111
III.5	Results . . . . .	112
III.5.1	Subcollisions at midrapidity . . . . .	112
III.5.2	Sub-collisions off midrapidity . . . . .	114
III.5.3	Comparison with experiment . . . . .	115
III.5.4	Comment on the definition of $b$ . . . . .	117
III.6	Conclusions and outlook . . . . .	117
	References . . . . .	121
<b>IV</b>	<b>Inclusive and Exclusive observables from dipoles in high energy collisions</b>	<b>125</b>
IV.1	Introduction . . . . .	126
IV.2	The Lund dipole cascade model for inclusive cross sections . . . . .	128
IV.2.1	Mueller's cascade model and the eikonal formalism . . . . .	128



IV.2.2	The Lund dipole cascade model . . . . .	131
IV.2.3	Initial dipole configurations . . . . .	133
IV.3	From inclusive to exclusive observables . . . . .	133
IV.3.1	The chain of $k_{\perp}$ -changing gluons . . . . .	133
IV.3.2	Reabsorption of virtual emissions . . . . .	134
IV.3.3	Giving proper weights to the emissions . . . . .	135
IV.3.4	Going from transverse coordinate space to momentum space . . . . .	138
IV.3.5	Final state radiation and hadronization . . . . .	140
IV.4	Generating the exclusive final states . . . . .	140
IV.4.1	Selecting the interactions . . . . .	141
IV.4.2	Identifying the backbone gluons . . . . .	142
IV.4.3	Reweightings outer $q_{\perp}$ maxima . . . . .	142
IV.4.4	FSR matching and ordering . . . . .	143
IV.4.5	Colour flow . . . . .	144
IV.4.6	Higher order corrections . . . . .	144
IV.5	Self-consistency and tuning . . . . .	146
IV.5.1	Achieving frame independence . . . . .	146
IV.5.2	Tuning to experimental data . . . . .	150
IV.5.3	Comparison with experiments . . . . .	152
IV.6	Conclusions and outlook . . . . .	157
IV.A	$q_{\perp}$ max reweighting in DIPSY . . . . .	161
IV.B	Absorbed partons and ordering . . . . .	163
IV.B.1	Coherence . . . . .	164
IV.B.2	Ordering in the interaction . . . . .	166
IV.C	Saturation effects . . . . .	168
IV.C.1	Multiple interaction . . . . .	169
IV.C.2	The Swing . . . . .	169
IV.C.3	colour flow in saturated cascades . . . . .	171
	References . . . . .	173

# Introduction

This introduction will have readers ranging from interested friends and family without background in physics, through undergraduate and graduate physics students, to the referees and opponent with decades of experience in particle physics research. I have tried to dedicate at least a few pages to every possible level of the reader, but let me warn you, the reader, that you will find part of the introduction too trivial, or too involved.

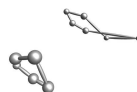
Non-physicists will probably find section *i.1* the most interesting, with a historical introduction leading up to today's situation of particle physics, and description of the problems and solutions that this thesis addresses. If you are reading this at the defence, you should consider skipping ahead to section *i.5* for an explanation of what is going on, and how you can make the most of it.

Section *i.2* introduces particle physics in a more mathematical way, as well as the basic concepts that form the foundation of my research.

Section *i.3* goes into more detail of the work, and assumes some experience from particle physics, and in section *i.4* the publications are summarised.

## ***i.1* Particle Physics: history up to today**

The first mentions of matter being built up of some smallest object, an elementary particle, trace back to around 600 B.C. in ancient India and Greece, where the word “atomos”, meaning unsplittable, was coined. At that time there was however no experiment capable of supporting or rejecting this idea, and the concept could not be developed very far.



### i.1.1 The atom

The first elementary particle model with experimental support was Dalton's atomic theory in early 19:th century, describing early chemistry in terms of elementary particles. One of the strong experimental supports for this theory was the law of multiple proportions.

**The law of multiple proportions** Oxygen and carbon can combine in two ways: either each carbon atom pairs up with each oxygen atom forming CO, the toxic gas carbon monoxide, or each carbon atom pairs up with two oxygen atoms, forming CO<sub>2</sub>, carbon dioxide that help plants transform sunlight into chemical energy (and recently maybe more known from global warming contexts).

Splitting up 1 kg of carbon monoxide in oxygen and carbon, you will get as many carbon atoms as oxygen atoms, but as the oxygen atom is a heavier by 33%, you will get 429 grams of carbon, and 571 grams of oxygen, that is, 1.33 times as much oxygen as carbon in weight.

Repeating the experiment with 1 kg of carbon dioxide, splitting it up in carbon and oxygen, you will get double the number of oxygen atoms, meaning 273 grams of carbon and 727 grams of oxygen. That is, 2.66 times as much oxygen as carbon.

The ratio in the second experiment, 2.66, is exactly the double of 1.33 in the first experiment. Today we know that this is because each carbon atom in CO<sub>2</sub> is coupled with 2 oxygen atoms, while CO is coupled to only one, but to the chemists in early 19:th century found this property very curious, and it was an important reason for John Dalton to formulate his atomic theory.

Not everyone believed that the success that Dalton's atomic theory had in explaining experiments meant that all matter really was built up of tiny elementary particles, but saw it more as a mathematical trick. A more direct observation was the analysis of Brownian motion.

**Brownian motion** Water is made of a very small water molecules that moves around in the liquid. If a sufficiently small object is placed in the water, it will feel the individual collisions with the water molecules, and will be bouncing around randomly from the collisions, even if initially left at rest. An example of this kind of motion, Brownian motion, is shown in figure i.1.

Robert Brown was in 1827 observing pollen grains in water with a microscope, and saw small pieces of the grains break off and move around erratically and randomly. Brown reported the observation, but it was not until the end of the 19:th century, or even beginning of 20:th, that

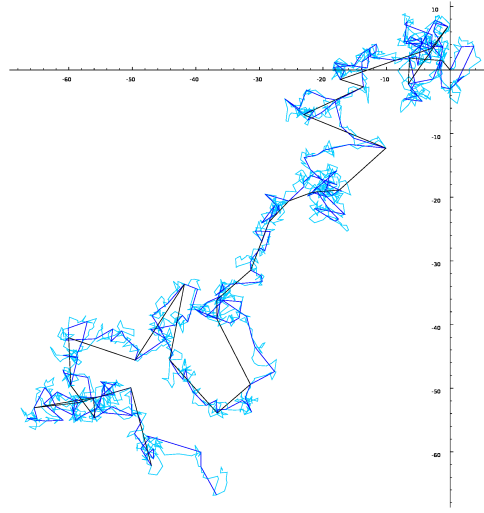


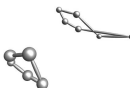
Figure i.1: Brownian motion. The lines describes the motion of a dust particle in for example water. The black line is measuring at longer time intervals, while the blue lines measure the position more frequently.

a mathematical explanation in terms of atoms was made, confirming Dalton's theory.

### i.1.2 The atom as electrons and nucleus

While most matter is formed from atoms, the atoms are not elementary particles, in the sense that they are not unsplittable. It was known that a neutral atom can give off a negative electric charge, and the atom itself will get a positive charge. This is what happens for example with static electricity built up from rubbing a balloon on hair.

In 1897, J.J. Thomson showed that the negative electric charge is actually a very light particle, now known as the electron. This was done by stripping negative charge of atoms (like when rubbing a balloon) and then sending the charges through vacuum to a positive charge (for example the sweater you just rubbed the balloon against). It turned out that putting an object in the path of the negative charges stopped them from arriving to the positive charge, and it was concluded that the negative charges were carried by some type of particle that got named electron. It was realised that the atom contains electrons, which were as-



sumed to be floating around in a positively charged “pudding”. So the atom was seen as a pudding with the small electrons in it like raisins and the picture got named the “plum pudding model”.

Soon after though, another experiment would again change how the atom was seen. Ernest Rutherford decided in 1909 to shoot alpha rays at a very thin gold foil. Alpha rays were seen as helium atoms stripped of both of their electrons, that is just the pudding part of the atom in the plum pudding model. The purpose was to study how the helium pudding would break up on the gold atoms, but to Rutherfords surprise, some of the alpha particles bounced back out almost the same way as the came from. This was as surprising as throwing a cream cake at a brick wall, and see it bounce off it completely intact like a tennis ball.

The explanation was that the positive charge in an atom was not spread out, but concentrated in a small nucleus in the centre of the atom, that also would have most of the mass of the atom. The electrons were suggested to rotate around this nucleus, similar to how the planets rotate around the sun, but rather than gravity keeping the planets to stay around the sun, it would be the electromagnetic attraction between the positively charged nucleus and the negatively charged electrons that kept the atom together.

### i.1.3 The nucleus as protons and neutrons

As the atom has a neutral charge in total, the amount of positive charge of the nucleus determines how many electrons it would collect around itself, and the number of electrons would determine the chemical properties of the atom. So it was understood that there was one nucleus for each kind of atom, distinguished by their charge and their mass.

In 1913, isotopes were discovered, that is, two nuclei with the same charge, but with different masses. Further it was discover that the masses of the different isotopes, the different nuclei, increased in steps of the same size.

**The mass of a nucleus** Today the atomic nucleus is understood as a compound of positively charged protons, and uncharged neutrons, both with a mass of about  $1.7 \cdot 10^{-24}$  g. Although this may not seem very heavy, this means that more than 99.9% of the mass of an atom is concentrated in the nucleus, which is less than 0.01% of the diameter of the electron orbits.

For some reason physicists like to compare particles to fruits and vegetables, and following that convention, the relation in size an weight can be illustrated as follows: If the nucleus has the size and



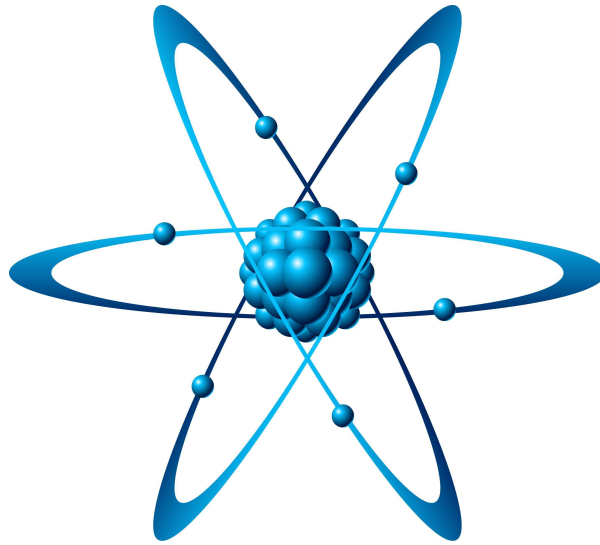
*i*

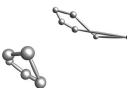
Figure i.2: An atom. The nucleus contains protons and neutrons, and the electrons orbit the nucleus. Not to scale: as the orbits are about 100,000 times the size of the nucleus, the nucleus would be just a fraction of a pixel in this picture.

mass of a watermelon in the city centre of Lund, then the electrons would have the mass of peas, and the orbit would be covering the bigger part of Lund.

That said, as the nucleus is built of protons and neutrons with the same mass, the total mass of a nucleus will be a whole number times that mass. For example an oxygen nucleus has 8 protons (setting the electric charge of the nucleus to +8), and in general 8 neutrons. As the proton and neutron masses are almost the same, this would put the total mass close to 16 times the mass of the proton. Similarly, a carbon nucleus will most often have a mass 12 times that of the proton and so on, but one will never find a nucleus with the mass of 16.5 times the proton mass.

Scientists found this too much to be a coincidence, and by 1932 the nucleus was described as a set of protons and neutrons, both with about the same mass.

While the electrons were kept in place by the electromagnetic attraction between the positive nucleus and the negative electrons, there was no clear answer to what held the protons and neutrons together in the nucleus. In fact, the positively charged protons confined in such a small volume as the nucleus would push each other away very strongly. The



conclusion was that there must be some other, even stronger, force that kept the neutrons and protons together. This somewhat mysterious force was named, in lack of better suggestions, “the strong force”. It should here be mentioned that much of today’s particle physics, including the thesis you are currently reading, is about understanding exactly how the strong force works.

### **i.1.4 The protons and neutrons as quarks**

Around 1950 technical development had reached the point where the first particle accelerators were built, propelling electrons, protons and neutrons to almost the speed of light. Most of these experiments included crashing the particles into something at high speed, and in these collisions, many new particles were found. The new particles had similar masses to the protons and neutrons, none as light as the electron, and all of them were interacting using the strong force. As the particles were accelerated to higher and higher speed (particle physicists usually say “to higher energy”), hundreds of new particles were found, to the extent that the situation was referred to as a “particle zoo”. All of these strongly interacting particles, the neutron and the proton, plus all the new ones, were called “hadrons”.

As happened with Dalton in discovering the law of multiple proportions, and as in the case with masses of the isotopes, also in this particle zoo, some systems and regularities were found. While they were not as straightforward regularities as the two examples mentioned, they still pointed towards the hadrons being built up from smaller particles, called “quarks”. Scientists welcomed the effort to find some order in the zoo, but without more direct proof of the existence of quarks, the idea did not get accepted immediately.

**Hadrons from quarks** Today we know that there are six different flavours (yes, physicists actually call them flavours) of quarks. However, only the two lightest flavours, the “up” quark and the “down” quark, are light enough to appear naturally. The other 4 flavours are only seen in high energy particle collisions.

Each of the six flavours come in 3 different colours (again, yes, they are actually referred to as colours): red, green and blue. Quarks can be combined to form hadrons in any way, as long as they combine in a colour-neutral way. This works in the same way as real-life colours do, that is, red green and blue can combine to give white. “Colour-neutral” means that the quarks have to combine in a way that results in the colour white.

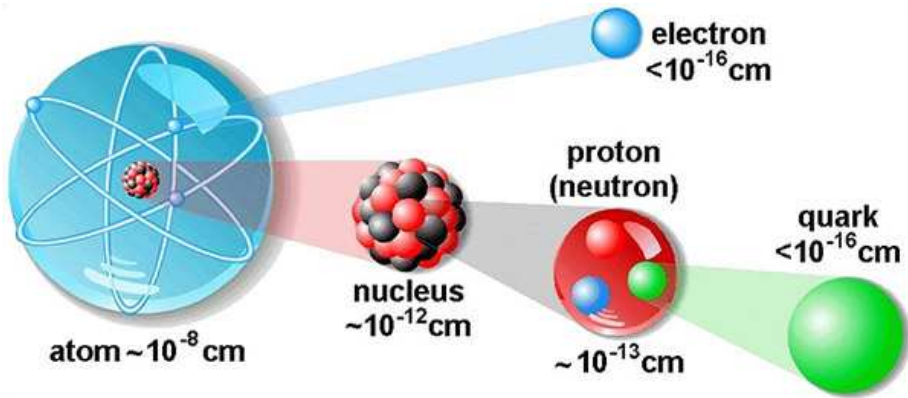
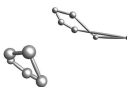


Figure i.3: How matter is built as we see it today. The atom is electrons orbiting the nucleus, which is built from protons and neutrons, which in turn are built from quarks.

A proton for example is built up from three quarks, two up quarks, and one down quark. Of these three quarks, there is one red, one blue and one green. Similarly for neutrons, which are built from *one* up quark and *two* down quarks, but still with one of each colour. By combining the different flavours in different ways, and with different colour combination, the particle zoo of the hundreds of different hadrons is formed.

Recall Rutherford and his experiment with the gold foil and the helium nuclei. He thought he was colliding plum pudding, but he saw collisions as if he was hitting something very small and very heavy. Now we know that this very small and very heavy thing was the nucleus of the atom, and it is indeed much smaller than the atom (recall the water-melon analogy).

A similar experiment was done with the proton. There were theories saying that the proton was built up by smaller quarks, and one would be able to see the internal structure if one collided it with something sufficiently hard. Luckily, by 1968 the technical development since the first accelerators had arrived at a point where this could be done, and indeed, in what was called “deep inelastic scattering”, one could see the substructure of the proton. And while there were some difficulties in confirming that this substructure actually was originating from the quarks suggested to explain the zoo, the model with the flavoured and coloured quarks eventually got widely accepted.



### i.1.5 The properties of the forces

This is how we see the structure of matter today: The quarks are held together by the strong force to form hadrons. The only two hadrons seen in the nature: the proton and the neutron, form the nucleus while the electrons orbit the nucleus, together being the atom. Thus the elementary particles building up matter are the quarks and the electrons.

However, to understand nature, it is not enough to know its building blocks, one also has to understand how they interact with each other. We know today that each force is mediated through a force carrier, a sort of particle, but a different kind of particle than the electrons and quarks which build up matter.

**Force carriers** We know that opposite electric charges attract, and that equal charges repel each other. But how can one of the charges know that the other charge is there? Is it a “mysterious force at a distance”, where the particle just *knows* that the other charge is there, and will feel the force?

From the way the (highly rethorical) question was asked, it should be clear that the answer is “no, it does not just feel it”. It feels the force of the other charge because the two particles exchange photons all the time, that carry the information about the charges between the two particles. The photon is the force carrier of the electromagnetic force.

So how do we know this? Has anyone seen photons? And again, from the way the question is asked, the answer should be obvious: “yes, someone has seen photons”. In fact, you are reading this text right now by seeing photons, as the light from the book is nothing more than photons that hit the back of your eyes and cause weak electrical (as photons are the force carriers of electromagnetism) signals to be sent to the brain. So the force carrier that keep the atom together, is the same particle that enables us to see things around us. Just to add to the list, radio, satellite, TV, mobile phone, bluetooth and infrared communication are also just photons.

The subject of this thesis however is the strong force, and a central role will be played by its force carrier: the gluon. The gluon is however much less visible, as it is exchanged only between the quarks in a hadron, and to some extent between the neutrons and protons in a nucleus. But as we will see, when you collide two hadrons at high energy, as is done at the Large Hadron Collider, LHC, it is of great importance to understand the nature of the gluon.

### i.1.6 The standard model

The three forces that affect particle physics: electromagnetism, the weak force<sup>1</sup> and the strong force, are described together with all the matter particles in what is known as the Standard Model. It was developed between 1960 and 1967, and has been found consistent with basically every experiment since.

**The Standard Model** The standard model describes which the elementary particles are, and how they interact, summarised in fig. i.4.

The matter particles (also known as Fermions), are divided up in three families, or generations, that each consist of four kinds of particles (known as flavours): 2 quarks, one electron and the (almost) massless neutrino. The three families differ only in the fact that the particles get heavier for each family, otherwise they are identical. It is only the first family that appear in nature, the second and third family have only been seen in high energy particle collisions.

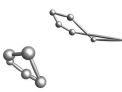
The three forces are described by the force carrying particles (known as Bosons). The electromagnetic force is carried by the photon, connecting to all particles with electric charge, that is all particles except the neutrinos, gluons, Z and itself. The strong force is carried by the gluons (they come in 8 different colours), and connects to coloured particles (the quarks and the gluons themselves). The weak force is carried by the W and Z Bosons, and connects to flavour, which includes all particles except the gluons and the photon.

From this, it is possible to derive all of physics (and chemistry and a large fraction of biology for that matter) except gravity.

It is however known that the standard model, for a number of reasons, will have to be modified. The most straightforward reason being that gravity is missing in the model, but also other more technical problems. There are many different ideas about how these flaws can be corrected by extending the model, but since no experiment has shown deviations from the standard model, it is hard to say which extension may be the correct one. This is why today's experimental particle physics is mainly about colliding particles at higher and higher energies, hoping to see deviations from the standard model that can give us a hint of where to go next.

---

<sup>1</sup>The weak force is responsible for some types of nuclear decay and radioactivity. It is not important for this thesis, and will not be mentioned much further.



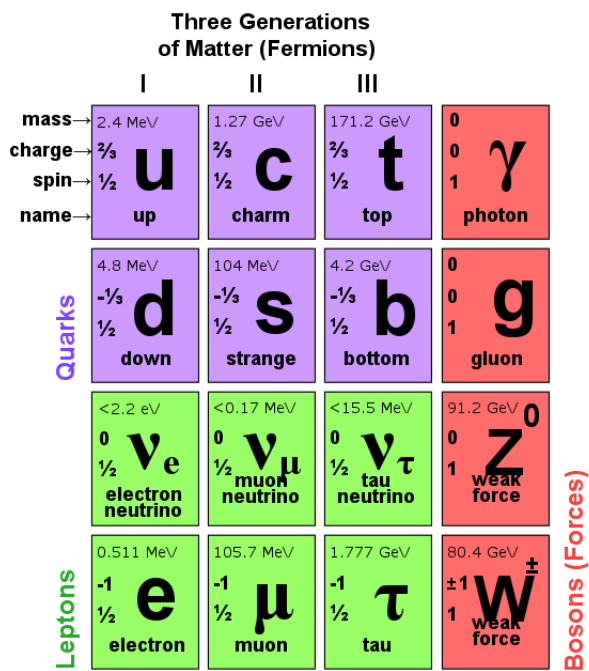


Figure i.4: The particle content of the standard model, 3 families of matter particles, and the force carriers for the electromagnetic ( $\gamma$ ), weak (W and Z) and strong (g) forces.

i.1.7 The strong force at hadron colliders

When exploring collisions at higher energies, it would be easiest to collide electrons, as they do not interact with the strong force. When colliding hadrons, it is more complicated than just colliding three quarks, as there is a constant swarm of gluons exchanged between the quarks. This is not at all as clean an experiment as electron collisions, and the particles coming out from the collisions are harder to interpret.

However, it is technically easier to accelerate a hadron to a high energy<sup>2</sup>. For example, the newly finished Large Hadron Collider, LHC, collides, as the name suggests, hadrons. Or to be more precise, it collides protons. This choice allows the LHC to go up to an energy of

<sup>2</sup>The reason for this is that the proton is heavier than the electron. Following the previous analogy, compare with throwing a watermelon or a pea at a box full of tomatoes as hard as you can. The watermelon will produce the more spectacular result, due to its larger mass.

14 TeV (although it is currently runs at only 7 TeV), which is about 100 times as much as the most energetic electron collider<sup>3</sup>.

While the energy is much higher at a hadron collider, it also presents the challenge to understand exactly how the quarks and swarms of gluons work in a collision. To determine if the experiments deviate from the standard model, we must understand what the standard model predicts, and in the case of hadron collisions, this is an extremely difficult task. The reason is, in short, that the strong force is strong. This means that there will a large number of gluons flying around between the quarks. To make things worse, gluons can not only be exchanged between the quarks, but also between the gluons. So every gluon exchanged between the quarks has the opportunity to halfway across exchange another gluon, which in turn can exchange more gluons. This goes on to create infinitely many gluons in any hadron, which is the main reason why the calculations are so difficult for hadron colliders.

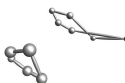
However, if we want to make use of the 100 times higher energy in the LHC, we must try to understand this procedure as exactly as possible, so that we can understand if LHC results are showing any deviations from the standard model, and if so, exactly what the deviations are.

And this finally is the problem which this thesis is addressing. It describes a model of the incoming quarks in a hadron, and how the quarks emit gluons before the hadron is collided with another hadron that has emitted gluons on its own. The model further studies what happens when the hadrons collide, and predictions are made for what we can expect to see coming out of the collisions. The model is based on “dipoles” which represent the strong force connecting the quarks and the gluons.

The model uses a computer program to simulate a collisions one gluon at a time. An example of such a collision from the program can be seen in the lower right corner, and by quickly flipping through all pages, a collision of two protons at the LHC can be seen. Here the two colliding protons are represented by three spheres (for the three quarks), connected by dipoles (for the continuous exchange of gluons). As the protons move towards each other, more and more gluons appear, which in turn form new dipole links to the previous gluons. After collision, the gluons go out in all directions, but still linked by the dipoles, and still

---

<sup>3</sup>Coincidentally, LHC is in the very same 27 km long circular tunnel as the previous electron collider, LEP, was in. This tunnel is at CERN, about 100 meters underground, close to Geneva.



more gluons and quarks are appearing.

## **i.2 Mathematical foundation**

In this section I will summarise the mathematical foundation of the work I have done. I will gradually go more and more into technical details in this section. Anyone without experience from physics arriving to the end of this section with a clear picture of what is going on is strongly encouraged to sign up to the theoretical physics education program at Lund University.

### **i.2.1 The observables**

To compare theory to experiments it is essential to understand exactly what is possible to measure, to know what should be calculated. To confirm or reject a model, it is of no help to have calculations of things that cannot be measured in reality. So let us review what kind of experiments and observations are made in particle physics.

The first observation is that it is not possible to directly observe what happens inside a particle collision, but the only thing measurable is what particles went in, and what particles came out. Thus, all observables must be formulated in terms of the incoming and outgoing particles only.

In practice, one will have a stream of particles showering some target, and the known number are the density of incoming particles per unit area, and the number of targets per unit area. So if there are  $a$  particles of type A incoming per  $\text{mm}^2$  showering  $b$  particles of type B incoming from the opposite direction, how often will I see particles X, Y and Z come out from collisions? The answer must clearly<sup>4</sup> be proportional to both  $a$  and  $b$ , and it will depend on both the incoming and outgoing particles. The expected number of times to see X, Y and Z

---

<sup>4</sup>The use of words like “clearly” and “obviously” is common in education, and does in general mean that the lecturer/author has a clear intuitive understanding of something, but has troubles in communicating this intuition to the students/readers with a brief explanation. In this specific case, it is useful to think of proportionalities by doubling one of the numbers and think what will happen: Imagine a shower of incoming particles hitting a number of particles incoming from the opposite direction, and collisions of different kinds will happen, spraying particles in all angles. If the incoming shower is turned up to double the number of particles per second, then there will be double as many particles spraying out, showing that  $N$  is proportional to  $a$ .



come out from a collision of  $A$  and  $B$  can then be written as

$$N_{AB \rightarrow XYZ} = ab\sigma(AB \rightarrow XYZ).$$

$\sigma(AB \rightarrow XYZ)$  must, from dimensional analysis, be an area, and can be interpreted as the area the incoming particles  $A$  has to hit on each particle  $B$  to produce the outgoing state  $XYZ$ .  $\sigma(AB \rightarrow XYZ)$  is called the cross section for  $AB$  going to  $XYZ$ , and is what is measured at any particle physics experiment.

i

### i.2.2 Feynman diagrams, and calculating a cross section

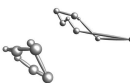
To calculate cross sections in particle physics, the by far most used mathematical framework is perturbative quantum field theory. Quantum field theory can be interpreted as a sum over histories:

Between two measurements, all involved particles can do literally anything before arriving at the second measurement, including turning into new particles, or merging with other particles. These infinitely many different histories of the particles are referred to as paths, so that each path represents what the particles did between the measurements. Each of the paths can be assigned an amplitude which to some extent can be interpreted as how probable that specific history is. The amplitude is calculated from the path using a so called *Lagrangian*, which is setting the rules for what particles are likely to do, and not to do. Thus, the Lagrangian can describe physics such as energy conservation, electromagnetism and so on. To find the probability, which is proportional to the cross section, to reach a certain final state for the second measurement, one has to sum all the amplitudes of the histories leading to that specific final state, and then square the sum:

$$\sigma(AB \rightarrow XYZ) \propto \left| \sum_{\text{paths from } AB \text{ to } XYZ} A_{\text{path}} \right|^2$$

The sum is over an uncountably infinite dimensional space, making it practically impossible to calculate directly. However, there are simplifications to be made.

The most common, and convenient, one is the Born approximation, where a minimum number of interactions happen. For example to calculate the cross section of an electron and a positron going to a quark and an antiquark, the Born approximation would include only one sin-



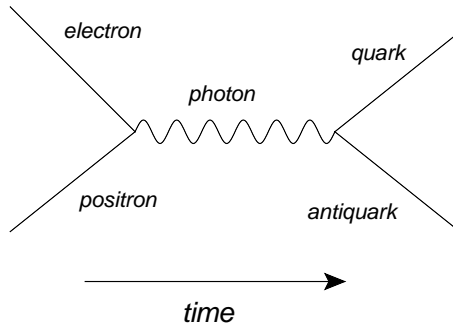


Figure i.5: The only Feynman diagram for  $e^-e^+ \rightarrow q\bar{q}$  in the Born approximation.

gle history, where the electron and positron merges to a photon, which then splits into a quark and an antiquark<sup>5</sup>, as is shown in figure i.5.

There are infinitely many other ways in which this can happen, which means that we are ignoring all but one of the terms in the sum over histories, but in this specific case the history in the Born approximation is dominating the sum, and the cross section is well described by this single term.

The drawings of these histories as lines and vertices as in figure i.5 are called Feynman diagrams, and are very helpful in calculating the amplitudes. In fact, each internal line (only the photon in this case) and each vertex is associated with a factor of the amplitude. These factors, called propagators for the lines and coupling constants for the vertices, depend on the Lagrangian. For the standard model Lagrangian which will be the only one considered in this thesis, the (simplified) factors are the ones marked in the figure, and the amplitude can easily be calculated to  $g_{\text{EM}}^2/q^2$ . Here, many details have been left out, such as the spin and charge of the particles, but it nonetheless illustrates the principle of how a cross section is calculated.

### i.2.3 QCD, not so simple

The above example was an electromagnetic interaction, where the Born approximation often is a good approximation. Other diagrams not included in the Born approximation have loops with extra vertices like the

<sup>5</sup>Actually, it is still infinitely many histories, since the particles are allowed to merge and split at any point in time and space. “One single history” here refers to which particles merges and splits in which order, not exactly when and where.

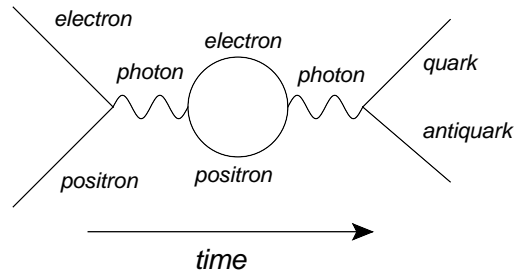


Figure i.6: A typical next to leading order diagram. The photon fluctuates into an electron-positron pair a short while before finally splitting into a quark and an antiquark.

one in figure i.6. These diagrams will have more factors of the coupling constant ( $g_{\text{EM}}$  in the case of electromagnetic vertices), and these contributions are referred to as “next to leading order” and “next to next to leading order”, or simpler NLO and NNLO, with one “next to” for each loop in the diagram. Thus the Born approximation is exactly the leading order calculation. In the case of electromagnetism, the coupling constant is small, so each extra factor of  $g_{\text{EM}}$  will make the amplitude smaller, which is the reason that the Born approximation reproduces experimental cross sections well for electromagnetism<sup>6</sup>.

In the case of QCD, short for quantum chromodynamics, the theory of the strong force, this is however not the case. As the name implies, the coupling in the strong force is much stronger than the electromagnetic one, and Feynman diagrams (histories) with more particles and vertices become increasingly important. Still the full sum over all histories is far too complicated to calculate, so some other way to sort out the most important terms in the sum is required.

**The DGLAP approximation** One of the most common simplifications is the DGLAP approach, where the transverse momentum (often referred to as  $Q^2$ ) of the outgoing particle is assumed to be large. Then a subset of the Feynman diagrams will dominate the sum over histories, and even though it is still very many diagrams, it is possible to sum them up and do calculations. In this limit, it is possible to express

<sup>6</sup>One can play the devil’s advocate and say that even if each diagram at higher order is smaller than the Born diagrams, there may be much more of the NLO diagrams and the sum of them can still be large. This is of course true, and it is an important effect, but in the case of electromagnetism, NLO is in general much smaller than LO.



the probability to find a gluon or a quark (or a parton as common name) with a given energy fraction  $x$  of the proton, and a given transverse momentum  $Q^2$ :

$$\frac{\partial q(x, Q^2)}{\partial \ln Q^2} = \frac{\alpha_s}{2\pi} \int_x^1 \frac{dy}{y} P(x/y) q(y, Q^2)$$

$q$  is the distribution of partons and  $P$  is the splitting function in this somewhat simplified version of the DGLAP equation. This formalism describes how the partons in a proton splits up, until finally one parton interacts with a parton from the colliding particle and bounces out at an angle respective to the incoming direction. The DGLAP approximation is valid as long as this last interaction is violent enough, that is if the outgoing particles have a large sideways (transverse) energy with respect to the incoming direction.

Most of the new physics that for example LHC is looking for involves very violent collisions, and the DGLAP formalism can in general describe these collisions. However, these collisions where new physics is expected to show up are very rare. Almost every collision involves comparably low transverse energies and the DGLAP approximation is pushed to its limit.

### i.2.4 BFKL: a high energy approximation

There is another common approach known as the BFKL equation. In this case the partons are assumed to carry only a small fraction of the incoming particles energy. This approximation is increasingly valid as the collision energy of particles increase, as the protons will tend to split up in more particles, each carrying a smaller fraction of the total energy. So at LHC BFKL is expected to better describe collisions than at previous, lower energy, colliders.

The BFKL equation is mathematically more complicated than the DGLAP equation though and significantly harder to use for predictions. As in the DGLAP formalism, the BFKL approximation selects a subset of all the possible histories, and calculates and sums only those amplitudes. These amplitudes are referred to as the “leading logarithm” (or just “LL” for short) amplitudes, as they contain the largest power of  $\ln(1/x)$ .  $x$  is here the fraction of the protons energy that the colliding parton carries, and in the BFKL approximation, this is a small number (hence also referred to as “low  $x$ ”). With  $x$  small,  $\ln(1/x)$  will be large, which motivates that only the “leading logarithm” amplitudes are considered.

There are however some technical problems. One is that the chosen LL amplitudes are actually not as dominating as one would like. In fact, if not only the LL diagrams are included, but also the amplitudes at the next highest power in  $\ln(1/x)$ , “next to leading logarithm” (NLL), the cross sections can change significantly.

BFKL has mainly been used to determine the probability that a collision will happen at all (so called “inclusive” observables), rather than to calculate exactly what all the outgoing particles will be (“exclusive” observables). Some approaches have been made to calculate these final states, but with very limited results.

During my PhD studies, I and my supervisors have been working on a formulation of the BFKL equation with colour dipoles that describes how the incoming hadronic particles evolve. While it originally was used only for inclusive observables, it is now developed to describe fully exclusive final states. It is implemented in a computer simulator called DIPSY than can generate collisions between particles such as protons, photons or heavy ions.

i

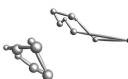
### i.3 The Lund Dipole Model: my contribution

This section will present the work done during my time in Lund, and I will from here on assume that the reader has previous experience from particle physics phenomenology.

I have continued the work on the dipole model in transverse coordinate space developed by Emil Avsar with Leif Lönnblad and Gösta Gustafson [1–3], and developed it further. Some studies were done on inclusive and semi-inclusive observables in deep inelastic scattering in paper I, on fluctuations in the interaction probability in paper II, and on the correlations between subcollisions in paper III, but the majority of the effort has been put into providing fully exclusive final states, and implementing an event generator with final state radiation and hadronization from ARIADNE [4] and PYTHIA 8 [5–8].

I will first describe the model as it is in the current implementation of the event generator, but bear in mind that the first three publication used an earlier version based on Avsar’s implementation. As this information is already in paper IV, this will be a shorter summary to get a good picture without having to read through all the details. Further details can be found in the paper.

After that will follow a discussion about future applications in different reaction, and what parts of the model can be further improved.



### i.3.1 Our model

Mueller formulated a dipole model [9–11] in transverse coordinate space and lightcone momentum space that could calculate inclusive cross section equivalently to leading logarithm BFKL. The transverse coordinate representation is excellent for taking saturation into account, both through multiple interactions, and in the cascade.

It was however known that BFKL has large NLL corrections, and Mueller’s model also suffered from computational problems as a diverging number of small dipoles with vanishing interaction probabilities were created.

**Energy conservation and NLL** Both of these problems can be solved by introducing energy conservation. Energy conservation is known to be a major part of the error in LL BFKL<sup>7</sup>, and by assigning lightcone momenta to the partons in the shower, one gets a dynamic cutoff for small dipoles. Here the small dipoles are related to a large transverse momentum  $q_{\perp} \propto 1/r$  with  $r$  the dipole size. To account for a larger part of the NLL corrections in BFKL, also a running coupling and  $q_+$  and  $q_-$  ordering (projectile-target symmetry in [12]) was added, both of which could easily be done dynamically for each emission in a Monte Carlo implementation. Also a confinement correction was added, suppressing very large dipole emissions.

Using a well defined transverse position and transverse momentum at the same time is at conflict with the uncertainty principle. The transverse points can be thought of as smeared out in coordinate space over a radius about the size of the smallest connecting dipole, giving an uncertainty in transverse momentum space  $\propto 1/r$ , which will set  $q_{\perp}$ .

**Saturation in the cascade** The interaction frame, the rapidity that each cascade is evolved to before collided, can be chosen to any point between the two particles, and the cross sections should be the same independently of this choice. The formulation in transverse coordinate space allows an easy inclusion of saturation in the interaction, but this does not provide a frame independent description as it only allows 1-to-2 vertex in the cascade. That is, for a frame independent description, a saturation effect is needed in the cascade as well.

---

<sup>7</sup>Most of the non-singular terms in [12] are simulated by energy conservation suppressing the large  $z$  region.

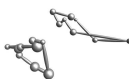
This triggered the inclusion of the dipole swing, a 2-to-2 interaction in the cascade that “swings” two dipoles by replacing them with two other dipoles connecting the colour charge of one dipole with the anticharge of the other dipole. The amplitude for the swing tends to replace large dipoles with small dipoles. Each dipole is randomly assigned a colour index, and only dipoles of the same colour are allowed to swing, to account for colour suppression in saturation. The swing can be interpreted as an exchange of soft gluons, or as a quadrupole effect. It was seen that the inclusive observables model got almost frame independent with this addition. It also turned out to dampen the energy growth of the  $pp$  cross sections to a level that agreed with data.

In general the Monte Carlo turned out to accurately describe a wide range of observables:

- Total and elastic  $pp$  cross section as function of  $\sqrt{s}$ .
- Elastic  $pp$  cross section as function of  $t$ .
- Diffractive excitation in  $pp$  as function of  $M_X^2$ .
- Total and elastic (DVCS) cross section in  $\gamma^*p$  as function of  $W$  and  $Q^2$ .
- Elastic cross section in  $\gamma^*p$  as function of  $t$ .
- $\gamma^*p \rightarrow pp$  (and other vector mesons) as function of  $W$ ,  $Q^2$  and  $t$ .

This was done with only four tunable parameters:  $\Lambda_{\text{QCD}}$ , the proton size  $r_p$ , the fluctuation in proton size  $\Delta r_p$  and the confinement scale  $r_{\text{max}}$ , also used for  $\alpha_S(r)$  freezeout. Notice that all four of these parameters are restricted (although  $\Delta r_p$  a bit less), in the sense that these quantities are to some extent known from experiments.

**Final states** Seeing the predictability for inclusive observables, we embarked on the project to extend the model to completely exclusive final states. The first observation is that the non-diffractive cross section can be rewritten in terms of independent subcollisions, so that it can be determined event-by-event which dipoles in the virtual cascade actually interact. Then, by tracing them back through the evolution, it is possible to divide up the partons in real partons that go to the final state and virtual partons that are reabsorbed. These gluons are the  $q_+$  and  $q_-$  ordered “backbone gluons”, that determine the inclusive cross section, and the remaining phase space for lower transverse momenta will be covered by final state radiation by the Linked Dipole Chain model based on the CCFM formalism. As the colour flow is considered all the way through this process it is natural to hadronize using the string



fragmentation model.

**Corrections needed: reweighting** It is however not as straightforward as it may sound in the paragraph above. One of the biggest problems is that, since Mueller's original model was designed for inclusive variables, the weights for small non-interacting dipoles will sometimes be overestimated. This does not affect any previous results, as non-interacting dipole do not affect the inclusive cross section, but it will give a too strong tail to large  $q_{\perp}$  in the final state. This is compensated for by removing some of the real gluons corresponding to this overestimate, and the weights of the gluon chains are restored.

**Ordering in the virtual cascade** As the kinematics of the real gluons are not known until the virtual gluons are reabsorbed, it is impossible to know what phase space should be allowed for real emissions during the virtual cascade. This problem is extended by the fact that some of the real gluons will be removed in the reweighting in the previous paragraph. To solve this, an overestimate of the allowed phase space is used during the virtual cascade. However, a balance has to be found, as too large overestimate will overproduce virtual dipoles, and the interaction probability will be inflated. Much care has been taken to find an allowed phase space that covers most of the important final states, while still not inflating the inclusive observables.

**Self consistency constraint: frame independence** The above problems get increasingly involved to handle in a saturated environment, where a gluon chain can split or merge at any point. Thus it has been very hard to use perturbative QCD to directly solve these issues. One of the most important tools has been the frame independence, that is that every observable should be the same no matter where the interaction frame is placed. It should not matter if the interaction frame is placed in the detector frame or in the rest frame of one of the incoming particles, all observables should still give the same result.

This symmetry is not exactly manifested in this model at fixed order, as the corrections to the LL formulation are not cover in exactly equivalent ways in the cascade and in the interaction. Thus, the cross section will differ depending on which part of the gluon chain is handled as the interaction, and which part as a cascade.

So when perturbative QCD cannot provide a clear solution to these problems, we have let this full-order symmetry guide the choices.



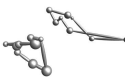
**Tuning** Now that the model is extended to exclusive observables, a number of new undetermined parameters and choices have been introduced. Every choice and parameter can not be fixed by theoretical considerations and frame independence alone; some has to be tuned to experimental data. We have started by tuning to inclusive observables: total and elastic  $pp$  and total  $\gamma^*p$ , before looking at exclusive observables. As it turned out, many of the parameters and choices could be set from the frame independence and inclusive data, leaving only little freedom to tune to exclusive observables. As many of the degrees of freedom are heavily correlated, basically only the charged particle multiplicity could be affected much. Once that was tuned to data, it was hard to move other observables much without destroying inclusive observables or frame independence.

It should be kept in mind that the tuning has been done by hand, and the data set that has been compared to is enormous: a big set of inclusive data for  $pp$  and  $\gamma^*p$ , and all minimum bias data available from for example CDF, ALICE and ATLAS. And further, each one of these observables is required to be frame independent. With a more systematic approach to tuning, the result can probably be significantly better.

### i.3.2 Further applications

The exclusive observables presented in the last paper has been from  $pp$  only, but there is in principle nothing that stops us from colliding any hadronic particle and generate final states. There is implemented support for virtual photons and heavy ions, but it has not been tuned or compared to data.

**AA** Maybe the most interesting reaction would be heavy ion collisions. With the dipole swing, there is a very detailed interaction between partons in the initial state, both within and between the nucleons. There are currently no collective effects in the final state evolution, so DIPSY would probably not reproduce data in its present state, but it can provide transverse position and momentum for every parton just after collision, giving all the necessary initial conditions for any final state models, be it jet quenching on a parton level, or hydrodynamics. Here it should be mentioned that DIPSY describes all the fluctuations in the initial state evolution, and could be used for observables such as triangular flow which are based on event-by-event fluctuations that are often neglected in heavy ion observables.



**$v_2$  in  $pp$  from elliptic flow** As example of how the real gluons just after the interaction can be used as input for collective effects, it has been used to measure elliptic flow in  $pp$  at the LHC. This work has been done in collaboration with Emil Avsar, Yoshitaka Hatta, Jean-Yves Ollitrault and Takahiro Ueda. The transverse configuration of the real gluons are used to calculate the participant eccentricity and the density of the state. An empirical formula from hydrodynamics is used to calculate  $v_2$  from the transverse  $t = 0$  configuration on an event-by-event basis. This is an example of where DIPSY shines, as we get the full fluctuations in the transverse shape and density from the BFKL dynamics.

This is then compared to the  $v_2$  obtained from the event generator with the default treatment of the final state with final state radiation and hadronization as normal. These two can be compared, and are showing the cases of no collective effects in the final state, and completely hydrodynamical collective behaviour. As one goes to higher multiplicities, one expects the collective effects to be more important, and a possible signal for collective effects could be in  $v_2$  deviating from the default DIPSY towards the hydrodynamical result.

This work can be found in a preprint [13] based on a preliminary version of DIPSY, but is not included in the thesis as there is a technical problem with the  $v_2$  observable in default DIPSY. This problem is related to the pointlike valence partons in section *i.3.3*, and the balancing jet will too often end up outside of the detector range, giving a too small  $v_2$ . At the time of printing, this problem is yet not solved, but we hope to soon have improvements to present.

**$pA, \gamma^*A$**  While  $AA$  is expected to have significant collective effects in the final state evolution,  $pA$  and especially  $\gamma^*A$  will have much less, and DIPSY can be directly used to describe both inclusive and exclusive observables.

**$\gamma^*p$**  This reaction was well tested for inclusive observables, and dipole models are traditionally successful in describing DIS. It is a somewhat different situation, as the valence partons of the photon will start the evolution with a large  $q_\perp$ , while the proton will start with a much lower  $q_\perp$ . This asymmetric evolution between a large and a small transverse momentum scale may highlight effects that were previously negligible and thus allow for further tuning of the model. So with the possible exception of a few corrections, we expect DIPSY to be able to reproduce exclusive  $\gamma^*p$  data as well.

### i.3.3 Future development

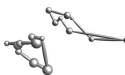
The recent publication of the final state Monte Carlo does not provide a final answer to how to get exclusive observables out of this dipole model. In fact, there is ample space for development, and I expect that more work in this model can significantly improve agreement with experiment. Here follows a list of areas where further attention could be useful.

**Real gluon ordering** We are allowing real gluon chains ordered in  $q_+$  and  $q_-$ , to approximately account for NLL BFKL and to match final state radiation phase space, but as observables are very sensitive to this, further investigations should be made.

**Ordering in the virtual cascade** Ideally we want to keep the ordering in the cascade open enough so that every conceivable ordered real gluon chain always is considered, no matter which partons are reabsorbed. However, as the real chain is not known during the virtual cascade, this would mean a large overestimate of emissions, and the inclusive cross sections would be inflated. It is possible to make a compromise that can describe inclusive cross section without affecting the final state too much (in fact DIPSY does this), but more systematic work has to be done on this problem.

**Full NLL splitting functions in momentum space** The interaction probability was recalculated in momentum space for the exclusive observables, as the coordinate space version had a logarithmic divergence for small distances. As the momentum space splitting function in the cascade had no such serious flaws, it never got recalculated in momentum space. However, it could still improve the description of the final states. At that point, a closer comparison to the NLL splitting function could be made.

**Pointlike valence partons** A proton at the LHC comes in with an  $p_+$  of 7 TeV, and this energy is split up on the three valence partons in our model. Some of this will radiate away during the cascade, but most of it will remain in the valence parton, which means that there will be three partons with a very large  $q_+$  still when the cascades has evolved almost all the way to the interaction frame. This will allow emissions with very large  $q_\perp$  from three partons in almost every collision. Even



though the large  $q_{\perp}$  is properly weighted with  $d^2q_{\perp}/q_{\perp}^4$ , one expects a further suppression from the small energy fractions of most of the incoming parton.

The cause of the problem is that modeling the proton as three point-like partons is not realistic, so to remedy this issue, a natural approach would be to smear out the valence partons in transverse space. This would disallow hard emissions, as the small wavelength would only resolve a small part of the valence parton, effectively being the opposite effect of coherence. Work is currently ongoing on this problem, and we hope to soon have new results.

## i.4 Introduction to papers

### i.4.1 Paper I: Elastic and quasi-elastic $pp$ and $\gamma^*p$ scattering in the Dipole Model

In this paper the model for inclusive observables developed previously is compared to a large set of observables in both  $pp$  and  $\gamma^*p$ . The total and elastic  $pp$  cross section had been described previously as function of  $\sqrt{s}$ , but now the elastic cross section as function of  $t$  is introduced, and the fluctuations in the proton wavefunctions has to be strongly reduced for the model to fit data. With this extra parameter introduced (bringing the total number of parameters up to 4), all  $pp$  data can be explained by the model. Some predictive power is also seen, as the energy dependence is to large extent independent of tuning but still agrees with data.

To better describe  $\gamma^*p$  at low  $Q^2$ , some soft correction are made to the photon wavefunction, and to describe semi-inclusive  $\gamma^*p \rightarrow \rho p$ , a dipole wavefunction is needed to describe the vector meson. The soft corrections introduce model dependence at low  $Q^2$  which is tuned to  $\sigma_{\text{tot}}(\gamma^*p)$  data, and two meson wavefunctions are used for comparison.

A large set of experimental data from HERA is compared to, and the model is in agreement with data for all observables, even for very low  $Q^2$ . The good agreement with experiments from very few parameters is very encouraging, and encourages the step to exclusive observables.

### i.4.2 Paper II: Fluctuations, Saturation, and Diffractive Excitation in High Energy Collisions

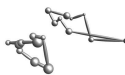
In this paper diffraction is studied, and it is shown how the fluctuations in interaction probability causes diffractive excitation. Saturation is proven to play an important role in limiting the fluctuations, and thus the diffractive excitations, in  $pp$ , and saturation is suggested to explain why diffractive excitation in  $\gamma^*p$  is larger than expected compared to  $pp$ . The impact parameter profile for diffraction is shown to take the shape of a ring that grows with energy. This analysis takes full advantage of the dynamic way in which the BFKL fluctuations are incorporated in the model, and can provide deep understanding of diffraction in this formalism.

Further, our dipole model in the Good–Walker formalism is compared to the triple–Regge formalism. Although saturation is an integral part of most triple–Regge models, and our dipole model, the comparison is made at a completely unsaturated level to easier compare the formalisms. It turns out that our dipole model without saturation reproduces the powerlike energy dependence at the foundation of any triple–Regge model. The energy dependence of our model for total, elastic and diffractive cross sections corresponds to pomeron trajectories and pomeron couplings, which are in the range spanned by traditional triple–Regge analyses. This makes a connection between our perturbative BFKL-based model and triple–Regge. Note however that the NLL corrections and confinement was still present in the comparison: only saturation was taken out. Pure LL BFKL may not be as similar to the triple–Regge formalism.

This paper triggers the question if final states for diffractive excitation are possible to simulate. It turns out that the situation is significantly more complicated, as the cross section does not split into dipole–dipole interaction probabilities as neatly as in the non-diffractive case. Nonetheless, we hope to return to this problem.

### i.4.3 Paper III: Correlations in double parton distributions at small $x$

In this paper we study correlations between two hard scatterings in a  $pp$  collision. It is done by collding a proton with two small dipoles representing the two hard interactions. The dependence on  $x_1, x_2, Q_1^2, Q_2^2$  and distance  $b$  between the interactions are studied, giving a full double parton distribution including all correlations. This again takes advan-



tage of the model including all fluctuations in the initial state cascade dynamically from BFKL.

We observe a strong dependence on  $Q^2$  and a weaker dependence on  $x$ . The factorisation of the  $b$  dependence is broken as hotspots appear at low  $x$  and large  $Q^2$ , and the distribution falls off quicker for large  $b$  if  $Q^2$  is large.

Events where one collision is in midrapidity, and the other shifted to a rapidity  $y$  are also studied. It turns out that the dependence on  $y$  is weak for the correlations, but not because the individual parton distribution functions depend weakly on  $y$ , but because the product of the distribution functions from the two sides have opposite  $y$  dependencies.

#### **i.4.4 Paper IV: Inclusive and Exclusive observables from dipoles in high energy collisions**

This paper presents the work started several years earlier, to model fully exclusive observables with the model, and to implement an event generator. It turns out to be more involved than initially expected and there are many non-leading corrections that are hard or impossible to treat with perturbative calculations, but that still affects observables. Nonetheless many options can be excluded as they give effects conflicting with known calculations (most frequently the  $d^2q_{\perp}/q_{\perp}^4$  tail to large  $q_{\perp}$ ), and other corrections turn out to not be needed in tuning (for example colour reconnections). Of the remaining uncertainties, many can be fixed by demanding frame independence, *i.e.* a self-consistency constraint, and most of the rest can be fixed from inclusive observables already studied in previous publications. The last remaining choices are tuned to exclusive data.

The resulting Monte Carlo, DIPSY, while not as accurate as PYTHIA 8 tune 4C, is providing a competitive description of minimum bias and underlying event data at the Tevatron and LHC. As it is conceptually different from the other event generators, it provides a good comparison, and the dynamic description of the incoming virtual cascade provides a unique opportunity for many studies, not least in heavy ion physics.

#### **i.4.5 List of contributions**

- **Paper I: Elastic and quasi-elastic  $pp$  and  $\gamma^*p$  scattering in the Dipole Model**

I wrote the new computer code necessary and ran all the simulations. I also contributed to the theoretical work and wrote a small part of the paper.

- **Paper II: Fluctuations, Saturation, and Diffractive Excitation in High Energy Collisions**

For this paper I again did all the simulations, contributed to the theoretical work and wrote parts of the paper.

- **Paper III: Correlations in double parton distributions at small  $x$**

I prepared the computer program for the new observables, but did not run the simulations. I contributed to the theoretical work, but wrote only little of the paper.

- **Paper IV: Inclusive and Exclusive observables from dipoles in high energy collisions**

This paper cover the bigger part of the thesis, and included rewriting the entire computer program. While Leif Lönnblad organised most of the structure, I wrote almost all the code, and designed many of the algorithms. I contributed to the theoretical work and wrote most of the paper.

i

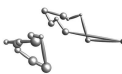
## i.5 A PhD defence for a non-physicist

This section is mainly aimed at those going to their first PhD defence in physics, and some general information and advice is presented.

### i.5.1 The schedule

The day begins with the defence at 10.15 (you probably want to be about 5-10 minutes early so you can get a good seat<sup>8</sup>, and an extra 5 minutes if you want to get coffee or tea). At the defence, the opponent start with a short presentation about the general area at as low level as possible, and will then hand over to me to shortly present my work which will be more technical. This will be about 30-45 minutes in total, and after that the main session starts, where the opponent will ask me questions about my work. After that, the 3 jury members will ask me a few questions each as well and finally the audience is allowed to ask me questions. There is no formal time limit, but usually the questions are done a bit after 12.

<sup>8</sup>You will notice that the jury and supervisors in general sit in the front rows, while most of the rest of the staff (specially the other PhDs) sit in the very back.



After the defence there will be mingling in the coffee room while waiting for the jury to make a decision that will be announced. Some small lunch is also served at this point. After lunch people go back to work for a few hours before preparing for the party at 19.

### **i.5.2 What to do during the defence?**

First, if you know that you tend to fall asleep when bored, make sure to get coffee before the defence! Ask someone that looks like a physicist for directions on where to get it.

Once at the defence, the presentation by the opponent will probably be the easiest to follow, so try to stay awake at least that part. After that, it will be increasingly hard to follow the details. However, the defence can still be enjoyed even without understanding every single subtlety. Some examples:

- One can often understand if a question was tricky or not from tone of voice, body language and how fast the reply is.
- If you would like to understand the physics a bit more, but can't follow the discussion, try reading the introduction above.
- Drinking game. Pick keywords such as "dipole", "parton", "interaction", "cascade", "proton", and drink every time your word is mentioned<sup>9</sup>.
- Hangman is great fun. Open a random page in the articles in the second half of the thesis, and pick a word that you have no idea what it means, and make a friend try to guess it. If you don't have pen and paper, you can scribble in the blank pages at the start/end of the thesis, and you can silently ask to borrow a pen from someone else in the audience.

---

<sup>9</sup>No responsibility taken for caffeine overdose.



## Acknowledgments

I am very lucky to have my two supervisors Leif Lönnblad and Gösta Gustafson, who have always been available for me. Leif has shown me how powerful computers can be for solving physics, and I have tried to absorb some of Gösta's ability to formulate even the most complex argument in a short, yet convincingly clear, manner.

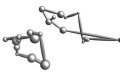
I want to thank Emil Avsar, Yoshitaka Hatta, Jean-Yves Ollitrault and Takahiro Ueda for inviting me to work with them, it has been a very useful experience. It has also been a pleasure to work with Andras Ster, I have always enjoyed your visits to Lund.

Apart from my supervisors, there are many others in Lund that have helped me with my work. For example Richard Corke who gave me computer support when I was too embarrassed to ask Leif a third time. Torbjörn Sjöstrand who always has time for a full explanation. Peter Christiansen who is always full of ideas, and a source for heavy ion expertise. And not least Alejandro Alonso for helping me with the ATLAS data.

I am grateful for a big group of proof-readers: Torbjörn Sjöstrand for taking the time to read through and provide top-notch feedback on the introduction and all the papers, making the end result so much better. Konrad Tywoniuk, Angela Pizzolla, Nils Lavesson and my family for reading and correcting this introduction.

The main reason I went into physics rather than mathematics towards the end of my undergraduate studies was that in physics people seemed more fun. The people here at theoretical physics in Lund, and our experimentalist friends, certainly delivered; it has been a lot of fun. You are too many to list here, but a special mention has to go to the group of seven from the Lund-HEP EST graduate school that helped me so much in feeling at home from the first day. Thanks to everyone for the company, see you around and stay sharp. ;)

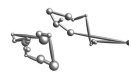
Last, I want to thank Angela for company and support. Now let's go somewhere warmer.



## *i* References

- [1] E. Avsar, G. Gustafson, and L. Lönnblad, “Energy conservation and saturation in small- $x$  evolution,” *JHEP* **07** (2005) 062, arXiv:hep-ph/0503181.
- [2] E. Avsar, G. Gustafson, and L. Lönnblad, “Small- $x$  dipole evolution beyond the large- $N(c)$  limit,” *JHEP* **01** (2007) 012, arXiv:hep-ph/0610157.
- [3] E. Avsar, G. Gustafson, and L. Lönnblad, “Diffractive Excitation in DIS and pp Collisions,” *JHEP* **12** (2007) 012, arXiv:0709.1368 [hep-ph].
- [4] L. Lönnblad, “ARIADNE version 4: A Program for simulation of QCD cascades implementing the color dipole model,” *Comput. Phys. Commun.* **71** (1992) 15–31.
- [5] B. Andersson, G. Gustafson, and B. Soderberg, “A GENERAL MODEL FOR JET FRAGMENTATION,” *Z. Phys.* **C20** (1983) 317.
- [6] B. Andersson, G. Gustafson, G. Ingelman, and T. Sjostrand, “Parton fragmentation and string dyanmics,” *Phys. Rept.* **97** (1983) 31.
- [7] T. Sjöstrand, S. Mrenna, and P. Z. Skands, “A Brief Introduction to PYTHIA 8.1,” *Comput. Phys. Commun.* **178** (2008) 852–867, arXiv:0710.3820 [hep-ph].
- [8] T. Sjöstrand, S. Mrenna, and P. Z. Skands, “PYTHIA 6.4 Physics and Manual,” *JHEP* **05** (2006) 026, arXiv:hep-ph/0603175.
- [9] A. H. Mueller, “Soft gluons in the infinite momentum wave function and the BFKL pomeron,” *Nucl. Phys.* **B415** (1994) 373–385.
- [10] A. H. Mueller and B. Patel, “Single and double BFKL pomeron exchange and a dipole picture of high-energy hard processes,” *Nucl. Phys.* **B425** (1994) 471–488, hep-ph/9403256.
- [11] A. H. Mueller, “Unitarity and the BFKL pomeron,” *Nucl. Phys.* **B437** (1995) 107–126, hep-ph/9408245.
- [12] G. P. Salam, “An introduction to leading and next-to-leading BFKL,” *Acta Phys. Polon.* **B30** (1999) 3679–3705, hep-ph/9910492.

- [13] E. Avsar, C. Flensburg, Y. Hatta, J.-Y. Ollitrault, and T. Ueda, “Eccentricity and elliptic flow in proton-proton collisions from parton evolution,” [arXiv:1009.5643](#) [hep-ph].





# I

## Elastic and quasi-elastic $pp$ and $\gamma^*p$ scattering in the Dipole Model

Christoffer Flensburg, Gösta Gustafson and Leif Lönnblad

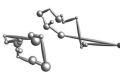
Department of Theoretical Physics, Lund University,  
Sölvegatan 14A, SE-223 62 Lund, Sweden

*European Physics Journal* **C60** (2009) 233-247 [hep-ph/0807.0325].

I

We have in earlier papers presented an extension of Mueller's dipole cascade model, which includes sub-leading effects from energy conservation and running coupling as well as colour suppressed saturation effects from pomeron loops via a "dipole swing". The model was applied to describe the total and diffractive cross sections in  $pp$  and  $\gamma^*p$  collisions, and also the elastic cross section in  $pp$  scattering. In this paper we extend the model to describe the corresponding quasi-elastic cross sections in  $\gamma^*p$ , namely the exclusive production of vector mesons and deeply virtual compton scattering. Also for these reactions we find a good agreement with measured cross sections. In addition we obtain a reasonable description of the  $t$ -dependence of the elastic  $pp$  and quasi-elastic  $\gamma^*p$  cross sections.

With kind permission of The European Physics Journal (EPJ).



## I.1 Introduction

We have in a series of papers [1–3] presented an extension of Mueller’s dipole cascade model [4–6] implemented in a Monte Carlo program, which includes sub-leading effects from energy conservation and running coupling, as well as colour suppressed effects from pomeron loops via a *dipole swing* mechanism. It also includes a consistent treatment of non-perturbative confinement effects, which suppress dipoles with large transverse extension.

The advantage of a cascade model formulated in transverse coordinate space is the possibility to include effects of multiple collisions and saturation in a straight forward way. While analytic results have mainly been presented for the asymptotic behavior of total and diffractive cross sections, Monte Carlo simulations facilitate studies of non-leading effects and more quantitative results. A simulation of Mueller’s initial model was presented by Salam in ref. [7]. Although giving finite results for the total cross section, this leading log evolution suffers from divergences for small dipoles, which caused numerical problems with very large gluon multiplicities and prevented simulations at higher energies. One important result from this analysis was the very large fluctuations in the evolution [8]. As the ratio between the elastic and the total cross sections is determined by the fluctuations in the scattering process, this implies that less fluctuations is needed in the impact parameter dependence, to reproduce the experimental data. As a result we found in ref. [3] that including the fluctuations in the evolution implies that the impact parameter profile is not as “black and white” as in analyses where only fluctuations in the impact parameter are taken into account.

In the model described in refs. [1–3] we include a number of sub-leading effects, with the aim that we in the end will be able to describe not only the total and diffractive cross sections, but also to generate fully exclusive final states. The main ingredient in our model is energy conservation, which is included by assigning a transverse momentum to each emitted gluon given by the maximum inverse size of the neighboring dipoles. As a result this also implies that the singularities for small dipoles are avoided. Other features are saturation effects in the evolution through a dipole swing mechanism, and a consistent treatment of confinement and running coupling effects in both dipole emissions and dipole–dipole interactions.

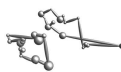
Taken together with a very simple model for the initial proton wave-

function, these features allow us to obtain a Lorentz-frame independent description of total cross sections, both for  $pp$  and DIS, using basically only two free parameters, a confinement scale  $\rho_{\max}$  and  $\Lambda_{\text{QCD}}$  [3]. The model gives a good description of measurements of the total and diffractive cross sections in  $pp$  and  $\gamma^*p$  collisions, and also for the elastic cross section in  $pp$ . In this paper we will continue our investigations with an analysis of exclusive production of vector mesons and real photons in  $\gamma^*p$ . The aim is to further test our model, and in particular to study the effect of the fluctuations in the cascade. We also extend the analyses to include the  $t$ -dependence of the (quasi-)elastic cross sections, including also elastic  $pp$  scattering, which in particular gives information about the properties of the incoming proton state. We here include effects of scewedness in the photon wavefunction, but argue that such effects in the proton wavefunction ought to be small at HERA and proton collider energies.

In the eikonal approximation the quasi-elastic  $\gamma^*p$  collisions contain three elements: the virtual photon–dipole vertex, the dipole–proton scattering amplitude, and the vertex for the transition between the dipole and the final vector meson or real photon. Here the first component can be calculated perturbatively, although a hadronic component must be included at lower  $Q^2$ -values. In an extensive study Forshaw *et al.* [9,10] have analyzed the results obtained from a set of models for the dipole–proton scattering and for the vector meson wavefunctions, and compared them with experimental data. In this paper we want to carry out a similar analysis, but now use our dipole cascade model for the dipole–proton scattering. We are here particularly interested in effects of fluctuations in the cascade evolution, which are not included in the analyses by Forshaw *et al.* We also want to use this study to put constraints on the state of the incoming proton.

An approach to describe both  $pp$  and  $\gamma^*p$  collisions in a dipole formalism has also been presented by Shoshi *et al.* [11]. One essential difference is that in their approach the energy dependence is described by a combination of a soft and a hard pomeron, with parameters fitted to data. In our model the energy dependence is fully determined by the perturbative dipole cascade evolution. Naturally this dynamical description limits the application of our model to relatively high energies.

We begin in section 1.2 with discussing the eikonal formalism for exclusive vector meson production, whereafter we describe our model for dipole evolution and dipole–dipole scattering in section 1.3 and the models we use for the proton, photon and vector meson wavefunctions



in section I.4. In section I.5 we retune the parameters of our model to data on total and elastic  $pp$  cross sections and the total  $\gamma^*p$  cross section before we present our results on quasi-elastic  $\gamma^*p$  cross sections on section I.6. Finally we present our conclusions in section I.7

## I.2 Formalism

### I.2.1 The dipole cascade model and the eikonal approximation

As discussed in the introduction, our model for  $pp$  collisions and DIS is an extension of Mueller's dipole cascade model [4–6]. In this formalism the probability per unit rapidity  $Y$  that a dipole  $(x, y)$  emits a gluon at transverse position  $z$  is given by

$$\frac{d\mathcal{P}}{dY} = \frac{\bar{\alpha}}{2\pi} d^2z \frac{(x-y)^2}{(x-z)^2(z-y)^2}, \quad \text{with } \bar{\alpha} = \frac{3\alpha_s}{\pi}. \quad (\text{I.1})$$

The evolution of this cascade agrees with the leading order BFKL evolution. As a consequence, the total number of dipoles grows exponentially. This also implies a strong growth for the total cross section which, however, is tamed by taking multiple dipole interactions into account. The scattering probability between two elementary colour dipoles with coordinates  $(x_i, y_i)$  and  $(x_j, y_j)$  respectively, is given by

$$\begin{aligned} f_{ij} &= f(x_i, y_i | x_j, y_j) \\ &= \frac{\alpha_s^2}{8} \left[ \log \left( \frac{(x_i - y_j)^2 (y_i - x_j)^2}{(x_i - x_j)^2 (y_i - y_j)^2} \right) \right]^2. \end{aligned} \quad (\text{I.2})$$

Within this eikonal formalism the transverse coordinates are not changed under the emission or scattering processes in eqs. (I.1) and (I.2). Therefore unitarity constraints and multiple scattering are easily accounted for by the exponentiated expression

$$T(\mathbf{b}) = 1 - e^{-\sum f_{ij}} \equiv 1 - e^{-F}, \quad (\text{I.3})$$

which implies that the scattering probability never exceeds 1. We note that the splitting probability in eq. (I.1) is singular for small dipole sizes  $x - z$  or  $z - y$ , but these small dipoles have a small probability to interact with the target, and the eikonal  $F = \sum f_{ij}$  is finite.

In the model developed in refs. [1–3], we extended Mueller's cascade model to include sub-leading effects from energy conservation and a



running coupling, saturation effects not only in the dipole–dipole sub-collisions but also within the individual cascades, and effects of confinement. These features are further discussed in sec. I.3.

The model is supplemented by a non-perturbative model for an initial proton in terms of three dipoles. In the eikonal approximation the total and the diffractive (including the elastic) cross sections are then given by

$$\begin{aligned}\sigma_{\text{tot}} &= 2 \int d^2b \langle (1 - e^{-F}) \rangle, \\ \sigma_{\text{diff}} &= \int d^2b \langle (1 - e^{-F})^2 \rangle.\end{aligned}\quad (\text{I.4})$$

The diffractive cross section can be separated in elastic scattering and diffractive excitation:

$$\begin{aligned}\sigma_{\text{el}} &= \int d^2b \langle (1 - e^{-F})^2 \rangle, \\ \sigma_{\text{diff exc}} &= \int d^2b \left\{ \langle (1 - e^{-F})^2 \rangle - \langle (1 - e^{-F}) \rangle^2 \right\}.\end{aligned}\quad (\text{I.5})$$

Thus the separation between elastic and inelastic diffraction is determined by the fluctuations in the scattering amplitude. The average in eqs. (I.4) and (I.5) is taken over the different incoming dipole configurations and different cascade evolutions, which thus give two separate sources for fluctuations.

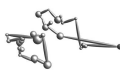
### I.2.2 DVCS and exclusive vector meson production in $\gamma^* p$ collisions

We want to study the exclusive processes

$$\gamma^* p \rightarrow V p, \quad V = \gamma, \rho, \psi, \dots \quad (\text{I.6})$$

In the dipole model the virtual photon is split into a  $q\bar{q}$  pair long before the collision. This dipole scatters elastically against the proton, and after the scattering the pair joins again forming a real photon or a vector meson. The formulation in the transverse coordinate plane makes it easier to study these pseudo-elastic reactions, and in the eikonal approximation the scattering amplitude is expressed in terms of three components:

$$\begin{aligned}\Im A_\lambda(s, \mathbf{b}) &= s \sum_{f, h, \bar{h}} \int \int dz \, d^2\mathbf{r} \, \Psi_{fh\bar{h}}^{*V\lambda}(\mathbf{r}, z) \Psi_{fh\bar{h}}^{\gamma\lambda}(\mathbf{r}, z, Q^2) \\ &\quad \times \hat{\sigma}_{dp}(s, \mathbf{r}, \mathbf{b}, z).\end{aligned}\quad (\text{I.7})$$



Here  $\mathbf{r}$  is the transverse size of the dipole,  $z$  and  $1 - z$  the fractions of the photon or vector meson carried by the quark and antiquark respectively, and  $h$  and  $\bar{h}$  their helicities.  $\lambda$  denotes the photon or vector meson helicity,  $\hat{\sigma}_{dp}$  is the dipole-proton scattering probability with  $\mathbf{b}$  the impact parameter, and  $s$  the total energy squared.

Neglecting the small contribution from the real part of the amplitude, the total cross section is given by

$$\sigma_\lambda(\gamma^*p \rightarrow Vp) = \frac{1}{4s^2} \int d^2\mathbf{b} |A_\lambda(s, \mathbf{b})|^2. \quad (1.8)$$

### 1.2.3 Differential cross sections

For scattering of a point particle the differential cross section  $d\sigma_{\text{el}}/dt$  is obtained from the Fourier transform of the scattering amplitude in eq. (1.3):

$$\frac{d\sigma_\lambda}{dt} = \frac{1}{4\pi} \left| \int d^2\mathbf{b} e^{i\mathbf{q}\mathbf{b}} \langle 1 - e^{-F} \rangle \right|^2, \quad (1.9)$$

with  $t = -\mathbf{q}^2$ . For a  $q\bar{q}$  dipole described by an extended wavefunction  $\Psi(\mathbf{r}, z)$ , Bartels, Golec-Biernat and Peters [12] have shown that the effect of non-forward amplitudes (also referred to as scewedness) are properly taken into account by replacing the exponential  $e^{i\mathbf{q}\mathbf{b}}$  by  $e^{i\mathbf{q}(\mathbf{b} - (1-z)\mathbf{r})}$ . Thus we obtain the following expression for the differential cross sections:

$$\begin{aligned} \frac{d\sigma_\lambda}{dt} = \frac{1}{16\pi} & \left| \sum_{f,h,\bar{h}} \int \int \int dz \, d^2\mathbf{r} \, d^2\mathbf{b} e^{i\mathbf{q}(\mathbf{b} - (1-z)\mathbf{r})} \right. \\ & \times \Psi_{f h \bar{h}}^{*V\lambda}(\mathbf{r}, z) \Psi_{f h \bar{h}}^{\gamma\lambda}(\mathbf{r}, z, Q^2) \\ & \left. \times \hat{\sigma}_{dp}(s, \mathbf{r}, \mathbf{b}, z) \right|^2. \end{aligned} \quad (1.10)$$

The effect of including the factor  $e^{-i(1-z)\mathbf{q}\mathbf{r}}$  is small for large  $Q^2$ , where the width of the  $\mathbf{r}$ -distribution  $\sim 1/\sqrt{z(1-z)Q^2}$  is small compared to the extension of the proton target, which in our model is determined by the parameter  $R_p$  estimated to be around  $3 \text{ GeV}^{-1}$ . As an example we find in section 1.6 (figure 1.7) that for DVCS the slope of the  $t$ -distribution at  $Q^2 = 8 \text{ GeV}^2$  is increased by about 7%. The effect is correspondingly reduced (increased) for higher (lower)  $Q^2$ .

Naturally a similar scewedness effect should come from the dipoles within the proton. This is more difficult to estimate, but the effect should

also here be determined by the ratio  $((1-z)r_{\text{dipole}}/R_p)^2$ . In our simulations of  $pp$  collisions at the Tevatron ( $W=2$  TeV) we find a typical value for *those dipoles which do interact* in the collision is about  $1/(1.5\text{GeV})$ . (The typical size is here estimated from the median of the distribution.) Thus we estimate the effect from scewedness in the proton wave function to be of the order  $((1-z)r_{\text{typical}}/R_p)^2 \sim 0.01$ , if typical  $z$ -values are around 0.5. A similar estimate can also be obtained from fits to minimum bias and underlying events in  $pp$  scattering. As an example, the PYTHIA 8 event generator [13] gives a good description of the underlying events at the Tevatron if a cutoff of around 2 GeV is introduced to regularize the (mini-)jet cross section, which diverges like  $dp_{\perp}^2/p_{\perp}^4$  in collinear factorization. This cutoff value can be interpreted as a screening length which in turn can be related to a typical dipole size.

It would be valuable to study this effect in more detail to find a better quantitative estimate. However, in view of the small value of the rough estimates above, we will in the present analysis neglect the effects of scewedness in the proton wave function. We note that in the rest frame of a 2 TeV  $pp$ -collision, the energy corresponds to an evolution over 7 units of rapidity for each of the protons. This corresponds to the proton evolution in DIS at  $W \approx 100$  GeV, and the estimate above is therefore also relevant for the proton wavefunction in DIS at HERA energies.

I

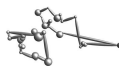
## I.3 The improved dipole cascade

As discussed in the introduction, the model developed in refs. [1–3]. is an extension of Mueller’s dipole cascade model, which includes sub-leading effects from energy conservation and a running coupling, saturation effects not only in the dipole–dipole subcollisions but also within the individual cascades, and effects of confinement. As mentioned above, an essential point is here that we include the effect of fluctuations in the dipole cascades in the calculation of the elastic or quasi-elastic cross sections.

### I.3.1 Non-leading perturbative effects

#### Energy-momentum conservation

It is known that the large NLO corrections to the BFKL evolution are reduced significantly if proper energy conservation is included in the leading order. In our model a small transverse extension is interpreted



as a large transverse momentum. This interpretation is supported by the resulting analogies between the dipole chains in coordinate space and the chains in the LDC model, which is formulated in momentum space and interpolates smoothly between DGLAP and BFKL evolution. Taking energy-momentum conservation into account is most easily done in a Monte Carlo (MC) simulation. Conserving both light-cone components,  $p_+$  and  $p_-$ , implies that we also satisfy the so called consistency constraint [14]. As small dipoles in our formalism correspond to large transverse momenta, energy conservation also gives a dynamical cutoff for the otherwise diverging number of small dipoles, and thus makes the MC simulation much more efficient.

### Running coupling

In our simulations we also include non-leading effects from the running of  $\alpha_s$ , both in the dipole splitting and in the dipole–dipole scattering probability. In the dipole emissions the scale in the coupling is given by  $\min(r, r_1, r_2)$ , where  $r$  is the size of the mother dipole which splits into  $r_1$  and  $r_2$ . This is the most natural choice and is also consistent with recent NLO calculations [15–17]. For the dipole–dipole scattering the situation is somewhat more complicated with basically six different dipole sizes involved. We have chosen to use the scale  $\min(|x_i - y_i|, |x_j - y_j|, |x_i - y_j|, |y_i - x_j|)$ . In order to avoid divergencies the coupling is in all cases frozen so that  $\alpha_s(r) \rightarrow \alpha_s(\min(r, r_{\max}))$ , where  $r_{\max}$  is the confining scale discussed in section 1.3.3 below.

### 1.3.2 Saturation within the cascades

Mueller’s cascade includes saturation effects from multiple collisions in the Lorentz frame chosen for the calculation, but not saturation effects from gluon interaction within the individual cascades. The result is therefore dependent on the chosen Lorentz frame. In ref. [2] we improved our model by allowing (colour suppressed) recouplings of the dipole chain during the evolution, a “dipole swing”. The swing is a process in which two dipoles  $(x_i, y_i)$  and  $(x_j, y_j)$  are replaced by two new dipoles  $(x_i, y_j)$  and  $(x_j, y_i)$ . The process can be interpreted in two ways. There is a probability  $1/N_c^2$  that the two dipoles may have the same colour, and the quark at  $x_i$  and the antiquark at  $y_j$  form a colour singlet. In this case the best approximation of the quadrupole field ought to be obtained by the closest charge-anticharge combinations. Here the

swing is therefore naturally suppressed by  $1/N_c^2$ , and it should be more likely to replace two given dipoles with two smaller ones. Secondly, we may see it as the result of a gluon exchange between the dipoles, which results in a change in the colour flow. In this case the swing would be proportional to  $\alpha_s^2$ , which again is formally suppressed by  $N_c^2$ , compared to the splitting process in eq. (I.1), which is proportional to  $\bar{\alpha} = N_c \alpha_s / \pi$ .

In the MC implementation each dipole is randomly given one of  $N_c^2$  possible colour indices. Only dipoles with the same colour can swing, and the weight for a swing  $(x_1, y_1), (x_2, y_2) \rightarrow (x_1, y_2), (x_2, y_1)$  is determined by a factor proportional to

$$\frac{(x_1 - y_1)^2 (x_2 - y_2)^2}{(x_1 - y_2)^2 (x_2 - y_1)^2}. \quad (\text{I.11})$$

This implies that the swing favors the formation of smaller dipoles. The number of dipoles is not reduced by the swing, but the fact that smaller dipoles have smaller cross sections gives the desired suppression of the total cross section. Although not explicitly frame independent the results from the MC simulations are very nearly independent of the Lorentz frame used for the calculations.

I

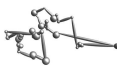
### I.3.3 Confinement effects

Mueller's dipole model is a purely perturbative process. It should therefore be applied to small dipoles, *e.g.* to heavy quarkonium states. When applying the dipole formalism to collisions with protons it is necessary to take confinement into account, in order to prevent the formation of very large dipoles. Confinement effects must also suppress long range interactions between colliding dipoles. In ref. [3] a consistent treatment of confinement was presented by replacing the Coulomb potentials in eqs. (I.2) and (I.13) by screened potentials, with a screening length  $r_{\max}$ .

Obviously the dipoles produced in the splitting process in eq. (I.1) cannot become too large, and it is natural to introduce a scale  $r_{\max}$ , so that larger dipoles are suppressed. In a similar way confinement must suppress long range interactions between colliding dipoles.

The formula for  $f_{ij}$  in eq. (I.2) is just the two dimensional Coulomb potential, and can be written as

$$f(x_i, y_i | x_j, y_j) = \frac{g^4}{8} \left[ \Delta(x_i - x_j) - \Delta(x_i - y_j) - \Delta(y_i - x_j) + \Delta(y_i - y_j) \right]^2 \quad (\text{I.12})$$



where  $\Delta(\mathbf{r})$  is the Green's function given by

$$\Delta(\mathbf{r}) = \int \frac{d^2\mathbf{k}}{(2\pi)^2} \frac{e^{i\mathbf{k}\cdot\mathbf{r}}}{k^2}. \quad (\text{I.13})$$

To take confinement into account we replace the infinite range Coulomb potential with a screened Yukawa potential. This implies that the Coulomb propagator  $1/k^2$  in eq. (I.13) is replaced by  $1/(k^2 + M^2)$ , where  $M = 1/r_{\text{max}}$  is the confinement scale. As a result, the four functions  $\Delta$  in eq. (I.12) will be replaced by

$$\int \frac{d^2\mathbf{k}}{(2\pi)^2} \frac{e^{i\mathbf{k}\cdot\mathbf{r}}}{k^2 + 1/r_{\text{max}}^2} = \frac{1}{2\pi} K_0(r/r_{\text{max}}) \quad (\text{I.14})$$

with  $K_0$  a modified Bessel function. For small separations, where  $r \ll r_{\text{max}}$ , the function  $K_0(r/r_{\text{max}})$  behaves like  $\ln(r_{\text{max}}/r)$ , and we then recognize the result in eq. (I.2). For large separations,  $r \gg r_{\text{max}}$ ,  $K_0(r/r_{\text{max}})$  falls off exponentially  $\sim \sqrt{\frac{\pi r_{\text{max}}}{r}} e^{-r/r_{\text{max}}}$ , as expected from confinement.

In a similar way, the underlying Coulomb potential in the dipole splitting function in eq. (I.1) can be replaced by a screened Yukawa potential, using again the replacement  $1/k^2 \rightarrow 1/(k^2 + 1/r_{\text{max}}^2)$ . The modified splitting probability is then given by

$$\begin{aligned} \frac{d\mathcal{P}}{dY} \rightarrow \frac{\bar{\alpha}}{2\pi} d^2\mathbf{z} \quad & \left\{ \frac{1}{r_{\text{max}}} \frac{\mathbf{x} - \mathbf{z}}{|\mathbf{x} - \mathbf{z}|} K_1\left(\frac{|\mathbf{x} - \mathbf{z}|}{r_{\text{max}}}\right) \right. \\ & \left. - \frac{1}{r_{\text{max}}} \frac{\mathbf{y} - \mathbf{z}}{|\mathbf{y} - \mathbf{z}|} K_1\left(\frac{|\mathbf{y} - \mathbf{z}|}{r_{\text{max}}}\right) \right\}^2. \end{aligned} \quad (\text{I.15})$$

For small arguments  $K_1(r/r_{\text{max}}) \approx r_{\text{max}}/r$ , from which we get back the result in eq. (I.1), while for large arguments  $K_1(r/r_{\text{max}}) \sim \sqrt{\pi r_{\text{max}}/r} \cdot e^{-r/r_{\text{max}}}$ , and once again we obtain an exponentially decaying field.

## I.4 Initial wave functions

### I.4.1 Proton wave function

In ref. [2] we also introduced a simple model for the proton in terms of three dipoles with extensions determined by a Gaussian distribution. The resulting model was in good agreement with total cross sections

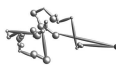
for both DIS and  $pp$  collisions. It was shown in [18] that, although a full gluon cascade from three valence quarks in a proton is not a simple expression, the emission of the first gluon has the same distribution in transverse space as three dipoles, only with half the intensity. Thus, by modeling the proton with a closed chain of three gluons we emulate the fact that a proton at rest may contain more charges than its valence quarks. This is analogous to the finding of Glück, Reya and Vogt, who needed a large valence-like gluon component when trying to fit parton densities evolved from a very low scale [19]. Thus, although not a fully realistic description of the initial non-perturbative proton state, the model appears to give a fair representation of the multi-dipole system obtained at the low  $x$ -values, which are important for the high energy collisions.

The results turned out to be almost independent of the shape of the three starting gluons, except for the size of the triangle. In fact, equilateral triangles that were allowed to vary in only size and orientation turned out to model the proton as well as more complicated formations. With a Gaussian distribution for the size of equilateral triangles, motivated by the exponential dependence on  $t$  for the elastic cross section, data on total cross sections for DIS and  $pp$  collisions are well reproduced, when the width of the Gaussian was tuned to  $3.5 \text{ GeV}^{-1} \approx 0.66 \text{ fm}$ .

As discussed above, the differential and elastic cross sections are determined by the fluctuations in the scattering amplitude, and in ref. [3] it was pointed out that a Gaussian wavefunction as discussed above must overestimate the fluctuations of the incoming state in its rest frame. The probability for the three quarks to simultaneously be located in a single point ought to be suppressed, and it was emphasized that the exponential  $t$ -dependence of the elastic cross section, which motivated the Gaussian shape, is only observed for  $|t| < 0.15 \text{ GeV}^2$ , corresponding to  $b \gtrsim 1 \text{ fm}$ . A wavefunction of the form

$$|\Psi|^2 = C e^{-(r-R_p)^2/w^2} \quad (\text{I.16})$$

was also tested, and found to give essentially identical total cross sections. The fluctuations are here suppressed by a small value of  $w$ , and in ref. [3] it was observed that reducing the fluctuations to a minimum gave good agreement with the integrated elastic and diffractive cross sections in  $pp$  collisions. Lacking further constraints we could, however, only present an upper limit for  $\sigma_{\text{el}}$ , by neglecting the fluctuations in the wavefunction, thus including only those in the cascade evolution.



An essential motivation for the present analysis of quasi-elastic  $\gamma^*p$  cross sections and of the  $t$ -dependence of the  $pp$  elastic cross section, is to check whether the fluctuations in the dipole cascade model are also consistent with these observables, and if more constraints can be put on the shape of the initial proton state. In this analysis we will use the two-parameter form in eq. (I.16), and see if this can be adjusted to reproduce also the (quasi-)elastic cross sections.

At this point we also note that in many analyses the fluctuations in the cascade evolution are neglected. This means that  $e^{-F}$  is replaced by  $e^{-\langle F \rangle}$  in eqs. (I.4) and (I.5). Including also the fluctuations in the cascade implies that the impact parameter profile has to be more “gray” and less “black and white”. As an example the amplitude  $\langle T(b=0) \rangle$  is a factor 2/3 smaller in our formalism than in the analysis by Kowalski and Teaney [20], for a dipole of size  $2\text{GeV}^{-1}$  and  $x = 10^{-4} - 10^{-5}$ .

## I.4.2 Photon wavefunction

### Large $Q^2$

For large  $Q^2$  the coupling of the  $\gamma^*$  to the  $q\bar{q}$  pair can be calculated perturbatively. The well known result to leading order is

$$\begin{aligned}\Psi_{f\bar{h}\bar{h}}^{\gamma 0}(Q, r, z) &= \frac{\sqrt{\alpha_{EM}N_C}}{\pi} Qz(1-z)e_f K_0(r\varepsilon_f)\delta_{h\bar{h}} \\ \Psi_{f\bar{h}\bar{h}}^{\gamma +}(Q, r, z) &= \frac{\sqrt{\alpha_{EM}N_C/2}}{\pi} e_f \\ &\times \left( ie^{i\theta} (z\delta_{h+}\delta_{\bar{h}-} - (1-z)\delta_{h-}\delta_{\bar{h}+}) \varepsilon_f K_1(r\varepsilon_f) \right. \\ &\quad \left. + \delta_{h+}\delta_{\bar{h}+} m_f K_0(r\varepsilon_f) \right)\end{aligned}\quad (\text{I.17})$$

with

$$\varepsilon_f = \sqrt{z(1-z)Q^2 + m_f^2}. \quad (\text{I.18})$$

Here  $\lambda = 0$  and  $+$  denote the longitudinal and transverse wavefunctions respectively,  $f$  denotes the quark flavour, and  $K_0$  and  $K_1$  are modified Bessel functions.  $e_f$  is the electric charge of the quark in units of the proton charge and  $m_f$  the effective mass of the quark.

### Smaller $Q^2$

For smaller  $Q^2$  the photon has also a hadronic component. In [21] it was shown that also the total  $\gamma^*p$  cross section at HERA could be



well described over a wide range of energies and virtualities, when the hadronic component was simulated by a relatively small effective quark mass  $\approx 60$  MeV. For the exclusive reactions studied here we need a more careful treatment of the hadronic component, and we expect that these processes can provide relevant constraints on the photon wavefunction. The hadronic component should be particularly important for the real photons produced in Deeply virtual Compton scattering (DVCS).

For small  $Q^2$  a small effective quark mass allows for rather large dipoles with a corresponding large cross section. In the present analysis we include an improved description of confinement effects in the dipole evolution (see section I.3.3), and we will therefore try to include confinement effects also in the photon wavefunction. Our photon model is inspired by the Vector Meson Dominance modeling introduced by Forshaw *et al.* in [9] (which, in turn, was inspired by [22]). This model contains an enhancement factor for dipoles of a typical hadronic size, together with a large quark mass which suppresses dipoles larger than the confinement scale. In our model we will use the same enhancement factor, but we use a suppression of large dipoles related to the confinement scale  $\rho_{\max}$ , instead of the large quark mass used in ref. [9].

The actual implementation in our MC program relies on shrinking dipoles larger than  $\rho_{\max}$  by reducing the size  $r_{\text{pert}}$  generated according to the perturbative photon wavefunction to  $r_{\text{soft}}$ , defined by

$$r_{\text{soft}}(r_{\text{pert}}) = R_{\text{shrink}} \sqrt{\ln \left( 1 + \frac{r_{\text{pert}}^2}{R_{\text{shrink}}^2} \right)}. \quad (\text{I.19})$$

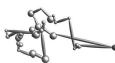
For small dipoles this gives  $r_{\text{soft}} \approx r_{\text{pert}}$ , but for large dipoles it gives a Gaussian suppression. The parameter  $R_{\text{shrink}}$  is adjusted to give the same effective cutoff,  $\rho_{\max}$ , as the one obtained for large dipoles in the cascade evolution. This is obtained for  $R_{\text{shrink}} = 4.3 \text{ GeV}^{-1}$ .

The enhancement factor for dipoles with a typical hadronic size, introduced in ref. [9], is given by the form

$$f(r) = \frac{1 + B_V \exp(-(r - R_V)^2/w_V^2)}{1 + B_V \exp(-R_V^2/w_V^2)} \quad (\text{I.20})$$

This factor multiplies the squared photon wavefunction after the shift in eq. (I.19). The enhancement resembles very much the shape we use for the proton wavefunction in eq. (I.16), and we can think of the whole correction

$$|\Psi_\gamma(r_{\text{pert}})|^2 \rightarrow |\Psi_\gamma(r_{\text{soft}})|^2 f(r_{\text{soft}}) \quad (\text{I.21})$$



as the modeling of the virtual photon fluctuating into vector meson states with  $r$ -values of a hadronic scale. Partly this enhancement can be thought of as due to a longer lifetime of these states, and partly a simulation of a gluonic component in the vector meson, in a way similar to our model of the initial proton wavefunction in section I.4.1. The photon model contains three adjustable parameters,  $B_V$ ,  $R_V$ , and  $w_V$ , which have to be determined from experiments.

### I.4.3 Meson wavefunctions

The wavefunction of a vector meson cannot be calculated perturbatively, and has to be described by models. In the rest frame it is generally assumed that the lowest Fock state with a single  $q\bar{q}$  pair dominates. This component must then be normalized to 1, in contrast to the photon for which the  $q\bar{q}$  state is a perturbative fluctuation. In addition the wavefunction at the origin is determined by the decay rate of the vector meson. Thus there are two constraints allowing two parameters in an ansatz to be determined. In a boosted frame higher Fock states may then be generated by gluon emission. Different models can differ in the functional form used for the wavefunction in the rest frame, and in the description of the transition from coordinate space to the momentum fractions  $z$  and  $1 - z$  used in the light-cone wavefunction. We will here concentrate on the DGKP model [23] and the boosted Gaussian model [9], which in the analysis by Forshaw *et al.* give the best agreement with the experimental data.

In both models, the wavefunction in momentum light-cone coordinates is assumed to have the same spin structure as the photon wavefunction, and the relative scalar factor is parametrised by a function  $\Gamma_\lambda(k, z)$ , such that

$$\begin{aligned} \Psi_{hh}^{V\lambda}(k, z) &= \sqrt{\frac{N_c}{4\pi}} \frac{\bar{u}_h(\mathbf{k})}{\sqrt{z}} (\gamma, \varepsilon_V^\lambda) \frac{v_h(-\mathbf{k})}{\sqrt{1-z}} \\ &\times \frac{z(1-z)\Gamma_\lambda(k, z)}{-z(1-z)M_V^2 + k^2 + m_f^2}. \end{aligned} \quad (\text{I.22})$$

If the polarisation vectors are written out explicitly, the longitudinal meson wavefunction is proportional to

$$\frac{z(1-z)2M_V\Gamma_\lambda(k, z)}{-z(1-z)M_V^2 + k^2 + m_f^2} + \frac{\Gamma_\lambda(k, z)}{M_V}. \quad (\text{I.23})$$

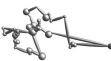
In the case of a photon the second term corresponds to a term equal to  $-1/Q$ . This represents a dipole of vanishing size, and would not contribute to the cross section. The dependence on  $\mathbf{k}$  in the meson case implies that also the second term contributes, which creates problems with gauge invariance. Apart from choosing different functions  $\Gamma_\lambda(k, z)$ , the two models also differ in that DGKP neglects this second term, while this term is kept in the boosted Gaussian model. This is represented by a parameter  $\delta$ , taking the values 0 (DGKP) or 1 (boosted Gaussian). More details can be found in [9] and references therein.

### The DGKP model

In this model for the meson wavefunction, proposed by Dosch, Gousset, Kulzinger, and Pirner [23], it is assumed that the dependence on the transverse and longitudinal coordinates,  $r$  and  $z$ , factorizes. The transverse part of the wavefunction is assumed to be a pure Gaussian, consistent with soft hadron-hadron collisions. For the longitudinal component it assumes the form proposed by Wirbel, Stech and Bauer [24]. The resulting light-cone wavefunction has the following form:

$$\begin{aligned}
 \Psi_{fh\bar{h}}^{V0}(r, z) &= \mathcal{N}_0 M_V \delta_{-h\bar{h}} z(1-z) \sqrt{z(1-z)} \\
 &\times \exp\left(-\frac{r^2 \omega_L^2}{2}\right) \exp\left(-\frac{M_V^2 (z-0.5)^2}{2\omega_L^2}\right) \\
 \Psi_{fh\bar{h}}^{V+}(r, z) &= \mathcal{N}_+ \sqrt{z(1-z)} \\
 &\times \left(\omega_T^2 r i e^{i\theta} (z\delta_{h+}\delta_{\bar{h}-} - (1-z)\delta_{h-}\delta_{\bar{h}+}) + m_f\right) \\
 &\times \exp\left(-\frac{M_V^2 (z-0.5)^2}{2\omega_T^2}\right) \exp\left(-\frac{r^2 \omega_T^2}{2}\right). \quad (\text{I.24})
 \end{aligned}$$

Here  $M_V$  is the mass of the vector meson, and the size parameter  $\omega$  and the normalization constant  $\mathcal{N}$  are determined from the electronic decay rate and the normalization condition. (Our notation differs from the original paper, as we have collected the multiplicative factors in the normalization constant  $\mathcal{N}$ .) The shape of the wavefunction of the  $\rho$  with the parameters we have used (see table I.1) can be seen in figure I.1.



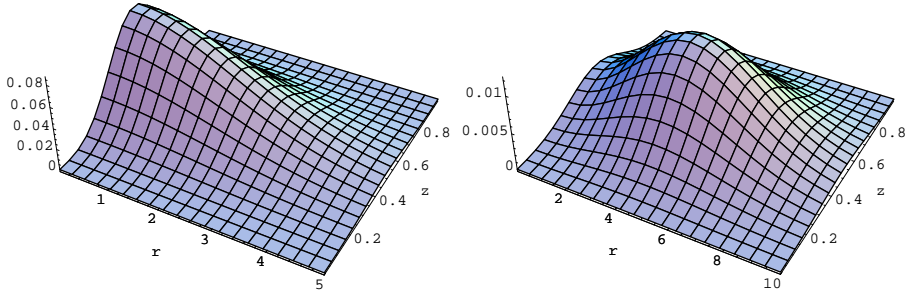


Figure I.1: The wavefunctions  $|\Psi_L(r, z)|^2$  (left) and  $|\Psi_T(r, z)|^2$  (right) of the DGKP model for a  $\rho$  meson with our quark mass of 60 MeV. Note the different scales in  $r$ , both in  $\text{GeV}^{-1}$ .

#### Boosted Gaussian

$V$	$M_V$	$m_f$	$R^2$	$\mathcal{N}_0$	$\mathcal{N}_+$
$\rho$	0.77	0.06	12.3	0.44	0.68
$\phi$	1.02	0.15	10	0.41	0.63
$\psi$	3.1	1.4	5.95	0.23	0.32

#### DGKP

$V$	$M_V$	$m_f$	$\omega_L$	$\omega_T$	$\mathcal{N}_0$	$\mathcal{N}_+$
$\rho$	0.77	0.06	0.33	0.22	1.63	2.18
$\phi$	1.02	0.15	0.37	0.26	1.86	1.91
$\psi$	3.1	1.4	0.69	0.56	1.28	0.79

Table I.1: The parameters used for the boosted Gaussian and DGKP wavefunctions in this paper in  $\text{GeV}$ -based units.

### The boosted Gaussian model

The “boosted” models are obtained by assuming a given wavefunction in the meson rest frame. This is then boosted into a light-cone wavefunction using the Brodsky-Huang-Lepage prescription [25], in which the invariant mass of the quark-antiquark pair is the same in the rest frame and the light-cone frames. The result of this procedure is not factorizing in  $r$  and  $z$ . In the simplest version the initial wavefunction in the rest frame is a simple Gaussian. In an alternative version by Nemchik *et al.* [26] a hard Coulomb contribution is added, dominating for small  $r$ . For the pure Gaussian version suggested by Forshaw *et al.*, which we

assume in this analysis, the resulting wavefunction has the following form

$$\begin{aligned}\Psi_{fh\bar{h}}^{V0}(r, z) &= \frac{\mathcal{N}_0}{M_V} \exp\left(-\frac{m_f^2 R^2}{8z(1-z)}\right) \\ &\times \exp\left(-2z(1-z)\frac{r^2}{R^2}\right) \exp\left(\frac{R^2}{2}m_f^2\right) \\ &\times \left(z(1-z)M_V^2 + m_f^2 + 8\frac{z(1-z)}{R^2}\right. \\ &\quad \left.- \left(4\frac{z(1-z)r}{R^2}\right)^2\right) \delta_{h\bar{h}}\end{aligned}\quad (\text{I.25})$$

$$\begin{aligned}\Psi_{fh\bar{h}}^{V+}(r, z) &= \mathcal{N}_+ \exp\left(-\frac{m_f^2 R^2}{8z(1-z)}\right) \\ &\times \exp\left(-2z(1-z)\frac{r^2}{R^2}\right) \exp\left(\frac{R^2}{2}m_f^2\right) \\ &\times \left(4z(1-z)\frac{r}{R^2}ie^{i\theta}(z\delta_{h+}\delta_{\bar{h}-} - (1-z)\delta_{h-}\delta_{\bar{h}+})\right. \\ &\quad \left.+ m_f\delta_{h+}\delta_{\bar{h}+}\right)\end{aligned}\quad (\text{I.26})$$

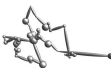
I

In this model the transverse size  $R$  of the meson, and the normalization  $\mathcal{N}_\lambda$  are the two parameters to be determined from normalisation and decay width. (In our notation all multiplicative constants have also here been included in a single normalization constant.) The shape of the wavefunction for the  $\rho$  meson using the parameters in table I.1 is shown in figure I.2.

## I.5 Tuning of parameters and the differential $pp$ cross section

### I.5.1 The total and elastic $pp$ cross section

We start by tuning the model to  $pp$  scattering data. Here the model contains 4 parameters,  $\Lambda_{\text{QCD}}$  and  $r_{\text{max}}$  describing the dipole evolution, and  $R_p$  and  $w$  determining the proton wave function in eq. (I.16) (with  $C$  fixed by normalization). In ref. [3] we found that the values for  $\Lambda_{\text{QCD}}$  and  $r_{\text{max}}$  are correlated, such that a larger  $r_{\text{max}}$  can be compensated by a smaller  $\Lambda_{\text{QCD}}$ . It was also noted that the integrated elastic



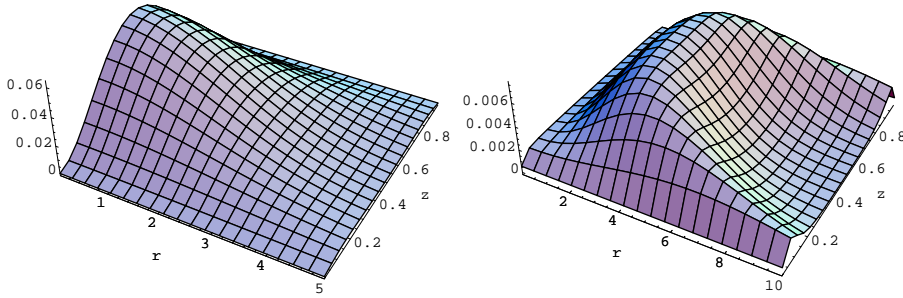


Figure 1.2: The wavefunctions  $|\Psi_L(r, z)|^2$  (left) and  $|\Psi_T(r, z)|^2$  (right) of the Boosted Gaussian model for a  $\rho$  meson with our quark mass of 60 MeV. Note the different scales in  $r$ , both in  $\text{GeV}^{-1}$ .

cross section favors a narrow proton wave function, corresponding to a small value for the parameter  $w$ . A large  $w$ -value, or a single Gaussian  $\propto \exp(-\mathbf{r}^2/R_p^2)$ , gives too large fluctuations and correspondingly a too small elastic cross section. To constrain the fit we here add the differential cross section  $d\sigma/dt$  to the integrated cross sections  $\sigma_{\text{tot}}$ ,  $\sigma_{\text{diff}}$ , and  $\sigma_{\text{el}}$  studied in [3]. We will then in next section check if the result also can reproduce the quasi-elastic cross sections in  $\gamma^*p$  collisions.

With the proton wavefunction given by eq. (1.16) the total and elastic cross sections are given by

$$\sigma_{\text{tot}} = 2 \int d^2\mathbf{b} \int d^2\mathbf{r}_{p1} d^2\mathbf{r}_{p2} |\Psi_p(\mathbf{r}_{p1})|^2 |\Psi_p(\mathbf{r}_{p2})|^2 \langle 1 - e^{-F} \rangle_{12}, \quad (1.27)$$

$$\sigma_{\text{el}} = \int d^2\mathbf{b} \left| \int d^2\mathbf{r}_{p1} d^2\mathbf{r}_{p2} |\Psi_p(\mathbf{r}_{p1})|^2 |\Psi_p(\mathbf{r}_{p2})|^2 \langle 1 - e^{-F} \rangle_{12} \right|^2. \quad (1.28)$$

Here  $\mathbf{b}$  is the impact parameter,  $\mathbf{r}_{pi}$  ( $i = 1, 2$ ) parameterizes the size and orientation of the triangles describing the colliding protons. The Monte Carlo is used to simulate the dipole evolution in the rest frame of the collision, and to calculate  $1 - e^{-F}$ . The average  $\langle 1 - e^{-F} \rangle_{12}$  is over simulations for fixed impact parameter and starting dipole states  $\mathbf{r}_1$  and  $\mathbf{r}_2$ . Note that in the elastic cross section the average over evolutions and

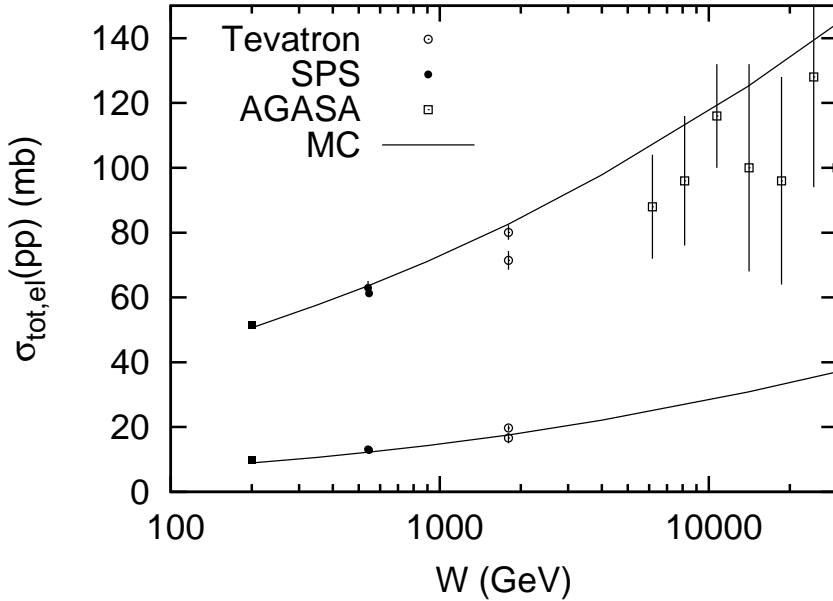


Figure I.3: The total and elastic cross section for  $pp$  collision. The upper cross sections are total cross sections, while the lower cross sections are the elastic ones. Tevatron data are from [27–30], SPS data are from [31] and cosmic ray data are from [32]. The lines are our model with tuned parameters.

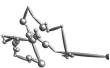
I

the integrals over the wave functions is taken on amplitude level before taking the absolute square.

When tuning the parameters we find that all observables are almost independent of  $w$  below  $0.5 \text{ GeV}^{-1}$ . We therefore decided to neglect the fluctuations in the proton size completely and set the width to zero, turning the proton wavefunction into a delta function at  $R_p$ .

If the total and integrated elastic cross sections are tuned at one energy, we find that the energy dependence of these cross sections depends very weakly, if at all, on the parameters of the model. Thus this energy dependence cannot be tuned, and the fact that it is close to the experimental results is therefore a direct consequence of the model. Our results for the total and elastic  $pp$  cross sections can be seen in figure I.3.

Extrapolating to higher energies we find the total cross section at the LHC nominal energy, 14 TeV, to be about 125 mb (117 mb at 10 TeV). We note that this is a rather high value compared to other predictions. Thus the Donnachie-Landshoff parameterization gives 101.5 mb at 14 TeV [33], while an analysis by Khoze, Martin, and Ryskin gives



$\Lambda_{\text{QCD}}$	0.2 GeV
$r_{\text{max}}$	2.9 GeV <sup>-1</sup>
$R_p$	3.0 GeV <sup>-1</sup>
$w$	0 GeV <sup>-1</sup>

Table I.2: The tuned values the parameters for the proton wavefunction and the perturbative evolution used for our model throughout this paper.

about 90 mb [34]. The predicted elastic cross section is about 31 mb for the LHC at 14 TeV (28 mb at 10 TeV).

### I.5.2 The differential elastic $pp$ cross section

The differential elastic  $pp$  cross section is given by

$$\frac{d\sigma_{\text{el}}}{dt} = \frac{1}{4\pi} \left| \int d^2\mathbf{b} e^{-i\mathbf{q}\cdot\mathbf{b}} d^2\mathbf{r}_{p1} d^2\mathbf{r}_{p2} \right. \\ \left. |\Psi_p(\mathbf{r}_{p1})|^2 |\Psi_p(\mathbf{r}_{p2})|^2 \langle 1 - e^{-F} \rangle_{12} \right|^2, \quad (\text{I.29})$$

with . We here neglect the real part of the amplitude, and therefore  $d\sigma/dt$  will have zeroes from the Fourier transform of the amplitude in eq. (I.29). Even though the true complex amplitude will not be identically zero, the real part is still assumed to be small, producing a dip at some value  $t = t_0$ , related to the inverse square of the size of the proton at the relevant energy. This dip is visible in some of the experimental data shown in figure I.4, where we have also included the results from the simulations. The parameters which are most sensitive to these distributions are  $R_p$ , which determines the size of the proton at rest, and  $\rho_{\text{max}}$  which regulates the maximal size of new dipoles, and therefore the increase with energy of the proton radius and the variation of the dip position. However, the slope of the distribution is basically independent of our parameters, as is the cross section at large  $t$ -values. Nevertheless, we are able to get a very good description of the data at all  $t$ -values even though the cross sections vary over many orders of magnitude. In figure I.4 we also show our result for the LHC, which predicts the location of the dip in the  $t$ -dependence at  $0.43 \text{ GeV}^2$  at  $\sqrt{s} = 14 \text{ TeV}$  ( $0.47 \text{ GeV}^2$  at 10 TeV). The values of the tuned parameters can be found in table I.2.



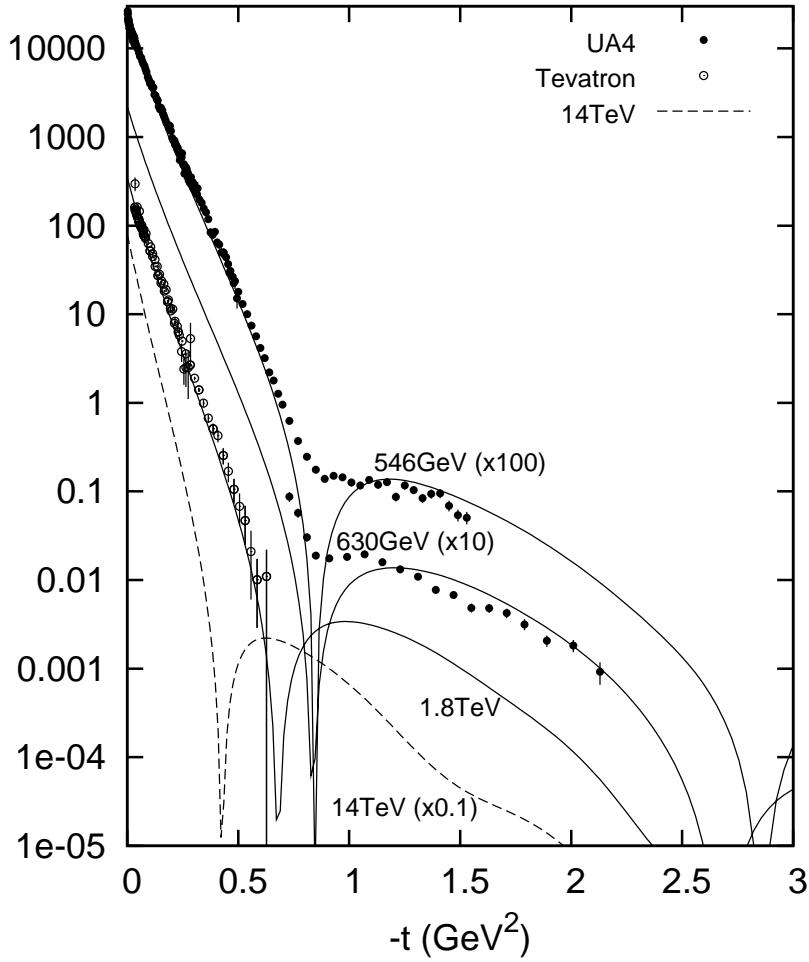
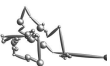


Figure I.4: The elastic cross section as function of  $t$  in  $\text{mb}/\text{GeV}^2$ . The numbers in parenthesis indicate how the data has been scaled. The lines are our model with tuned parameters. Predictions for 14 TeV is also included. Data are from [27, 35], [36] and [37].

### I.5.3 The total $\gamma^*p$ cross section and tuning the photon wave function

We will here use  $\Psi_\gamma(Q, \mathbf{r}, z)$  to denote the photon wavefunction in eq. (I.21), where for small  $Q^2$  the perturbative wavefunction is modified to account for the hadronic component of the photon. The total  $\gamma^*p$  cross section can be written



$$\sigma_{\text{tot}}(\gamma^*p) = \sum_{\lambda f} \int d^2\mathbf{b} d^2\mathbf{r}_p d^2\mathbf{r} dz \left| \Psi_p(\mathbf{r}_p) \right|^2 \left| \Psi_{\gamma,f}^\lambda(Q, \mathbf{r}, z) \right|^2 \langle 1 - e^{-F} \rangle_{dp}, \quad (1.30)$$

where  $\lambda$  is the polarization of the photon and  $f$  is the flavour of the quark-antiquark pair created by the photon.  $\langle 1 - e^{-F} \rangle_{dp}$  is now an average of the evolution of the dipole from the photon side and of the dipoles from the proton side. It depends not only on the total energy, the size of the proton and photon dipoles and  $b$ , but has also a weak dependence on  $z$ .

The three parameters  $B_V$ ,  $R_V$  and  $w_V$  in the enhancement factor in eq. (1.20) were fitted to the total  $\gamma^*p$  cross section as measured at HERA. Here the value of  $R_V$  determines the range in  $Q^2$  where the enhancement is significant, while  $w_V$  determines how fast it falls off for large  $Q^2$ . The parameter  $B_V$  is just an overall strength of the hadronic component.

A good fit to data was obtained with a wave function for the hadronic component similar to the proton wave function, having a size  $R_V \approx 3 \text{ GeV}^{-1}$  and a small width. The total  $\gamma^*p$  cross section with and without the effects of confinement and vector meson contributions are shown in figure 1.5. The tuned values are given in table 1.3. These parameters are quite different from the ones used by Forshaw *et al.*, who had an  $R_V$  of  $6.84 \text{ GeV}^{-1}$  and a fairly large width [38], which thus gives a stronger enhancement for large dipoles. For large dipole sizes the elementary dipole-proton cross section assumed in ref. [9] are also significantly different from the corresponding ones in our model. The reason why we anyhow can get similar results is that in [9] the very large dipoles are suppressed by a large quark mass, and the enhancement therefore not very effective. A reason for a smaller width in our wave-function is also that fluctuations in the dipole cascade are included in our formalism, which is compensated by less fluctuations in the wave-function.

We also note that the cross sections presented in fig. 1.5 are somewhat smaller than the corresponding results in refs. [3] and [21]. This is a consequence of the more consistent treatment of confinement in the present analysis, which gives a stronger suppression for larger dipoles. We believe, however, that a much stronger test of the hadronic component will rely on the results for the quasi-elastic reactions discussed in next section.

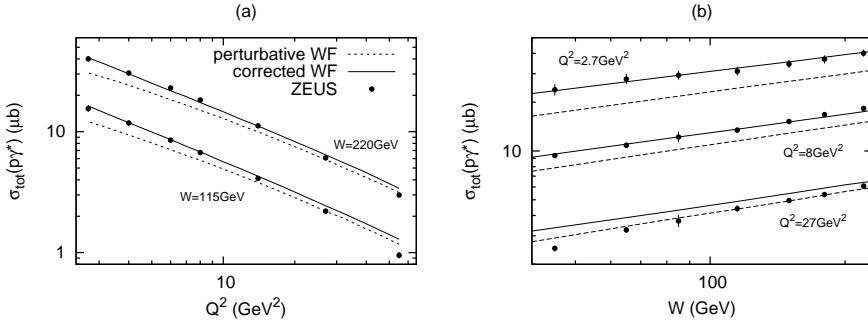


Figure I.5: The total cross section of photon–proton collision as function of photon virtuality and center-of-mass energy. The dashed line is calculated with a purely perturbative photon wavefunction, while the full line is with a photon wavefunction with both confinement and VMD corrections. Experimental data are from [39]

$R_V$	$3.0 \text{ GeV}^{-1}$
$w_V$	$0.2 \text{ GeV}^{-1}$
$B_V$	$9.0$

Table I.3: The tuned values of the parameters of the vector meson resonance function  $f(r)$  used for our model throughout this paper.

I

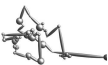
## I.6 Results for quasi-elastic $\gamma^*p$ collisions

In this section we will study predictions for quasi-elastic  $\gamma^*p$  collisions, using the photon wavefunction parameters determined in section I.5.3.

### I.6.1 Deeply Virtual Compton Scattering

In Deeply Virtual Compton Scattering, DVCS, the incoming particle is a virtual photon, while the outgoing particle is a real photon with wavefunction  $\Psi_{\gamma,f}^\lambda(0, \mathbf{r}, z)$ . According to eqs. (I.7, I.8) the cross section is given by

$$\begin{aligned}
 \sigma_{\text{DVCS}} = & \int d^2\mathbf{b} \sum_{\lambda} \\
 & \left| \int d^2\mathbf{r}_p d^2\mathbf{r} dz \sum_f |\Psi_p(\mathbf{r}_p)|^2 \right. \\
 & \left. \Psi_f^{*\gamma\lambda}(Q, \mathbf{r}, z) \Psi_f^{\gamma\lambda}(0, \mathbf{r}, z) \langle 1 - e^{-F} \rangle_{dp} \right|^2. \quad (\text{I.31})
 \end{aligned}$$



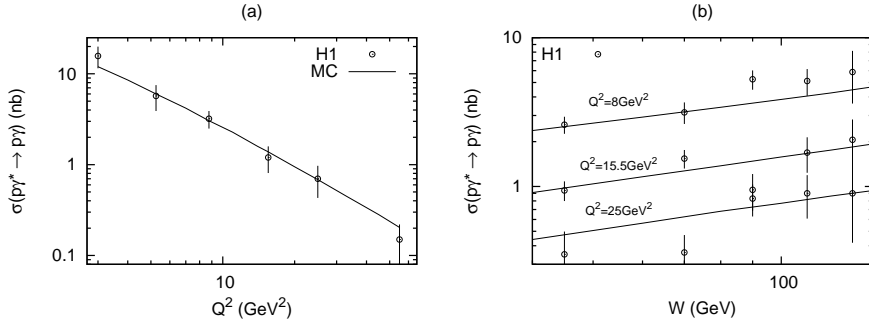


Figure 1.6: The cross section of  $\gamma^*p \rightarrow \gamma p$  for  $W = 82$  GeV as function of  $Q^2$  (a) and as function of  $W$  for three different  $Q^2$  (b). Experimental data are from [40,41].

The results obtained using the parameter values in table I.3 are presented in figure 1.6. We see that the results from the model indeed agree with the data, both in normalization and in the dependence on  $Q^2$  and  $W$ . As this quasi-elastic reaction is very sensitive to the fluctuations and the transverse size of the hadronic component of the real photon, this is a qualitative support for the proton-like wave function.

The differential cross section  $d\sigma/dt$  is obtained from the Fourier transform as shown in eq. (I.10). The result is presented in figure 1.7, which also shows the result obtained if the effects of scewedness are not included. We see that these effects increase the slope by about 7% at  $Q^2 = 8$  GeV<sup>2</sup> and 4% at  $Q^2 = 25$  GeV<sup>2</sup>. The agreement with data is quite good, both with and without scewedness effects. It is actually somewhat better without them, but we think that the difference is smaller than the uncertainty from the hadronic part of the photon wavefunction.

## I.6.2 Exclusive Production of Light vector Mesons

The cross section for exclusive vector meson production,  $\gamma^*p \rightarrow Vp$ , can be calculated in exactly the same way as for DVCS, only replacing the real photon wavefunction by a meson wavefunction:

$$\sigma_{\text{el}} = \int d^2\mathbf{b} \sum_{\lambda} \left| \int d^2\mathbf{r} d^2\mathbf{r}_p dz \sum_f |\Psi_p(\mathbf{r}_p)|^2 \right.$$

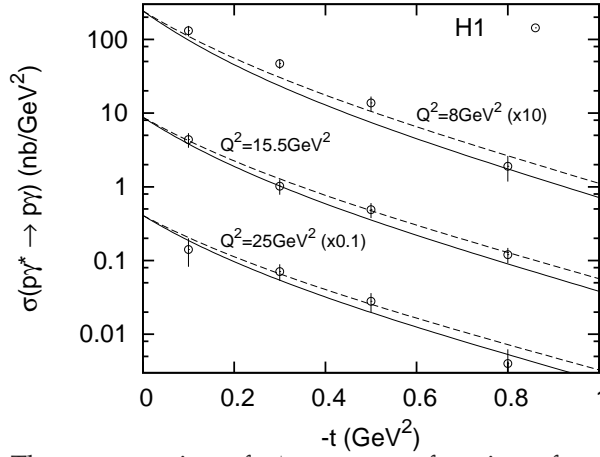


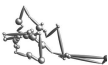
Figure I.7: The cross section of  $\gamma^*p \rightarrow \gamma p$  as function of  $t$  at  $W = 82$  GeV. Dashed lines are without the effects of scewedness (see section I.2.3), while the full lines are from the complete model. Note that the three series have been scaled by 10, 1, and 0.1 for better readability. Experimental data are from [41].

$$\Psi_f^{\star\gamma\lambda}(Q^2, \mathbf{r}, z) \Psi_f^{V\lambda}(\mathbf{r}, z) \langle 1 - e^{-F} \rangle_{dp} \Big|^2. \quad (\text{I.32})$$

As before we have ignored the real part of the amplitude. Contrary to the case of  $pp$  scattering it has been shown in [9] that in exclusive production of light vector mesons the real part can be quite large, for large  $Q^2$  or large  $W$  as large as one half of the imaginary part. This would mean that we underestimate the cross section by up to 25% in these regions. However, compared to the uncertainties in the vector meson wavefunctions, this error is small.

From our tuning of the hadronic part of the photon wavefunction, it could seem natural to assume some universal hadron size and maybe try to model the vector meson wavefunctions as a simple gluon–gluon dipole with a size of  $3 \text{ GeV}^{-1}$  and a small width. However, this would not naturally give us a  $z$ -dependence and we would not include the possibility that the vector meson may fluctuate into a photon, which could correspond to an enhancement at small  $r$ -values. Therefore we will simply use the boosted Gaussian and DGKP wavefunctions introduced in section I.4.3 to estimate the  $\gamma^*p \rightarrow Vp$  cross section. Throughout we will use the parameters listed in table I.1.

As before, the  $t$ -dependence of the cross section can be calculated through a Fourier transform of the amplitude. We are also able to calculate the ratio between the longitudinal to the transverse cross sections



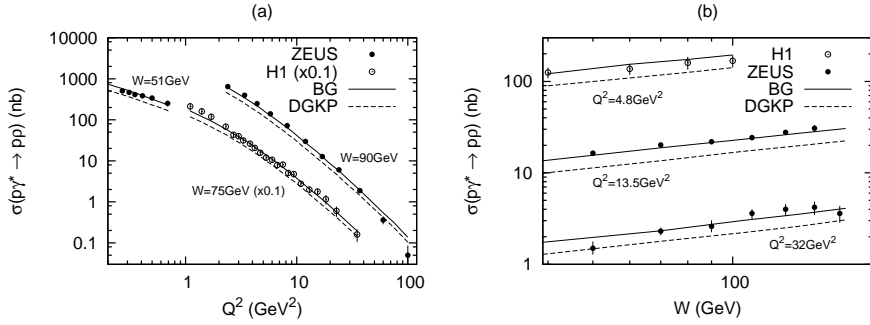


Figure 1.8: The cross section for  $\gamma^*p \rightarrow \rho p$ . (a) As function of the photon virtuality. The H1 data has been moved down a factor 10 for better readability. The full and dashed line are with the two different meson wavefunction described in I.4.3. (b) As function of the center-of-mass energy  $W$ . Experimental data are from [42–44].

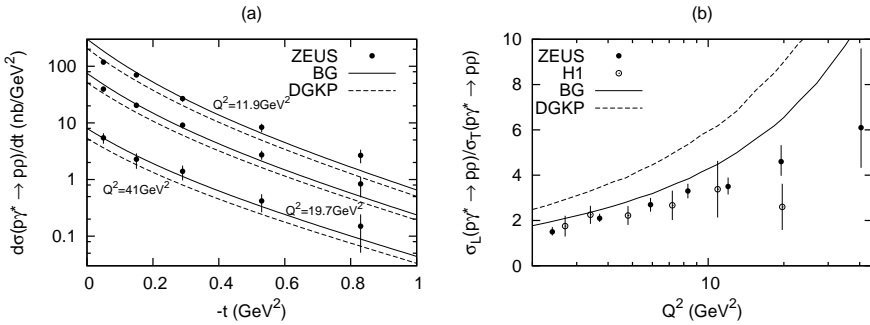


Figure 1.9: (a) The differential cross section for  $\gamma^*p \rightarrow \rho p$  as function of transferred momentum squared  $|t|$ . Three different  $Q^2$  has been used, all with a center-of-mass energy of 90 GeV. (b) The ratio of longitudinal and transverse cross section for  $\gamma^*p \rightarrow \rho p$  as function of the photon virtuality. Experimental data are from [42, 43].

and compare with experimental data.

Starting with  $\rho$  meson production, the results are shown in figures I.8 and I.9. We see that the model calculations reproduce experimental data rather well, including the dependence on virtuality  $Q^2$ , energy  $W$  and momentum transfer  $t$ . The  $t$ -dependence includes effects of scewedness (which are of the same size as for the DVCS-case in figure I.7) and is a bit too steep, especially for small  $Q^2$ . The Boosted Gaussian wavefunction is in general providing the closer fit, while DGKP is having problems mainly in the ratio between longitudinal and transverse cross sections. It should be noted, however, that this ratio could be changed if we de-

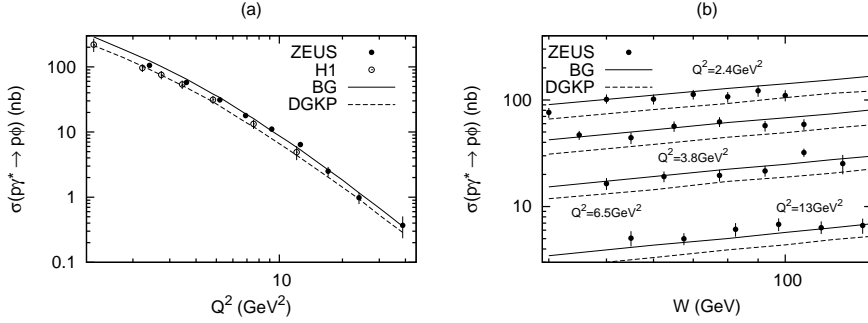


Figure I.10: The cross section for  $\gamma^*p \rightarrow \phi p$  (a) As function of the photon virtuality at center-of-mass energy 75 GeV. The full and dashed line are with the two different meson wavefunction described in section I.4.3. (b) As function of the center-of-mass energy for four different photon virtualities  $Q^2$ . Experimental data are from [45,46].

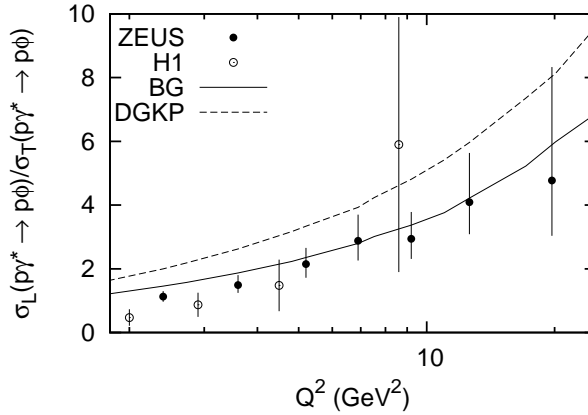
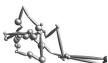


Figure I.11: The ratio of longitudinal and transverse cross section for  $\gamma^*p \rightarrow \phi p$  as function of the photon virtuality at a center-of-mass energy of 75 GeV. Experimental data are from [45,46].

cided to use different parameters for the resonance function in eq. (I.20) for the different polarizations.

Also in  $\phi$  production our model agrees well with experimental data, as can be seen in figures I.10 and I.11. The qualitative properties are similar to those of  $\rho$  production

We note that the more stringent test of the hadronic component of the photon is obtained from DVCS. The ratio between vector meson production and DVCS is then more a test of the vector meson wave-



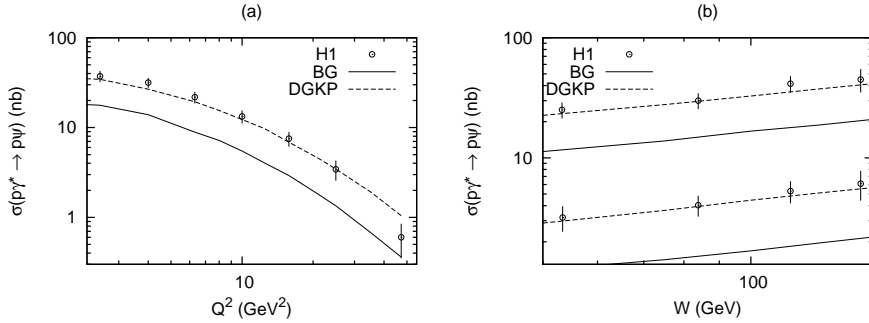


Figure 1.12: The cross section for  $\gamma^*p \rightarrow \psi p$  (a) As function of the photon virtuality at center-of-mass energy 90 GeV. The full and dashed line are with the two different meson wavefunction described in I.4.3. (b) As function of center-of-mass energy for  $Q^2 = 22.4 \text{ GeV}^2$  (lower data) and  $3.2 \text{ GeV}^2$  (upper data). Experimental data are from [47].

functions. It is therefore not surprising that we here get results similar to those in ref. [9]. The  $t$ -dependence presented in fig. 1.9 is, however, a result which in our model is sensitive to both the photon and vector meson wavefunctions, while in ref. [9] it was fixed by experimental data. From fig. 1.9 we see that for lower  $Q^2$  the slope in the model is somewhat too steep, thus indicating a too wide wavefunction for the  $\rho$  meson. We see from figs. 1.1 and 1.2 that the  $\rho$  wavefunctions for transverse polarization are extending well beyond  $5 \text{ GeV}^{-1}$ . A faster falloff for large  $r$ -values would here give a better agreement with the observed  $t$ -dependence.

### I.6.3 Exclusive $\psi$ Production

In the case of  $\psi$  production we necessarily encounter more uncertainties. The result is sensitive to the mass of the charm quark, and here we use the value  $1.4 \text{ GeV}$ , which in the analysis in ref. [21] gave the correct charm contribution,  $F_2^c$ , to the proton structure function. We have not included a  $\psi$  component in the photon wave function, although this would in principle be possible. For the  $\psi$  meson wavefunction we use the parameters in table I.1.

Our results are presented in figures 1.12 (dependence on  $Q^2$  and  $W$ ) and 1.13 (dependence on  $t$ ). We note that, in contrast to the results for the lighter mesons, the Boosted Gaussian wavefunction here gives a too low cross section over the entire kinematic region, while DGKP model agrees very well both in its normalization and in its dependence on  $Q^2$



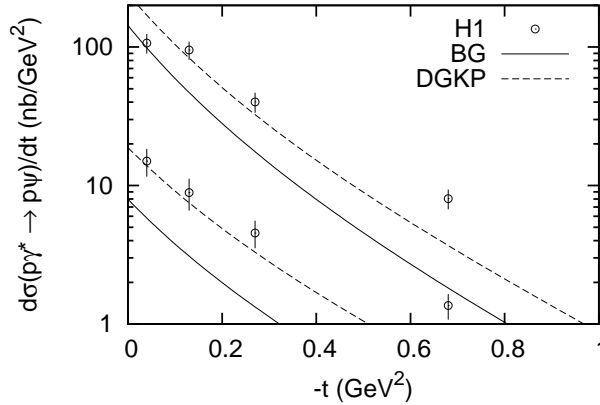


Figure I.13: The cross section for  $\gamma^*p \rightarrow \psi p$  as function of transferred momentum squared  $t$  for  $Q^2 = 22.4 \text{ GeV}^2$  (lower data) and  $3.2 \text{ GeV}^2$  (upper data). Experimental data are from [47].

and  $W$ . This result is a consequence of the stronger emphasis on small dipoles in the case of the  $\psi$ . Both models show, however, a somewhat steeper  $t$ -dependence than the experimental data. Again we find that this steepness is increased by including scewedness effects described in section I.2.3, by approximately the same amount as for the DVCS-case in figure I.7. Comparing to the corresponding result for  $\rho$  meson production, we conclude that also for the  $\psi$  meson the parameters in table I.1 give somewhat too wide wavefunctions.

I

## I.7 Conclusions and Outlook

In this paper we have spent some effort on the modeling of non-perturbative aspects of the proton, photon and vector meson wavefunctions. None of our models are in any way unique or on solid theoretical grounds. However, they do allow us to compare our dipole evolution model directly to experimental data. Fixing the wavefunction parameters at one energy we find that the energy dependence of both total and (quasi-)elastic cross sections are well described by the cascade evolution, and rather independent of our modeling of the wavefunctions. Also the slope in  $d\sigma/dt$  for elastic  $pp$  scattering and DVCS is in reasonable agreement with experimental data independently of the tuning. This indicates a very high predictive power of our evolution model both when it comes to the average multiplicity and sizes of the dipoles



(mainly influencing the total cross sections), the rate of increasing transverse size due to the dipole cascade (determining the energy variation in the position of the dip), and the fluctuations (mainly influencing the magnitude of elastic cross sections and their  $t$ -dependence).

Nevertheless, our modeling of the non-perturbative wavefunctions does give us valuable insights. Including the fluctuations in the cascade, the fluctuations in the proton wavefunction have to be rather small, in order to give the observed elastic cross section. The photon wavefunction clearly needs a hadronic component with a wavefunction with similar size as the proton and with similarly small fluctuations. The fact that the size comes out to be the same as the size of our proton may be a coincidence, but it could also indicate that there is a universal size of hadrons, at least when consisting of light quark flavours.

For the  $t$ -dependence of DVCS and vector meson production, we have included the effects of scewedness as calculated in [12], which gives an increase in the slope of the  $t$ -dependence. This effect is about 5% at  $Q^2 = 8 \text{ GeV}^2$ , and decreasing for larger  $Q^2$ -values. For the proton wavefunction we give arguments indicating that the effects should be small in  $pp$  at collider energies and in DIS at HERA.

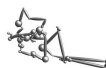
For the vector meson wavefunctions we have tested two different forms, which in the analysis by Forshaw *et al.* gave the best agreement with data for diffractive vector meson production. For light mesons the best result was obtained by the boosted Gaussian wavefunctions, while for  $\psi$  production the DGKP wavefunction was favored. In both cases the  $t$ -dependence was somewhat too steep, indicating that these wavefunctions extend out to too large  $r$ -values, where in particular the wavefunctions for transverse polarization are much wider than our wavefunctions for the proton and the photon.

The robustness of our model for dipole evolution, both for inclusive and exclusive cross sections increases our confidence that it can be used to also model fully exclusive final states. In future publications we will therefore concentrate on turning our Monte Carlo simulation program into a full-fledged event generator, which would then be able to model multi-particle production at e.g. the LHC, with special emphasis on the underlying event and multiple scatterings.

## Acknowledgment

We want to thank Emil Avsar for valuable discussions. This work is supported in part by the Marie Curie research training network “MCnet”

(contract number MRTN-CT-2006-035606) and by the Swedish Foundation for International Cooperation and Higher Education – STINT, contract number 2006/080. Gösta Gustafson also acknowledges support from the Deutsche Forschungsgemeinschaft.



## I References

- [1] E. Avsar, G. Gustafson, and L. Lönnblad, “Energy conservation and saturation in small- $x$  evolution,” *JHEP* **07** (2005) 062, arXiv:hep-ph/0503181.
- [2] E. Avsar, G. Gustafson, and L. Lönnblad, “Small- $x$  dipole evolution beyond the large- $N(c)$  limit,” *JHEP* **01** (2007) 012, arXiv:hep-ph/0610157.
- [3] E. Avsar, G. Gustafson, and L. Lönnblad, “Diffractive Excitation in DIS and  $pp$  Collisions,” *JHEP* **12** (2007) 012, arXiv:0709.1368 [hep-ph].
- [4] A. H. Mueller, “Soft gluons in the infinite momentum wave function and the BFKL pomeron,” *Nucl. Phys.* **B415** (1994) 373–385.
- [5] A. H. Mueller and B. Patel, “Single and double BFKL pomeron exchange and a dipole picture of high-energy hard processes,” *Nucl. Phys.* **B425** (1994) 471–488, hep-ph/9403256.
- [6] A. H. Mueller, “Unitarity and the BFKL pomeron,” *Nucl. Phys.* **B437** (1995) 107–126, hep-ph/9408245.
- [7] G. P. Salam, “OEDIPUS: Onium evolution, dipole interaction and perturbative unitarisation simulation,” *Comput. Phys. Commun.* **105** (1997) 62–76, hep-ph/9601220.
- [8] A. H. Mueller and G. P. Salam, “Large multiplicity fluctuations and saturation effects in onium collisions,” *Nucl. Phys.* **B475** (1996) 293–320, hep-ph/9605302.
- [9] J. R. Forshaw, R. Sandapen, and G. Shaw, “Colour dipoles and rho, Phi electroproduction,” *Phys. Rev.* **D69** (2004) 094013, arXiv:hep-ph/0312172.
- [10] J. R. Forshaw, R. Sandapen, and G. Shaw, “Further success of the colour dipole model,” *JHEP* **11** (2006) 025, arXiv:hep-ph/0608161.
- [11] A. I. Shoshi, F. D. Steffen, and H. J. Pirner, “S-matrix unitarity, impact parameter profiles, gluon saturation and high-energy scattering,” *Nucl. Phys.* **A709** (2002) 131–183, arXiv:hep-ph/0202012.

- [12] J. Bartels, K. J. Golec-Biernat, and K. Peters, "On the dipole picture in the nonforward direction," *Acta Phys. Polon.* **B34** (2003) 3051–3068, arXiv:hep-ph/0301192.
- [13] T. Sjöstrand, S. Mrenna, and P. Z. Skands, "PYTHIA 6.4 Physics and Manual," *JHEP* **05** (2006) 026, arXiv:hep-ph/0603175.
- [14] J. Kwiecinski, A. D. Martin, and P. J. Sutton, "Constraints on gluon evolution at small  $x$ ," *Z. Phys.* **C71** (1996) 585–594, hep-ph/9602320.
- [15] I. Balitsky, "Quark contribution to the small- $x$  evolution of color dipole," *Phys. Rev.* **D75** (2007) 014001, hep-ph/0609105.
- [16] Y. V. Kovchegov and H. Weigert, "Quark loop contribution to BFKL evolution: Running coupling and leading- $N(f)$  NLO intercept," *Nucl. Phys.* **A789** (2007) 260–284, hep-ph/0612071.
- [17] I. Balitsky and G. A. Chirilli, "NLO Evolution of Color Dipoles," *Acta Phys. Polon. Supp.* **1** (2008) 545.
- [18] M. Praszalowicz and A. Rostworowski, "Problems with proton in the QCD dipole picture," *Acta Phys. Polon.* **B29** (1998) 745–753, hep-ph/9712313.
- [19] M. Glück, E. Reya, and A. Vogt, "Dynamical parton distributions revisited," *Eur. Phys. J.* **C5** (1998) 461–470, hep-ph/9806404.
- [20] H. Kowalski and D. Teaney, "An impact parameter dipole saturation model," *Phys. Rev.* **D68** (2003) 114005, hep-ph/0304189.
- [21] E. Avsar and G. Gustafson, "Geometric scaling and QCD dynamics in DIS," *JHEP* **04** (2007) 067, hep-ph/0702087.
- [22] L. Frankfurt, V. Guzey, and M. Strikman, "Cross section fluctuations of photon projectile in generalized vector meson dominance model," *Phys. Rev.* **D58** (1998) 094039, arXiv:hep-ph/9712339.
- [23] H. G. Dosch, T. Gousset, G. Kulzinger, and H. J. Pirner, "Vector meson leptonproduction and nonperturbative gluon fluctuations in QCD," *Phys. Rev.* **D55** (1997) 2602–2615, arXiv:hep-ph/9608203.
- [24] M. Wirbel, B. Stech, and M. Bauer, "Exclusive Semileptonic Decays of Heavy Mesons," *Z. Phys.* **C29** (1985) 637.



- [25] S. J. Brodsky, T. Huang, and G. P. Lepage, "THE HADRONIC WAVE FUNCTION IN QUANTUM CHROMODYNAMICS," . Shorter version contributed to 20th Int. Conf. on High Energy Physics, Madison, Wisc., Jul 17-23, 1980.
- [26] J. Nemchik, N. N. Nikolaev, E. Predazzi, and B. G. Zakharov, "Color dipole phenomenology of diffractive electroproduction of light vector mesons at HERA," *Z. Phys.* **C75** (1997) 71–87, arXiv:hep-ph/9605231.
- [27] CDF Collaboration, F. Abe *et al.*, "Measurement of small angle  $\bar{p}p$  elastic scattering at  $\sqrt{s} = 546$  GeV and 1800 GeV," *Phys. Rev.* **D50** (1994) 5518–5534.
- [28] CDF Collaboration, F. Abe *et al.*, "Measurement of the  $\bar{p}p$  total cross-section at  $\sqrt{s} = 546$  GeV and 1800-GeV," *Phys. Rev.* **D50** (1994) 5550–5561.
- [29] E-710 Collaboration, N. A. Amos *et al.*, "A LUMINOSITY INDEPENDENT MEASUREMENT OF THE anti-p p TOTAL CROSS-SECTION AT  $S^{*(1/2)} = 1.8$ -TeV," *Phys. Lett.* **B243** (1990) 158–164.
- [30] E-811 Collaboration, C. Avila *et al.*, "The ratio, rho, of the real to the imaginary part of the anti-p p forward elastic scattering amplitude at  $s^{*(1/2)} = 1.8$ -TeV," *Phys. Lett.* **B537** (2002) 41–44.
- [31] UA4/2 Collaboration, C. Augier *et al.*, "Measurement of the proton - anti-proton total cross- section at the S anti-p p S collider by a luminosity dependent method," *Phys. Lett.* **B344** (1995) 451–454.
- [32] M. M. Block, F. Halzen, and T. Stanev, "Extending the frontiers: Reconciling accelerator and cosmic ray p p cross sections," *Phys. Rev.* **D62** (2000) 077501, arXiv:hep-ph/0004232.
- [33] A. Donnachie and P. V. Landshoff, "Total cross-sections," *Phys. Lett.* **B296** (1992) 227–232, hep-ph/9209205.
- [34] M. G. Ryskin, A. D. Martin, and V. A. Khoze, "Soft diffraction at the LHC: a partonic interpretation," *Eur. Phys. J.* **C54** (2008) 199–217, arXiv:0710.2494 [hep-ph].
- [35] E-710 Collaboration, N. A. Amos *et al.*, "Anti-proton - proton elastic scattering at  $s^{*(1/2)} = 1.8$ - TeV from  $|t| = 0.034$ -GeV/c\*\*2 to 0.65-GeV/c\*\*2," *Phys. Lett.* **B247** (1990) 127–130.

- [36] **UA4** Collaboration, D. Bernard *et al.*, “LARGE  $t$  ELASTIC SCATTERING AT THE CERN SPS COLLIDER AT  $S^{**}(1/2) = 630\text{-GeV}$ ,” *Phys. Lett.* **B171** (1986) 142.
- [37] **NA22** Collaboration, M. Adamus *et al.*, “STUDY OF ELASTIC  $\pi^+p$ ,  $K^+p$  AND  $p p$  SCATTERING AT  $250\text{-GeV}/c$ ,” *Phys. Lett.* **B186** (1987) 223–226.
- [38] J. R. Forshaw, G. Kerley, and G. Shaw, “Extracting the dipole cross-section from photo- and electro-production total cross-section data,” *Phys. Rev.* **D60** (1999) 074012, hep-ph/9903341.
- [39] **ZEUS** Collaboration, S. Chekanov *et al.*, “Study of deep inelastic inclusive and diffractive scattering with the ZEUS forward plug calorimeter,” *Nucl. Phys.* **B713** (2005) 3–80, hep-ex/0501060.
- [40] **H1** Collaboration, A. Aktas *et al.*, “Measurement of deeply virtual Compton scattering at HERA,” *Eur. Phys. J.* **C44** (2005) 1–11, arXiv:hep-ex/0505061.
- [41] **H1** Collaboration, F. D. Aaron *et al.*, “Measurement of Deeply Virtual Compton Scattering and its  $t$ -dependence at HERA,” *Phys. Lett.* **B659** (2008) 796–806, arXiv:0709.4114 [hep-ex].
- [42] **H1** Collaboration, C. Adloff *et al.*, “Elastic electroproduction of rho mesons at HERA,” *Eur. Phys. J.* **C13** (2000) 371–396, arXiv:hep-ex/9902019.
- [43] **ZEUS** Collaboration, S. Chekanov *et al.*, “Exclusive  $\rho^0$  production in deep inelastic scattering at HERA,” *PMC Phys.* **A1** (2007) 6, arXiv:0708.1478 [hep-ex].
- [44] **ZEUS** Collaboration, J. Breitweg *et al.*, “Exclusive electroproduction of  $\rho^0$  and  $J/\psi$  mesons at HERA,” *Eur. Phys. J.* **C6** (1999) 603–627, arXiv:hep-ex/9808020.
- [45] **H1** Collaboration, C. Adloff *et al.*, “Measurement of elastic electroproduction of  $\Phi$  mesons at HERA,” *Phys. Lett.* **B483** (2000) 360–372, arXiv:hep-ex/0005010.
- [46] **ZEUS** Collaboration, S. Chekanov *et al.*, “Exclusive electroproduction of  $\Phi$  mesons at HERA,” *Nucl. Phys.* **B718** (2005) 3–31, arXiv:hep-ex/0504010.



- [47] **H1** Collaboration, A. Aktas *et al.*, “Elastic J/psi production at HERA,” *Eur. Phys. J.* **C46** (2006) 585–603, arXiv:hep-ex/0510016.



# II

## Fluctuations, Saturation, and Diffractive Excitation in High Energy Collisions

Christoffer Flensburg and Gösta Gustafson

Department of Theoretical Physics, Lund University,  
Sölvegatan 14A, SE-223 62 Lund, Sweden

*Journal of High Energy Physics* **1010** (2010) 014 [hep-ph/0503293].

II

Diffractive excitation is usually described by the Good–Walker formalism for low masses, and by the triple-Regge formalism for high masses. In the Good–Walker formalism the cross section is determined by the fluctuations in the interaction. In this paper we show that by taking the fluctuations in the BFKL ladder into account, it is possible to describe both low and high mass excitation by the Good–Walker mechanism. In high energy  $pp$  collisions the fluctuations are strongly suppressed by saturation, which implies that pomeron exchange does not factorise between DIS and  $pp$  collisions. The Dipole Cascade Model reproduces the expected triple-Regge form for the bare pomeron, and the triple-pomeron coupling is estimated.



## II.1 Introduction

Diffractive excitation represents large fractions of the cross sections in  $pp$  collisions or DIS. In most analyses of  $pp$  collisions low mass excitation is described by the Good–Walker formalism [1], while high mass excitation is described by a triple-Regge formula [2, 3]. In the Good–Walker formalism the state of the incoming projectile is written as a superposition of eigenstates to the  $T$ -matrix, and the cross section for diffractive excitation is given by the fluctuations in the eigenvalues. In the triple-Regge formulation it is instead determined by the reggeon couplings to the projectile and the target, and a set of triple-reggeon couplings, determined by fits to data (for recent analyses see e.g. refs. [4,5]). The fluctuations in the pomeron ladder are here not included in the Good–Walker formalism, which therefore limits the application to low masses. It is, however, well known that the fluctuations in the evolution of a BFKL pomeron are very large [6]. As we will discuss in the following, by including these fluctuations it is possible to describe both low and high mass diffraction in a uniform way, within the Good–Walker formalism.

In central  $pp$  collisions the interaction is approaching the black limit at increasing energy, and therefore saturation effects are very important. The triple-Regge formula would violate unitarity and predict a diffractive cross section exceeding the total cross section if saturation and multiple pomeron interactions are not included. These are accounted for in terms of gap-survival form factors and “enhanced diagrams”, as in the references cited above, or as saturation effects in the pomeron flux [7]. In the Good–Walker approach these effects are taken into account by reduced fluctuations, when the interaction approaches the black limit.

Data from HERA show a very large cross section for diffractive excitation of the virtual photon. In DIS the photon couples initially to a virtual  $q\bar{q}$  pair. To improve the description of diffractive excitation of the photon, gluon radiation has been included. The incoming virtual photon has been treated as a mixture of  $q\bar{q}$  and  $q\bar{q}g$  states, and the data has been fitted to diffractive proton structure functions or parton distributions in the pomeron [8–10]. In a description in transverse coordinate space also effects of saturation for small  $Q^2$  have been taken into account [11]. Although important for very small  $x$  and small  $Q^2$ , saturation is much less essential in DIS than in  $pp$  collisions, which can explain the lack of factorisation in the comparison of DIS and  $pp$  collisions [12] (see e.g. ref. [13]).

The eikonal approximation, formulated in impact parameter space, is a formalism which efficiently accounts for saturation effects and unitarity constraints in high energy reactions. If the colliding particles have a substructure, the eikonal formalism can also describe diffractive excitation within the Good–Walker formalism. Miettinen and Pumplin [14] suggested that the scattering eigenstates correspond to parton showers, which interact via parton-parton scattering. (They also suggested that the partons might be identical to quarks and gluons, which at the time were still hypothetical.) The model predicted that diffractive excitation is dominantly peripheral, with a maximum for impact parameter  $b \approx 0.5$  fm at  $\sqrt{s} = 53$  GeV.

Mueller and coworkers have developed a dipole cascade model in transverse coordinate space, which at the same time reproduces leading log BFKL evolution and satisfies  $s$ -channel unitarity [15–17]. The evolution of the cascade gives dipole chains, which interact via gluon exchange. Multiple interactions then correspond to the exchange of multiple pomerons. It was pointed out by Mueller and Salam [6] that the dipole evolution contains very large fluctuations. This caused a technical problem for their MC simulations, but, as discussed below, including the fluctuations in the pomeron ladder gives the possibility to treat also higher mass excitations in the Good–Walker formalism.

In a series of papers [18–21] a generalisation of Mueller’s model is presented, which includes the following improvements:

- NLL BFKL effects
- Nonlinear effects within the evolution
- Confinement effects
- A simple model for the proton wavefunction

This model describes successfully total and (quasi)elastic cross sections for DIS and  $pp$  collisions. While taking into account not only fluctuations in the projectile wave function, but in the whole evolution between the projectile and the target, the model is also able to describe diffractive excitation, not only to low, but also to high masses [20]. Studying a collision in a frame, where the projectile is evolved a distance  $Y_p$  in rapidity, and the target a distance  $Y_t = Y - Y_p$ , it is possible to calculate diffractive scattering where the rapidity range of the excited projectile, approximately given by  $\ln M_{X'}^2$ , is smaller than  $Y_p$ . (See sec. II.3.3 for details.) Varying  $Y_p$  then gives the mass distribution  $d\sigma/d\ln M_X^2 \sim d\sigma/dY_p$ .

In a similar way it is possible to calculate double diffractive excitation for  $M_{Xp}^2 < \exp(Y_p)$  and  $M_{Xt}^2 < \exp(Y - Y_t)$ , where the projectile



and target are excited to  $M_{Xp}$  and  $M_{Xt}$  respectively. We note that final states, where the two excited states overlap in rapidity, cannot be calculated in this way; in this formalism they are instead included in the inelastic cross section. (We want to return to this problem in a future publication.)

The aim of this paper is to study the nature of the fluctuations in the evolution of parton cascades in more detail, in order to understand the relation between the Good–Walker and the triple-Regge formalism for diffractive excitation. We will see that within the dipole cascade model the Good–Walker mechanism indeed reproduces the expected bare pomeron trajectory and the triple-Regge result for diffraction. We will also investigate the effects of saturation in more detail, and how the absorptive effects and enhanced diagrams correspond to saturation effects in dipole cascade evolutions, and how this describes the breaking of factorisation between DIS and  $pp$  scattering.

In the present paper we will not discuss the properties of exclusive final states in diffraction, or events with multiple rapidity gaps. We hope to return to these questions in future publications. We are also here not discussing the nature of hard diffraction, which has been analysed in terms of a hard parton scattering supplemented with extra gluon exchange neutralising the colour exchange, together with Sudakov form factors describing the gap survival probability (see e.g. ref. [22–25]).

Section 2 of this paper introduces the Good–Walker formalism and how it can be applied to parton cascades. Section 3 summarises the features of the Lund dipole cascade model used in our analysis. The nature of the fluctuations and effects of saturation in DIS and  $pp$  collisions is analysed in section 4, and in section 5 we study the impact parameter profile and the  $t$ -dependence in  $pp$  scattering. The results of the Good–Walker analysis is compared to the triple-Regge formalism in section 6, and the bare pomeron couplings are estimated. Our conclusions are summarised in section 7.

## II.2 The eikonal approximation and the Good–Walker formalism

### II.2.1 Eikonal approximation

Diffraction, saturation, and multiple interactions are more easily described in impact parameter space. In transverse momentum space the amplitude for two successive interactions is represented by a convolu-

tion of the single interaction contributions, which in impact parameter space simplifies to a multiplication.

If the scattering is driven by absorption into a large number of inelastic states  $n$ , with Born amplitudes  $\sqrt{2f_n}$ , the optical theorem gives an elastic Born amplitude

$$F = \sum f_n. \quad (\text{II.1})$$

In our notation, where  $T \equiv 1 - S$ , these amplitudes are purely real. In the eikonal approximation multiple interactions exponentiates, and the amplitude

$$T = 1 - e^{-F} = 1 - e^{-\sum f_n} \quad (\text{II.2})$$

is always satisfying the unitarity constraint  $T \leq 1$ . For a structureless projectile we then find:

$$\begin{aligned} d\sigma_{\text{tot}}/d^2b &\sim \langle 2T \rangle \\ d\sigma_{\text{el}}/d^2b &\sim \langle T \rangle^2 \\ d\sigma_{\text{inel}}/d^2b &\sim \langle 1 - e^{-\sum 2f_n} \rangle = d\sigma_{\text{tot}}/d^2b - d\sigma_{\text{el}}/d^2b \end{aligned} \quad (\text{II.3})$$

## II.2.2 Good-Walker formalism

If the projectile has an internal structure, the mass eigenstates can differ from the eigenstates of diffraction. We denote the diffractive eigenstates  $\Phi_n$ , with eigenvalues  $T_n$ , and the mass eigenstates  $\Psi_k = \sum_n c_{kn} \Phi_n$ , where the incoming state is given by  $\Psi_{\text{in}} = \Psi_1$ .

The elastic amplitude is then given by (assuming here that  $c_{1n}$  are real)

$$\langle \Psi_1 | T | \Psi_1 \rangle = \sum c_{1n}^2 T_n = \langle T \rangle \quad (\text{II.4})$$

which implies that

$$d\sigma_{\text{el}}/d^2b = (\sum c_{1n}^2 T_n)^2 = \langle T \rangle^2. \quad (\text{II.5})$$

The amplitude for diffractive transition to the mass eigenstate  $\Psi_k$  becomes

$$\langle \Psi_k | T | \Psi_1 \rangle = \sum_n c_{kn} T_n c_{1n}, \quad (\text{II.6})$$

which gives a total diffractive cross section (incl. elastic scattering)

$$d\sigma_{\text{diff}}/d^2b = \sum_k \langle \Psi_1 | T | \Psi_k \rangle \langle \Psi_k | T | \Psi_1 \rangle = \langle T^2 \rangle. \quad (\text{II.7})$$



Subtracting the elastic scattering we find the cross section for diffractive excitation

$$d\sigma_{\text{diff ex}}/d^2b = d\sigma_{\text{diff}}/d^2b - d\sigma_{\text{el}}/d^2b = \langle T^2 \rangle - \langle T \rangle^2 \equiv V_T, \quad (\text{II.8})$$

which thus is determined by the fluctuations in the scattering process.

### II.2.3 What are the diffractive eigenstates?

As mentioned in the introduction, Miettinen and Pumplin [14] assumed that the diffractive eigenstates correspond to parton cascades, which can come on shell through interaction with the target. This was also the assumption in our earlier analysis of diffractive excitation in [20]. The process is illustrated in fig. II.1. Fig. *a* shows the virtual cascade before the collision, and fig. *b* illustrates an inelastic interaction, where gluon exchange gives a colour connection between the projectile and the target. Fig. *c* shows an elastic interaction, where two gluons scatter coherently on the partons in the projectile cascade. It is obtained from the projection of the scattered state onto the incoming mixture of different cascades. Fig. *d*, finally, shows the contribution of the scattered state, which is orthogonal to the incoming state, and thus corresponds to diffractive excitation. The lines can symbolise gluons in a traditional cascade, or dipoles in a dipole cascade. In fig. *d* the dashed lines corresponds to virtual emissions in the cascade, which cannot come on shell via momentum exchange from the exchanged gluon pair.

A similar approach was also used by Hatta *et al.* [26]. Their analysis was, however, limited to relatively low mass excitations. As the authors sought an analytic solution, they studied very high energies, where the fluctuations in the pomeron evolution could be neglected due to saturation. Thus only fluctuations coming from ordered DGLAP chains close to the virtual photon end of the process were included, and therefore it was not possible to treat excitation to larger masses.

## II.3 The dipole cascade model

### II.3.1 Mueller's dipole model

Mueller's dipole cascade model [15–17] is a formulation of BFKL evolution in transverse coordinate space. Gluon radiation from the colour charge in a parent quark or gluon is screened by the accompanying anticharge in the colour dipole. This suppresses emissions at large transverse separation, which corresponds to the suppression of small  $k_\perp$  in

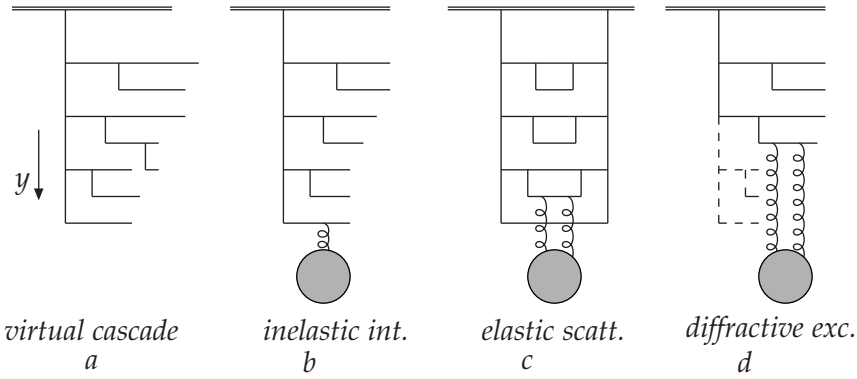


Figure II.1: (a) An example of a parton (or dipole) cascade evolved in rapidity. (b) The exchange of a gluon gives rise to an inelastic interaction. (c) Elastic scattering is obtained from coherent scattering of different partons in different cascades, via the exchange of two gluons. (d) Diffractive excitation is obtained when the result of the two-gluon exchange does not correspond to the coherent initial proton state. Here the dashed lines indicate virtual emissions, which are not present in the diffractive final state.

BFKL. For a dipole  $(x, y)$  the probability per unit rapidity ( $Y$ ) for emission of a gluon at transverse position  $z$  is given by

$$\frac{d\mathcal{P}}{dY} = \frac{\bar{\alpha}}{2\pi} d^2z \frac{(x-y)^2}{(x-z)^2(z-y)^2}, \quad \text{with } \bar{\alpha} = \frac{3\alpha_s}{\pi}. \quad (\text{II.9})$$

This emission implies that the dipole is split into two dipoles, which (in the large  $N_c$  limit) emit new gluons independently. The result is a cascade, where the number of dipoles grows exponentially with  $Y$ .

In a high energy collision, the dipole cascades in the projectile and the target are evolved from their rest frames to the rapidities they will have in the specific Lorentz frame chosen for the analysis. The growth in the number of dipoles also implies a strong growth for the scattering probability, which, however, is kept below 1 by the possibility to have multiple dipole interactions in a single event. The scattering probability between two elementary colour dipoles with coordinates  $(x_i, y_i)$  and  $(x_j, y_j)$  in the projectile and the target respectively, is given by  $2f_{ij}$ , where (in Born approximation)

$$f_{ij} = f(x_i, y_i | x_j, y_j) = \frac{\alpha_s^2}{8} \left[ \log \left( \frac{(x_i - y_j)^2 (y_i - x_j)^2}{(x_i - x_j)^2 (y_i - y_j)^2} \right) \right]^2. \quad (\text{II.10})$$

The optical theorem then implies that the elastic amplitude for dipole  $i$  scattering off dipole  $j$  is given by  $f_{ij}$ . Summing over  $i$  and  $j$  gives the



one-pomeron elastic amplitude

$$F = \sum f_{ij}. \quad (\text{II.11})$$

In the eikonal approximation the unitarised amplitude is given by the exponentiated expression

$$T(\mathbf{b}) = 1 - e^{-F}, \quad (\text{II.12})$$

and the total, diffractive, and elastic cross sections are given by the expressions in eqs. (II.3, II.8).

### II.3.2 The Lund dipole cascade model

In refs. [18,19,21] we describe a modification of Mueller's cascade model with the following features:

- It includes essential NLL BFKL effects.
- It includes non-linear effects in the evolution.
- It includes effects of confinement.

The model also includes a simple model for the proton wavefunction, and is implemented in a Monte Carlo simulation program called DIPSY. Here the NLL effects significantly reduce the production of small dipoles, and thereby also the associated numerical difficulties with very large dipole multiplicities are avoided. As discussed in the cited references, the model is able to describe a wide range of observables in DIS and  $pp$  scattering, with very few parameters.

#### NLL effects

The NLL corrections to BFKL evolution have three major sources [27]:

*The running coupling:*

This is relatively easily included in a MC simulation process.

*Non-singular terms in the splitting function:*

These terms suppress large  $z$ -values in the individual parton branchings, and prevent the daughter from being faster than her recoiling parent. Most of this effect is taken care of by including energy-momentum conservation in the evolution. This is effectively taken into account by associating a dipole with transverse size  $r$  with a transverse momentum  $k_{\perp} = 1/r$ , and demanding conservation of the lightcone momentum  $p_+$  in every step in the evolution. This gives an effective cutoff for small



dipoles, which eliminates the numerical problems encountered in the MC implementation by Mueller and Salam [6].

*Projectile-target symmetry:*

This is also called energy scale terms, and is essentially equivalent to the so called consistency constraint. This effect is taken into account by conservation of both positive and negative lightcone momentum components,  $p_+$  and  $p_-$ . The treatment of these effects includes also effects beyond NLL, in a way similar to the treatment by Salam in ref. [27]. Thus the power  $\lambda_{\text{eff}}$ , determining the growth for small  $x$ , is not negative for large values of  $\alpha_s$ .

### Non-linear effects and saturation

As mentioned above, dipole loops (or equivalently pomeron loops) are not included in Mueller's cascade model, if they occur within the evolution, but only if they are cut in the Lorentz frame used in the calculations, as a result of multiple scattering in this frame. The result is therefore not frame independent. (The situation is similar in the Colour Glass Condensate or the JIMWLK equations.) As for dipole scattering the probability for such loops is given by  $\alpha_s$ , and therefore formally colour suppressed compared to dipole splitting, which is proportional to  $\bar{\alpha} = N_c \alpha_s / \pi$ . These loops are therefore related to the probability that two dipoles have the same colour. Two dipoles with the same colour form a quadrupole. Such a field may be better approximated by two dipoles formed by the closest colour-anticolour charges. This corresponds to a recoupling of the colour dipole chains. We call this process a dipole "swing". The swing gives rise to loops within the cascades, and makes the cross section frame independent up to a few percent. We note that a similar effect would also be obtained from gluon exchange between the two dipoles.

In the MC implementation each dipole is assigned one of  $N_C^2$  colours, and dipoles with the same colour are allowed to recouple. The weight for the recoupling is assumed to be proportional to  $r_1^2 r_2^2 / (r_3^2 r_4^2)$ , where  $r_1$  and  $r_2$  are the sizes of the original dipoles and  $r_3$  and  $r_4$  are the sizes of the recoupled dipoles. We note that in this formulation the number of dipoles is not reduced. The given weight favours the formation of smaller dipoles, and the saturation effect is obtained because the smaller dipoles have smaller cross sections. Thus in an evolution in momentum space the swing would not correspond to an absorption of gluons below the saturation line  $k_\perp^2 = Q_s^2(x)$ ; it would rather correspond to lifting the



gluons to higher  $k_\perp$  above this line.

Although this mechanism does not give an explicitly frame independent result, MC simulations show that it is a very good approximation.

### Confinement effects

Confinement effects are included via an effective gluon mass, which gives an exponential suppression for very large dipoles [20]. This prevents the proton to grow too fast in transverse size, and is also essential to satisfy Froisart's bound at high energies [28].

### Initial dipole configurations

#### Photon wavefunction

An initial photon is split into a  $q\bar{q}$  pair, and for larger  $Q^2$  the wavefunction for a virtual photon can be determined perturbatively. The well known result has the following form:

$$\begin{aligned}\Psi_{f\bar{h}\bar{h}}^{\gamma 0}(Q, r, z) &= \frac{\sqrt{\alpha_{EM} N_C}}{\pi} e_f Q z (1-z) K_0(r \varepsilon_f) \delta_{h\bar{h}} \\ \Psi_{f\bar{h}\bar{h}}^{\gamma +}(Q, r, z) &= \frac{\sqrt{\alpha_{EM} N_C / 2}}{\pi} e_f \\ &\times \left\{ i e^{i\theta} (z \delta_{h+} \delta_{\bar{h}-} - (1-z) \delta_{h-} \delta_{\bar{h}+}) \varepsilon_f K_1(r \varepsilon_f) \right. \\ &\quad \left. + \delta_{h+} \delta_{\bar{h}+} m_f K_0(r \varepsilon_f) \right\}\end{aligned}\tag{II.13}$$

with

$$\varepsilon_f = \sqrt{z(1-z)Q^2 + m_f^2}.\tag{II.14}$$

Here  $r$  is the transverse size of the dipole, and  $z$  is the energy fraction carried by the quark,  $\lambda = 0$  and  $+$  denote the longitudinal and transverse wavefunctions respectively,  $f$  denotes the quark flavour, and  $K_0$  and  $K_1$  are modified Bessel functions.  $e_f$  is the electric charge of the quark in units of the proton charge and  $m_f$  the effective mass of the quark. For smaller  $Q^2$  a hadronic component has to be added, as described in more detail in ref. [21].

#### Proton wavefunction

The internal structure of the proton is governed by soft QCD, and is not possible to calculate perturbatively. In our model it is represented by an equilateral triangle formed by three dipoles, and with a radius of  $3 \text{ GeV}^{-1} \approx 0.6 \text{ fm}$ . The model should be used at low  $x$ , and

when the system is evolved over a large rapidity range the observable results depend only weakly on the exact configuration of the dipoles, or whether the charges are treated as (anti)quarks or gluons.

### II.3.3 Application to diffraction

We now want to apply the Good–Walker result in eq. (II.8) to the situation where two different cascades collide. The elastic scattering amplitude is obtained when  $T$  is averaged over both the projectile and the target states, while the total diffractive cross section is obtained by averaging  $T^2$ . Thus we have

$$d\sigma_{\text{el}}/d^2b = \langle T \rangle_{\text{pt}}^2 \quad (\text{II.15})$$

$$d\sigma_{\text{diff}}/d^2b = \langle T^2 \rangle_{\text{pt}} \quad (\text{II.16})$$

Here the indices p and t indicate averaging over the projectile and target evolutions respectively. If we average the amplitude over possible evolutions of the target system, we get the amplitude representing elastic scattering of the target. If we then square, and average over projectile states, we get according to eq. (II.7), the cross section for total diffractive scattering of the projectile, while the target is only scattered elastically. Subtracting the cross section for elastic scattering of both the projectile and the target gives the cross section for single diffractive excitation of the projectile:

$$d\sigma_{\text{proj diff ex}}/d^2b = \langle \langle T \rangle_{\text{t}}^2 \rangle_{\text{p}} - \langle T \rangle_{\text{pt}}^2 \quad (\text{II.17})$$

The process is illustrated in fig. II.2. If the expression is calculated in a Lorentz frame in which the projectile is evolved a rapidity range  $Y_{\text{p}}$ , the partons in the projectile cascade are confined to the rapidity range  $y < Y_{\text{p}}$ . The result in eq. (II.17) includes all cascades limited to this range, also those which have no partons close to  $Y_{\text{p}}$ . This corresponds to all possible excitation masses  $M_{\text{X}}^2 \leq \exp(Y_{\text{p}}) \cdot 1\text{GeV}^2$ . By varying  $Y_{\text{p}}$  it is then possible to calculate the differential cross section  $d\sigma_{\text{diff ex}}/dM_{\text{X}}^2$ . Final states with  $M_{\text{X}}^2 > \exp(Y_{\text{p}}) \cdot 1\text{GeV}^2$  are thus not included in the cross section in eq. (II.17), in the frame chosen for the calculation. These states are in our formalism instead included in the inelastic cross section, because in such a frame there is colour exchange connecting the forward- and backward-moving systems. To get the full cross section for single diffractive excitation of the projectile, we must do the calculation in the target rest frame, where  $Y_{\text{p}} = Y \equiv \ln s$ . In the same way it is possible to calculate single excitation of the target, by replacing the role of projectile and target.



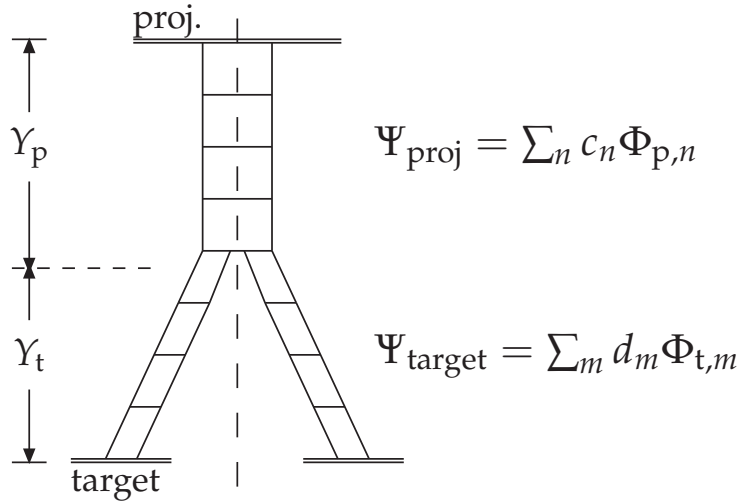


Figure II.2: Single diffractive excitation with no final state particles in the  $Y_t$  range. The virtual target evolutions are summed on amplitude level, while the real projectile evolutions are summed on cross section level.

The cross section for diffractive scattering of both the projectile and the target is obtained by  $\langle T^2 \rangle_{\text{pt}}$ . This expression includes both elastic scattering and single diffractive excitation of the projectile or the target. Subtracting these contributions using eqs. (II.15) and (II.17), we get the cross section for double diffractive excitation given by

$$d\sigma_{\text{DD}}/d^2b = \langle T^2 \rangle_{\text{pt}} - \langle \langle T \rangle_t^2 \rangle_p - \langle \langle T \rangle_p^2 \rangle_t + \langle T \rangle_{\text{pt}}^2. \quad (\text{II.18})$$

This expression gives the cross section for  $M_{\text{xp}}^2 \leq \exp(Y_p) \cdot 1\text{GeV}^2$  and  $M_{\text{xt}}^2 \leq \exp(Y_t) \cdot 1\text{GeV}^2$ , where  $Y_p + Y_t$  equals the total rapidity range  $Y$ . As was the case for single diffractive excitation, events with excitation to larger masses are in this formalism included in the inelastic cross section. For single diffraction it was possible to include excitation of e.g. the projectile to all masses by performing the calculation in the target rest frame. This is not the case for double diffraction. Even if we change Lorentz frame, we can never include events where the two excited states overlap in rapidity. Those states will always be included in the inelastic cross section. (Thus although the total and elastic cross sections have to be independent of the Lorentz frame used, only the sum of the cross sections for inelastic scattering and diffractive excitation is frame independent.)

The results from MC simulations of single and double diffractive excitation were presented in ref. [20], in good agreement with data from HERA and the Tevatron. Fig. II.3 shows the diffractive cross sections

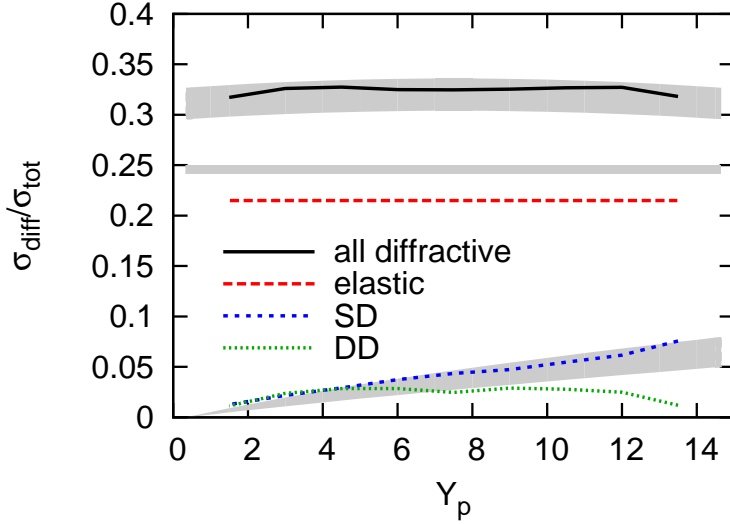


Figure II.3: The fraction of elastic, single diffractive and double diffractive events at 1800 GeV as function of interaction frame. For single diffractive excitation the figure shows masses of the excited projectile integrated over  $M_{Xp}^2 \leq \exp(Y_p) \cdot 1\text{GeV}^2$ . For double diffraction the projectile and target masses are integrated over  $M_{Xp}^2 \leq \exp(Y_p) \cdot 1\text{GeV}^2$  and  $M_{Xt}^2 \leq \exp(Y_t) \cdot 1\text{GeV}^2$  respectively, with  $Y_p + Y_t = Y = \ln(1800^2) \approx 15$ . (For details see the main text.) The two lower error bands are single diffractive excitation and elastic cross section estimated from CDF data [29, 30]. The top area is the sum of the two, thus not including double diffraction.

II

for  $pp$  collisions at 1800 GeV. In this figure the projectile is evolved over  $Y_p$  units of rapidity, and the target over  $Y_t = Y - Y_p$  units, setting the limits for the diffracted masses to  $M_{Xp}^2 \leq \exp(Y_p) \cdot 1\text{GeV}^2$  and, in case of double diffraction,  $M_{Xt}^2 \leq \exp(Y - Y_p) \cdot 1\text{GeV}^2$ .

We will in the next two sections study how the results follow from the nature of the fluctuations causing the excitations, and how the fluctuations are suppressed by saturation effects. We also note that in this approach the effective triple-pomeron coupling is fixed by the constraint, that it is the same dynamics that determines both the coupling between the three pomeron ladders in fig. II.2, and the evolution within the individual ladders. The relation to the triple-Regge formalism will be discussed in sec. 6.



## II.4 The nature of the fluctuations and effects of saturation

### II.4.1 $\gamma^*p$ scattering

The photon wavefunction in eq. (II.14) is divergent for small dipole sizes, which means that infinitely many small dipoles are created with infinitely small cross sections. To illustrate the fluctuations in the dipole cascade we show in fig. II.4 MC results for the probability distribution,  $P(F)$ , for the one pomeron amplitude  $F$  in eq. (II.1) for a dipole with a fixed size  $r = 1/Q$  at a fixed impact parameter  $b$ . The distribution  $P(F)$  is here defined so that  $P(F)dF$  is the probability for the formation of a pair of a projectile and a target cascade, for which the Born amplitude  $F = \sum f_{ij}$  lies between  $F$  and  $F + dF$ . The calculations are performed in the hadronic cms, which implies that the diffractive masses are integrated over the range  $M_X^2 < \sqrt{W^2} \cdot 1 \text{ GeV}$ .

As seen in fig. II.4, the probability distributions can for all  $b$ -values be well approximated by a power spectrum

$$P(F) \approx A F^{-p}, \quad (\text{II.19})$$

with a cutoff for small  $F$ -values. These approximations are shown by the dotted lines. The two parameters  $A$  and  $p$  are tuned to fit the MC results for different values of the energy  $W$ , dipole size  $1/Q$ , and impact parameter  $b$ . (The cutoff is then adjusted to satisfy the normalization condition  $\int P(F)dF = 1$ .) As we will see below, it is particularly interesting to note, that the fitted value for the power  $p$  is independent of the impact parameter  $b$ . It varies, however, slowly with  $Q^2$  and  $W$  as can be seen in table II.1.

The cross sections obtained from these distributions can most easily be estimated from the approximation in eq. (II.19). We see in fig. II.4 that the Born amplitudes are generally small, which implies that unitarity effects are small, and  $T = 1 - e^{-F} \approx F$ . We also note that the widths of the distributions are large, which means that  $\langle T \rangle^2$  can be neglected compared to  $\langle T^2 \rangle$ . The approximation in eq. (II.19) then gives the result

$$\begin{aligned} \frac{d\sigma_{\text{tot}}}{d^2b} &= 2\langle T \rangle = 2A \int_0^\infty (1 - e^{-F}) F^{-p} dF = -2A \Gamma(1 - p); \\ \frac{d\sigma_{\text{diff ex}}}{d^2b} &= V_T \equiv \langle T^2 \rangle - \langle T \rangle^2 \approx \langle T^2 \rangle = \\ &= A \int (1 - e^{-F})^2 F^{-p} dF = \left(1 - \frac{1}{2^{(2-p)}}\right) \times 2\langle T \rangle. \end{aligned} \quad (\text{II.20})$$

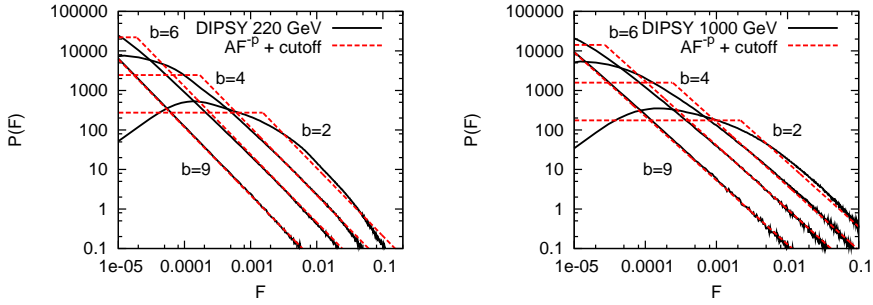


Figure II.4: Probability distribution,  $P(F)$ , for the one-pomeron amplitude  $F$  in DIS, represented by a dipole with size  $r = 1/Q$ , for  $Q^2 = 14 \text{ GeV}^2$  and  $W = 220 \text{ GeV}$  (left) and  $W = 1000 \text{ GeV}$  (right).  $b$  is in units of  $\text{GeV}^{-1}$ . The dotted lines are fits of the form in eq. (II.19).

$\gamma^*p$

$W/\text{GeV}$	220	220	1000	1000
$Q^2/\text{GeV}^2$	14	50	14	50
$p$	1.7	1.8	1.6	1.7

$pp$

$W/\text{GeV}$	100	100	2000	2000
$b \cdot \text{GeV}$	0	6	0	6
$a$	1.4	1.4	0.8	0.8
$p$	1.2	-0.7	1.5	-0.5

II

Table II.1: The values of the parameters in the fits to  $P(F)$  for  $\gamma^*p$ , eq. (II.19), and  $pp$ , eq. (II.22), for some sample energies and  $b$ -values. The power  $p$  is independent of impact parameter in  $\gamma^*p$ , while for  $pp$  it is the exponential suppression  $a$  that does not depend on  $b$ .

From these results we note that the ratio  $d\sigma_{\text{diff ex}}/d\sigma_{\text{tot}} = V_T/(2\langle T \rangle)$  depends only on the value of the parameter  $p$ . As we have found that  $p$  is independent of the impact parameter for fixed  $W$  and  $Q^2$ , we can integrate over  $b$ , and find

$$\frac{\sigma_{\text{diff ex}}}{\sigma_{\text{tot}}} = \frac{V_T}{2\langle T \rangle} \approx 1 - \frac{1}{2^{2-p}} \quad (\text{II.21})$$

Thus the parametrisation in eq. (II.19) gives  $\sigma_{\text{diff ex}}/\sigma_{\text{tot}} \sim 0.18$  for  $Q^2 = 14 \text{ GeV}^2$  falling to  $\sim 0.13$  at  $Q^2 = 50 \text{ GeV}^2$ . Although the simple parametrisation overestimates the result of the MC, it gives a qualitatively correct result.



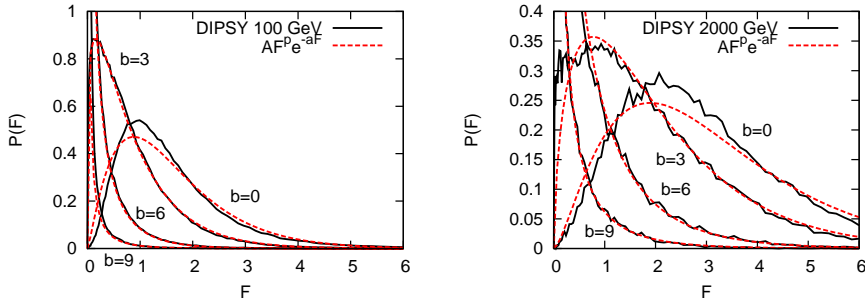


Figure II.5: Probability distribution,  $P(F)$ , for the one-pomeron amplitude  $F$  in  $pp$  collisions for  $W = 100$  GeV (left) and  $W = 2000$  GeV (right).  $b$  is in units of  $\text{GeV}^{-1}$ . The dotted lines are fits of the form in eq. (II.22).

For a virtual photon in DIS the fluctuations will be further enhanced by adding the fluctuations in the photon wave function, but this will not alter the conclusions presented above.

#### II.4.2 $pp$ scattering

The corresponding Born amplitude distributions in  $pp$  collisions are shown in fig. II.5 for  $W = 100$  and  $W = 2000$  GeV and different  $b$ -values. We note that here the interaction probability is large, which implies large saturation effects. The distributions can be well approximated by Gamma functions of the form

$$P(F) = A F^p e^{-aF}. \quad (\text{II.22})$$

The distributions have two parameters,  $p$  and  $a$ , which are tuned to the MC results for different values of energy and impact parameter. The parameter  $A$  is then fixed by the normalisation condition. The result of the fit is shown in table II.1, and we note here that  $a$  is essentially independent of the impact parameter, but falling with energy. For a fixed energy, the decrease in  $\langle F \rangle$  for more peripheral collisions is related to a decrease in  $p$  for larger  $b$ -values, pushing the distribution to smaller values of  $F$ . For fix  $b$  the parameter  $p$  also grows with increasing energy, reflecting the larger interaction probability.

The parametrisation in eq. (II.22) gives

$$\begin{aligned} \langle F \rangle &= \frac{p+1}{a} \\ \frac{V_F}{2\langle F \rangle} &= \frac{1}{2a} \sim 0.35 \text{ for } W = 100 \text{ GeV}, \end{aligned} \quad (\text{II.23})$$



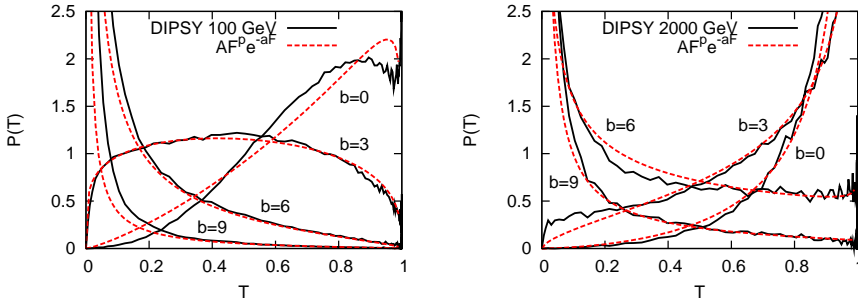


Figure II.6: Probability distribution,  $P(T)$ , for the full amplitude  $T$  for  $pp$  collisions at  $W = 100$  GeV (left) and  $W = 2000$  GeV (right).  $b$  is in units of  $\text{GeV}^{-1}$ . The dotted lines correspond to fits of the form in eq. (II.22).

where  $V_F \equiv \langle F^2 \rangle - \langle F \rangle^2$  is the variance of  $F$ . Thus we find also here that the ratio between the variance and the average of the Born amplitude is independent of  $b$ . We note that this ratio is large, and similar to the result for  $\gamma^*p$  collisions at lower  $Q^2$ -values. Thus, without saturation we would have a correspondingly large value for  $d\sigma_{\text{diff ex}}/d\sigma_{\text{tot}}$  also in  $pp$  collisions.

However, as the one pomeron amplitude  $\langle F \rangle$  is large in  $pp$  scattering, unitarity corrections are very important. The probability distribution for the unitarised amplitude,  $P(T; b)$ , with  $T = 1 - e^{-F}$ , is shown in fig. II.6 for  $W = 100$  and  $2000$  GeV and different  $b$ -values. We see that for the central collisions the distributions are very peaked close to the unitary limit  $T = 1$ . This reduces the fluctuations very strongly. For the parametrisation in eq. (II.22) the average and the variance for the distribution in  $T$  are also easily calculated, and given by

$$\begin{aligned} \langle T \rangle &= 1 - \left( \frac{a}{a+1} \right)^{p+1} \\ V_T &= \left( \frac{a}{a+2} \right)^{p+1} - \left( \frac{a}{a+1} \right)^{2p+2}. \end{aligned} \quad (\text{II.24})$$

We see that at high energies and central collisions, where the Born amplitude  $\langle F \rangle$ , and thus also the parameter  $p$ , become large,  $\langle T \rangle$  will approach 1 and  $V_T$  will go towards 0. For central collision at  $W = 100$  GeV the ratio of diffractive events  $V_T / (2\langle T \rangle)$  is about 0.035, a factor 10 lower than without unitarisation. Therefore in central collisions diffractive excitation is suppressed, and diffractive scattering is dominantly elastic.

The large effect of saturation in  $pp$  collisions has also the effect that factorization is broken when comparing diffractive excitation in DIS and  $pp$  collisions [12].



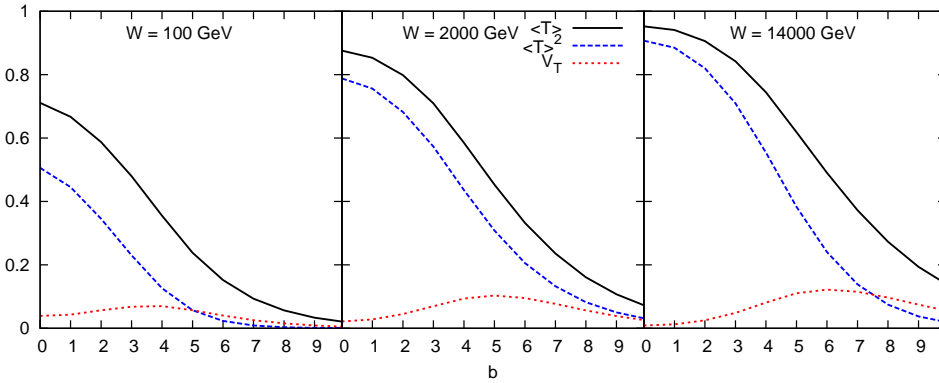


Figure II.7: Impact parameter distributions from the MC for  $\langle T \rangle = (d\sigma_{\text{tot}}/d^2b)/2$ ,  $\langle T \rangle^2 = d\sigma_{\text{el}}/d^2b$ , and  $V_T = d\sigma_{\text{diff ex}}/d^2b$  in  $pp$  collisions at  $W = 100, 2000$ , and  $14000$  GeV.  $b$  is in units of  $\text{GeV}^{-1}$ .

## II.5 Impact parameter profile and $t$ -dependence in $pp$ -collisions

In the previous section we showed the amplitude fluctuations for different impact parameter values. We will here study the  $b$ -dependence, and the corresponding  $t$ -dependence, in more detail. As mentioned above, diffractive excitation is small in central  $pp$  collisions as  $\langle T \rangle$  is approaching 1. In highly peripheral collisions both  $\langle T \rangle$  and  $V_T$  are small, again giving little diffractive excitation. Therefore diffractive excitation is dominated by moderately peripheral collisions, where  $\langle T \rangle \sim 0.5$  and  $\langle F \rangle \sim 1$ . The  $b$ -dependence of  $\sigma_{\text{tot}}/2$ ,  $\sigma_{\text{el}}$ , and  $\sigma_{\text{diff ex}}$  in the MC is shown in fig. II.7.

As pointed out also in earlier analyses (*e.g.* in refs. [14, 31]), this implies that diffractive excitation in  $pp$  collisions appears in a ring with a radius which grows slowly with energy. In a purely perturbative calculation with massless gluons, the total cross section will grow very fast due to the formation of very large dipoles, and eventually violate Froisart's bound. However, as demonstrated by Avsar [28], the inclusion of confinement effects via a massive gluon (as in the simulations described above) implies that very large dipoles are suppressed, and the black disk radius grows proportional to  $\ln s$ . This means that the total and elastic cross sections grow like  $\ln^2 s$  for very large energies. In addition the results in [28] show that the slope, when the interaction drops from black in central to white for more peripheral collisions, is approximately constant with energy. Thus the width of the ring with large diffractive

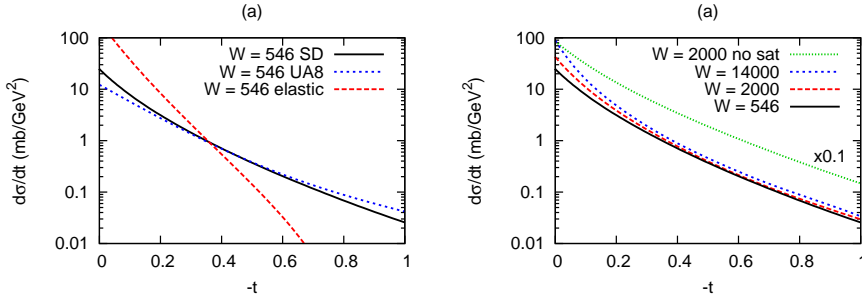


Figure II.8: (a)  $t$ -dependence for the single diffractive cross section at 546 GeV from the MC, together with a fit to UA8 data. The elastic cross section is included for comparison. (b) MC results for the energy dependence of the  $t$ -distribution for single diffractive excitation. The effect of saturation is demonstrated by the dotted line, which shows the result at 2000 GeV without saturation, scaled by a factor 0.1.

excitation is approximately constant at high energies. Consequently the cross section for diffractive excitation will for very large energies grow proportional to the radius of the ring, i.e. proportional to  $\ln s$ .

In our model the interaction is driven by absorption into inelastic channels, and with our definition, where  $S \equiv 1 - T$ , the imaginary part of the amplitude  $T$  is neglected. It is therefore straight forward to take the Fourier transform and calculate the  $t$ -dependence. The result for the differential elastic  $pp$  cross section was presented in ref. [21], and the result for single diffractive excitation is shown in fig. II.8. Figure II.8a shows the result at 546 GeV, together with an extrapolation of a fit to UA8 data [32], normalised to the model result. The UA8 data cover only the range  $0.8 < |t| < 2.5 \text{ GeV}^2$ , but we note that the  $t$ -slope in the model agrees well with this fit. For comparison also the elastic cross section is included in the figure, and we see that the diffractive slope is significantly smaller than the slope in elastic scattering. This is a consequence of the larger  $b$ -values for diffractive excitation shown in fig. II.7.

Figure II.8b shows how the differential cross section for diffractive excitation is varying with energy. We see that the increase is quite slow, as a result of saturation and unitarity constraints. Note that for low  $t$ , the energy dependence is stronger, due to the growth of the radius of the ring, while the energy dependence for high  $t$  is much slower, showing that the width of the ring is almost energy independent, in agreement with ref. [28].

To further illustrate the effect of saturation we show in fig. II.8b



also the  $t$ -dependence of the single diffractive cross section obtained from the unsaturated Born amplitude. We see that saturation reduces the cross section by roughly a factor 25 at 2000 GeV. The slope is less affected, but the suppression for small  $b$ -values implies that the  $t$ -dependence deviates more from a pure exponential, when saturation is included.

## II.6 Relation Good–Walker – Triple-Regge

In this section we will discuss the relation between the results using the Good–Walker formalism described above, and the triple-Regge formalism. In this comparison we want to study the contribution from the bare pomeron, meaning the one-pomeron amplitude without contributions from saturation, enhanced diagrams or gap survival form factors. We want to see if the fluctuations in the dipole cascades reproduce the powerlike energy dependence expected in the Regge formalism.

When  $s$ ,  $M_X^2$ , and  $s/M_X^2$  are not small, pomeron exchange should dominate. If the pomeron is a simple pole we expect the following expressions for the  $pp$  total and diffractive cross sections:

$$\begin{aligned}\sigma_{\text{tot}} &= \beta^2(0)s^{\alpha(0)-1} \equiv \sigma_0^{p\bar{p}}s^\varepsilon, \\ \frac{d\sigma_{\text{el}}}{dt} &= \frac{1}{16\pi}\beta^4(t)s^{2(\alpha(t)-1)}, \\ M_X^2 \frac{d\sigma_{\text{SD}}}{dt d(M_X^2)} &= \frac{1}{16\pi}\beta^2(t)\beta(0)g_{3P}(t)\left(\frac{s}{M_X^2}\right)^{2(\alpha(t)-1)}(M_X^2)^\varepsilon.\end{aligned}\tag{II.25}$$

Here  $\alpha(t) = 1 + \varepsilon + \alpha't$  is the pomeron trajectory, and  $\beta(t)$  and  $g_{3P}(t)$  are the proton-pomeron and triple-pomeron couplings respectively. (We have here omitted the scale  $s_0$  in the powers  $(s/s_0)^\alpha$  or  $(M_X^2/s_0)^\alpha$ . This scale is in the following is assumed to be 1 GeV<sup>2</sup>.)

The results of the MC for the total, elastic, and single diffractive cross sections are shown by the crosses in fig. II.9. The elastic and diffractive cross sections are integrated over  $t$  and  $M_X^2$ . The single diffractive cross section is calculated in the total cms, which corresponds to an integration over masses in the range  $M_X^2 < \sqrt{s} \cdot 1$  GeV, and it corresponds to excitation of one side only. We see that the result indeed has the powerlike increase with energy, which is characteristic for a Regge pole. We also note that in the one-pomeron approximation the elastic cross section is larger than the total for  $\sqrt{s} > 15$  GeV.

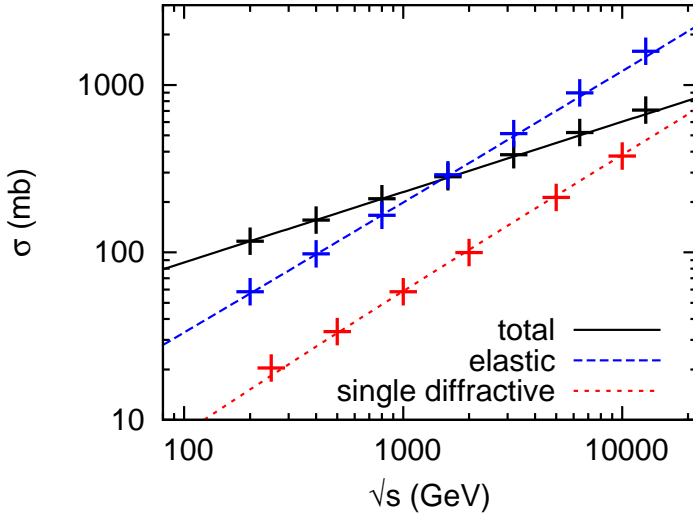


Figure II.9: The total, elastic and single diffractive cross sections in the *one-pomeron* approximation. The crosses are from the dipole cascade model without saturation, and the lines are from a tuned triple Regge parametrisation.

If we assume a simple exponential form for the proton-pomeron coupling,  $\beta(t) = \beta(0) \exp(b_{0,\text{el}} t/4)$ , we can integrate the elastic cross section in eq. (II.26) over  $t$ , and obtain

$$\sigma_{\text{el}} = \frac{\sigma_{\text{tot}}^2}{16\pi B(s)}, \quad \text{with } B(s) = b_{0,\text{el}} + 2\alpha' \ln s. \quad (\text{II.26})$$

Besides the shrinking of the elastic peak, the pomeron slope  $\alpha'$  also gives a logarithmic correction to the powerlike increase of the elastic cross section. A consistent fit to both quantities is obtained for  $\alpha' = 0.2 \text{ GeV}^{-2}$ . In fig. II.9 the lines are obtained from the expressions in eqs. (II.26, II.26) with the parameter values

$$\begin{aligned} \alpha(0) &= 1 + \epsilon = 1.21, \quad \alpha' = 0.2 \text{ GeV}^{-2}, \\ \sigma_0^{p\bar{p}} &= \beta^2(0) = 12.6 \text{ mb}, \quad b_{0,\text{el}} = 8 \text{ GeV}^{-2}, \\ g_{3P}(t) &= \text{const.} = 0.3 \text{ GeV}^{-1}. \end{aligned} \quad (\text{II.27})$$

We have here assumed a constant triple-pomeron coupling, and we see that the MC results in fig. II.9 are very well reproduced by this fit.

The  $t$ -dependence of elastic scattering and diffractive excitation, shown in fig. II.10, are however not pure exponentials, as assumed in



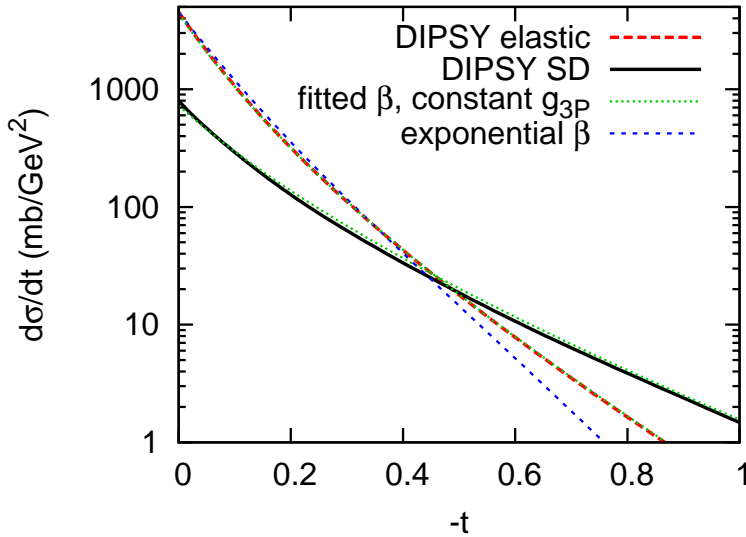


Figure II.10:  $t$ -dependence for elastic and single diffractive excitation without saturation effects, at 1800 GeV. A very close fit to  $d\sigma_{\text{el}}/dt$  is obtained from the proton-pomeron coupling in eq. (II.28). Including a constant triple-pomeron coupling in the expression for diffractive excitation gives the thin dotted line, which gives a good description of the model result. For comparison also a pure exponential fit to the elastic cross section is included.

the fit above. (For diffractive excitation a minor deviation from a pure exponent originates from the integration over  $M_X^2$ .) We want to study this dependence in some more detail, and are here in particular interested in the  $t$ -dependence of the triple-pomeron coupling  $g_{3P}(t)$ . A very close fit to  $d\sigma_{\text{el}}/dt$  is obtained for (with  $t$  measured in  $\text{GeV}^2$ )

$$\beta^4(t) = \beta^4(0) \exp\left(\frac{10t}{1 - 1.8t}\right), \quad (\text{II.28})$$

which cannot be distinguished from the MC result in fig. II.10. Inserting this fit into the expression for the diffractive cross section integrated over  $M_X^2$ , and assuming a constant triple-pomeron coupling equal to  $0.27 \text{ GeV}^{-2}$ , gives the thin dotted line in fig. II.10. We see that this is quite a good fit. It is slightly less steep for  $|t|$ -values below  $0.1 \text{ GeV}^2$ , but deviating less than 10% from the result of the model. We also note that these modifications of the  $t$ -dependence for the elastic and diffractive cross sections do not modify the good fits to the integrated cross sections in fig. II.9.

We here want to make the following comments:

- *Comparison with perturbative QCD*

The expressions in eq. (II.26) correspond to a pomeron which is a simple pole. This is not the case in perturbative QCD. In the LL approximation the pomeron is a cut in the angular momentum plane, which gives logarithmic corrections to the proton-pomeron coupling:  $\beta(0) \sim 1/(\ln s)^{1/4}$  while  $\beta(t) \sim 1/(\ln s)^{3/4}$  for  $t \neq 0$  [16,33]. The different  $s$ -dependence when  $t$  is equal to, or different from, zero is associated with a cusp in the  $t$ -dependence at  $t = 0$ . However, at these small  $t$ -values perturbative QCD is not applicable, and non-perturbative effects are important. It was also pointed out by Lipatov [34], that a running coupling can modify the cut to a series of poles. (Note that a running coupling is included in our model simulations.) A strong increase in the elastic cross section at very small  $t$ -values is not seen in the experimental data, and also not present in our result in fig. II.10. An extra factor of  $1/(\ln s)^{1/4}$  in  $\beta(0)$  and  $\beta(t)$  would give an equally good fit to the results in fig. II.9, provided the pomeron intercept is increased to  $\alpha(0) = 1.25$ . It is, however, not possible to find a good fit if  $\beta(t)$  is proportional to  $1/(\ln s)^{3/4}$ , inside a  $t$ -region essential for the integrated elastic cross section.

In LL perturbative QCD also the triple-pomeron coupling has a singular behaviour at  $t = 0$  [16,33]:

$$g_{3P}(t) \sim \frac{1}{(\ln M_X^2)^{1/4} (\ln s/M_X^2)^{3/4}} \frac{1}{\sqrt{-t}} \quad (\text{II.29})$$

We saw above that our results were well reproduced by a constant triple-pomeron coupling, only slightly underestimating the slope for small  $t$ -values below  $|t| = 0.1$ , and our analysis does not support a triple-pomeron coupling with a strong  $t$ -dependence. A slowly varying triple-pomeron coupling is also in agreement with early analyses [35,36]. We note, however, that the magnitude of the triple-pomeron coupling agrees (within the large uncertainties) with the perturbative estimate in ref. [33], which in our notation corresponds to  $\pi g_{3P} \sim 0.2 - 1.7 \text{ GeV}^{-1}$  for  $0.25 < |t| < 4 \text{ GeV}^2$ .

- *Comparison with other analyses*

We should also note that the bare pomeron is not an observable. Here we have included NLL effects and confinement in the evo-



lution, but not nonlinear effects from saturation or multiple collisions. The effect of nonlinearity will appear differently if one first adds NLL effects and then compares the results with and without saturation, as compared with an approach where the LL result is compared with and without saturation, before NLL effects are included. Therefore the bare pomeron may look different, depending upon the scheme used to remove the nonlinear effects.

Keeping this in mind, we want to compare our result in eq. (II.28) with some recent more traditional Regge analyses. As examples the bare pomeron in the analysis by Ryskin *et al.* [4] has three components with different dependence on the impact parameter, or  $t$ , in order to mimic the branch cut structure of the pomeron singularity. The three poles have the same intercept equal to  $\alpha(0) = 1.3$ , and quite small slopes. The dominant component has  $\alpha' = 0.05 \text{ GeV}^{-2}$ , and the slope of the other components are even smaller. Ostapchenko [37] finds in an approach with two pomerons  $\alpha(0) \approx 1.35, \alpha' \approx 0.08 \text{ GeV}^{-2}$  and  $\alpha(0) \approx 1.15, \alpha' \approx 0.14 \text{ GeV}^{-2}$  for the hard and soft pomerons respectively. Gotsman *et al.* [24] find in an analysis with a single pomeron  $\alpha(0) = 1.335$  and  $\alpha' = 0.01 \text{ GeV}^{-2}$ . In another fit with a single pomeron pole Kaidalov *et al.* [38] find  $\alpha(0) = 1.12$  and  $\alpha' = 0.22 \text{ GeV}^{-2}$ . We can also compare with the results by Goulianos [7, 13], who in a formalism with a renormalised pomeron flux finds the values  $\alpha(0) \approx 1.11$  and  $\alpha' = 0.26 \text{ GeV}^{-1}$ . We see here that the way saturation is taken into account can have a large effect on the result for the bare pomeron. We also note that our result lies somewhere in between these examples.

In conclusion we see that the Born amplitude in our dipole cascade model indeed reproduces the triple-Regge formula for a bare pomeron pole with  $\alpha(0) = 1.21, \alpha' = 0.2$ , and an almost constant triple-pomeron coupling. The  $t$ -dependence of both the elastic and the diffractive cross sections is close to an exponential. There is no indication for more dramatic variations, like those obtained in LL perturbative QCD, where the pomeron is a cut singularity in the angular momentum plane. Here one also expects  $\beta(0) \sim 1/(\ln s)^{1/4}$  while  $\beta(t) \sim 1/(\ln s)^{3/4}$  for  $t \neq 0$ . Our result would be consistent with a proton-pomeron coupling proportional to  $1/(\ln s)^{1/4}$ , if the intercept is increased to 1.25, but not with  $\beta(t) \sim 1/(\ln s)^{3/4}$ .



## II.7 Conclusions

Diffraction excitation represents a large fraction of the cross section in  $pp$  collisions or DIS. In the Good–Walker formalism diffractive excitation is determined by the fluctuations in the scattering amplitude. In traditional applications this formalism has been limited to small mass excitation, while excitation to high masses has been described in the triple-Regge formalism, introducing a set of parameters for the pomeron couplings. It was demonstrated by Mueller and Salam [6] that BFKL evolution contains large fluctuations, and in this paper we demonstrate that, by including these fluctuations in the analysis, it is possible to describe diffractive excitation to both low and high masses.

The Lund Dipole Cascade model, implemented in the DIPSY MC, describes successfully the total, elastic, and diffractive cross sections in DIS and  $pp$  collisions [18, 19, 21]. In this paper we show how the fluctuations in the BFKL evolution can reproduce diffractive excitation to low and high masses within the Good–Walker formalism, with parameters determined only from the total and elastic cross sections. In DIS at HERA the fluctuations give a diffractive cross section of the order of 10%, and saturation has a relatively small effect on the result. However, in  $pp$  collisions unitarity constraints and saturation reduce the fluctuations, when the scattering approaches the black disc limit. Therefore diffractive excitation in high energy  $pp$  collisions is dominated by peripheral collisions, and pomeron exchange in DIS and  $pp$  collisions does not factorise.

In the triple-Regge formalism, saturation effects are included in terms of “enhanced diagrams”, gap-survival form factors or saturation effects in the pomeron flux, which reduce the effect of the “bare pomeron”. In this paper we have also studied the effective bare pomeron, corresponding to the result obtained when non-linear effects are not included. We see that the result indeed is well described by a bare pomeron pole, with  $\alpha(0) = 1.21$  and  $\alpha' = 0.2 \text{ GeV}^{-2}$ . The triple-pomeron coupling is fixed by the couplings in the BFKL ladder, and the results are well reproduced by a constant coupling  $g_{3P} \approx 0.3 \text{ GeV}^{-1}$ . Although our model is based on perturbative QCD, with non-perturbative effects introduced only in the incoming proton wavefunction and confinement effects via an effective gluon mass, this result contrasts to LL BFKL, where the pomeron is a cut singularity and the pomeron couplings have strong  $t$ -dependencies.

In this paper we have not discussed the properties of exclusive final



states in diffractive excitation (apart from the mass distribution). We hope to return to this problem and to hard diffraction in future work.

The main results can be summarised as follows:

- The *fluctuations* in a BFKL ladder are large. Taking these fluctuations into account as in the DIPSY MC, it is possible to describe diffractive excitations to both low and high masses within the Good–Walker formalism.

- *Saturation* effects are small in DIS, but large in  $pp$  collisions. Therefore diffractive excitation is a peripheral process in  $pp$  scattering, and factorisation of pomeron exchange is broken.

- The result of the Good–Walker formalism *reproduces the triple-Regge* result for diffractive excitation, with a bare pomeron pole with  $\alpha(0) = 1.21$ ,  $\alpha' = 0.2 \text{ GeV}^{-2}$ , and an almost constant triple-pomeron coupling  $g_{3P} \approx 0.3 \text{ GeV}^{-1}$ .

## II.8 Acknowledgements

We want to thank Leif Lönnblad for valuable discussions. Work supported in part by the Marie Curie RTN “MCnet” (contract number MRTN-CT-2006-035606).

## II References

- [1] M. L. Good and W. D. Walker, "Diffraction dissociation of beam particles," *Phys. Rev.* **120** (1960) 1857–1860.
- [2] A. H. Mueller, "O(2,1) ANALYSIS OF SINGLE PARTICLE SPECTRA AT HIGH- ENERGY," *Phys. Rev.* **D2** (1970) 2963–2968.
- [3] C. E. DeTar *et al.*, "Helicity poles, triple-regge behavior, and single-particle spectra in high-energy collisions," *Phys. Rev. Lett.* **26** (1971) 675–676.
- [4] M. G. Ryskin, A. D. Martin, and V. A. Khoze, "Soft processes at the LHC, I: Multi-component model," *Eur. Phys. J.* **C60** (2009) 249–264, arXiv:0812.2407 [hep-ph].
- [5] A. B. Kaidalov and M. G. Poghosyan, "Description of soft diffraction in the framework of reggeon calculus. Predictions for LHC," arXiv:0909.5156 [hep-ph].
- [6] A. H. Mueller and G. P. Salam, "Large multiplicity fluctuations and saturation effects in onium collisions," *Nucl. Phys.* **B475** (1996) 293–320, hep-ph/9605302.
- [7] K. Goulianos, "Renormalization of hadronic diffraction and the structure of the pomeron," *Phys. Lett.* **B358** (1995) 379–388, arXiv:hep-ph/9502356.
- [8] N. Nikolaev and B. G. Zakharov, "Pomeron structure function and diffraction dissociation of virtual photons in perturbative QCD," *Z. Phys.* **C53** (1992) 331–346.
- [9] J. Bartels and M. Wusthoff, "A perturbative approach to diffractive deep inelastic scattering," *J. Phys.* **G22** (1996) 929–936.
- [10] J. Bartels, J. R. Ellis, H. Kowalski, and M. Wusthoff, "An analysis of diffraction in deep-inelastic scattering," *Eur. Phys. J.* **C7** (1999) 443–458, hep-ph/9803497.
- [11] K. J. Golec-Biernat and M. Wusthoff, "Diffractive parton distributions from the saturation model," *Eur. Phys. J.* **C20** (2001) 313–321, arXiv:hep-ph/0102093.



- [12] **H1 Collaboration**, F.-P. Schilling, “NLO QCD fit to H1 diffractive DIS data,” *Acta Phys. Polon.* **B33** (2002) 3419–3424, arXiv:hep-ex/0209001.
- [13] K. Goulianos, “Hadronic diffraction: Where do we stand?,” arXiv:hep-ph/0407035.
- [14] H. I. Miettinen and J. Pumplin, “Diffraction Scattering and the Parton Structure of Hadrons,” *Phys. Rev.* **D18** (1978) 1696.
- [15] A. H. Mueller, “Soft gluons in the infinite momentum wave function and the BFKL pomeron,” *Nucl. Phys.* **B415** (1994) 373–385.
- [16] A. H. Mueller and B. Patel, “Single and double BFKL pomeron exchange and a dipole picture of high-energy hard processes,” *Nucl. Phys.* **B425** (1994) 471–488, hep-ph/9403256.
- [17] A. H. Mueller, “Unitarity and the BFKL pomeron,” *Nucl. Phys.* **B437** (1995) 107–126, hep-ph/9408245.
- [18] E. Avsar, G. Gustafson, and L. Lönnblad, “Energy conservation and saturation in small- $x$  evolution,” *JHEP* **07** (2005) 062, arXiv:hep-ph/0503181.
- [19] E. Avsar, G. Gustafson, and L. Lönnblad, “Small- $x$  dipole evolution beyond the large- $N(c)$  limit,” *JHEP* **01** (2007) 012, arXiv:hep-ph/0610157.
- [20] E. Avsar, G. Gustafson, and L. Lönnblad, “Diffractive Excitation in DIS and pp Collisions,” *JHEP* **12** (2007) 012, arXiv:0709.1368 [hep-ph].
- [21] C. Flensburg, G. Gustafson, and L. Lonnblad, “Elastic and quasi-elastic  $pp$  and  $\gamma^*p$  scattering in the Dipole Model,” *Eur. Phys. J.* **C60** (2009) 233–247, arXiv:0807.0325 [hep-ph].
- [22] M. G. Ryskin, A. D. Martin, and V. A. Khoze, “Soft processes at the LHC, II: Soft-hard factorization breaking and gap survival,” *Eur. Phys. J.* **C60** (2009) 265–272, arXiv:0812.2413 [hep-ph].
- [23] M. Boonekamp, R. B. Peschanski, and C. Royon, “Inclusive Higgs boson and dijet production via double pomeron exchange,” *Phys. Rev. Lett.* **87** (2001) 251806, arXiv:hep-ph/0107113.

- [24] E. Gotsman, E. Levin, U. Maor, and J. S. Miller, “A QCD motivated model for soft interactions at high energies,” *Eur. Phys. J.* **C57** (2008) 689–709, arXiv:0805.2799 [hep-ph].
- [25] B. Cox, J. Forshaw, and L. Lönnblad, “Hard colour singlet exchange at the Tevatron,” *JHEP* **10** (1999) 023, hep-ph/9908464.
- [26] Y. Hatta, E. Iancu, C. Marquet, G. Soyez, and D. N. Triantafyllopoulos, “Diffusive scaling and the high-energy limit of deep inelastic scattering in QCD at large  $N(c)$ ,” *Nucl. Phys.* **A773** (2006) 95–155, hep-ph/0601150.
- [27] G. P. Salam, “An introduction to leading and next-to-leading BFKL,” *Acta Phys. Polon.* **B30** (1999) 3679–3705, hep-ph/9910492.
- [28] E. Avsar, “On the High Energy Behaviour of The Total Cross Section in the QCD Dipole Model,” *JHEP* **04** (2008) 033, arXiv:0803.0446 [hep-ph].
- [29] **CDF Collaboration**, F. Abe *et al.*, “Measurement of  $\bar{p}p$  single diffraction dissociation at  $\sqrt{s} = 546$  GeV and 1800 GeV,” *Phys. Rev.* **D50** (1994) 5535–5549.
- [30] **CDF Collaboration**, F. Abe *et al.*, “Measurement of the  $\bar{p}p$  total cross-section at  $\sqrt{s} = 546$  GeV and 1800-GeV,” *Phys. Rev.* **D50** (1994) 5550–5561.
- [31] S. Sapeta and K. J. Golec-Biernat, “Total, elastic and diffractive cross sections at LHC in the Miettinen-Pumplin model,” *Phys. Lett.* **B613** (2005) 154–161, arXiv:hep-ph/0502229.
- [32] P. Bruni and G. Ingelman, “Diffractive W and Z production at p anti-p colliders and the pomeron parton content,” *Phys. Lett.* **B311** (1993) 317–323.
- [33] J. Bartels, M. G. Ryskin, and G. P. Vacca, “On the triple pomeron vertex in perturbative QCD,” *Eur. Phys. J.* **C27** (2003) 101–113, arXiv:hep-ph/0207173.
- [34] L. N. Lipatov, “The Bare Pomeron in Quantum Chromodynamics,” *Sov. Phys. JETP* **63** (1986) 904–912.
- [35] A. B. Kaidalov, V. A. Khoze, Y. F. Pirogov, and N. L. Ter-Isaakyan, “On determination of the triple pomeron coupling from the ISR data,” *Phys. Lett.* **B45** (1973) 493–496.



- [36] R. D. Field and G. C. Fox, "Triple Regge and Finite Mass Sum Rule Analysis of the Inclusive Reaction  $p + p \rightarrow p + x$ ," *Nucl. Phys.* **B80** (1974) 367.
- [37] S. Ostapchenko, "Total and diffractive cross sections in enhanced Pomeron scheme," *Phys. Rev.* **D81** (2010) 114028, [arXiv:1003.0196 \[hep-ph\]](#).
- [38] A. B. Kaidalov and M. G. Poghosyan, "Predictions of Quark-Gluon String Model for pp at LHC," [arXiv:0910.2050 \[hep-ph\]](#).

# III

## Correlations in double parton distributions at small $x$

Christoffer Flensburg<sup>1</sup>, Gösta Gustafson<sup>1</sup>, Leif Lönnblad<sup>1,2</sup> and Andras Ster<sup>1,3</sup>

<sup>1</sup>Dept. of Astronomy and Theoretical Physics, Lund University,  
Sweden

<sup>2</sup>CERN Theory Department, Geneva, Switzerland

<sup>3</sup>KFKI-RMKI, Hungary

LU-TP 11-12

CERN-PH-TH-2011-059

MCnet-11-09

e-Print: [arXiv:1103.4320]

We present a dynamical study of the double parton distribution in impact parameter space, which enters into the double scattering cross section in hadronic collisions. This distribution is analogous to the generalized parton densities in momentum space. We use the Lund Dipole Cascade model, presented in earlier articles, which is based on BFKL evolution including essential higher order corrections and saturation effects. As result we find large correlation effects, which break the factorization of the double scattering process. At small transverse separation we see the development of "hot spots", which become stronger with increasing  $Q^2$ . At smaller  $x$ -values the distribution widens, consistent with the shrinking of the diffractive peak in elastic scattering. The dependence on  $Q^2$  is, however, significantly stronger than the dependence on  $x$ , which has implications for extrapolations to LHC, *e.g.* for results for underlying events associated with the production of new heavy particles.

III



### III.1 Introduction

Analyses of high energy  $pp$  collisions show that multiple hard parton collisions are quite common. Four-jet events, in which the jets balance each other pairwise, were observed at  $\sqrt{s} = 63$  GeV by the AFS collaboration at the CERN ISR [1], and at the Tevatron events with four jets, or with three jets +  $\gamma$ , have been observed by the CDF [2,3] and D0 [4,5] collaborations. These results also show that the hard subcollisions are correlated, and double interactions occur with a larger probability than expected for uncorrelated hard interactions.

Knowing the cross section for double subcollisions is important for an estimate of the underlying event. A good understanding of the correlations is therefore also essential for the interpretation of signals for new physics at the LHC. The aim of this paper is to study what kind of dynamical correlations in momentum space and impact parameter space are to be expected at higher energies, as a result of parton evolution to small  $x$  and of saturation effects.

Correlations which follow from energy and flavour conservation have been discussed *e.g.* in refs. [6–8], and from an impact parameter picture in ref. [9]. Nontrivial correlations which are consequences of DGLAP evolution have been studied in refs. [7, 10, 11]. However, in these references the connection between correlations in momentum and  $b$ -space have not been studied. Correlation effects also follow from fluctuations in the number of particles in the parton cascades, which is discussed in refs. [6, 7].

In the model by Sjöstrand and van Zijl [8], later modified in ref. [12] and implemented in the PYTHIA 8 event generator [13–15], it is assumed that the dependence of the double parton density on the kinematic variables ( $x$  and  $Q^2$ ) and the separation in impact parameter space ( $\mathbf{b}$ ) factorizes. The correlation is described by a distribution in the separation  $\mathbf{b}$ , where a denser central region implies that central collisions have on average more hard interactions, and peripheral collisions fewer. The relative shape of this distribution is kept constant, but the width is scaled with energy, to accommodate the growth of the total (non-diffractive) and the multiple interaction cross sections with increasing energy. For the dependence on  $x$  and  $Q^2$  effects of energy and flavour conservation are taken into account. In a recent modification of the model, the shape is also varying with  $x$  [16], in a way which gives smaller correlations for smaller  $x$ . At a fixed energy, higher  $Q^2$  is related to larger  $x$ , which implies that the production of heavy mass objects is more common in



high multiplicity events. Similar approaches are also implemented in the HERWIG++ event generator [17–19].

While it is straight forward to compare the models in PYTHIA 8 and HERWIG with experimental data on double parton scattering, it is not trivial to disentangle exactly the sources of possible correlations in the underlying models. This makes it difficult to extrapolate to higher energy and/or higher  $Q^2$ . Here we will instead use a detailed dynamical model for parton evolution, for a study of the correlations between gluons inside hadrons.

In a series of papers we have presented a model based on BFKL [20, 21] evolution and saturation, which well reproduces data on total, elastic and diffractive cross sections in DIS and  $pp$  collisions [22–26]. It is based on Mueller’s dipole cascade model [27–29], but includes also non-leading effects from energy conservation and running coupling, as well as confinement effects and saturation within the evolution. The model is implemented in a Monte Carlo (MC) program, which makes it easy to study in detail the types of correlations and fluctuations in  $x$  and  $Q^2$  as well as in impact parameter space, which are consequences of the parton evolution.

The correlations come from two different sources. First the distribution in transverse separation will vary with energy and virtuality, as the impact parameter profile widens at higher energy, but at the same time the development of “hot spots” makes the effective double scattering profile more narrow. Secondly, BFKL dynamics implies large fluctuations in the cascade evolution. This implies that double scattering is more probable in events with a higher than average number of partons. This effect is neglected in most phenomenological analyses, which are based on average parton densities.

The outline of this paper is as follows. First we will go through experimental aspects and the theoretical framework for double parton scattering in section III.2. In section III.3 we will then briefly describe the dipole model in the DIPSY Monte Carlo, followed by a description in section III.4 of how we will use this model to investigate correlations in the double parton densities. The results are presented in section III.5 followed by conclusions and outlook in section III.6.



## III.2 Double Parton Scattering and Double Parton Distributions

### III.2.1 Experimental results

A measure of the correlation is given by the quantity  $\sigma_{\text{eff}}$  defined by the relation

$$\sigma_{(A,B)}^D = \frac{1}{(1 + \delta_{AB})} \frac{\sigma_A^S \sigma_B^S}{\sigma_{\text{eff}}}. \quad (\text{III.1})$$

Here  $\sigma_{(A,B)}^D$  is the cross section for the two hard processes  $A$  and  $B$ ,  $\sigma_A^S$  and  $\sigma_B^S$  the corresponding single inclusive cross sections, and  $(1 + \delta_{AB})^{-1}$  is a symmetry factor equal to  $1/2$  if  $A = B$ . If the hard interactions were uncorrelated,  $\sigma_{\text{eff}}$  would be equal to the total non-diffractive cross section. The CDF and D0 measurements give instead  $\sigma_{\text{eff}} \sim 15$  mb, which thus is significantly smaller.

As mentioned in the introduction, experimental results on double parton interactions have been published from the ISR and the Tevatron. (The UA2 collaboration at the CERN  $S\bar{p}\bar{p}S$  collider has presented a lower limit for  $\sigma_{\text{eff}}$ .) The ISR experiment [1] studied events with four jets with a summed transverse energy above 29 GeV in  $pp$  collisions at  $\sqrt{s} = 63$  GeV. The observed rate corresponds to  $\sigma_{\text{eff}} = 5$  mb, indicating a very strong correlation between the partons. As the sum of  $E_{\perp}$  for the four jets is about 30 GeV, the typical  $x$ -values for the partons is about 0.25. These partons must be dominated by valence quarks, and therefore not representative for the partons involved at higher energies and smaller  $x$ .

The CDF collaboration studied 4-jet events with  $\sum p_{\perp \text{jet}} > 140$  GeV at  $\sqrt{s} = 1.8$  TeV [2], which implies  $x$ -values  $\sim 0.04$ . The result obtained was  $\sigma_{\text{eff}} = 12.1_{-5.4}^{+10.7}$  mb. CDF also studied events with  $\gamma+3$ jets [3]. This gave a more clear signal than the 4-jet events, and the result is  $\sigma_{\text{eff}} = 14.5 \pm 1.7_{-2.3}^{+1.7}$  mb. The photons had  $E_{\perp \gamma} > 16$  GeV, and the jets  $E_{\perp \text{jet}} > 5$  GeV, and thus the  $x$ -values are smaller. No dependence on the Feynman scaling variable for the two pairs was observed within the ranges  $0.01 < x_F(\gamma + \text{jet}) < 0.4$  and  $0.002 < x_F(\text{dijet}) < 0.2$ . We note, however, that the 4-jet and  $\gamma+3$ jet processes are not equivalent, as the production of a photon are particularly sensitive to quark distributions.

While the D0 4-jet signal is rather weak [4], this collaboration also measures a clear signal for  $\gamma+3$ jets [5]. The transverse momenta, and thus the parton  $x$ -values, are larger than those in the CDF analysis;  $p_{\perp \gamma} > 60$  GeV and  $p_{\perp \text{jet}2} > 15$  GeV. The result obtained is  $\sigma_{\text{eff}} =$

$16.4 \pm 0.3 \pm 2.3$  mb. D0 also studied the dependence on  $p_\perp$  of the second jet. Here  $\sigma_{\text{eff}}$  dropped by 24% when  $p_\perp$  increased from 17.5 to 27.5 GeV, but this variation was fully within the errors of the measurement.

### III.2.2 Formalism

Following ref. [11] we define the “double parton distribution”  $\Gamma_{ij}(x_1, x_2, b; Q_1^2, Q_2^2)$ , which describes the inclusive density distribution for finding a parton of type  $i$  with energy fraction  $x_1$  at scale  $Q_1^2$ , together with a parton of type  $j$  with energy fraction  $x_2$  at scale  $Q_2^2$ , and with the two partons separated by a transverse distance  $b$ . The distributions  $\Gamma_{ij}$  are via a Fourier transformation related to the “two-parton generalized parton distributions” in transverse momentum space,  $D(x_1, x_2, Q_1^2, Q_2^2, \vec{\Delta})$ , studied by Blok *et al.* [30].

Assuming factorisation of two hard subprocesses  $A$  and  $B$ , the cross section for double scattering is given by<sup>1</sup>

$$\sigma_{(A,B)}^D = \frac{1}{1 + \delta_{AB}} \sum_{i,j,k,l} \int \Gamma_{ij}(x_1, x_2, b; Q_1^2, Q_2^2) \hat{\sigma}_{ik}^A(x_1, x'_1) \hat{\sigma}_{jl}^B(x_2, x'_2) \times \Gamma_{kl}(x'_1, x'_2, b; Q_1^2, Q_2^2) dx_1 dx_2 dx'_1 dx'_2 d^2b. \quad (\text{III.2})$$

Here  $\hat{\sigma}$  is the cross section for a parton-level subprocess.

The approximation used in the event generators PYTHIA8 and HERWIG means that, apart from effects of energy and flavour conservation (which are quite important),  $\Gamma$  factorizes in the form

$$\Gamma_{ij}(x_1, x_2, b; Q_1^2, Q_2^2) \sim D^i(x_1, Q_1^2) D^j(x_2, Q_2^2) F(b; s). \quad (\text{III.3})$$

Here  $D^i$  denotes the single parton distribution for parton type  $i$ , and  $F(b; s)$  describes the distribution in the transverse separation between the two partons, and is assumed to be independent of  $x_i$  and  $Q_i^2$ , and to be the same for quarks and gluons. (As mentioned in the introduction, in a recent option in PYTHIA8,  $F$  depends also on  $x$  [16].) The width is adjusted by tuning the model to reproduce the total cross section and multiple interactions, and thus depends on the collision energy  $\sqrt{s}$ , as indicated in eq. eq. (III.3).

As mentioned in the introduction, the relation in eq. (III.3) is not consistent with DGLAP evolution. Gaunt and Sterling [11] assume the

<sup>1</sup>This result is true if the parton-parton scattering is local in impact parameter space, which ought to be the case for hard collisions with large  $Q^2$ -values.



weaker relation

$$\Gamma_{ij}(x_1, x_2, b; Q_1^2, Q_2^2) = D^{ij}(x_1, x_2; Q_1^2, Q_2^2) F_j^i(b). \quad (\text{III.4})$$

The relations in eq. eq. (III.2) and eq. eq. (III.3) or eq. (III.4) imply that the effective cross section in eq. (III.1) is determined by the relation

$$\sigma_{\text{eff}} = \left[ \int d^2b (F(b))^2 \right]^{-1}. \quad (\text{III.5})$$

In the following we want to use the Lund Dipole Cascade model to study the correlations and fluctuations, which follow from the parton evolution in a proton, and see how well the approximations in eqs. eq. (III.3) and eq. (III.4) are satisfied. We note, however, that as our model is based on the BFKL evolution, it contains only gluons and should only be trusted at small  $x$ -values where the gluons dominate.

We define the distribution  $F(b; x_1, x_2, Q_1^2, Q_2^2)$  by the relation

$$\Gamma(x_1, x_2, b; Q_1^2, Q_2^2) = D(x_1, Q_1^2) D(x_2, Q_2^2) F(b; x_1, x_2, Q_1^2, Q_2^2). \quad (\text{III.6})$$

Thus  $F$  is a density in transverse coordinate space  $\mathbf{b}$ , which may depend on all four variables  $x_1, x_2, Q_1^2$ , and  $Q_2^2$ , and which contains all information about correlations between the two partons. In case *e.g.* some kind of “hot spots” develop for small  $x$  and/or large  $Q^2$ , this will show up as an increase in  $F$  for small  $b$ -values. With this definition  $F$  is related to the double scattering cross section via eq. eq. (III.1) and the relation

$$\sigma_{\text{eff}} = \left[ \int d^2b F(b; x_1, x_2, Q_1^2, Q_2^2) F(b; x'_1, x'_2, Q_1^2, Q_2^2) \right]^{-1}, \quad (\text{III.7})$$

with the constraint

$$s = \frac{Q_1^2}{x_1 x'_1} = \frac{Q_2^2}{x_2 x'_2}. \quad (\text{III.8})$$

For hard subcollisions at midrapidity we have  $x_1 \approx x'_1$  and  $x_2 \approx x'_2$ , and thus recover eq. eq. (III.5), with the difference that  $\sigma_{\text{eff}}$  may now depend on the variables  $x_i$  and  $Q_i^2$  (with  $Q_1^2/x_1^2 = Q_2^2/x_2^2 = s$ ). We note, however, that for subcollisions away from midrapidity we get different  $x$ -values in the two  $F$ -distributions in eq. eq. (III.7). This feature will be further discussed in sec. III.5.

### III.2.3 Correlations

There are two different sources for correlations between the partons, which both give contributions to  $\sigma_{\text{eff}}$ .

### Distribution in impact parameter space

More central collisions are expected to have more hard subcollisions than peripheral collisions. This feature causes correlations, which depend on the matter distribution within the colliding protons. To understand the effect of the matter distribution, we here study a simplified version of the model implemented in the PYTHIA 8 event generator. A discussion of the results in our model, and a comparison with more refined versions of PYTHIA 8, are presented in sec. III.5.

Assume that the parton density inside a proton is given by a Gaussian distribution  $\rho \propto \exp(-r^2/a^2)$ . Integrating over the longitudinal coordinate  $z$  gives a factor  $\sqrt{\pi}a$  independent of the impact parameter  $b = \sqrt{x^2 + y^2}$ . Thus the density in impact parameter space is also given by

$$\rho \propto \exp(-b^2/a^2). \quad (\text{III.9})$$

The two parton density is then given by

$$F(b) \propto \int d^2r \rho(\mathbf{r}) \rho(\mathbf{r} - \mathbf{b}) \propto \exp(-b^2/2a^2). \quad (\text{III.10})$$

The  $F$ -distribution is normalized to 1, and has therefore a normalization constant equal to  $(\pi 2a^2)^{-1}$ . This implies that

$$\sigma_{\text{eff}} = \left( \int d^2b F^2 \right)^{-1} = 4\pi a^2. \quad (\text{III.11})$$

In PYTHIA 8 it is assumed that for two colliding protons, the average number of hard subcollisions is proportional to the overlap of the two distributions. For a collision at impact parameter  $b$ , this overlap is given by

$$\mathcal{O}(b) = \int d^2r \rho(\mathbf{r}) \rho(\mathbf{r} - \mathbf{b}) \propto \exp(-b^2/2a^2), \quad (\text{III.12})$$

We note that the integral in eq. eq. (III.12) is exactly the same as the one determining  $F$  in eq. eq. (III.10). The distribution  $F$  is normalized to 1, and we therefore find

$$F(b) = \mathcal{O}(b) / \int d^2b \mathcal{O}(b). \quad (\text{III.13})$$

Since in PYTHIA 8 the average number of hard subcollisions at a fixed impact parameter,  $\bar{n}(b)$ , is proportional to the overlap,  $\mathcal{O}(b)$ , it can be written as

$$\bar{n}(b) \propto \mathcal{O}(b) \cdot \hat{\sigma}, \quad (\text{III.14})$$



where the cross section for parton–parton collisions is approximated by  $\hat{\sigma} \delta^{(2)}(\mathbf{b})$ . The number of subcollisions is assumed to be given by a Poisson distribution with average  $\bar{n}(b)$ , and a non-diffractive event is obtained if  $n \neq 0$ . This implies that the total non-diffractive cross section is given by

$$\sigma_{\text{ND}} = \int d^2b (1 - e^{-\bar{n}(b)}), \quad (\text{III.15})$$

and the average number of subcollisions is

$$\langle n \rangle = \frac{\int d^2b \bar{n}(b)}{\sigma_{\text{ND}}}. \quad (\text{III.16})$$

In PYTHIA 8  $\hat{\sigma}$  depends on a parameter  $p_{\perp 0}$ , which acts as a smooth cutoff for small  $p_{\perp}$  in parton–parton scattering. We have therefore two adjustable parameters,  $a$  and  $p_{\perp 0}$ , which can be used to fit  $\sigma_{\text{ND}}$  and  $\langle n \rangle$ . A result from such a fit is presented in ref. [16], with the result  $a \approx 0.48$  fm, giving  $\sigma_{\text{eff}} \approx 28$  mb, at the Tevatron and  $\sigma_{\text{eff}} \approx 34$  mb at LHC.

These values could be regarded as a kind of benchmarks. If the evolution gives smaller regions with higher parton density, the width of the  $F$ -distribution will be wider, and  $\sigma_{\text{eff}}$  will be smaller. We here note that, although the single Gaussian fit gives the proper number of subcollisions, the correlations appear to be too weak. More successful tunes to data have a distribution  $\rho$  (and thus also  $\mathcal{O}$ ), which is given by a sum of two Gaussian. This enhances small and large  $b$ -values, and gives a somewhat smaller  $\sigma_{\text{eff}}$ . In a recent modification to the model [16], the width of the density  $\rho$  is assumed to vary with  $x$ , which also has the effect of enhancing small and large  $b$ -values increasing the correlations and reducing  $\sigma_{\text{eff}}$ .

### Fluctuations in the parton cascade

Another source for correlations is coming from fluctuations within the cascades, and affects  $\sigma_{\text{eff}}$  even if the double parton distribution factorizes as in eq. (III.3). This effect is discussed in refs. [6] and [7], but is normally neglected in phenomenological analyses. Double hard scattering is more likely in collisions with protons that have more than the average number of partons. A measure of this effect is given by the integral of  $F$  as follows:

The cascade evolution is a random process, which can lead to different partonic states. We label the states by the parameter  $n$ , and the parton distribution in state  $n$  is denoted  $D_n(x, Q^2)$ . The probability to

obtain this state is denoted  $P_n$ , with  $\sum P_n = 1$ . Assuming the factorized form in eq. (III.3) we then get

$$\begin{aligned} \int d^2b F(b) &= \frac{\sum_n P_n D_n(x_1, Q_1^2) D_n(x_2, Q_2^2)}{\sum_n P_n D_n(x_1, Q_1^2) \cdot \sum_n P_n D_n(x_2, Q_2^2)} \\ &= \frac{\langle D(x_1, Q_1^2) D(x_2, Q_2^2) \rangle}{\langle D(x_1, Q_1^2) \rangle \langle D(x_2, Q_2^2) \rangle}. \end{aligned} \quad (\text{III.17})$$

Here  $\langle \dots \rangle$  denotes an average over the different cascades  $n$ . For the special case of  $Q_1^2 = Q_2^2$  and  $x_1 = x_2$ , we get

$$\int d^2b F(b) = \frac{\langle D^2(x, Q^2) \rangle}{\langle D(x, Q^2) \rangle^2}. \quad (\text{III.18})$$

Thus the integral of  $F$  equals  $1 + V / \langle D(x, Q^2) \rangle^2$ , with the variance  $V$  equal to the square of the width of the distribution. We see that the fluctuations imply that the  $F$ -distribution is enhanced, which also implies a larger correlation and a smaller  $\sigma_{\text{eff}}$ . When presenting our results in section III.5, we will also include values for the integral of  $F$ , in order to facilitate the interpretation of the results. Note that in the Gaunt-Stirling approximation in eq. (III.4),  $F$  is normalized to 1, and all correlation effects are included in the function  $D^{ij}(x_1, x_2; Q_1^2, Q_2^2)$ .

## III.3 The Lund Dipole Cascade Model

### III.3.1 Mueller's dipole cascade

Mueller's dipole cascade model [27–29] is a formulation of the leading logarithmic (LL) BFKL evolution in transverse coordinate space. Gluon radiation from the colour charge in a parent quark or gluon is screened by the accompanying anti-charge in the colour dipole. This suppresses emissions at large transverse separation, which corresponds to the suppression of small  $k_\perp$  in BFKL. For a dipole  $(x, y)$  the probability per unit rapidity ( $Y$ ) for emission of a gluon at transverse position  $z$  is given by

$$\frac{d\mathcal{P}}{dY} = \frac{\bar{\alpha}}{2\pi} d^2z \frac{(x - y)^2}{(x - z)^2 (z - y)^2}, \quad \text{with } \bar{\alpha} = \frac{3\alpha_s}{\pi}. \quad (\text{III.19})$$

This emission implies that the dipole is split into two dipoles, which (in the large  $N_c$  limit) emit new gluons independently. The result is a cascade, where the number of dipoles grows exponentially with  $Y$ .



In a high energy collision, the dipole cascades in the projectile and the target are evolved from their rest frames to the rapidities they will have in the specific Lorentz frame chosen for the analysis. The scattering probability between two elementary colour dipoles with coordinates  $(x_i, y_i)$  and  $(x_j, y_j)$  in the projectile and the target respectively, is given by  $2f_{ij}$ , where in the Born approximation

$$f_{ij} = f(x_i, y_i | x_j, y_j) = \frac{\alpha_s^2}{8} \left[ \log \left( \frac{(x_i - y_j)^2 (y_i - x_j)^2}{(x_i - x_j)^2 (y_i - y_j)^2} \right) \right]^2. \quad (\text{III.20})$$

The optical theorem then implies that the elastic amplitude for dipole  $i$  scattering off dipole  $j$  is given by  $f_{ij}$ . Summing over  $i$  and  $j$  gives the one-pomeron elastic amplitude

$$F = \sum f_{ij}. \quad (\text{III.21})$$

The growth in the number of dipoles also implies a strong growth for the interaction probability, but the total scattering probability is kept below 1 by the possibility to have multiple dipole–dipole subcollisions in a single event. In the eikonal approximation the unitarized elastic amplitude is given by the exponentiated expression

$$T(\mathbf{b}) = 1 - e^{-F}, \quad (\text{III.22})$$

and the total, elastic, and diffractive cross sections are given by

$$\begin{aligned} d\sigma_{\text{tot}}/d^2b &= \langle 2T \rangle, \\ d\sigma_{\text{el}}/d^2b &= \langle T \rangle^2, \\ d\sigma_{\text{diff ex}}/d^2b &= \langle T^2 \rangle - \langle T \rangle^2. \end{aligned} \quad (\text{III.23})$$

### III.3.2 The Lund dipole cascade model

In refs. [22,23,25] we describe a modification of Mueller's cascade model with the following features:

- It includes essential NLL BFKL effects.
- It includes non-linear effects in the evolution.
- It includes effects of confinement.

The model also includes a simple model for the proton wavefunction, and is implemented in a Monte Carlo simulation program called DIPSY. As discussed in the cited references, the model is able to describe a wide range of observables in DIS and  $pp$  scattering, with very few parameters.



## NLL effects

The NLL corrections to BFKL evolution have three major sources [31]:

*The running coupling:*

This is relatively easily included in a MC simulation process. The scale in the running coupling is chosen as the largest transverse momentum in the vertex [32].

*Non-singular terms in the splitting function:*

These terms suppress large  $z$ -values in the individual parton branchings, and prevent the daughter from being faster than her recoiling parent. Most of this effect is taken care of by including energy-momentum conservation in the evolution. This is effectively taken into account by associating a dipole of transverse size  $r$  with a transverse momentum  $k_{\perp} = 1/r$ , and demanding conservation of the light-cone momentum  $p_+$  in every step in the evolution. This gives an effective cutoff for small dipoles, which also eliminates the numerical problems encountered in the MC implementation by Mueller and Salam [33].

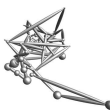
*Projectile-target symmetry:*

This is also called energy scale terms, and is essentially equivalent to the so called consistency constraint [34]. This effect is taken into account by conservation of both positive and negative light-cone momentum components,  $p_+$  and  $p_-$ . The treatment of these effects includes also effects beyond NLL, in a way similar to the treatment by Salam in ref. [31]. Therefore the power  $\lambda_{\text{eff}}$ , determining the growth for small  $x$ , does not turn negative for large values of  $\alpha_s$ .

## III

## Non-linear effects and saturation

As mentioned above, dipole loops (or equivalently pomeron loops) are not included in Mueller's cascade model, if they occur within the evolution. They are only included if they are cut in the Lorentz frame used in the calculations, as a result of multiple scattering in this frame. The result is therefore not frame independent. (The situation is similar in the Color Glass Condensate [35–37] or the JIMWLK [38,39] equations.) As for dipole scattering the probability for such loops is given by  $\alpha_s$ , and therefore formally colour suppressed compared to dipole splitting, which is proportional to  $\bar{\alpha} = N_c \alpha_s / \pi$ . These loops are therefore related to the probability that two dipoles have the same colour. Two dipoles with the same colour form a quadrupole field. Such a field may be better



approximated by two dipoles formed by the closest colour–anticolour charges. This corresponds to a recoupling of the colour dipole chains, favouring the formation of small dipoles. We call this process a dipole “swing”. The swing gives rise to loops within the cascades, and makes the cross section frame independent to a good approximation. We note that a similar effect would also be obtained from gluon exchange between the two dipoles.

In the MC implementation each dipole is assigned one of  $N_C^2$  colour indices, and dipoles with the same colour index are allowed to recouple [23]. The weight for the recoupling is assumed to be proportional to  $(r_1^2 r_2^2)/(r_3^2 r_4^2)$ , where  $r_1$  and  $r_2$  are the sizes of the original dipoles and  $r_3$  and  $r_4$  are the sizes of the recoupled dipoles. Dipoles with the same colour are allowed to swing back and forth, which results in an equilibrium, where the smaller dipoles have a larger weight. We note that in this formulation the number of dipoles is not reduced, and the saturation effect is obtained because the smaller dipoles have smaller cross sections. Thus in an evolution in momentum space the swing would not correspond to an absorption of gluons below the saturation line  $k_\perp^2 = Q_s^2(x)$ ; it would rather correspond to lifting the gluons to higher  $k_\perp$  above this line. Although this mechanism does not give an explicitly frame independent result, MC simulations show that it is a very good approximation.

### Confinement effects

Confinement effects are included via an effective gluon mass, which gives an exponential suppression for very large dipoles [24]. This prevents the proton from growing too fast in transverse size, and is also essential to satisfy Froisart’s bound at high energies [40].

### Initial dipole configurations

In DIS an initial photon is split into a  $q\bar{q}$  pair, and for larger  $Q^2$  the wavefunction for a virtual photon can be determined perturbatively. The internal structure of the proton is, however, governed by soft QCD, and is not possible to calculate perturbatively. In our model it is represented by an equilateral triangle formed by three dipoles, and with a radius of  $3 \text{ GeV}^{-1} \approx 0.6 \text{ fm}$ . The model should be used at low  $x$ , and when the system is evolved over a large rapidity range the observable results depend only weakly on the exact configuration of the initial dipoles, or whether the charges are treated as (anti)quarks or gluons.

### III.4 Application to double parton distributions

In principle we could estimate the gluon density in the proton from the cross section for  $\gamma^*p$  collisions. The photon would then be treated as a superposition of dipoles of varying sizes, with weights determined by QED. However, in order to more easily isolate the correlations and fluctuations in the proton, without the complications from the additional fluctuations in the photon wave functions, we prefer instead to calculate the cross section for a dipole with a fixed transverse size. The photon coupling to a  $q\bar{q}$  pair contains a factor  $(z(1-z))^{2-i} K_i^2(\sqrt{z(1-z)} Qr)$ . Here  $K_i$  are generalized Bessel functions,  $r$  is the transverse separation between the quark and the antiquark,  $z$  is the fractional energy taken by the quark, and the index  $i$  is 1 for transverse and 0 for longitudinal photons. Important contributions are obtained for  $z \sim 0.5$ , and since the Bessel functions fall off exponentially when the argument is larger than 1, characteristic  $r$ -values are given by the relation  $r \approx 2/Q$ .

To determine the parton distributions  $D(x, Q^2)$  we thus calculate the cross section for scattering of a single dipole of size  $r = 2/Q$  colliding with a proton. The projectile dipole has a large cross section when colliding with equally large or larger dipoles in the proton, while the interaction with smaller dipoles is suppressed. The dipoles in the proton are also connected to gluons with  $k_\perp$  of the order  $1/r$ , and therefore the  $D$ -distributions obtained correspond to the *integrated* gluon distributions.

The double parton density  $\Gamma(x_1, x_2, b; Q_1^2, Q_2^2)$  is in the same way proportional to the cross section,  $\sigma^{(1,2)}$ , for simultaneous scattering of two dipoles with size  $r_i = 2/Q_i$ , separated by a distance  $b$ , and colliding with a proton. Thus also  $\Gamma$  is defined as an integrated density. From these relations we conclude that the  $F$ -distribution is directly related to the ratio between the corresponding cross sections, and in an obvious notation we have

$$F(b; x_1, x_2, Q_1^2, Q_2^2) \equiv \frac{\Gamma^{(1,2)}}{D^{(1)}D^{(2)}} = \frac{\sigma^{(1,2)}}{\sigma^{(1)}\sigma^{(2)}}. \quad (\text{III.24})$$

In principle the double scattering cross section, and thus also  $F$ , depends in the dipole model on the three vectors, the dipole sizes  $\mathbf{r}_1$ ,  $\mathbf{r}_2$ , and the distance between them  $\mathbf{b}$ . This implies that the estimate of  $\sigma_{\text{eff}}$  should be given by a 6-dimensional integral over these variables. For the results presented in the next section we have calculated  $F$  keeping the separation between two gluons constant equal to  $\mathbf{b}$ , but averaging over the directions of the dipoles,  $\mathbf{r}_1$  and  $\mathbf{r}_2$ . To check this approximation



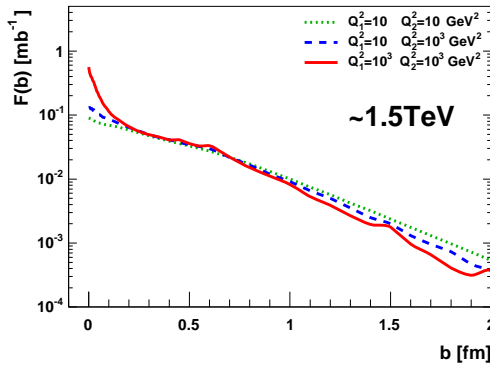


Figure III.1: Correlation function  $F(b)$  corresponding to central subcollisions at  $\sqrt{s} \approx 1.5$  TeV, and three combinations of  $Q_1^2$  and  $Q_2^2$ . The  $x$ -values corresponding to  $Q^2 = 10$  and  $1000$  GeV<sup>2</sup> are  $10^{-3}$  and  $10^{-2}$  respectively.

we have also calculated the result obtained when keeping the distance between the centers of the dipole fixed. The results presented in sec. III.5 show that the correlations obtained are insensitive to how the averages are taken.

## III.5 Results

In this section we show some results relevant for  $pp$  collisions at  $\sqrt{s} = 1.5$  and  $15$  TeV, qualitatively representing Tevatron and LHC energies. We calculate the cross sections for one or two dipoles against a proton, where the rapidity separation between the projectile and the target is given by  $y = \ln(1/x_i) + \ln(Q_i/2)$ . Thus for subcollisions at midrapidity, with  $y = \ln \sqrt{s}$ , we have  $x = Q/(2\sqrt{s})$ .

### III.5.1 Subcollisions at midrapidity

In figs. III.1 and III.2 we show the  $Q^2$ -dependence for  $x$ -values corresponding to central production at a fixed energy. Fig. III.1 shows the result for  $\sqrt{s} = 1.5$  TeV and three combinations<sup>2</sup> of  $Q_1^2$  and  $Q_2^2$ . The corresponding  $x$ -values are given by  $x = Q/(2\sqrt{s})$ . Fig. III.2 shows similar results for  $\sqrt{s} = 15$  TeV.

<sup>2</sup>The chosen values of  $Q^2$  of  $10$ ,  $10^3$  and  $10^5$  GeV<sup>2</sup>, correspond to dipole sizes of  $\approx 0.13$ ,  $0.013$  and  $0.0013$  fm respectively.

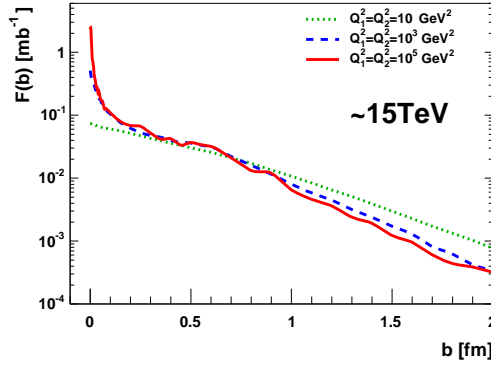


Figure III.2: Correlation function  $F(b)$  corresponding to central subcollisions at  $\sqrt{s} \approx 15$  TeV. The curves correspond to  $Q_1^2 = Q_2^2 = 10, 10^3$ , and  $10^5$  GeV<sup>2</sup>. The corresponding  $x$ -values are  $10^{-4}$ ,  $10^{-3}$ , and  $10^{-2}$ .

We see that the distribution is not well described by a Gaussian. Instead there is an almost exponential dependence in the range  $0.2 < b < 0.6$  fm. For larger  $b$ -values the distribution drops faster, and this effect is stronger for higher  $Q^2$ . The position of the break is related to the size of the initial proton configuration in the model. For small  $b$ -values a spike is developing, growing stronger with increasing  $Q^2$ . This is associated with a faster drop for larger  $b$  for high  $Q^2$ . Results with one softer and one harder subcollision lie (as expected) in between the results for two soft or two hard collisions, but closer to the result for two softer subcollisions (not shown for  $\sqrt{s} = 15$  TeV).

In fig. III.3 we show the energy dependence by comparing the results for  $Q^2 = 10^3$  GeV<sup>2</sup> at the two different energies. We see here that the peaks at small  $b$  are almost identical, but at the higher energy the distribution becomes a little wider, with a slightly larger tail out to large  $b$ -values.

The corresponding values for  $\sigma_{\text{eff}} = (\int d^2b F(b))^2$  and  $\int d^2b F(b)$  were calculated numerically, and are presented in table III.1. The rather slow fall off for  $F$  at large  $b$  gives a large  $\sigma_{\text{eff}}$  for small  $Q^2$ , but the more narrow distributions for higher  $Q^2$  imply a very strong  $Q^2$ -dependence. At 15 TeV  $\sigma_{\text{eff}}$  drops by a factor 2 when  $Q^2$  is changed from 10 to  $10^2$  GeV<sup>2</sup>. For fixed  $Q^2$  the wider distribution at higher energy, implies a slightly larger  $\sigma_{\text{eff}}$ . The variation with  $\sqrt{s}$  is, however, much weaker than the variation with  $Q^2$ .

We also note that the effect of fluctuations in the cascades, repre-



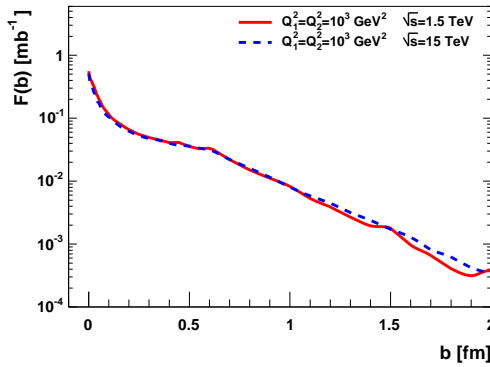


Figure III.3: The energy dependence of the correlation functions  $F(b)$ . The curves show  $F$  for  $Q_1^2 = Q_2^2 = 10^3 \text{ GeV}^2$ , solid line for  $\sqrt{s} = 1.5$  and dashed line for  $\sqrt{s} = 15 \text{ TeV}$ .

$Q_1^2, Q_2^2 [\text{GeV}^2], x_1, x_2$				$\sigma_{\text{eff}} [\text{mb}]$	$\int F$
1.5 TeV, midrapidity					
10	10	0.001	0.001	35.3	1.09
10	$10^3$	0.001	0.01	31.0	1.07
$10^3$	$10^3$	0.01	0.01	23.1	1.06
15 TeV, midrapidity					
10	10	0.0001	0.0001	40.4	1.11
$10^3$	$10^3$	0.001	0.001	26.3	1.07
$10^3$	$10^5$	0.001	0.01	24.2	1.05
$10^5$	$10^5$	0.01	0.01	19.6	1.03
1.5 TeV, $y_{\text{pair } 2} = 2.3$					
10	10	0.001	0.0001	} 37.1	1.08
10	10	0.001	0.01		

Table III.1: Summary of results for  $\sigma_{\text{eff}}$  and corresponding integrals of the double distribution functions. (The numerical uncertainties are about 1%.)

sented by the difference from 1 of  $\int d^2b F$ , is of the order 5-10% (contributing 10-20% to  $\sigma_{\text{eff}}$ ), and is smaller for large  $Q^2$ .

### III.5.2 Sub-collisions off midrapidity

As mentioned in sec. III.2.2, for subcollisions away from midrapidity, the effective cross section is given by eq. eq. (III.7), which contains

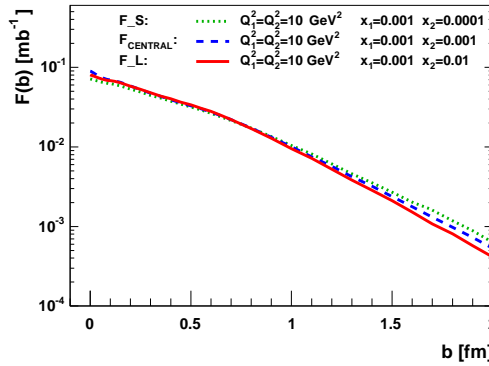


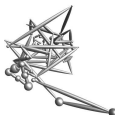
Figure III.4: Correlation function  $F(b)$  relevant for subcollisions at  $y_{\text{pair}2} = 2.3$  for  $\sqrt{s} \approx 1.5$  TeV and  $Q_1^2 = Q_2^2 = 10$  GeV<sup>2</sup>.  $F_S \equiv F(b; 0.001, 0.0001, 10, 10)$  and  $F_L \equiv F(b; 0.001, 0.01, 10, 10)$ . ( $Q^2$  in GeV<sup>2</sup>) The distribution  $F(b; 0.001, 0.001, 10, 10)$  for two subcollisions at midrapidity is included for comparison.

a product of two  $F$ -distributions with different  $x$ -values. In fig. III.4 we show results relevant for two subcollisions with  $Q^2 = 10$  GeV<sup>2</sup> at 1.5 TeV. One collision is at rapidity zero, with  $x_1 = x'_1 = 0.001$ , while the other subcollision has  $x_2 = 0.01$  and  $x'_2 = 0.0001$ , which corresponds to a rapidity for the pair of jets (or a produced massive particle) given by  $y_{\text{pair}} = \ln(x_2/x'_2)/2 \approx 2.3$ . The corresponding  $F$ -distributions are called  $F_S$  (for small  $x_2 = 0.0001$ ) and  $F_L$  (for large  $x_2 = 0.01$ ). We see that in the tail  $F_S$  and  $F_L$  lie on opposite sides of the distribution  $F_{\text{central}}$ , which is the relevant one for two subcollisions at midrapidity (both with  $x_i = x'_i = 0.001$ ). As  $\sigma_{\text{eff}}$  is given by  $(\int d^2b F_S F_L)^{-1}$ , this implies that although the  $F$ -distributions vary with  $x$ ,  $\sigma_{\text{eff}}$  is approximately independent of  $y_{\text{pair}}$ . This result is further illustrated in fig. III.5, which shows the ratio  $\sqrt{F_S F_L}/F_{\text{central}}$ . We see that this ratio is close to 1 except for small  $b$ -values, which have a low weight in the integral over  $d^2b$ . As a consequence also the result for  $\sigma_{\text{eff}}$  varies very little with rapidity, in this case from 35.3 to 37.1 mb when  $y_{\text{pair}}$  is changed from 0 to 2.3 (see table III.1). Actually, for small shifts  $\delta y_{\text{pair}}$ , the difference between the product  $F_L F_S$  and  $F_{\text{central}}^2$  must be only second order in  $\delta y_{\text{pair}}$ . This must then also be the case for the corresponding values for  $\sigma_{\text{eff}}$ .

### III

#### III.5.3 Comparison with experiment

The result for  $\sigma_{\text{eff}}$  is larger than the effective cross section observed for  $\gamma + 3\text{jet}$  events at the Tevatron. We note, however, that these data de-



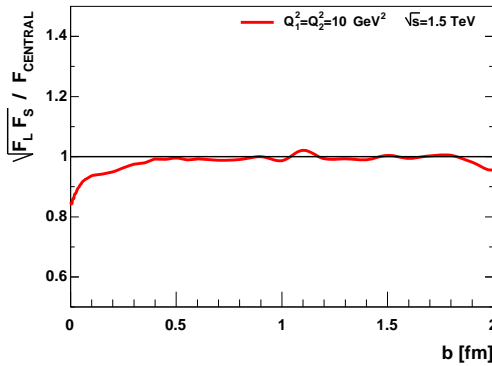


Figure III.5: The ratio  $\sqrt{F_L F_S} / F_{\text{central}}$ .  $Q_1^2 = Q_2^2 = 10 \text{ GeV}^2$ , and  $\sqrt{s} = 1.5 \text{ TeV}$ .

pend on quark distributions, and not only on the gluon distributions. It would be interesting to try to estimate the difference, but this goes beyond the scope of this paper. For  $Q^2 = 10^3 \text{ GeV}^2$  at 1.5 TeV we find  $\sigma_{\text{eff}} = 23 \text{ mb}$ . Within the errors this is in agreement with the 4-jet results from CDF, which however, have large uncertainties. It would also be interesting to have, for comparison, the values for  $\sigma_{\text{eff}}$  in the tuned versions of PYTHIA 8, not only for the less successful single Gaussian approximation used in section III.2.3.

We also note that there are two observed features, which are well reproduced by our model:

*i.* The D0 collaboration [5] has observed a reduction in  $\sigma_{\text{eff}}$  for growing  $p_{\perp}$  of the jet pair in  $\gamma + 3\text{jet}$ -events. Although the errors are large, the central values for  $\sigma_{\text{eff}}$  drop from 18.2 to 13.9 mb, when  $\langle p_T^{\text{jet}2} \rangle$  increases from 17.6 to 27.3 GeV. This agrees qualitatively with the variation with  $Q^2$  found in our model.

*ii.* The CDF collaboration [3] observes in the same reaction, that  $\sigma_{\text{eff}}$  is very insensitive to a change in the rapidity  $y_{\text{pair}}$  (or equivalently  $x_F^{\text{pair}}$ ) for one of the subcollisions. As discussed in sec. III.5.2 this is also consistent with our model. We note, however, that this result is mainly a consequence of the fact that the product  $F_L F_S$  is close to  $F_{\text{central}}^2$ , and does not necessarily show that  $F$  does not vary with  $x$ .

These qualitative agreements with experimental data may indicate that, also if our model possibly underestimates the correlations, we may believe that the qualitative features, and variations with  $Q^2$  and  $\sqrt{s}$ , are correct. The indicated strong dependence on  $Q^2$  should then be very im-



portant for the interpretation of multiple hard interactions at LHC. We here note a possible qualitative difference between our model and the model with  $x$ -dependent matter densities in ref. [16]. Our result shows a larger variation with  $Q^2$  for fixed energy, than with  $x$  (or energy) for fixed  $Q^2$ . At fixed energy a variation with  $Q^2$  is equivalent to a variation with  $x = Q/\sqrt{s}$ . However, the two models may give different results when data at different energies are compared. We would like to study this question more in the future.

### III.5.4 Comment on the definition of $b$

As mentioned in sec. III.4, in the dipole model  $F$  depends in principle on three vectors: the size of the two dipoles ( $\mathbf{r}_1, \mathbf{r}_2$ ) and the separation between them. For the results presented above we have defined the separation as the distance between two gluons, and averaged over  $\mathbf{r}_1$  and  $\mathbf{r}_2$ . When calculating  $\int d^2b F(b)$  this gives exactly the correct result. This is, however, not the case for the integral  $\int d^2b F^2(b)$ , which determines  $\sigma_{\text{eff}}$ . When the separation is of the same order of magnitude as the size of the dipoles, the averaging does not give the correct result. To estimate this error we have changed the definition of  $\mathbf{b}$ , to the separation between the centers of the dipoles, keeping this fixed when averaging over angles for  $\mathbf{r}_1$  and  $\mathbf{r}_2$ . The ratio between the two different  $F$ -distributions is shown in fig. III.6. In this example we have  $Q_1^2 = Q_2^2 = 10 \text{ GeV}^2$  and  $\sqrt{s} = 15 \text{ TeV}$ . We can here see a difference when  $b$  is of the same order of magnitude as the dipoles, around 0.1 fm. The contribution from small  $b$ -values is, however, suppressed in the integral over  $d^2b$ , and as mentioned above  $\int d^2b F^2(b)$  obtains its major contribution for  $b$  in the range 0.5-1 fm. The difference between the two estimates of  $\sigma_{\text{eff}}$  is only about 2.5%. For larger  $Q^2$  the difference is even smaller, as the region where the two  $b$ -definitions give different results moves towards smaller  $b$ -values. This effect can therefore be safely neglected.

III

## III.6 Conclusions and outlook

The Lund Dipole Cascade model offers unique possibilities to study the evolution of gluons inside hadrons at small  $x$ . The formalism is based on BFKL evolution including essential higher-order corrections and saturation effects. By following the evolution, emission-by-emission, in rapidity and in transverse position, we can investigate the correlations and fluctuations of the gluon distribution in great detail.



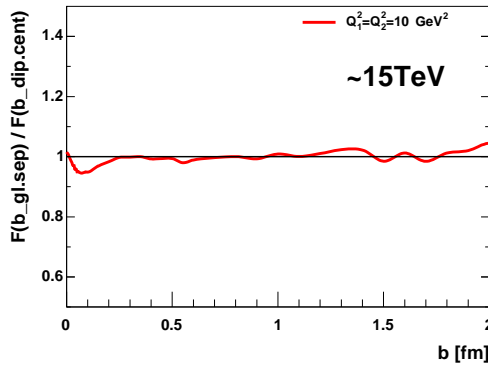


Figure III.6: The ratio between the  $F$ -distributions obtained by two different definitions of  $b$ .  $Q_1^2 = Q_2^2 = 10 \text{ GeV}^2$ , and  $\sqrt{s} = 15 \text{ TeV}$ .

We have here concentrated on the double parton distribution, which enters into the multiple parton scattering cross section in proton-proton collisions. The double parton distribution in transverse coordinate space is the analogy of the generalized parton density in momentum space. The correlations can be described by a distribution in impact parameter space,  $F(b; x_1, x_2, Q_1^2, Q_2^2)$ . In many applications this distribution is assumed to be independent of the energy fractions and scales of the partons, and the same for quarks and gluons. In the PYTHIA 8 event generator the width of the distribution does vary with energy, and in a recent study it is assumed to vary with  $x$ . Gaunt and Stirling have demonstrated that DGLAP evolution implies non-trivial correlations depending on  $x$  and  $Q^2$ , but this analysis does not give information about the  $b$ -dependence. In our analysis we find that the two-parton correlation function  $F(b)$  depends in a non-trivial way on all the kinematic variables  $x_1, x_2, Q_1^2, Q_2^2$ .

For subcollisions at *midrapidity*,  $F$  is directly connected to the “effective cross section” used in experimental analyses, via the relation  $\int d^2b F^2 = \sigma_{\text{eff}}^{-1}$ . The result that  $F$  depends on  $x_i$  and  $Q_i^2$  implies, however, that for subcollisions away from  $y = 0$ ,  $\sigma_{\text{eff}}$  is determined by an integral of a product of two  $F$ -functions with different  $x$ -values, connected by the relation  $x_i x'_i = Q^2/s$ . Therefore  $\sigma_{\text{eff}}$  is very insensitive to the rapidity of a hard subcollision; when one of the two  $F$ -functions in the product is above, the other is below the  $F$ -distribution relevant for midrapidity subcollisions. An experimental result showing a weak dependence on rapidity is therefore not a proof that  $F$  does not depend on

the scaling parameters  $x_i$ .

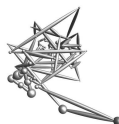
In our formalism we can also study event-by-event fluctuations in the density of partons, which are usually neglected in other analyses. Neglecting the fluctuations  $F$  satisfies the normalization condition  $\int d^2b F = 1$ , but when taking them into account we obtain a larger value for this integral, and therefore larger two-parton correlations. In our analysis this effect contributes 10-20% to the value of  $\sigma_{\text{eff}}$ .

By studying the correlation function  $F$ , we can see explicitly how the emission of high- $p_{\perp}$  gluons result in so-called *hot spots* developing for small  $b$ -values at large  $Q^2$ . For fixed  $Q^2$  the emission of larger dipoles, related to low- $p_{\perp}$  gluons, implies that the distribution widens as we go down in  $x$ . (This effect is related to the shrinking of the diffractive peak at higher energies.) As a result  $\sigma_{\text{eff}}$  is reduced for higher  $Q^2$  at fixed energy, but increases at higher energy for fixed  $Q^2$ . We see, however, that the result appears to depend much stronger on  $Q^2$  than on  $x$  or collision energy.

It is not straight-forward to compare our results for the effective cross section with data from the Tevatron and ISR, which correspond to lower values for  $\sigma_{\text{eff}}$  and thus stronger correlations. The ISR data are obtained for very high  $x$ -values, and the more exact Tevatron results are for  $\gamma + 3\text{jet}$  events, which necessarily involves quarks. Our calculations include only gluons, and should therefore only be applied at small  $x$ . It is also difficult to estimate a possible difference between quark and gluon distributions. Our results are, however, compatible within errors with the four-jet measurement at CDF, where gluons should be dominating, and they show qualitative agreements with the observed rapidity independence at CDF and the hints of strong  $Q^2$ -dependence at D0. We also note that our results appear to be in qualitative agreement with results from PYTHIA 8 tuned to multiple interactions and underlying events.

Even if it is possible that we overestimate the result for  $\sigma_{\text{eff}}$  to some degree, we are more confident about the variation with  $x$  and  $Q^2$ , which should have relevance for extrapolations to the LHC. Our model here predicts a very strong decrease of the effective cross section with increasing  $Q^2$  (especially when both  $Q_1^2$  and  $Q_2^2$  increases), while the dependence on the total energy ( $\sim 1/x$ ) for fixed  $Q^2$  is rather weak. Also the dependence on the rapidity of the two subcollisions is quite weak, which follows as  $\sigma_{\text{eff}}$  here is given by a product of two  $F$ -distribution, one which is smaller and one which is larger than the  $F$ -distribution relevant for midrapidity subcollisions.

When comparing to the recent option in PYTHIA 8, with an  $x$ -



dependent impact parameter profile [16], our result may be quite similar if we study the dependence on  $Q^2$  at a fixed cms energy  $\sqrt{s}$ . In our model the correlations increase as a direct consequence of higher  $Q^2$ , and in the PYTHIA 8 model they increase because  $x$  is higher for large  $Q^2$  at fixed energy. The difference between the two models might therefore show up in the extrapolation of Tevatron data to LHC energies.

It should be noted, however, that the extraction of the effective cross sections from data is very hard, and it will still be difficult to compare future LHC results to the numbers we have presented here. For this reason it is important to compare to event generator predictions for the experimental observables. Fortunately we have now developed the DIPSY MC to also generate exclusive final states [41], which means that in the future we can in detail simulate exclusive final state observables related to double parton scattering.

## Acknowledgments

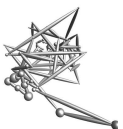
Work supported in part by the EU Marie Curie RTN MCnet (MRTN-CT-2006-035606), and the Swedish research council (contracts 621-2008-4252 and 621-2009-4076).

L.L. gratefully acknowledges the hospitality of the CERN theory unit.

A.S. gratefully acknowledges the support of the Hungarian OTKA grants T49466 and NK 73143.

### III References

- [1] **Axial Field Spectrometer** Collaboration, T. Åkesson *et al.*, “DOUBLE PARTON SCATTERING IN p p COLLISIONS AT  $S^{**}(1/2) = 63\text{-GeV}$ ,” *Z. Phys.* **C34** (1987) 163.
- [2] **CDF** Collaboration, F. Abe *et al.*, “Study of four jet events and evidence for double parton interactions in  $p\bar{p}$  collisions at  $\sqrt{s} = 1.8\text{ TeV}$ ,” *Phys. Rev.* **D47** (1993) 4857–4871.
- [3] **CDF** Collaboration, F. Abe *et al.*, “Double parton scattering in  $p\bar{p}$  collisions at  $\sqrt{s} = 1.8\text{TeV}$ ,” *Phys. Rev.* **D56** (1997) 3811–3832.
- [4] **D0** Collaboration, V. M. Abazov *et al.*, “Multiple jet production at low transverse energies in  $p\bar{p}$  collisions at  $\sqrt{s} = 1.8\text{ TeV}$ ,” *Phys. Rev.* **D67** (2003) 052001, arXiv:hep-ex/0207046.
- [5] **D0** Collaboration, V. M. Abazov *et al.*, “Double parton interactions in photon+3 jet events in p p- bar collisions sqrts=1.96 TeV,” *Phys. Rev.* **D81** (2010) 052012, arXiv:0912.5104 [hep-ex].
- [6] J. Kuti and V. F. Weisskopf, “Inelastic lepton - nucleon scattering and lepton pair production in the relativistic quark parton model,” *Phys. Rev.* **D4** (1971) 3418–3439.
- [7] V. P. Shelest, A. M. Snigirev, and G. M. Zinovev, “THE MULTIPARTON DISTRIBUTION EQUATIONS IN QCD,” *Phys. Lett.* **B113** (1982) 325.
- [8] T. Sjöstrand and M. van Zijl, “A Multiple Interaction Model for the Event Structure in Hadron Collisions,” *Phys. Rev.* **D36** (1987) 2019.
- [9] T. T. Chou and C. N. Yang, “GEOMETRICAL MODEL OF MULTIPARTICLE PRODUCTION IN HADRON - HADRON COLLISIONS,” *Phys. Rev.* **D32** (1985) 1692.
- [10] A. M. Snigirev, “Double parton distributions in the leading logarithm approximation of perturbative QCD,” *Phys. Rev.* **D68** (2003) 114012, arXiv:hep-ph/0304172.
- [11] J. R. Gaunt and W. J. Stirling, “Double Parton Distributions Incorporating Perturbative QCD Evolution and Momentum and Quark Number Sum Rules,” *JHEP* **03** (2010) 005, arXiv:0910.4347 [hep-ph].



- [12] T. Sjöstrand and P. Z. Skands, “Multiple interactions and the structure of beam remnants,” *JHEP* **03** (2004) 053, arXiv:hep-ph/0402078.
- [13] T. Sjöstrand and P. Z. Skands, “Transverse-momentum-ordered showers and interleaved multiple interactions,” *Eur. Phys. J.* **C39** (2005) 129–154, arXiv:hep-ph/0408302.
- [14] T. Sjöstrand, S. Mrenna, and P. Z. Skands, “A Brief Introduction to PYTHIA 8.1,” *Comput. Phys. Commun.* **178** (2008) 852–867, arXiv:0710.3820 [hep-ph].
- [15] T. Sjöstrand, S. Mrenna, and P. Z. Skands, “PYTHIA 6.4 Physics and Manual,” *JHEP* **05** (2006) 026, arXiv:hep-ph/0603175.
- [16] R. Corke and T. Sjöstrand, “Multiparton Interactions with an  $x$ -dependent Proton Size,” arXiv:1101.5953 [hep-ph].
- [17] M. Bähr, S. Gieseke, and M. H. Seymour, “Simulation of multiple partonic interactions in Herwig++,” *JHEP* **07** (2008) 076, arXiv:0803.3633 [hep-ph].
- [18] M. Bähr, J. M. Butterworth, S. Gieseke, and M. H. Seymour, “Soft interactions in Herwig++,” arXiv:0905.4671 [hep-ph].
- [19] M. Bähr *et al.*, “Herwig++ Physics and Manual,” *Eur. Phys. J.* **C58** (2008) 639–707, arXiv:0803.0883 [hep-ph].
- [20] E. A. Kuraev, L. N. Lipatov, and V. S. Fadin, “The Pomeranchuk Singularity in Nonabelian Gauge Theories,” *Sov. Phys. JETP* **45** (1977) 199–204.
- [21] I. I. Balitsky and L. N. Lipatov, “The Pomeranchuk Singularity in Quantum Chromodynamics,” *Sov. J. Nucl. Phys.* **28** (1978) 822–829.
- [22] E. Avsar, G. Gustafson, and L. Lönnblad, “Energy conservation and saturation in small- $x$  evolution,” *JHEP* **07** (2005) 062, arXiv:hep-ph/0503181.
- [23] E. Avsar, G. Gustafson, and L. Lönnblad, “Small- $x$  dipole evolution beyond the large- $N(c)$  limit,” *JHEP* **01** (2007) 012, arXiv:hep-ph/0610157.
- [24] E. Avsar, G. Gustafson, and L. Lönnblad, “Diffractive Excitation in DIS and pp Collisions,” *JHEP* **12** (2007) 012, arXiv:0709.1368 [hep-ph].

- [25] C. Flensburg, G. Gustafson, and L. Lonnblad, “Elastic and quasi-elastic  $pp$  and  $\gamma^*p$  scattering in the Dipole Model,” *Eur. Phys. J.* **C60** (2009) 233–247, arXiv:0807.0325 [hep-ph].
- [26] C. Flensburg and G. Gustafson, “Fluctuations, Saturation, and Diffractive Excitation in High Energy Collisions,” *JHEP* **10** (2010) 014, arXiv:1004.5502 [hep-ph].
- [27] A. H. Mueller, “Soft gluons in the infinite momentum wave function and the BFKL pomeron,” *Nucl. Phys.* **B415** (1994) 373–385.
- [28] A. H. Mueller and B. Patel, “Single and double BFKL pomeron exchange and a dipole picture of high-energy hard processes,” *Nucl. Phys.* **B425** (1994) 471–488, hep-ph/9403256.
- [29] A. H. Mueller, “Unitarity and the BFKL pomeron,” *Nucl. Phys.* **B437** (1995) 107–126, hep-ph/9408245.
- [30] B. Blok, Y. Dokshitzer, L. Frankfurt, and M. Strikman, “The four jet production at LHC and Tevatron in QCD,” arXiv:1009.2714 [hep-ph].
- [31] G. P. Salam, “An introduction to leading and next-to-leading BFKL,” *Acta Phys. Polon.* **B30** (1999) 3679–3705, hep-ph/9910492.
- [32] I. Balitsky and G. A. Chirilli, “NLO evolution of color dipole,” *Acta Phys. Polon.* **B39** (2008) 2561–2566.
- [33] A. H. Mueller and G. P. Salam, “Large multiplicity fluctuations and saturation effects in onium collisions,” *Nucl. Phys.* **B475** (1996) 293–320, hep-ph/9605302.
- [34] J. Kwiecinski, A. D. Martin, and P. J. Sutton, “Constraints on gluon evolution at small  $x$ ,” *Z. Phys.* **C71** (1996) 585–594, hep-ph/9602320.
- [35] E. Iancu, A. Leonidov, and L. McLerran, “The Color glass condensate: An Introduction,” arXiv:hep-ph/0202270 [hep-ph].
- [36] E. Iancu and R. Venugopalan, “The Color glass condensate and high-energy scattering in QCD,” arXiv:hep-ph/0303204 [hep-ph]. To be published in QGP3, Eds. R.C. Hwa and X.N.Wang, World Scientific.



- [37] F. Gelis, E. Iancu, J. Jalilian-Marian, and R. Venugopalan, “The Color Glass Condensate,” arXiv:1002.0333 [hep-ph]. \*  
Temporary entry \*.
- [38] E. Iancu, A. Leonidov, and L. D. McLerran, “Nonlinear gluon evolution in the color glass condensate. 1.,” *Nucl.Phys.* **A692** (2001) 583–645, arXiv:hep-ph/0011241 [hep-ph].
- [39] J. Jalilian-Marian, A. Kovner, A. Leonidov, and H. Weigert, “The BFKL equation from the Wilson renormalization group,” *Nucl.Phys.* **B504** (1997) 415–431, arXiv:hep-ph/9701284 [hep-ph].
- [40] E. Avsar, “On the High Energy Behaviour of The Total Cross Section in the QCD Dipole Model,” *JHEP* **04** (2008) 033, arXiv:0803.0446 [hep-ph].
- [41] C. Flensburg, G. Gustafson, and L. Lonnblad, “Inclusive and Exclusive observables from dipoles in high energy collisions,” arXiv:1103.4321 [hep-ph].



# IV

## Inclusive and Exclusive observables from dipoles in high energy collisions

Christoffer Flensburg<sup>1</sup>, Gösta Gustafson<sup>1</sup>, Leif Lönnblad<sup>1,2</sup>

<sup>1</sup>Dept. of Astronomy and Theoretical Physics, Lund University,  
Sweden

<sup>2</sup>CERN Theory Department, Geneva, Switzerland

**LU-TP 11-13**

**CERN-PH-TH-2011-058**

**MCnet-11-08**

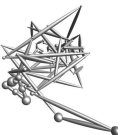
e-Print: [arXiv:1103.4321]

We present a new model for simulating exclusive final states in minimum-bias collisions between hadrons.

In a series of papers we have developed a Monte Carlo model based on Mueller's dipole picture of BFKL-evolution, supplemented with non-leading corrections, which has shown to be very successful in describing inclusive and semi-inclusive observables in hadron collisions. In this paper we present a further extension of this model to also describe exclusive final states. This is a highly non-trivial extension, and we have encountered many details that influence the description, and for which no guidance from perturbative QCD could be found. Hence we have had to make many choices based on semi-classical and phenomenological arguments.

The end result is a new event generator called DIPSY which can be used to simulate complete minimum-bias non-diffractive hadronic collision events. Although the description of data from the Tevatron and LHC is not quite as good as for PYTHIA 8, the most advanced of the general purpose event generator programs for these processes, our results are clearly competitive, and can be expected to improve with careful tuning. In addition, as our model is very different from conventional multiple scattering scenaria, the DIPSY program can be used to gain deeper insight in the soft and semi-hard processes involved both in hadronic and heavy ion collisions.

IV



## IV.1 Introduction

In high energy collisions the high density of gluons at small  $x$  imply that typical events contain several hard partonic subcollisions, and that saturation effects become important. A dynamical model based on BFKL evolution [1, 2] for small  $x$  and including saturation effects, has been presented in a series of papers [3–7]. It is based on Mueller’s dipole cascade model [8–10], which is a formulation of the leading logarithmic (LL) BFKL evolution approximation in impact-parameter space. In our model we also include essential beyond LL corrections to BFKL. The transverse coordinate space is particularly suitable for treating unitarity constraints, multiple collisions, and saturation effects. Mueller’s model includes multiple subcollisions in the frame used for the analysis. Our cascade model also includes saturation effects within the parton evolution, in a way which is similar to the Color Glass Condensate [11–13] or JIMWLK [14, 15]. Also effects of confinement are included and important for the result.

In the dipole picture the colour charge in a gluon is screened by a corresponding anticharge in a neighbouring gluon. Gluon radiation implies that one dipole is split in two dipoles, and the result of the cascade is a chain of colour connected gluons. When two cascades collide, they can interact via gluon exchange. This implies an exchange of colour, producing two colour chains forming a BFKL ladder between projectile and target. Multiple interaction and saturation represent multiple pomeron exchange and pomeron loops. Note here that what is multiple interaction in one Lorentz frame is related to saturation within the cascade in another frame.

The BFKL formalism is directly applicable to inclusive observables, and the cited articles include results for total, (quasi)elastic, and diffractive cross sections in  $pp$  scattering and in DIS, in very good agreement with experimental data. The numerical results are obtained with a Monte Carlo (MC) event generator called DIPSY<sup>1</sup>.

In the present paper we want to generalize the model to describe exclusive final states. Here it is necessary to take into account colour coherence and angular ordering as well as soft radiation. The latter includes contributions from the  $z = 1$  singularity in the gluon splitting function. These effects are taken into account in the CCFM formalism [16, 17], which also reproduces the BFKL result for the inclusive cross section. In ref. [18], describing the Linked Dipole Chain model, it

---

<sup>1</sup>Acronym for Dipoles in Impact-Parameter Space and rapidity (Y)

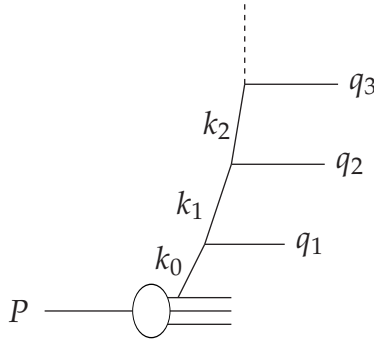
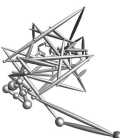


Figure IV.1: A chain of initial state gluon emissions. We denote the real emitted gluons in a gluon ladder  $q_{\perp i}$ , and the virtual links  $k_{\perp i}$ .

was demonstrated that the inclusive cross section is fully determined by a subset of the gluons in the CCFM approach, denoted “ $k_{\perp}$ -changing” gluons. As illustrated in fig. IV.1, we denote the real emitted gluons in a gluon ladder  $q_{\perp i}$ , and the virtual links  $k_{\perp i}$ . Momentum conservation here implies that  $\mathbf{k}_{\perp i-1} = \mathbf{k}_{\perp i} + \mathbf{q}_{\perp i}$ . In a  $k_{\perp}$ -changing emission the difference is large between two adjacent virtual links,  $k_{\perp i-1}$  and  $k_{\perp i}$ . This means that  $q_{\perp i} \approx \max(k_{\perp i-1}, k_{\perp i})$ . Softer emissions with smaller  $q_{\perp i}$  have  $k_{\perp i-1} \approx k_{\perp i}$ , and are “ $k_{\perp}$ -conserving”. In CCFM gluon emission is associated with “non-Sudakov” form factors, and in ref. [18] it was demonstrated that these gluons can be summed up in such a way, that the total cross section is fully specified by the  $k_{\perp}$ -changing emissions with no associated non-Sudakov form factors. The remaining  $k_{\perp}$ -changing gluons  $q_{\perp i}^{\text{prim}}$  are called “primary gluons” in ref. [18] and “backbone gluons” in ref. [19]. They are ordered in both lightcone variables  $q_+$  and  $q_-$ , and therefore also in rapidity or angle, in accordance with QCD coherence. (In the LDC model [18] emissions with  $k_{\perp i} \approx k_{\perp i-1}$ , on the boundary between  $k_{\perp}$ -conserving and  $k_{\perp}$ -changing emissions, were treated slightly different from the BFKL prescription, which also implied a slightly different value for the exponent  $\lambda$  in the power-like increase  $\propto 1/x^{\lambda}$ . In the present model the LL BFKL result is exactly reproduced.)

The chains of primary gluons also determine the structure of the final state, but as discussed above, to get the full exclusive states softer emissions must be added as final state radiation. In summary the generation of exclusive final states contains the following steps:



1. The generation of two dipole cascades from the projectile and the target, in accordance with BFKL dynamics and saturation.
2. Calculating which pairs of one parton in the projectile and one parton in the target do interact. In BFKL the emission of gluons is a Poissonian type process, and the interaction probability is calculated in the eikonal approximation.
3. Extracting the primary,  $k_{\perp}$ -changing, gluons, and checking that they are given the correct weight. These gluons form colour connected chains between the projectile and the target, including branchings and loops. This step includes the removal of branches in the cascade which do not interact, and restoring energy-momentum conservation.
4. Adding final state radiation in relevant parts of phase space. The result consists of chains of colour connected gluons.
5. Hadronization. Here we use Lund string hadronization, where colour strings are stretched between the colour-connected gluons.

The outline of the paper is as follows: In section IV.2 we describe our dipole cascade model for inclusive observables. The problems encountered when generating exclusive final states are discussed in section IV.3. In section IV.4 we describe the key procedures used in the MC for solving the problems presented in section IV.3, while some of the more technical details are left for the appendices. Some results and predictions are given in section IV.5, together with a discussion of tunable parameters in the program. Finally our conclusions are given in section IV.6.

## **IV.2 The Lund dipole cascade model for inclusive cross sections**

### **IV.2.1 Mueller's cascade model and the eikonal formalism**

Mueller's dipole cascade model [8–10] is a formulation of LL BFKL evolution in transverse coordinate space. Gluon radiation from the colour charge in a parent quark or gluon is screened by the accompanying anticharge in the colour dipole. This suppresses emissions at large transverse separation, which corresponds to the suppression of small  $k_{\perp}$  in BFKL. For a dipole  $(x, y)$  the probability per unit rapidity ( $Y$ ) for emis-

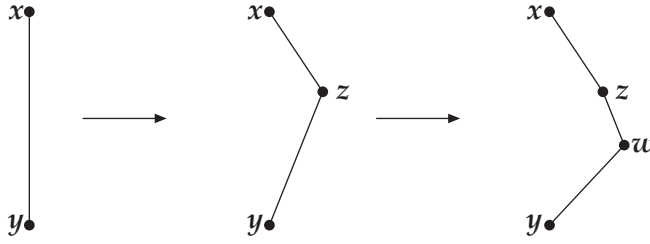


Figure IV.2: The evolution of the dipole cascade in transverse coordinate space. In each step, a dipole can split into two new dipoles with decay probability given by eq. (IV.1).

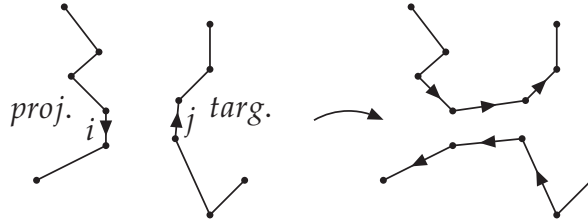


Figure IV.3: A dipole–dipole interaction implies exchange of colour and re-connection of the dipole chains in the colliding cascades. The arrows indicate the direction of the dipole going from colour charge to anticharge.

sion of a gluon at transverse position  $z$  is given by

$$\frac{d\mathcal{P}}{dY} = \frac{\bar{\alpha}}{2\pi} d^2z \frac{(x-y)^2}{(x-z)^2(z-y)^2}, \quad \text{with } \bar{\alpha} = \frac{3\alpha_s}{\pi}. \quad (\text{IV.1})$$

This emission implies that the dipole is split into two dipoles, which (in the large  $N_c$  limit) emit new gluons independently, as illustrated in fig. IV.2. The result reproduces the BFKL evolution, with the number of dipoles growing exponentially with  $Y$ .

In a high energy collision, the dipole cascades in the projectile and the target are evolved from their rest frames to the rapidities they will have in the specific Lorentz frame chosen for the analysis. Two colliding dipoles interact via gluon exchange, which implies a colour connection between the projectile and target remnants, as indicated in fig. IV.3. In the Born approximation the interaction probability between one dipole with coordinates  $(x_i, y_i)$  in the projectile, and one with coordinates  $(x_j, y_j)$  in the target, is given by (the factor 2 in the definition of  $f$  is



a convention)

$$2f_{ij} = 2f(x_i, y_i | x_j, y_j) = \frac{\alpha_s^2}{4} \left[ \log \left( \frac{(x_i - y_j)^2 (y_i - x_j)^2}{(x_i - x_j)^2 (y_i - y_j)^2} \right) \right]^2. \quad (\text{IV.2})$$

At high energies the strong increase in the number of dipoles gives a large probability for multiple dipole–dipole subcollisions, and the transverse coordinate space is particularly suitable for the treatment of multiple interactions and unitarity constraints. Assuming that the subcollisions are uncorrelated, multiple collisions are taken into account in the eikonal approximation, where the probability for an inelastic interaction is given by

$$\text{Int. prob.} = 1 - e^{-2F}, \quad \text{with } F = \sum f_{ij}. \quad (\text{IV.3})$$

The multiple interactions produce loops of dipole chains, corresponding to the pomeron loops in the reggeon formalism.

Assuming also that the elastic scattering amplitude,  $T$ , is driven by absorption into inelastic states, we find via the optical theorem

$$T = 1 - e^{-F}, \quad (\text{IV.4})$$

and thus the probability for an elastic interaction given by  $T^2$ . (We use a definition such that  $T$  in this case is purely real.)

To get the final result for the proton–proton cross sections we have to take averages over the projectile and target cascades, and integrate over impact parameter  $\mathbf{b}$ . For the total non-diffractive cross section we get

$$\sigma_{\text{inel}} = \int d^2\mathbf{b} \langle 1 - e^{-2F(\mathbf{b})} \rangle = \int d^2\mathbf{b} \langle 1 - (1 - T(\mathbf{b}))^2 \rangle. \quad (\text{IV.5})$$

When the projectile has an internal structure, which can be excited, the purely elastic cross section is obtained by taking the average of the amplitude  $T$ , before taking the square:

$$\sigma_{\text{el}} = \int d^2\mathbf{b} \langle T(\mathbf{b}) \rangle^2. \quad (\text{IV.6})$$

Taking first the square gives the total diffractive scattering (see ref. [20]):

$$\sigma_{\text{diff}} = \int d^2\mathbf{b} \langle T(\mathbf{b})^2 \rangle. \quad (\text{IV.7})$$

The cross section for diffractive excitation is consequently given by the difference

$$\sigma_{\text{diff ex}} = \sigma_{\text{diff}} - \sigma_{\text{el}} = \int d^2\mathbf{b} (\langle T(\mathbf{b})^2 \rangle - \langle T(\mathbf{b}) \rangle^2). \quad (\text{IV.8})$$

Thus diffractive excitation is determined by the fluctuations in the scattering amplitude. It is also possible to calculate *e.g.* the cross section for single diffractive excitation of the (right-moving) projectile by taking the average over the target cascade before, but over the projectile cascade after, squaring the amplitude. We also here have to subtract the elastic scattering, and thus get

$$\sigma_{\text{SD}} = \int d^2\mathbf{b} \left( \langle \langle T(\mathbf{b}) \rangle_L^2 \rangle_R - \langle T(\mathbf{b}) \rangle^2 \right), \quad (\text{IV.9})$$

where  $\langle \cdot \rangle_{L(R)}$  refers to the average over the left (right) cascade only.

## IV.2.2 The Lund dipole cascade model

The Lund dipole cascade introduces a number of corrections to Mueller's original formulation. They are all beyond the leading logarithmic approximation. While some of them correspond to the next-to-leading (NLL) corrections, others are not possible to completely associate with a given order in the perturbative logarithmic expansion, and we therefore simply denote them *beyond leading order*. The corrections are described in greater detail in previous articles [3–5], and a short summary is presented here.

### Beyond LL BFKL evolution

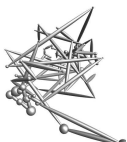
The NLL corrections to BFKL evolution have three major sources [21]:

*Non-singular terms in the splitting function:*

These terms suppress large  $z$ -values in the individual parton branchings, and prevent the child from being faster than its recoiling parent. Most of this effect is taken care of by including energy-momentum conservation in the evolution. This is effectively taken into account by associating a dipole with transverse size  $r$  with a transverse momentum  $k_\perp = 1/r$ , and demanding conservation of the lightcone momentum  $p_+$  in every step in the evolution. This gives an effective cutoff for small dipoles, which eliminates the numerical problems encountered in the MC implementation by Mueller and Salam [22].

*Projectile-target symmetry:*

A parton chain should look the same if generated from the target end as from the projectile end. The corresponding corrections are also called energy scale terms, and is essentially equivalent to the so called consistency constraint [23]. This effect is taken into account by conservation of



both positive and negative lightcone momentum components,  $p_+$  and  $p_-$ .

*The running coupling:*

This is relatively easily included in a MC simulation process. The scale in the running coupling is chosen as the largest transverse momentum in the vertex, in accordance with the results in ref. [24].

The treatment of these effects includes also effects beyond NLL, in a way similar to the treatment by Salam in ref. [21]. Therefore the power  $\lambda_{\text{eff}}$ , determining the growth for small  $x$ , is not negative for large values of  $\alpha_s$ .

### Non-linear effects and saturation

As mentioned above, multiple interactions produce loops of dipole chains corresponding to pomeron loops. Mueller's model includes all loops cut in the particular Lorentz frame used for the analysis, but not loops contained within the evolution of the individual cascades. As for dipole scattering the probability for such loops is given by  $\alpha_s$ , and therefore formally colour suppressed compared to dipole splitting, which is proportional to  $\bar{\alpha} = N_c \alpha_s / \pi$ . These loops are therefore related to the probability that two dipoles have the same colour. Two dipoles with the same colour form a quadrupole field. Such a field may be better approximated by two dipoles formed by the closest colour-anticolour charges. This corresponds to a recoupling of the colour dipole chains. We call this process a dipole "swing". In the MC, dipoles with the same colour are allowed to swing with a probability proportional to  $(r_1^2 r_2^2) / (r_3^2 r_4^2)$ , where  $r_1$  and  $r_2$  are the sizes of the original dipoles and  $r_3$  and  $r_4$  are the sizes of the recoupled dipoles. Dipoles with the same colour are allowed to swing back and forth, which results in an equilibrium, where the smaller dipoles have a larger weight. We note that in this formulation the number of dipoles is not reduced. The given weights favour the formation of smaller dipoles, and the saturation effect is obtained because the smaller dipoles have smaller cross sections.

### Confinement effects

Confinement effects are included via an effective gluon mass, which gives an exponential suppression for very large dipoles [5]. This prevents the proton from growing too fast in transverse size, and is also essential to satisfy Froisart's bound at high energies [25].



### IV.2.3 Initial dipole configurations

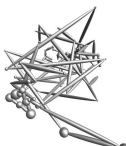
In DIS an initial photon is split into a  $q\bar{q}$  pair, and for larger  $Q^2$  the wavefunction for a virtual photon can be determined perturbatively. The internal structure of the proton is, however, governed by soft QCD, and is not possible to calculate perturbatively. In our model it is represented by an equilateral triangle formed by three dipoles, and with a radius of  $3 \text{ GeV}^{-1} \approx 0.6 \text{ fm}$ . The model should be used at low  $x$ , and when the system is evolved over a large rapidity range the observable results depend only weakly on the exact configuration of the initial dipoles, or whether the charges are treated as (anti)quarks or gluons.

## IV.3 From inclusive to exclusive observables

In this section we discuss the necessary steps when going from inclusive observables to exclusive final states. The technical details of the MC implementation are left to sec. IV.4 and the appendices.

### IV.3.1 The chain of $k_\perp$ -changing gluons

In the introduction we discussed briefly how the structure of an exclusive final state is determined by a backbone of gluons. The first step is therefore to extract this backbone chain of  $k_\perp$ -changing or primary gluons, with their proper weights. As discussed above, the different subcollisions are assumed to be uncorrelated, and the interaction probability for two dipoles,  $i$  and  $j$ , is given by  $1 - \exp(-2f_{ij})$ , with  $f_{ij}$  given by eq. (IV.2). When the interacting dipoles are determined, the backbone chains can be found by tracing their parents and previous ancestors backwards in rapidity. A resulting chain is shown in fig. IV.4a, and we here use the notation  $q_i$  for the real emitted gluons, and  $k_i$  for the virtual links in the evolution. The same chain is presented in fig. IV.4b in a  $(y, \ln q_\perp^2)$  diagram, with  $y$  being the rapidity. In this plot  $\ln q_+$  and  $\ln q_- (= y \pm \ln k_\perp)$  increase towards the upper right and upper left corners. Due to the “consistency constraint” [23], which is part of the NLL corrections to BFKL, the primary gluons are ordered not only in  $q_+$ , but also in  $q_-$ . This also implies an ordering in rapidity or angle, in accordance with QCD coherence. The real emissions satisfy the relation  $q_{i+}q_{i-} = q_{i\perp}^2$ , and are represented by points in fig. IV.4b. The space-like momenta for the virtual links  $k_i$  are not constrained by such a relation, and are represented by horizontal lines indicating their transverse momentum.



The weight for a particular chain with (real) gluons  $q_i$  is given by [18, 19] (assuming  $k_{\perp 0} = k_{\perp n} = 0$ )

$$\prod_i \frac{\bar{\alpha}}{\pi} \frac{d^2 q_{\perp i}}{q_{\perp i}^2} dy_i \delta(\Sigma \mathbf{q}_{\perp i}), \quad \text{with } \bar{\alpha} \equiv \frac{N_C \alpha_s}{\pi}. \quad (\text{IV.10})$$

We note in particular that this expression is symmetric under exchange of projectile and target. The result can also be expressed in terms of the virtual links  $k_i$ . We then have

$$\prod_{i=1}^n d^2 q_{\perp i} \delta(\Sigma \mathbf{q}_{\perp i}) = \prod_{i=1}^{n-1} d^2 k_{\perp i}, \quad (\text{IV.11})$$

and transverse momentum conservation implies that we have two different cases:

1. Step up:  $k_{\perp i} \approx q_{\perp i} \gg k_{\perp i-1}$ , with weight  $d^2 q_{\perp i} / q_{\perp i}^2 \approx d^2 k_{\perp i} / k_{\perp i}^2$ .
2. Step down:  $k_{\perp i} \ll q_{\perp i} \approx k_{\perp i-1}$ , with weight  $d^2 q_{\perp i} / q_{\perp i}^2 \approx d^2 k_{\perp i} / k_{\perp i-1}^2 = d^2 k_{\perp i} / k_{\perp i}^2 \times k_{\perp i}^2 / k_{\perp i-1}^2$ .

Thus steps down in  $k_{\perp}$  are suppressed by a factor  $k_{\perp i}^2 / k_{\perp i-1}^2$ . This implies that links with a local maximum  $k_{\perp}$ , as  $k_3$  in fig. IV.4, is given the weight  $d^2 k_{\perp i} / k_{\perp i}^4$ , and can be interpreted as a hard scattering between  $k_2$  and  $k_4$ , producing the two high- $p_{\perp}$  gluons  $q_3$  and  $q_4$ . For a link with  $k_{\perp}$  lower than the adjacent real gluons, like  $k_4$  in fig. IV.4, the transverse momentum of the real gluons will be determined by the neighbouring links  $k_3$  and  $k_5$ . Thus in such cases the associated weight will be  $d^2 k_{\perp i}$ , which is non-singular for small  $k_{\perp}$ . Note that no particular rest frame is specified for the collision between the two cascades. The result is the same if the “hard subcollision” is part of the projectile or target evolution, and thus independent of the Lorentz frame used for the analysis.

### IV.3.2 Reabsorption of virtual emissions

A dipole cascade generates a chain of dipoles linked together by gluons. A dipole–dipole interaction via gluon exchange implies exchange of colour, and the chains are recoupled as shown in fig. IV.3. Multiple interactions produce dipole loops as illustrated in the schematic picture in fig. IV.5. In this example two cascades are evolved in rapidity up to the dashed line in the center. Here three dipole pairs interact, forming two dipole loops. In a projectile cascade with a large lightcone momentum  $p_+$ , and initially small  $p_-$ , the partons need a contribution of  $p_-$

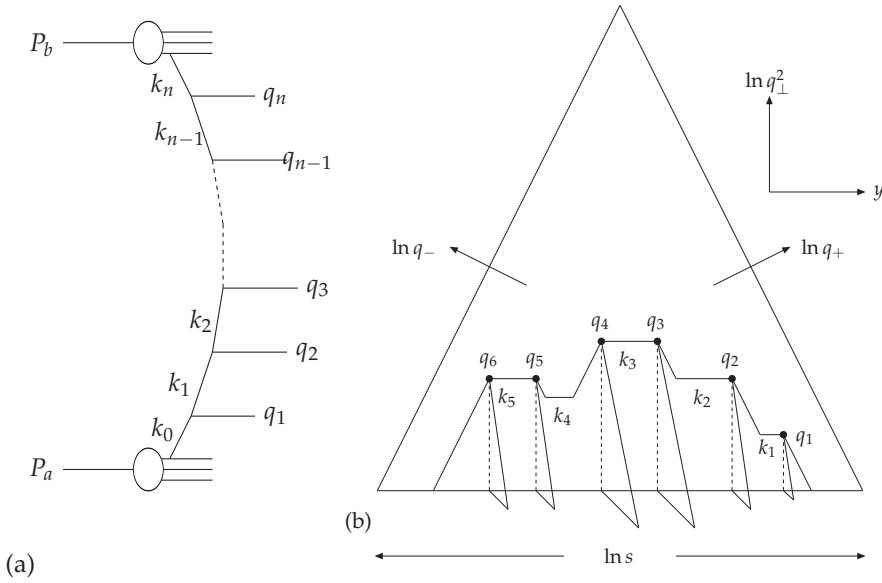


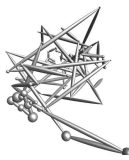
Figure IV.4: (a) A parton chain stretched between projectile and target. (b) A backbone of  $k_{\perp}$ -changing gluons in a  $(y, \ln q_{\perp}^2)$  plane. The transverse momentum of the virtual links  $k_i$  are represented by horizontal lines.

momentum from the target, in order to come on shell. Therefore the branches denoted *B* and *C* in fig. IV.5 have to be treated as virtual, and to be reabsorbed. The remaining gluons are coming on shell as real gluons, and are colour-connected along the solid lines in fig. IV.5. A colour loop formed by a swing, as the one denoted *A*, can come on shell also if it does not contain any interacting dipole. Such a process produces a closed colour loop not traversing the collision line at  $y = 0$ . A more detailed example of this effect can be found in appendix IV.3.2. The gluons in the virtual branches reabsorbed, the momenta for the real backbone gluons must be recalculated. This process is discussed in more detail in sec. IV.4.

IV

### IV.3.3 Giving proper weights to the emissions

In the cascade the gluons at the ends of a dipole are given opposite transverse momenta  $k_{\perp} = 1/r$  (see further sec. IV.3.4). In eq. (IV.1) an emitted dipole of length  $r$  is given a weight containing the factor  $d^2r/r^2$ . However, if this dipole emits further dipoles, the new weight is proportional to  $r^2$ . Thus the associated weight is just  $d^2r$  for dipoles which have split and been replaced by new dipoles. In the cascades shown in figs. IV.6 and IV.8 these dipoles are marked by dashed lines. In



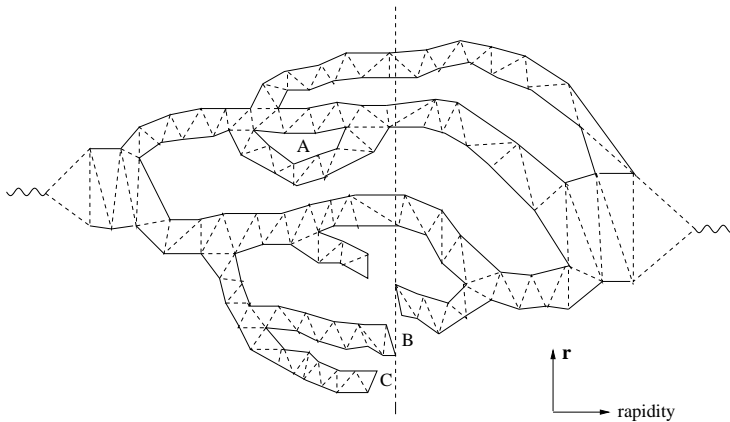


Figure IV.5: Collision of two dipole cascades in  $r$ -rapidity space. The dashed vertical line symbolizes the Lorentz frame in which the collision is viewed. The dipole splitting vertex can result in the formation of different dipole branches, and loops are formed due to multiple sub-collisions. The loop denoted by  $A$  is an effect of saturation within the cascade evolution, which can be formed via a dipole swing. Branches which do not interact, like those denoted  $B$  and  $C$  are to be treated as virtual, and to be absorbed.

the following they will be referred to as “inner dipoles”. The remaining dipoles, formed by colour-connected gluons, are marked by heavy lines, and they all get a weight proportional to  $1/r^2$ . They will be referred to as “outer dipoles”.

Let us study the cascade shown in fig. IV.6, obtained after the absorption of the virtual gluons as described in the previous subsection. The cascade starts from the dipole (01), followed by emission of gluons 2, 3, etc. Here the dipoles are first smaller and smaller,  $a \gg b \gg c \gg d$ . The corresponding  $k_{\perp}$ -values therefore become larger and larger in each step. After the minimum dipole, with size  $d$ , the subsequent emissions, 5, and 6, give again larger dipoles with correspondingly lower  $k_{\perp}$  values. The weight containing factors  $1/r^2$  for all “remaining dipoles” is proportional to

$$\frac{d^2 \mathbf{r}_2}{b^2} \cdot \frac{d^2 \mathbf{r}_3}{c^2} \cdot \frac{d^2 \mathbf{r}_4}{d^0} \cdot \frac{d^2 \mathbf{r}_5}{e^2} \cdot \frac{d^2 \mathbf{r}_6}{f^2} \cdot \frac{1}{f^2}. \quad (\text{IV.12})$$

In this event gluons 3 and 4 recoil against each other with large transverse momenta  $k_{\max} = 1/d$ . As all factors of  $d$  have canceled in eq. eq. (IV.12), this gives the proper weight  $d^2 \mathbf{r}_4 \propto d^2 \mathbf{k}_{\max} / k_{\max}^4$ . This reproduces exactly the proper weight for a hard gluon-gluon scattering.

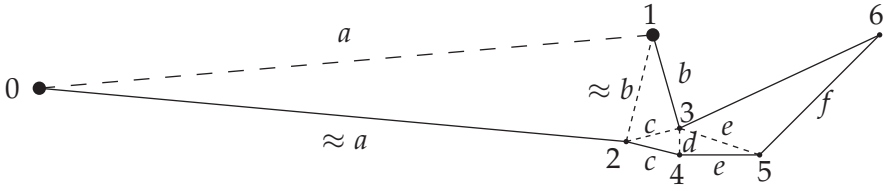


Figure IV.6: A dipole cascade in  $\mathbf{r}_\perp$ -space, in which a chain of smaller and smaller dipoles is followed by a set of dipoles with increasing sizes. The initial dipole between points 0 and 1 is marked by long dashes. Those dipoles which have split into two new dipoles, and thus disappeared from the chain, are marked by short dashes. The shortest dipole (34) corresponds to the maximum  $k_\perp$ , and represents a hard sub-collision.

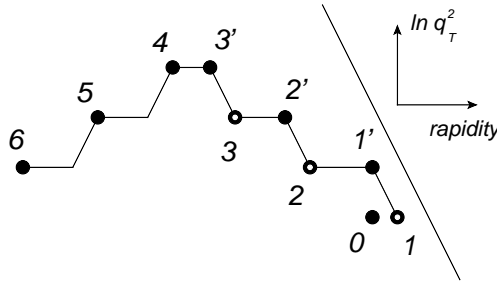
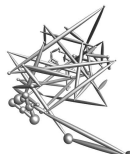


Figure IV.7: The same cascade as in fig. IV.7. The  $x$  direction shows rapidity, and  $y$  direction shows  $\ln(k_\perp^2)$ . The diagonal line is the constant  $p_+$  of the incoming particle.

The same cascade is shown in fig. IV.7 in the  $(y, \ln(k_\perp^2))$  diagram of fig. IV.4b. In this figure new emissions are first denoted by open circles, while filled circles mark their position after recoil from a later emission. Thus gluon 1 starts at the lower right corner. After the emission of gluon 2, it is recoiling to the position marked 1'. Similarly gluon 2 is shifted to position 2', when it emits gluon 3. When gluon 4 emits the softer gluon 5, its recoil is small and it keeps its position in the diagram.

Figure IV.8 shows instead a chain with increasing dipole sizes up to a maximum value,  $r_{\max}$ , which thus corresponds to a minimum transverse momentum,  $k_{\min}$ . Here we also get the correct weight  $d^2\mathbf{r}_{\max}/r_{\max}^4 \propto d^2\mathbf{k}_{\min}$ , which implies that there is no singularity for small  $k_\perp$ -values. Note that all gluons connected to the long dipoles are also connected to shorter dipoles, which determine most of their transverse momentum. Thus no gluon has  $q_\perp$  represented by  $k_{\min}$ .



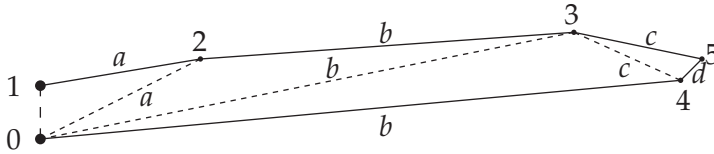


Figure IV.8: A cascade where the dipole sizes increase to a maximum, and then decrease. Here the size of the largest dipole, denoted  $b$ , corresponds to the minimum  $k_{\perp}$  in the chain.

### IV.3.4 Going from transverse coordinate space to momentum space

#### *Cascade evolution*

The dipole picture is formulated in transverse coordinate space, but experimental data are given in momentum space. We must therefore make a translation of our results from transverse coordinate to transverse momentum space. Note that most of the inclusive observables studied previously have been dominated by large dipoles, while the final-state observables are typically dominated by the large  $q_{\perp}$ , originating from the small dipoles. Thus effects such as proton size and confinement will be seen to affect observables very little, while new phenomena important for small dipoles will come into play. The one important exception to this is the deep inelastic cross section for large  $Q^2$ , which gauges small dipoles with an inclusive observable.

The weight  $d^2r/r^2$  for gluon emission in the dipole picture corresponds to  $d^2k_{\perp}/k_{\perp}^2$  in BFKL [1, 2] or DGLAP [26–28] evolution. We also found that a hard scattering, which in momentum space is proportional to  $d^2k_{\perp}/k_{\perp}^4$ , in the dipole picture corresponds to  $d^2r$ . These relations are consistent with the way we associate a dipole  $\mathbf{r}$  with a transverse momentum  $\mathbf{k} = \mathbf{r}/r^2$  (which also implies that  $\mathbf{r} = \mathbf{k}/k^2$ ). Thus, although the fixed relation between  $r$  and  $k_{\perp}$  is inconsistent with Heisenberg's uncertainty relation, it still reproduces the correct evolution also in momentum space. This result would also be obtained by the relation  $k_{\perp} = c/r$ , for any constant  $c$ . (Any result for a cross section would get the same number of extra factors of  $c$  in the numerator as in the denominator.) We make the choice of  $c = 1$  because it gives the correct  $\langle k_{\perp}^2 \rangle$  for a Gaussian distribution in  $r$ : A two-dimensional distribution  $\propto \exp(-\mathbf{r}^2/R^2)$  has the average  $\langle \mathbf{r}^2 \rangle = R^2$ . The Fourier transform of the amplitude  $\propto \exp(-\mathbf{r}^2/2R^2)$  is  $\propto \exp(-\mathbf{k}^2 R^2/2)$ , and thus the density is

$\propto \exp(-\mathbf{k}^2 R^2)$  and  $\langle \mathbf{k}^2 \rangle = 1/R^2$ .

#### *Dipole-dipole interaction*

It is, however, not possible to make the same identification in the dipole–dipole interaction cross section from gluon exchange. The logarithmic expression in eq. (IV.2) originates from a two-dimensional Fourier transform of the propagator  $1/k_\perp^2$ , including interference from interactions between the equal and unequal charges in the two dipoles. If we replace  $r$  by  $1/k_\perp$  in eq. (IV.2), we would obtain a cross section which grows like  $(dk_\perp^2/k_\perp^4) \cdot \ln^2 k_\perp$  for large  $k_\perp$ . Thus, taking the Fourier transform of the scattering amplitude, and then go back to momentum space via the relation  $k_\perp = 1/r$  does not give back the original cross section in momentum space. It is then more correct to use the original scattering cross section directly in momentum space.

The amplitude for scattering of an elementary charge against a target charge at position  $\mathbf{r}_{\text{target}}$  corresponds to the (two-dimensional) Fourier transform of the logarithmic Coulomb potential in two dimensions, denoted  $V(\mathbf{r} - \mathbf{r}_{\text{target}})$ :

$$A(\mathbf{k}) = \frac{1}{2\pi} \int d^2r e^{i\mathbf{k}\mathbf{r}} V(\mathbf{r} - \mathbf{r}_{\text{target}}) \propto \frac{\alpha_s e^{i\mathbf{k}\mathbf{r}_{\text{target}}}}{k^2}. \quad (\text{IV.13})$$

The phase is here inessential for the cross section, which is determined by  $|A|^2$ . The phase is, however, important when the target is a dipole. For scattering against a colour charge at  $\mathbf{r}_3$  and an anticharge at  $\mathbf{r}_4$ , we get

$$A(\mathbf{k}) \propto \frac{\alpha_s}{k^2} (e^{i\mathbf{k}\mathbf{r}_3} - e^{i\mathbf{k}\mathbf{r}_4}) = \frac{\alpha_s}{k^2} 2 \sin(\mathbf{k} \frac{\mathbf{r}_3 - \mathbf{r}_4}{2}) e^{i\mathbf{k}(\mathbf{r}_3 + \mathbf{r}_4)/2}. \quad (\text{IV.14})$$

For a dipole with charge and anticharge at respectively  $\mathbf{r}_1$  and  $\mathbf{r}_2$ , scattering against a dipole with coordinates  $\mathbf{r}_3$  and  $\mathbf{r}_4$ , we get

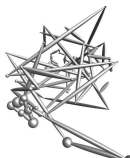
$$A \propto \frac{\alpha_s}{k^2} 4 \sin(\boldsymbol{\rho}_1 \cdot \mathbf{k}) \sin(\boldsymbol{\rho}_2 \cdot \mathbf{k}), \quad (\text{IV.15})$$

with  $\boldsymbol{\rho}_1 = (\mathbf{r}_1 - \mathbf{r}_2)/2$  and  $\boldsymbol{\rho}_2 = (\mathbf{r}_3 - \mathbf{r}_4)/2$ . Averaging and summing over colours this gives the scattering cross section

$$\frac{d\sigma}{d^2k} = 8 \frac{\alpha_s^2}{k^4} \sin^2(\boldsymbol{\rho}_1 \cdot \mathbf{k}) \sin^2(\boldsymbol{\rho}_2 \cdot \mathbf{k}). \quad (\text{IV.16})$$

To generate  $\mathbf{k}$ -values according to this distribution we simply select random impact-parameters  $\mathbf{r}_{\text{int}}$  and make the identification  $\mathbf{k} = \mathbf{r}_{\text{int}}/r_{\text{int}}^2$ . With  $d^2r_{\text{int}} = d^2k/k^4$  this corresponds to the interaction probability

$$f_{ij} = 8\alpha_s^2 \sin^2\left(\frac{\boldsymbol{\rho}_i \cdot \mathbf{r}_{\text{int}}}{r_{\text{int}}^2}\right) \sin^2\left(\frac{\boldsymbol{\rho}_j \cdot \mathbf{r}_{\text{int}}}{r_{\text{int}}^2}\right). \quad (\text{IV.17})$$



Note that for small  $r_{\text{int}}$ ,  $f_{ij}$  goes as a constant times the rapidly oscillating sine functions, with average  $(1/2)^2$ . This corresponds to the expected  $d^2k_{\perp}/k_{\perp}^4$  for large  $k_{\perp}$ . In the limit where the interaction distance is large compared to the dipole sizes,  $f_{ij}$  falls off as  $r_{\text{int}}^4$ , which gives the infrared stable result  $\propto d^2k_{\perp}$  for small  $k_{\perp}$ .

### IV.3.5 Final state radiation and hadronization

As discussed above, the backbone chain of  $k_{\perp}$ -changing gluons determines the inclusive inelastic cross section. To get the exclusive final states the soft  $k_{\perp}$ -conserving emissions have to be added as final state radiation [16, 18, 19]. As the  $k_{\perp}$ -conserving emissions have  $q_{\perp i} < k_{\perp i} \approx k_{\perp i-1}$ , they fill the area below the horizontal lines in fig. IV.4. Final state radiation is also emitted in the jets produced by the backbone gluons, here represented by the folds sticking out of the  $(y, \ln q_{\perp}^2)$  plane. The separation of e.g. the colour charge in gluon  $q_3$  and the corresponding anticharge in gluon  $q_2$  forms a colour dipole, and gives a gluon cascade similar to the cascade in an  $e^+e^-$ -annihilation event. The only difference is that emissions with  $q_{\perp} > k_{\perp 2}$  are not allowed.

The final-state radiation is thus added in much the same way as in the so-called LDC Monte Carlo [29, 30]. In the simulations we use the  $p_{\perp}$  ordered dipole cascade model [31, 32] as implemented in the ARIADNE program [33]<sup>2</sup>. In this formalism a gluon emission splits a dipole into two, both of which may continue radiating independently. Thus, also after final state radiation, the parton state consists of dipole chains formed by colour connected gluons.

In the final step the partons hadronize into final state particles. This is treated by the Lund string fragmentation model [34, 35] as implemented in the PYTHIA 8 program [36, 37]. Note that the parameters in ARIADNE have been thoroughly tuned together with the string fragmentation parameters to agree with LEP data, and we do not change any of these parameters here.

## IV.4 Generating the exclusive final states

The previous section outlined some of the conceptual problems encountered when describing exclusive final states in the dipole model, and how they can be solved. This chapter will go more into detail on how

---

<sup>2</sup>We will here use a preliminary reimplementaion in THEPEG of the old ARIADNE Fortran code.



the Monte Carlo handles different situations, and how the pieces of the model are fitted together.

The first step is to select the interacting dipoles from the virtual cascade, which makes it possible to identify the on-shell and virtual gluons. The on-shell gluons will form the backbone gluons in the previous section, while the virtual gluons are removed. It will turn out that some of the backbone gluons have to be reweighted and some of the  $q_{\perp}$  maxima will be removed, as will be described in sec. IV.4.3. Then a further check of ordering will be made to match phase space with final state radiation, and the colour flow between the remaining backbone gluons will be set based on the virtual cascade. These gluons will then undergo final state radiation, and hadronize to produce the final state.

Some of the more involved details, such as how the allowed phase space is chosen for emissions and interactions, and how saturation effects in the cascade and interaction complicate the procedure, will be discussed further in the appendices.

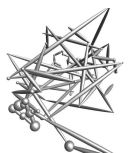
### IV.4.1 Selecting the interactions

As in our original Monte Carlo [3], the two incoming particles are first identified with a dipole state at their initial rapidity. These starting partons are called the valence partons, and are then evolved through rapidity to the interaction frame. Here, a relative transverse distance between the two incoming particles, the impact-parameter, is selected, and all the dipole–dipole scattering probabilities  $f_{ij}$  can be calculated. Since the individual dipole interactions are assumed to be independent, eq. (IV.17) can be used to find the probability for non-diffractive interaction between dipole  $i$  and  $j$ :

$$1 - e^{-2f_{ij}} = 1 - \exp \left( -16\alpha_s^2 \sin^2 \left( \frac{\boldsymbol{\rho}_i \cdot \mathbf{r}_{\text{int}}}{r_{\text{int}}^2} \right) \sin^2 \left( \frac{\boldsymbol{\rho}_j \cdot \mathbf{r}_{\text{int}}}{r_{\text{int}}^2} \right) \right). \quad (\text{IV.18})$$

The interaction distance  $r_{\text{int}}$  is set to the distance between two randomly selected partons, one from each dipole.

Just like in the cascade, the kinematics of the interaction is calculated. In this case, there will be two partons coming in from the left bringing with them  $p_+$ , but with a deficit in  $p_-$ , and correspondingly two partons from the right bringing  $p_-$ , but with a deficit in  $p_+$ . An interaction where the partons do not bring enough momentum to set all partons on shell is vetoed, that is  $f_{ij}$  is set to 0. The allowed phase space will be described more in detail in appendix IV.2.



It should be noted here that although the collision of two dipoles formally is a 4-to-4 reaction, with two incoming partons from each side, one of the partons in each dipole will have emitted the other parton. Thus a dipole interaction only connects the end of one backbone gluon chain, but the amplitude depends on the last two partons in the dipole picture.

#### IV.4.2 Identifying the backbone gluons

Once the interaction dipoles are selected, one can trace the parents of the interacting partons back, and identify the backbone gluons, as illustrated in figure IV.5. The rest of the partons will not get the necessary  $p_-$  from the colliding particle to come on shell, and will be reabsorbed as virtual emissions.

In a dipole picture, each emission is a coherent sum of emissions from the two partons at the end of the emitting dipole, and a unique parent cannot be determined. In the conventional parton cascade the radiation pattern is separated in two components representing independent emissions from the two different charges. The coherence effect is then approximated by angular ordering, and the recoil is taken by a single parent. For time-like cascades as in  $e^+e^-$ -annihilation or final state radiation this is not a dramatic effect. For the space-like cascades discussed here it is, however more important if both parents can get a recoil and be put on shell, or if the recoil effect for one of them may be so weak that this gluon has to be regarded as virtual and be reabsorbed. Naturally either alternative can only be approximate, and the question which of them gives the best description cannot be answered by perturbative QCD. We have therefore implemented both schemes in the event generator, and when comparing the results with experimental data we find best agreement when the parents share the recoil. For the results presented below, we have assumed that the relative shares are proportional to  $1/r_i^2$ , where  $r_1$  and  $r_2$  are the distances to the two parents.

#### IV.4.3 Reweighting outer $q_\perp$ maxima

Recalling sec. IV.3.3, two examples showed that giving the outer dipoles a weight of  $d^2r/r^2$ , and the inner dipoles a flat weight  $d^2r$  reproduced the correct weights for maxima and minima in  $q_\perp$ . In these examples the minimum or maximum dipole were both inner dipoles, that is dipoles that emitted further dipoles. If an outer dipole corresponds to a local minimum as in fig. IV.9, it is given a weight proportional to  $d^2r/r^2$ .

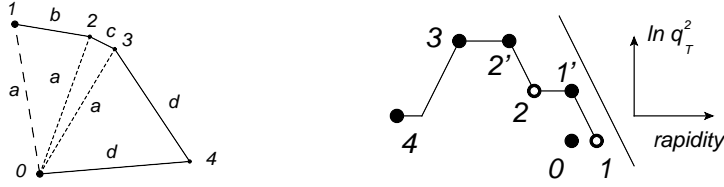


Figure IV.9: A cascade with a maximum in  $q_{\perp}$  where the small dipole corresponding to the large  $q_{\perp}$ , does not split. The outer  $q_{\perp}$  maximum is shown in impact-parameter space (left) and  $y$ - $q_{\perp}$  space (right).

As the two connected gluons both are given large transverse momenta  $q_{\perp} = 1/r$ , we get a distribution proportional to  $d^2 q_{\perp} / q_{\perp}^2$ , giving a too strong tail out to large  $q_{\perp}$ -values.

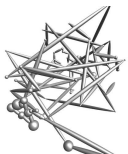
To get the correct weights, these small outer dipoles have to be suppressed by an extra factor  $r_{<}^2 / r_{>}^2$ , where  $r_{<}$  is the size of the small dipole giving the  $q_{\perp}$  maximum, and  $r_{>}$  is the corresponding maximum in dipole size later in rapidity. We note here in particular, that this extra reweighting was not needed in the calculation of inclusive observables presented in earlier articles. These observables depend only on interacting dipoles, which are never reweighted or absorbed in this way.

In the DIPSY event generator the reweighting is implemented by finding and reabsorbing some of the outer maxima, so that the correct weight is restored. The inner and outer dipoles are only known after the backbone gluons are identified, and therefore the reweighting can be performed only after selecting the interactions and the identification of the backbone gluons. This procedure is described in more detail in appendix IV.1.

#### IV.4.4 FSR matching and ordering

The kinematics for the reweighted backbone gluons can be significantly different from the kinematics in the virtual cascade. To exactly match the phase space covered by ARIADNE, the  $q_{+}$  and  $q_{-}$  ordering is checked again for the backbone gluons before being passed on from DIPSY.

In ARIADNE it is then checked that each gluon in the final state cascade is un-ordered w.r.t. the primary gluons, *i.e.*, that the positive (and negative) light-cone momentum of an emitted gluon is less than that of (one of) the primary gluons from which it is emitted. In this way all of phase space is covered exactly once.



#### IV.4.5 Colour flow

The backbone gluons are chosen and corrected looking only at the parent structure, that is, each gluon only remembers which two partons emitted it, independently of any subsequent dipole swings, as these are not changing the momenta of the backbone gluons. For final state radiation and hadronization it is, however, important to keep track of the colour flow between the backbone gluons, when the virtual emissions are reabsorbed.

This is done by going back to the colour flow of the virtual cascade, and absorb one virtual gluon at a time, until only the on-shell gluons are left. When a virtual gluon is removed, the two neighboring dipoles are combined to a single dipole. For events with no swing, this will always return the colour flow as if the virtual emissions never happened. For events with dipole swings the colour flow is more complicated, and will be discussed in appendix IV.3.

**The proton remnant:** The starting configuration of a proton is in our model represented by a triangle of three dipoles, roughly representing the positions of three valence quarks. However, three connected dipoles corresponds to the colour flow of three gluons rather than three quarks, and the extra charge may be regarded as representing the contribution from the gluons present in the proton wavefunction already at low virtuality.

This extra charge was introduced for inclusive observables, but for exclusive final states it has other effects that have to be handled. The three valence partons will in general continue down the beam-pipe, and if all three dipoles have interacted, then each of the valence partons will have two colour connections to the colliding projectile. This is an overestimate of the colour flow to the proton remnant, as the extra colour charges representing the gluonic component in general do not carry a large fraction of the proton energy. This is corrected for in DIPSY by re-connecting on average half of the colour flow to the valence partons by a dipole swing, which will move the gluonic content of the proton one “rung” down the gluon ladder.

#### IV.4.6 Higher order corrections

The above outlines the main points of how the backbone gluons are generated in DIPSY. There are, however, further details which, despite their non-leading nature, have to be accounted for. Below follows short

summaries of these corrections, while the detailed description of the algorithms implemented in DIPSY are left for the appendices.

### Coherence as relaxed ordering

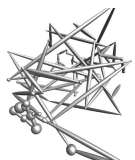
Previously in this section it was described how the outer  $q_{\perp}$  maxima were reweighted, and absorbed with a certain probability. A  $q_{\perp}$  maximum will through  $q_{\perp}$  ordering veto emissions at small  $q_{\perp}$  close in rapidity, but if the maximum is reabsorbed, the ordered phase space will be significantly larger. This is solved by overestimating the ordered phase space in the initial generation, making it possible to emit gluons with lower  $q_{\perp}$  in case the high- $q_{\perp}$  gluon is absorbed. This extra phase space can be regarded as an effect of coherence, in the sense that several close-by partons can coherently emit a gluon with a longer wavelength, and the gluon can use the combined energy in all the close-by partons. This process is described in detail in appendix IV.2, where it is also shown how the ordering and energy conservation in the interaction is implemented, based on how it is done in the cascade.

### Saturation effects

Previous considerations were all based on a single chain of dipoles, but at a 7 TeV collision there are on average more than three subcollisions, making saturation effects very important for the final state. In appendix IV.3 it is shown how the procedures described here has been developed to work also in events with both multiple interaction and swings. Multiple interactions give rise to splitting chains of backbone gluons while the swing can cause both splitting and merging chains, and together they are able to build any diagram of gluon chains.

In this section it is demonstrated how the reweighting of outer  $q_{\perp}$  maxima give the correct weight  $d^2q_{\perp} \alpha_s^2(q_{\perp}) / q_{\perp}^4$  in every situation, with the only exception being a special configuration in two merging chains, where one of the running couplings can get an incorrect scale. This is estimated to be a negligible effect.

The colour flow in a saturated cascade is more complicated as the dipole swing will reconnect the colour flow, simulating soft gluon exchanges between different parts of the gluon chains.



## IV.5 Self-consistency and tuning

There are several details in DIPSY that are not fixed by perturbative calculations, but nonetheless have a significant effect on the results. These details will have to be decided by other means, or tuned to experimental data. Many of them cannot be directly related to a tunable parameter, but are rather choices between different approximations or models. Other effects were tested, only to turn out to not give improved results. Thus, rather than trying to list which parameters and choices were tuned, we will in this section describe the constraints and data, which were used to fix the details of the model. After this we will compare the model to the remaining observables.

One of the most important self-consistency constraint is the frame-independence, that is the property that all observables should be the same no matter what collision frame  $y_0$  is used. This is a symmetry that is necessarily present in an all-order calculation, but can not be expected to be exactly manifested in a fix-order treatment as the non-leading effects enter differently in the interaction and the cascade. Thus, unknown non-leading effect will, if possible, be tuned to fit a known all-order property.

This section will first describe how the frame independence of different inclusive and exclusive observables fixes many of the details mentioned in sec. IV.4, and then how tuning to experimental data fixes the last uncertainties. The section is ended with a comparison of DIPSY with experimental data and other event generators for a selection of observables.

### IV.5.1 Achieving frame independence

Here the frame dependence of some observables are studied, and many non-leading subtleties can be fixed by requiring an approximately flat frame dependence. Notice that at this stage no comparison is made to experimental data.

**$\sigma_{pp}$  frame independence:** We find that the restrictions in the interaction have to be very generous to maintain a constant total  $pp$  cross section for  $y_0$  close to the valence rapidities. A proton evolved over the full range to the other protons rest frame, at the Tevatron this is 15 units of rapidity, will have large transverse momenta, while the valence partons of the unevolved proton will have very small transverse momenta. Requiring full ordering in lightcone momentum in this case will disallow

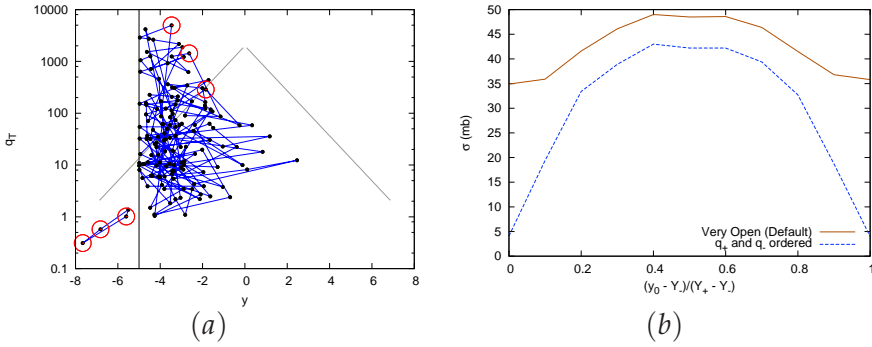
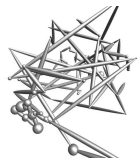


Figure IV.10: (a) Two colliding virtual cascades in the  $y$ - $q_{\perp}$  representation, generated by the Monte Carlo in an off-central frame. The lines show the colour flow between the partons, the dashed vertical line is the collision frame  $y_0$  and the circled partons are the starting valence partons. The outside triangle shows the incoming  $p_+$  and  $p_-$  of the protons. (b) The frame dependence of the total  $pp$  cross section at  $\sqrt{s} = 200$  GeV. The dashed curve has full  $q_{\pm}$  ordering in the interaction, the full one only requires enough energy to set the interaction on shell.

almost all dipole pairs, and the interaction probability will be strongly suppressed in off-central frames. This is illustrated in fig. IV.10a with a sample virtual cascade at the Tevatron. To maintain the cross section for all frames, a very open ordering in  $f_{ij}$  is needed, allowing interaction between partons even when they are not ordered from the virtual cascades. The minimum amount of ordering from appendix IV.2.2 gives a maximum deviation of about 20% at the endpoints as can be seen in fig. IV.10b. Anything stricter results in stronger frame dependence. The required ordering is thus set to this minimum

$$q_+ q_- > 16 q_{\perp \text{int}} \quad (\text{IV.19})$$

where  $q_+$  and  $q_-$  are the lightcone momenta the incoming partons bring, and  $q_{\perp \text{int}}$  is the interaction momentum used in  $f_{ij}$  in eq. (IV.17). This requirement only enforces that the incoming particles have sufficient energy to set the interacting partons on shell, without any additional ordering. This is significantly worse than previous versions of this model, where deviations between different frames were within a few percent. This is a sign that either the interaction ordering is too strict, blocking the interaction towards the end frames, or that the evolution does not grow fast enough, and a cascade evolved over a long rapidity range is not as strong as two cascades, each evolved only to the middle.



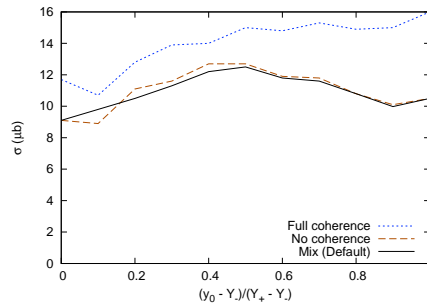


Figure IV.11: (a) Frame dependence of  $\gamma^*p$  at  $Q^2 = 14$  and  $W = 220$ , showing three different orderings in the virtual cascade. For low  $y_0$  the proton is evolved a larger part of the rapidity interval, and vice versa.

The first option is unlikely, as the ordering is already as generous as reasonable can be done, and in fact tests with no interaction ordering at all give no significant improvement. Likely, this problem is a result on the ordering in the virtual cascade, and how the coherence is used. During tuning it has shown that this frame dependence is quite sensitive to these choices, and further tuning could possibly solve this problem. For this tune however, the result is the one shown in fig. IV.10b.

**$\sigma_{\gamma^*p}$  frame independences:** The proton starts at a transverse momentum of about 0.3 GeV, while the two quarks from the photon start with a much higher transverse momentum. Here the key observation is that it is the  $q_+$  ordering that limits emissions of gluons with larger  $q_\perp$ , while the  $q_-$  ordering limits the emission of smaller  $q_\perp$ . Thus, with the interaction frame close to the photon, the cross section will be set by the protons ability to climb up to the higher  $q_\perp$ , dominated by the  $q_+$  ordering, and conversely, with an interaction frame close to the proton, the cross section will be determined by the  $q_-$  ordering in the photons cascade.

This provides an opportunity to use self consistency to determine which the ordered phase space in the cascade should be. In agreement with the arguments in appendix IV.2.1, it turns out that a fully coherent ordering will allow all emissions that may be ordered in the backbone chain. This is however done by overestimating emissions of large dipoles in the virtual cascade. This is seen in fig. IV.11 where the coherent ordering is tilted with a larger cross section when the dipole is allowed to evolve. Here the  $\gamma^*$  is incoming from the negative z-axis



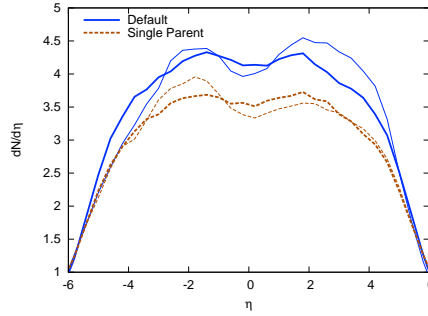
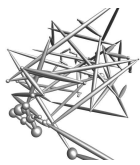


Figure IV.12:  $dN/d\eta$  for  $pp$  at 900 GeV with default DIPSY, and DIPSY with the “single parent” setting. The thick line is collided in midframe  $y_0 = 0$ , the thin line in  $y_0 = -2.7$ .

with a large  $p_+$ , and the proton in incoming form the positive  $z$ -axis with a large  $p_-$ . Ignoring coherence provides a symmetric frame dependence (although with the same bump as in  $pp$ ), but will cut away many emissions that may be ordered in the backbone chain.

A combination is used, where the  $q_\perp$  of the effective parton is used, but the rapidity of the single parent. This maintains a symmetric frame dependence while still covering as much as possible of the ordered phase space for the backbone gluons. The  $q_-$  ordering is also very important in deciding the energy dependence for inclusive observables, such as the  $pp$  total cross section. As will be seen later, it turns out that this combined ordering provides an energy dependence that fits very well with experimental data.

**Frame independence of  $dN/d\eta$ :** For this observable to be frame independent it is needed that any given rapidity produces the same density of charged particles independently of where the interaction frame is. This means that the  $q_\perp$  must behave the same coming from the cascade or from the interaction, and it should not depend on whether the cascade goes on for long, or if it interacts immediately. All this depends heavily on the ordered phase space in the virtual cascade and interaction, and in how the backbone gluons are handled. In practice, tuning for frame independence of  $dN/d\eta$  is equivalent to balancing the  $q_\perp$  in the interaction and in the cascade. If the interaction has too much transverse activity, then the charge particles will tend to clump up around the interaction frame when it is moved. Conversely, if the cascade provides too much  $q_\perp$ , then the side with the longer cascade will have more



charged particles, and the interaction on the other side in rapidity will not be enough to balance this.

With the virtual cascade and  $f_{ij}$  fixed from the inclusive observables according to the above arguments, it is only the handling of the backbone gluons left to tune. The problems connected to the reweighting of the outer  $q_\perp$  maxima mainly entered through the ordered phase space in the virtual cascade. Once the virtual cascade and interactions are determined, the ordering of the backbone gluons is fixed by matching to FSR, so few choices are left at this point.

One choice, though, is whether both or just one parent should come on shell, as was described in sec. IV.4.2. Keeping both parents will give more activity in the cascade as more particles will be kept, and more recoils will be done. Thus, the single parent choice will have the multiplicity more towards the interaction side, and the double parent choice more towards the cascade side, as is seen in fig. IV.12.

Neither of them deviate more than 10% at any pseudo-rapidity which is encouraging for the model, but neither of the options is much better than the other, so this observable cannot fix this choice. It will instead be tuned to the experimental value of this observable, which is close to line for double parent.

## IV.5.2 Tuning to experimental data

**Inclusive  $pp$  cross sections:** In the last published tune of the Monte Carlo [6], there were 4 parameters, set to:

$$\begin{aligned} \Lambda_{\text{QCD}} &= 0.2 \text{ GeV} & \rho_{\text{max}} &= 2.9 \text{ GeV}^{-1} \\ R_p &= 3.0 \text{ GeV}^{-1} & W_p &= 0 \text{ GeV}^{-1}, \end{aligned} \quad (\text{IV.20})$$

being the QCD scale, the confinement range, the proton size, and the fluctuation in the proton size. These parameters were tuned to the total and elastic  $pp$  cross section as function of  $\sqrt{s}$ , and the elastic differential cross section as function of  $t$ .

In principle the same can be done now, but one of the four parameters now hold a more important role than in previous papers. Recall from the discussion in section IV.3.4 that the large dipoles will dominate the inclusive  $pp$  cross section, while the small dipoles will dominate the exclusive observables. One should note that  $\rho_{\text{max}}$ ,  $R_p$  and  $W_p$  mainly affect large dipoles, while  $\Lambda_{\text{QCD}}$  also affects small dipoles. Thus the inclusive  $pp$  cross section can be tuned using  $\rho_{\text{max}}$ ,  $R_p$  and  $W_p$  without

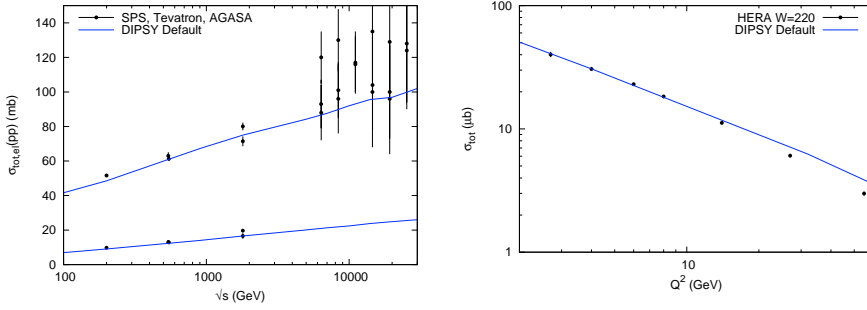


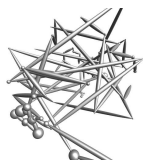
Figure IV.13: The inclusive data that was tuned to. (Left) The total and elastic cross section as function of  $\sqrt{s}$  for  $pp$ . Experimental data from [38–46]. (Right) The total  $\gamma^*p$  cross section as function of  $Q^2$  for  $W = 220$  GeV. Experimental data from [47–49].

affecting the exclusive observables much. A comparison of the default tune with data can be found in fig. IV.13.

It should be noted that further fluctuations have been included in the proton wavefunction other than the fluctuation in size. First, the partons are allowed to fluctuate in shape, making the normally equilateral triangle of valence partons distorted. This has essentially the same effect as the fluctuation in size as a flatter triangle will have a smaller cross section. Second, the valence partons have a Gaussian smear in rapidity. While they previously were all placed at the same rapidity, that of the proton, they are now a bit spread out. This has a small effect also for the exclusive observables, as the peak in  $dN/d\eta$  and  $dp_{\perp}/d\eta$  at the valence rapidity becomes more smeared out. As in previous publications, tuning shows that all these fluctuations have to be small to maintain the ratio between the elastic and total cross section. Although the fluctuations are not needed for any observable, the fluctuations in size, angle and rapidity are set to a Gaussian distribution of widths 0.1 GeV, 0.1 and 0.1 respectively.

## IV

**Inclusive  $\gamma^*p$  total cross sections:** As mentioned several times above, this is a key observable for tuning. Changes that affect the  $\gamma^*p$  cross section will also affect exclusive observables such as  $dN/d\eta$ , and changes to the virtual cascade that affects the  $dN/d\eta$  will also affect the  $\gamma^*p$  cross section. However, changes to how the backbone gluons are handled after the virtual cascade is made, will affect only the final state, not the inclusive observables.  $\sigma_{\gamma^*p}$  is allowing us to tune the virtual cascade for small dipoles separately, and after that is fixed, details in how



the backbone gluons are treated can be tuned separately.

This observable is affected, apart from the ordering that was fixed above, by  $\Lambda_{\text{QCD}}$  and  $c$  from sec. IV.3.4, that is the parameter that sets  $q_{\perp} = c/r$ . With  $c = 1$  as was motivated previously, the model can be made to agree with HERA data with a very reasonable<sup>3</sup>  $\Lambda_{\text{QCD}}$  of 0.23 GeV, see fig. IV.13.

**$dN/d\eta$ :** Now the virtual cascade is completely fixed, and all that is left is to fix the remaining uncertainties in how the backbone gluons are selected and handled. The remaining details essentially decide how many gluons will come on shell, and how many will be reabsorbed.

The most important choice left to be fixed is the problem in sec. IV.4.2, whether one or both of a partons parents should come on shell. Not keeping both parents produce about 20% less charged particles than keeping both, and comparing experimental data, this is a bit too low. Thus we will in this tune chose to keep both parents in each emission.

This fixes all the details of the tune in this paper, and are ready to compare the tuned Monte Carlo to experimental data.

### IV.5.3 Comparison with experiments

We will now compare the results from our program with experimental data on exclusive final-state observables, both from the LHC and the Tevatron.

The DIPSY program is written in C++ using THEPEG [50], which is a toolkit and framework for implementing event generation models. This framework is also used by HERWIG [51] and, more importantly here, a new version of ARIADNE [33], a pre-release of which we have been using for the results presented in the following. The Lund string fragmentation model of PYTHIA 8 has been interfaced to THEPEG and is also used with DIPSY. In this way we produce exclusive hadronic final-state, which can be directly compared to data.

We will use the RIVET8 framework [52] (version 1.5.0) for validating event generators, which is also available from within THEPEG. We have selected some representative observables from underlying event, and minimum bias studies by the ATLAS experiment at center of mass

---

<sup>3</sup>For comparison,  $\Lambda_{\text{QCD}} = 0.22$  GeV in the final state shower in ARIADNE, after a tune to LEP data.

energies of 900 GeV and 7 TeV [53,54]. We also show some comparisons with results from the CDF experiment at 1.8 TeV [55].

It should be noted that these observables are very difficult to describe also for the state-of-the-art general purpose event generators such as PYTHIA 8 [36] and HERWIG [51], which can be plainly seen from a recent review of event generators [56] and on the web site <http://mcplots.cern.ch/> where up-to-date comparisons between event generators and data are presented.

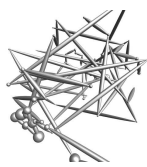
The most advanced of the general purpose event generators, PYTHIA 8, is the only one that gives a fair description of most minimum-bias and underlying-event data, and in the following we will compare our results, not only to data but also to a recent tuning of PYTHIA 8 (called 4C in [57]). In fact we will show two versions of this tuning, one which only includes non-diffractive events, and one which also includes elastic and diffractive scattering. Several experimental measurements include a correction to what is referred to non-single-diffractive events, which in principle should be directly comparable to our results. But this correction is very model-dependent (see *e.g.* [56] for a discussion on this) and we therefore give an indication of the size of this correction by including both non-diffractive and diffractive results from PYTHIA 8. Note that our results should be compared to the non-diffractive results from PYTHIA 8.

Also for DIPSY we show two sets of curves. As discussed above, a serious constraint for our model is that it should be independent of the Lorentz frame in which we perform the collisions. To quantify this independence we have performed simulations not only at central rapidity, where most measurements are made, but also in an asymmetric frame<sup>4</sup>. In the central rapidity frame, the transverse momenta of final-state gluons that are relevant for the observables are predominantly given by the dipole–dipole interactions, while in the asymmetric case the transverse momenta mainly comes from recoils in the evolution.

In the following we will only show small fraction of the plots we have produced with RIVET8. Further plots can be inspected on <http://home.thep.lu.se/~leif/DIPSY.html>.

**Minimum-bias observables:** In figures IV.14–IV.17 we show some standard minimum-bias observables as measure by ATLAS at 900 GeV and 7 TeV. A general observation is that DIPSY has a slightly too weak

<sup>4</sup>The rapidity of the collision frame is taken to be 2.7 for 900 GeV, 3.0 for 1800 GeV, and 3.5 for 7 TeV.



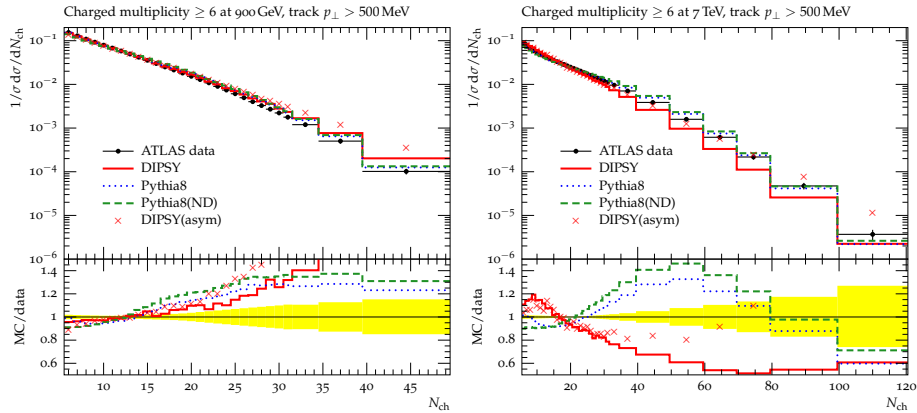


Figure IV.14: The charged multiplicity distribution at 0.9 (left) and 7 TeV (right). The data points are the ones given in RIVET 8 version 1.5.0 and are taken from [54] and include only tracks with  $p_{\perp} > 500$  MeV in events with more than 6 charged tracks. The full lines are the DIPSY results, the dotted lines are from PYTHIA 8 with diffractive and non-diffractive events, the dashed lines are PYTHIA 8 with only non-diffractive events, and the crosses are from a DIPSY simulation in an asymmetric frame.

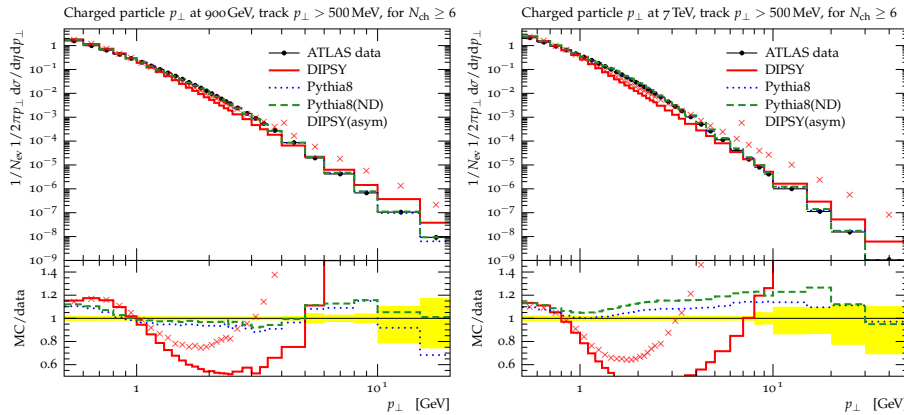


Figure IV.15: The transverse momentum distribution of charged particles at 0.9 (left) and 7 TeV (right). Data points and lines as in fig. IV.14.

energy dependence. Looking, *e.g.*, in figure IV.14 we see that DIPSY tend to overestimate high multiplicities at low energies and underestimate them at high energies. Note, however that the cross section for *e.g.* multiplicities between 40 and 50 increases by a factor 40, and a large part of the increase is described by DIPSY (a factor 25). The effect is more clearly

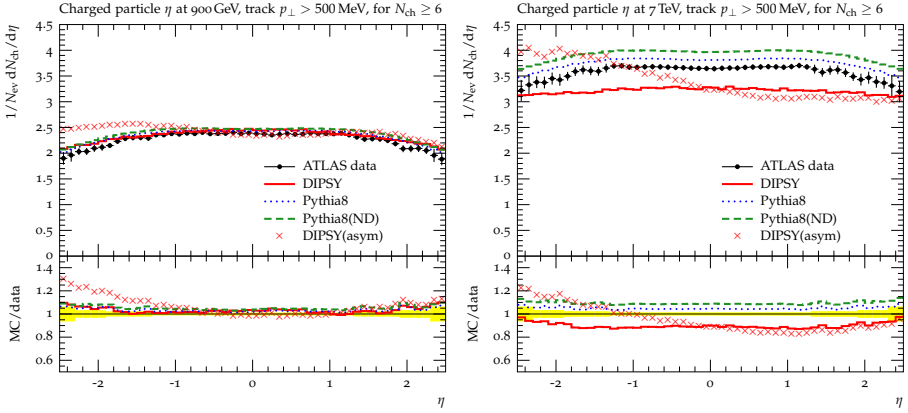


Figure IV.16: The pseudo-rapidity distribution of charged particles at 0.9 (left) and 7 TeV (right). Data points and lines as in fig. IV.14.

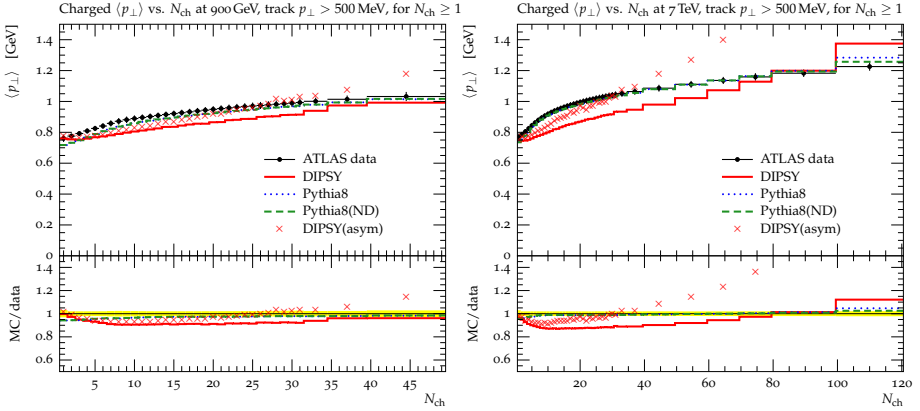
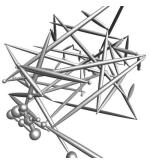


Figure IV.17: The average transverse momentum as a function of charged particle multiplicity at 0.9 (left) and 7 TeV (right). Data points and lines as in fig. IV.14.

IV

seen in the pseudo-rapidity dependence of the average multiplicity in figure IV.16, where again the energy dependence in DIPSY is a bit too weak.

For the transverse momentum distribution in figure IV.15, the energy dependence is a bit better, but DIPSY tend to overshoot both at small and large transverse momenta, while undershooting at medium values. For large transverse momenta, we believe that our description may improve if we include  $2 \rightarrow 2$  matrix element corrections for local  $q_{\perp}$  maxima, both in the evolution and in the interactions. For the softer part



of the spectrum, we believe that the discrepancy is related to the point-like valence partons in the proton wavefunction. Even when evolved to mid-rapidity, the valence partons will still have a large  $q_+$  and will allow emissions at large  $q_\perp$ . Even though these emissions will be in mid-rapidity, the balancing recoil will go with the valence partons down the beam-pipe, making the spectrum in the main ATLAS detectors too soft.

In the transverse momentum distribution we also see that DIPSY in the asymmetric frame gives a much harder spectrum, indicating that the transverse momentum generated in the virtual cascade is harder than the what is generated in the dipole–dipole interactions. The frame dependence is also clearly seen in the pseudo-rapidity distribution in figure IV.16, where we see an increased activity for large rapidities in the asymmetric case, where the particles mainly originate from the evolution rather than the interactions.

In figure IV.17 we see that DIPSY underestimate the average transverse momentum at small and medium multiplicities, which is related to the underestimate of the number of particles with medium transverse momentum.

**Underlying-event observables:** In figures IV.18–IV.20 we show observables related to the underlying event, many of which were introduced by Field [58]. The emphasis is to look at particle flow and transverse momenta away from jets and/or high transverse momentum charged particles to as much as possible isolate effects of the underlying events.

In figure IV.18 we show the multiplicity and summed transverse momentum as a function of the azimuth angle from a leading charged track with transverse momentum larger than 2 GeV. We see that all programs have difficulties reproducing the activity close to the trigger particle (the *towards* region) and in the opposite (*away*) region which should be dominated by the recoil from the leading track. In fact, all programs have similar problems, especially in the towards region, and while DIPSY in an asymmetric frame is clearly the worst, giving too much back-to-back activity, the default DIPSY actually gives a reasonable shape.

It is, however, the *transverse* region, defined as  $60^\circ < \Delta\phi < 120^\circ$ , which is the most sensitive to the underlying event. In figures IV.19 and IV.20 we show the number and summed transverse momenta of charged particles in this region as a function of the transverse momentum of the leading track. We see that the PYTHIA 8 here gives a better description of data, while DIPSY as before seem to have a bit too weak en-



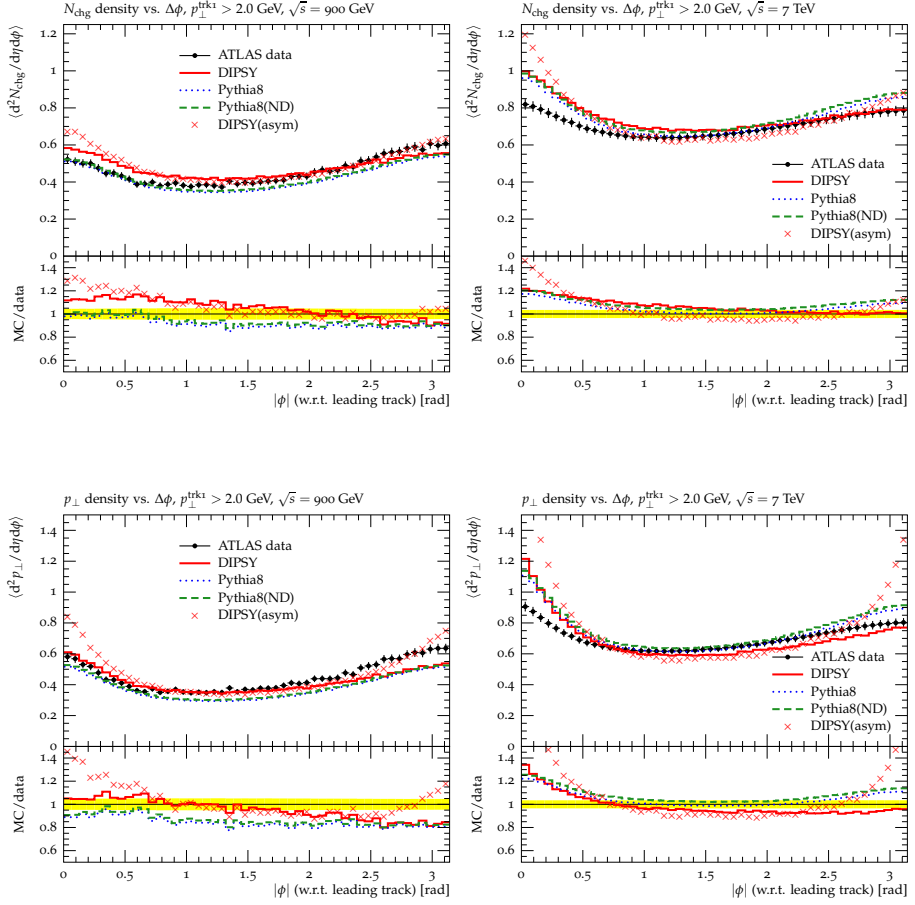


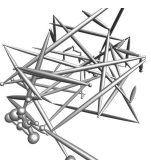
Figure IV.18: The multiplicity (top) and scalar sum of transverse momenta (bottom) of charge particles as a function of azimuth angle w.r.t. a leading charged particle of at least 2 GeV transverse momenta at 0.9 TeV (left), and 7 TeV (right). The data points are the ones given in RIVET 8 version 1.5.0 and are taken from [53]. The generated data as in fig. IV.14.

IV

ergy dependence and consistently seem to overestimate the activity at small transverse momentum of the trigger particle.

## IV.6 Conclusions and outlook

We have here presented a completely new model for exclusive final states in non-diffractive hadronic collisions. The model is dramatically different from conventional multiple-interaction scenaria implemented



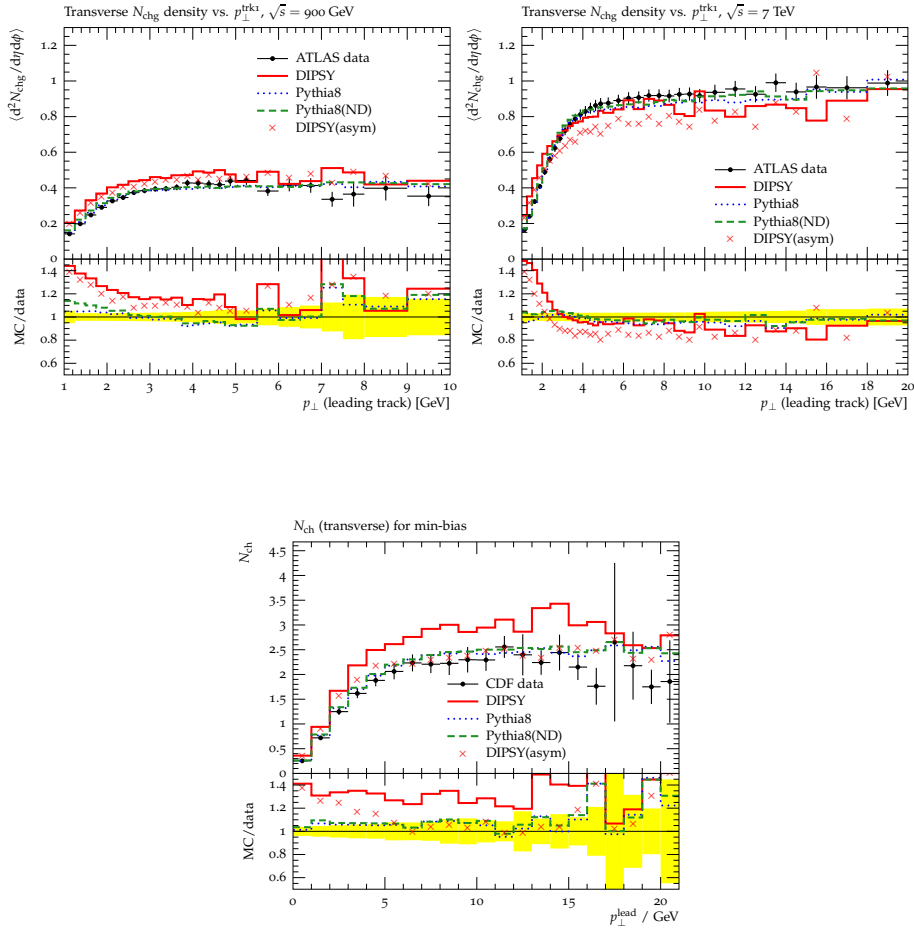


Figure IV.19: The multiplicity of charge particles in the *transverse* region, as a function of the transverse momentum of the leading charged particle at 0.9 (top left), 1.8 (bottom) and 7 TeV (top right). Data points and lines as in fig. IV.18. We also show data from CDF [55], but note that this data is differently normalized.

in state-of-the-art general purpose event generators such as PYTHIA8 and HERWIG.

On the theoretical side our model is based on BFKL-evolution, contrary to the DGLAP-based conventional approaches. As the processes of relevance in minimum-bias events involve very small  $x$ -values and small to moderate scales, it can be argued that BFKL is more appropriate.

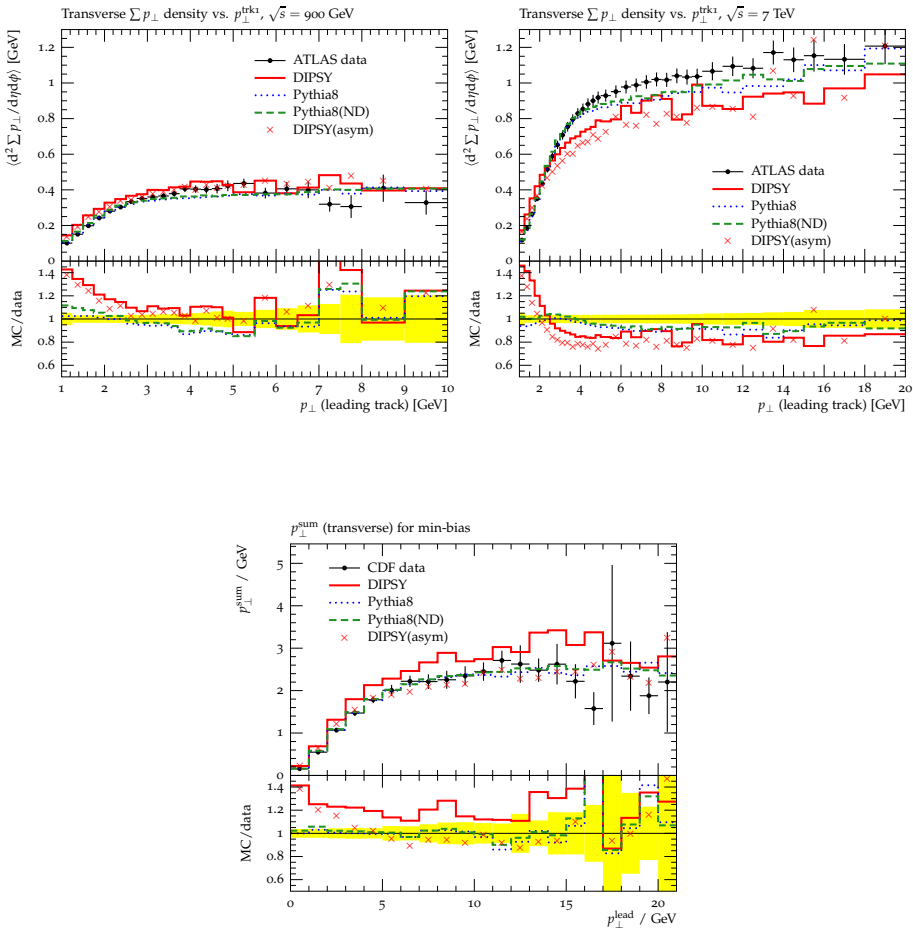
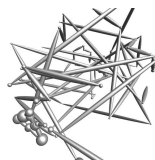


Figure IV.20: The scalar sum of transverse momenta of charge particles in the *transverse* region, as a function of the transverse momentum of the leading charged particle at 0.9 (top left), 1.8 (bottom) and 7 TeV (top right). Data points and lines as in fig. IV.19.

Also on the technical side, the differences are large. We use a forward evolution in impact-parameter space and rapidity, while conventional programs use backward evolution in momentum space. Our procedure has the advantage that colour screening and saturation effects are easily treated. In addition we have a detailed description of fluctuations and correlations in the proton wave function, which are typically averaged over in conventional approaches, and we can easily model correlations affecting *e.g.* the effective cross section in double-parton scattering [59].



On the down-side, our model, being based on BFKL evolution, suffers from uncertainties due to the very large higher order corrections to BFKL. We have here presented a number of non-leading effects which influence our results. We have had to make many choices, some of them guided by knowledge about next-to-leading logarithmic terms in the perturbative expansion, but in many cases our choices lack guidance from perturbative QCD, and have had to be made by semi-classical and phenomenological arguments.

Throughout the the development of our model the requirement that the results should be independent of the Lorentz frame in which the interactions are performed has been a very severe constraint. In addition, our choices have been constrained by the requirement that our description of inclusive and semi-inclusive observables, such as the total and elastic cross sections remains reasonable.

Although a big part of the framework from previous publications was reevaluated to describe exclusive observables, the part of the model that describes the inclusive observables remains basically unchanged. The reweighting of the final state gluons does not affect the interaction probability, and the ordering in the virtual cascade and interaction, which were tuned for frame-independence, are very similar to what we have presented in previous publications.

Thus, although the DIPSY program contains a fair amount of parameters and switches, maybe even as many as in the multiple-interaction model in PYTHIA 8, once the frame independence and inclusive cross sections are accounted for, there is little left that will influence the exclusive final states produced. As an example, the dependence on the collision energy of final-state observables is mainly determined by the energy dependence of the total and elastic cross sections. In the case of the multiple-interaction model in PYTHIA 8, in contrast, the energy dependence is a free parameter, although indirectly related to the increase of the total cross section with energy.

With this in mind, we are very pleased that our model gives quite reasonable results for minimum-bias and underlying-event observables at the Tevatron and the LHC. The results are, of course, not perfect, but this cannot be expected from a model which does not include quarks. Also, as pointed out above, the Lorentz-frame independence requirement is not quite satisfied. So, although we now publish this paper<sup>5</sup> we do not expect that the last word has been said and we expect the model

---

<sup>5</sup>The DIPSY program itself is not formally released, but is available on request from the authors.

to develop and improve.

Meanwhile the model can be used to make non-trivial predictions for observables related to correlations and fluctuations in the partonic cascades, both for hadronic collisions and heavy-ion collisions. Not least the latter is a very interesting feature of our model. We are able to produce complete hadronic final states in heavy-ion collision, including many non-trivial correlations between partons in different nucleons in the ions. Our model does not include any hydro-dynamical evolution of the final states, so we do not expect to describe the experimental data perfectly, but it will provide a reasonable base-line for effects of partonic evolution which will give deeper insight into the collective effects seen in heavy ion collisions.

## Acknowledgments

Work supported in part by the EU Marie Curie RTN MCnet (MRTN-CT-2006-035606), and the Swedish research council (contracts 621-2008-4252 and 621-2009-4076).

L.L. gratefully acknowledges the hospitality of the CERN theory unit.

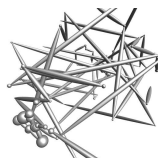
## IV.A $q_{\perp}$ max reweighting in DIPSY

As was described in sec. IV.4.3, the maxima in in  $q_{\perp}$  corresponding to an “outer” dipole in the cascade, that is a dipole that have emitted no on-shell emissions, come in with the wrong weight, and need to be reweighted.

This is in DIPSY obtained by finding and reabsorbing some of the outer maxima to restore the correct weight. The inner and outer dipoles are only known after the backbone gluons are identified, and thus the reweighting can be performed only after selecting the interactions and the identification of the backbone gluons.

To find the emissions that need to be reweighted, we note that an outer dipole corresponds to a parton that has not emitted on one side in colour flow, as parton 3 in fig. IV.9. The maximum in  $q_{\perp}$  is associated with the the backwards dipole being smaller than the forward dipole, that is, dipole  $c$  being smaller than dipole  $d$ .

Starting from the interaction frame, the backbone gluons are checked for partons fitting these criteria, and the ones found are reweighted by



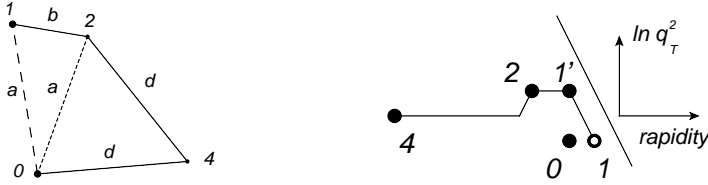


Figure IV.21: The backbone gluons after the outer  $q_\perp$  maximum in fig. IV.9 has been merged. The left figure is in impact-parameter space.

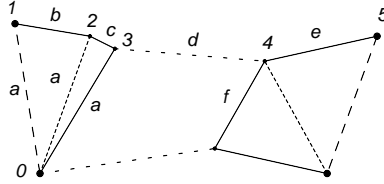


Figure IV.22: Partons 1 to 3 incoming from the left side collides with a cascade from the right, with partons 4 and 5. Dipole  $a$  interacts with dipole  $f$ , which makes dipole  $c$  an outer  $q_\perp$  maximum. The figure is in impact-parameter space.

an extra factor

$$R = \frac{r_{<}^2 \alpha_s(r_{<})}{r_{>}^2 \alpha_s(r_{>})}, \quad (\text{IV.21})$$

where the running couplings have been included for better accuracy. This changes the weight of the two dipoles from  $W_{\text{before}}$  to  $W_{\text{after}}$ , with

$$W_{\text{before}} = d^2 r_{<} d^2 r_{>} \frac{\alpha_s(r_{<})}{r_{<}^2} \frac{\alpha_s(r_{>})}{r_{>}^2}, \quad W_{\text{after}} = d^2 r_{<} d^2 r_{>} \frac{\alpha_s^2(r_{<})}{1} \frac{1}{r_{>}^4}. \quad (\text{IV.22})$$

In momentum space, this corresponds to

$$W_{\text{before}} = d^2 q_{>} d^2 q_{<} \frac{\alpha_s(q_{>})}{q_{>}^2} \frac{\alpha_s(q_{<})}{q_{<}^2}, \quad W_{\text{after}} = d^2 q_{>} d^2 q_{<} \frac{\alpha_s^2(q_{>})}{q_{>}^4}. \quad (\text{IV.23})$$

Notice that the small dipole size  $r_{<}$  is associated with the large recoil  $q_{>}$ , and conversely for the large dipole. The reweighting is done by reabsorbing partons of this type with a probability  $1 - R$ , as is illustrated in fig. IV.21. This reabsorption is done to the outer parent, so that their recoil will be canceled out, and the large  $q_\perp$  vanish.

Some care has to be taken with the definition of an outer  $q_\perp$  maximum close to the interacting frame, where it is not enough to look at the cascade from just one side. A dipole interacts with a probability roughly proportional to  $r^2$ , canceling out the  $1/r^2$  weight associated

with its emission, and the colour flow will be recoupled over to the other state. Looking at fig. IV.22, parton 3 will not fit the above definition for outer  $q_{\perp}$ , as it has no emissions on either side. However, since the dipole on one side is interacting, and the dipole on the other side is not, dipole  $c$  will still be a  $q_{\perp}$  maximum with incorrect weight. The Monte Carlo uses a generalized algorithm that covers also these cases, and uses the dipole  $d$  in fig. IV.22 as the larger dipole to reweight and possible reabsorb parton 3.

Outer  $q_{\perp}$  maxima from the interaction, for example if  $d$  would be smallest dipole, does not have to be corrected as the interaction amplitude  $f_{ij}$  already has the correct weight for large  $q_{\perp}$ .

This procedure ensures that the spectrum of large  $q_{\perp}$  from the cascade and interaction is indeed going as  $\frac{d^2 q_{\perp}^2(q_{\perp})}{q_{\perp}^4}$ . The proportionality constant is set from the known amplitude for a strictly increasing chain in  $q_{\perp}$ , and the known “penalty” for being unordered.

This extra reweighting was not needed before, as only inclusive observables were considered which are not affected by this procedure. An interacting dipole is always counted as an inner dipole in the final state, which means that no interacting dipole will be removed in this way, and the inclusive interaction probability for the two cascades is unchanged.

## IV.B Absorbed partons and ordering

In the previous sections, we describe how the backbone gluons are controlled for ordering and reweighted, and some partons are absorbed. An absorbed parton returns the  $q_{+}$  to its parents, and the transverse recoils are undone. This will in general move the parents back in rapidity and down in  $q_{\perp}$ , which opens up a larger ordered phase space for the parents as in fig. IV.23. After parton 2 is emitted, taking part of the  $q_{+}$  from the parent and giving a  $q_{\perp}$  recoil, 1' is still allowed to continue emitting. For these emissions to be ordered in  $q_{+}$  and  $q_{-}$ , they have to be between the dotted lines in fig. IV.23. If parton 2 was not emitted though, the larger order phase space between the dashed lines would have been or-

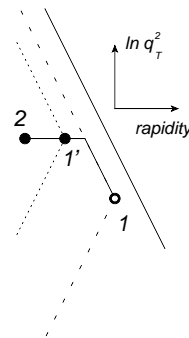
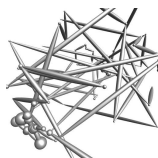


Figure IV.23: An emission limits the ordered phase space of the parents.



dered with respect to 1.

If the virtual cascade would only allow emissions ordered in  $q_+$  and  $q_-$ , every absorbed gluon would open a part of phase space for emissions from the parents that has not been considered in the virtual cascade. This is solved by partially relaxing the ordering in the virtual cascade, and thus overestimating the ordered phase space to cover the case of reabsorbed partons. Care has to be taken though, as the virtual cascade, before any reabsorptions, will be used to calculate inclusive observables. As the backbone gluons are not yet decided when the cascade is made, it is from this approach not possible to use the correct ordered phase space already for inclusive observables, and at the same time cover all necessary phase space for all possible sets of backbone gluons.

However, by estimating what the backbone gluons may look like already in the virtual cascade one can find a sufficiently good middle way: not too strict ordering so that an important part of the possible final states get cut away, but not too open overestimate so that the inclusive cross sections inflates.

### IV.B.1 Coherence

Three observation at this point will all point towards the same solution:

- Only large  $q_\perp$  emissions, like the one in fig. IV.23, significantly change the parents momenta. Thus it is only absorption of a step up in  $q_\perp$  that risks shadowing emissions from the parent.
- The phase space that get shadowed mainly concerns small  $q_\perp$  emissions. That is, the issue is when a large  $q_\perp$  parton is emitted and later absorbed, where the parent has not been allowed to emit with small  $q_\perp$ .
- Many of the absorbed backbone gluons are absorbed due to an outer  $q_\perp$  maximum. This is exactly the scenario described in the previous two points, that is an absorbed step up in  $q_\perp$  that shadows a step down in  $q_\perp$ .

In DIPSY, when a dipole is emitted in the virtual cascade, it is not only emitted by the parton at the end of the dipole, but coherently by all partons being close to the end of the dipole. This means that recoil and ordering is using an effective parton with the summed momenta of all the partons within range, where the range is set by the distance from the parent to the emitted gluon.



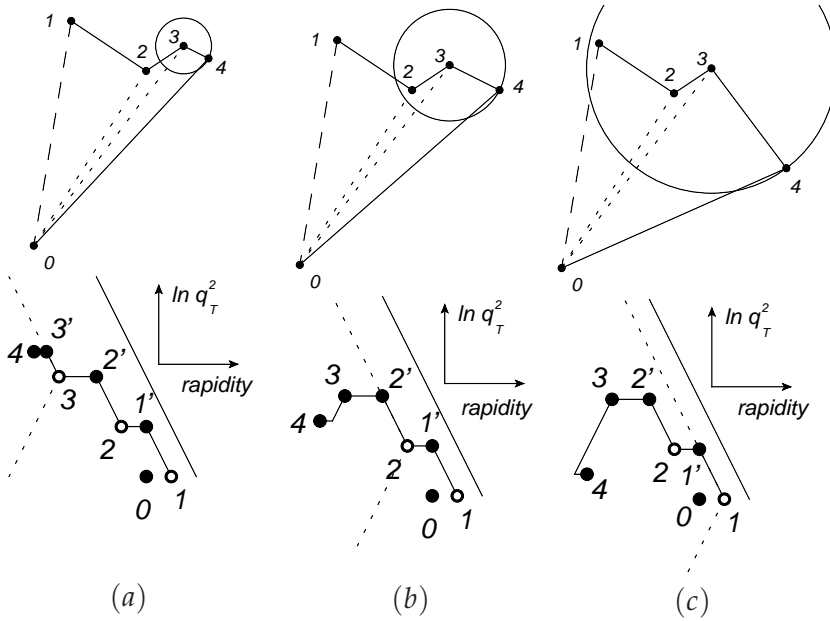
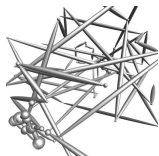


Figure IV.24: A parton emission (4), being emitted at different distances. The upper figures are in impact-parameter space, and the lower figures are in  $y$ - $q_{\perp}$  representation, where the dotted lines show the limits of the  $q_{+}$  and  $q_{-}$  ordering. The circles in the upper figures show the coherence range of the emission.

This procedure is shown in fig. IV.24, where parton 4 is emitted at different distances from its parent. In (a), the emission is a smaller dipole than the previous one, and the coherence range is smaller than the distance to the previous parton 2, so the recoil and ordering will be done by parton 3 only. If the emission is at a larger distance than the previous emission, as in (b), then the emission will be done by an effective parton with the merged momenta of parton 2 and 3. Notice that the recoil between 2 and 3 will cancel when their momenta are added, and the effective parton will have the momentum of the original parton 2, as shown in the lower figure (b). Emissions at larger distance will continue to add parton to the effective parton, and can allow emissions that are not ordered with the parent itself, as in (c).

An outer  $q_{\perp}$  maximum is always a small dipole followed by a larger dipole, and reweighting will sometimes merge the two close by partons to one. The extra ordered phase space opened by this merging is exactly the part of phase space used by the coherent emissions at long distance, which can be seen by comparing figures IV.9, IV.21 and IV.24(b). This



algorithm thus ensures that an absorbed outer  $q_{\perp}$  maximum can not open up a part of phase space that was not considered in the virtual cascade. By solving this issue, we have been forced to introduce coherence, where an emitted gluon cannot resolve partons that are closer together than its wavelength.

While this increased ordered phase space will cover all situations in the final state, some care has to be taken. First, some of the small dipoles that emit coherently will not be absorbed, and in that case the virtual cascade has emitted large dipoles in unordered regions. These large dipoles have a significant effect on inclusive observables, and the total cross sections may get inflated.

Second, the large unordered dipoles are emitted with the motivation that the previous small dipole may get emitted. However, the situation can be that the small dipole will be absorbed *because* the large dipole was emitted, as the large emission makes the previous small dipole a  $q_{\perp}$  maximum. Thus coherence is an estimate of how the final state will look which is to some extent self-fulfilling.

With this in mind, full coherence as described above may need to be scaled back to give a more accurate description. This was addressed in sec. IV.5.2 where frame independence was used in deciding exactly what phase space should be considered as ordered in the virtual cascade.

## IV.B.2 Ordering in the interaction

Like with the virtual cascade it is impossible to use an ordering that allows the correct part of phase space for both inclusive and exclusive observables, but again some observations can be made.

1. The final result should not depend on whether a recoil comes from the cascade or the interaction. Thus the ordering in the interaction should allow the same backbone gluons as the ordering in the cascade.
2. It is not possible to use the exact same ordering as in the virtual cascade, as the situation is fundamentally different. At a certain rapidity in the virtual cascade, the partons have not yet gotten recoils from emissions at later rapidities. Thus, ordering in the virtual cascade is checked when only recoils with partons in one direction have been made. The same is not true in the interaction, where all recoils in both cascades are already made.
3. Events where an outer  $q_{\perp}$  maximum next to an interaction, as in

fig. IV.22, is absorbed will allow more phase space for the interaction in exactly the same way as in the cascade. In the same way, coherence can be used to make sure all final states are still being considered.

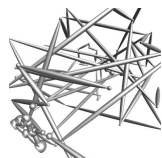
4. In the virtual cascade,  $q_+$  and  $q_-$  held two fundamentally different roles where  $q_+$  was the lightcone momentum the particle came in with, and  $q_-$  measured the increasing virtuality. In the interaction the situation is completely symmetric in  $q_+$  and  $q_-$ , so the orderings must be the same.
5. In the cascade, there is no absolute limit on how small  $q_-$  can be allowed at a certain rapidity, as no momentum,  $q_+$  or  $q_-$ , will be emitted in the limit of a soft gluon. However, energy conservation sets a hard limit on how much  $q_+$  can be allowed, namely the  $q_+$  of the parent.

Putting these observations together, we see that there is a limit for how much phase space can be allowed, as there always have to be enough energy for the interaction recoil to come on shell. Notice that this corresponds to both  $q_+$  and  $q_-$  ordering, as the particles from both states must bring sufficient energy. As in the previous section, the possibility of merged partons forces coherent ordering when the interaction distance is larger than the previous dipoles in the cascade. The allowed phase space is illustrated for two different impact-parameters in fig. IV.25.

In (a), parton 3 and 4 are close to each other, corresponding to a large interaction  $q_\perp$  that will recoil the partons past each other as can be seen in the lower figure. As 4' needs more  $q_-$  than 3 can supply, and conversely parton 3' needs more  $q_+$  than 4 supplies, the interaction  $q_\perp$  can not be set on shell, and  $f_{ij}$  will be set to 0. In this case, there is no outer  $q_\perp$  maximum in either cascade as the maximum is in the interaction, so no parton risk being absorbed and coherence will not include any extra partons.

If the impact-parameter between the two cascades would be such as in (b) where the partons 3 and 4 are farther away from each other, the interaction  $q_\perp$  is smaller and the coherence range larger. As can be seen in the lower figure, the smaller virtuality and the coherent interaction of partons 2 and 3 means that there is enough  $q_+$  and  $q_-$  to set the interaction on shell, and  $f_{ij}$  is calculated as normal.

Here it should also be taken into account that by transferring a fraction  $1 - z$  of the supplied  $q_+$  to the other state at fix  $q_\perp$  will increase the virtuality by a factor  $1/z$ , and conversely for the colliding parton, which



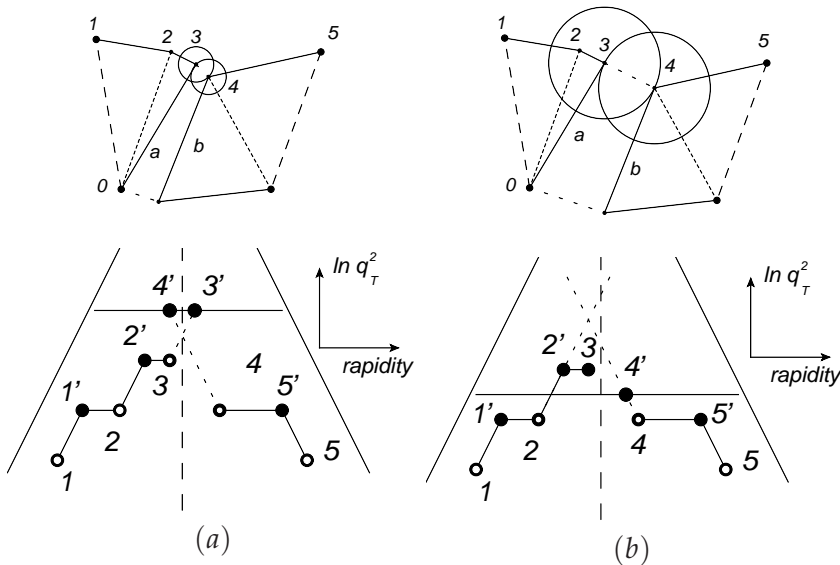


Figure IV.25: Ordering in an interaction for two different impact-parameters, where parton 1-3 are belonging to one cascade, and 4 and 5 to the other. The upper figures are in impact-parameter space, and the circles shows the coherence range in the interaction for parton 3 and 4. The lower figures are in  $y$ - $q_{\perp}$  representation, where vertical dashed line is the interaction frame  $y_0$ , the horizontal full line marks the interaction  $q_{\perp}$ , and the diagonal dotted lines marks the  $q_{-}$  and  $q_{+}$  parton 3 and 4 respectively brings to the interaction.

gives the limit for allowed interactions:

$$q_{+}q_{-} > 16q_{\perp\text{int}}^2, \quad (\text{IV.24})$$

where  $q_{+}$  and  $q_{-}$  are the supplied lightcone momenta from the interacting effective partons, and  $q_{\perp\text{int}}$  is the transverse recoil from the interaction.

This is a minimum for what has to be cut away in the ordering, and from frame independence it turns out that it can not be stricter (see section IV.5.1), thus motivating us to set the allowed phase space in  $f_{ij}$  to eq. eq. (IV.24).

## IV.C Saturation effects

All motivations and examples discussed above have been based on a single backbone gluon chain, but in LHC events there will be several chains branching of and merging due to multiple interactions and the

swing. This complicates the situation for most of the arguments presented previously in this section. However, the algorithms have been designed with saturation effects in mind, to give realistic results in all situations. Here follows some of the larger effects from saturation, and how the above algorithms handle them.

### IV.C.1 Multiple interaction

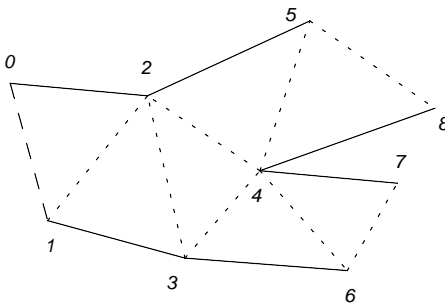


Figure IV.26: Two interactions makes a chain split in two. Dotted lines show parent structure, full lines show colour flow. The picture is in impact-parameter space.

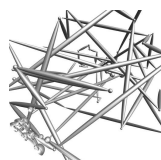
In the interaction, multiple scatterings are allowed, which means that there will be several chains cutting the interaction frame. These chains will merge at some point when following them back, if not before, they will always meet at the valence partons. This does not introduce any complications for the ordering. Each emission is controlled at the time of the emission, and if another branch has taken energy from the parents, then the ordered phase space for emission will be smaller, which is expected.

One has to be a bit careful with the reweighting however, but the algorithm described in sec. IV.4.3 is made to handle both splitting and merging chains. The dipoles created with a weight of  $d^2r/r^2$  are still the partons that have on-shell children on one side, but not on the other, and therefore the definition of an outer  $q_\perp$  maximum can remain.

This is illustrated in fig. IV.26, where a backbone chain splits up in two due to multiple interaction. Dipoles (24) and (34) both get the weight  $d^2r$  corresponding to  $d^2q_\perp/q_\perp^4$ , and they will get two factors of  $\alpha_s(r)$  in case of  $q_\perp$  maximum. Thus they do not need any extra suppression, and they do indeed not fit the definition of outer dipole, as parton 4 has children on both sides. For all other partons and dipoles, the arguments for the single chain can be applied as normal, so the reweighting algorithm works also with multiple interactions.

### IV.C.2 The Swing

IV



The dipole swing in the virtual cascade does not cause any recoils, but it does affect the parent structure of future emissions. In a non-swunged, single interaction chain, one of the two parents of each parton will also be parent to the other parent, making for the typical ladder-like structure seen in previous figures. However, with swung emissions this is no longer true, and the two parents can have 4 different parents.

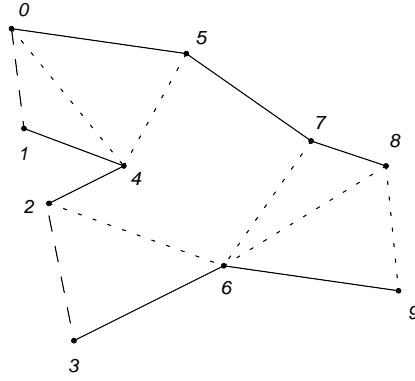


Figure IV.27: A swing between (45) and (26) causing two chains of backbone gluons to merge. Dotted lines show parent structure, full lines show colour flow. The picture is in impact-parameter space.

This is seen in fig. IV.27 where a swing has recoupled dipole (45) and (26) into (24) and (56), (56) then evolves further and interacts, while (24) does not interact.

Here the parents of parton 8 and 9 cover all the partons (notice that the parents of 7 are parton 5 and 6), so all partons are set on-shell. Notice in the figure that even though parton 4 is colour connected to 2 from the swing, parton 4 was not emitted by 2 (it was emitted by 0 and 1); thus no recoil has been made between the two partons, and no reweighting has to be made.

Dipole (14) has the weight  $1/r^2$  from the cascade and is an outer dipole as parton 4 has no children on that side. Thus (14) will, if smaller than (45), be reweighted by

$$\frac{r_{14}^2 \alpha_s(r_{14})}{r_{45}^2 \alpha_s(r_{45})} \quad (\text{IV.25})$$

from eq. eq. (IV.21), and reweighting again produces the correct weights. Correspondingly for parton 2, which is in the same situation as 4, but since 2 is a valence parton with no parents, there is no reweighting to be done. Dipole (45) is not an outer dipole because parton 7 is a child of 5 on the same side as (45), so no reweighting will be done. If (45) is a  $q_\perp$  maximum, it will be emitted with a weight  $\alpha(r_{45})/r_{45}^2$ , and the swing is made with a probability  $\frac{r_{45}^2 r_{26}^2}{r_{24}^2 r_{56}^2}$ , giving the weight

$$r_{45}^0 \alpha(r_{45}) \quad \leftrightarrow \quad \frac{\alpha(r_{45})}{q_{45\perp}^4}. \quad (\text{IV.26})$$

Notice that while the power of  $q_{\perp}$  is the correct one, a power in the running coupling is missing. This power of  $\alpha_s$  will instead come from the smallest dipole in the emission of parton 7 from 5 and 6. Thus, a saturated cascade can give rise to  $q_{\perp}$  maxima where one of the powers in  $\alpha_s$  is at the wrong scale.

This flaw can possibly be mended by introducing a running  $\alpha_s$  in the swing amplitude, but in the current version of DIPSY it is not implemented. As it is a next to leading order factor in the weight occurring only in special configurations of a saturated cascade, it is estimated to be a small effect.

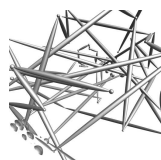
In conclusion, the algorithm in section IV.4.3 will still provide a satisfactory treatment of reweighting outer  $q_{\perp}$  maxima.

### IV.C.3 colour flow in saturated cascades

For a saturated cascade, the colour flow does not necessarily return to the original structure when the virtual emissions are removed according to IV.4.5. The swings are changing the colour structure, and after all the virtual emissions are reabsorbed, the colour flow does not necessarily reproduce the structure without the virtual emissions. An example of such a virtual cascade and backbone gluons is shown in fig. IV.28.

Swings where one of the swung dipoles go on to interact will merge two backbone chains, as was seen in sec. IV.3.2, and are very important for a frame-independent description. Swings by an outer dipole, such as A, will not influence the choice of backbone gluons, but can reconnect the colour flow between the backbone gluons. A colour reconnection between backbone gluons can also happen by a swing between virtual dipoles, if the dipoles originate from different parts of the backbone chain, as is the case for swing C. If the two swinging virtual dipoles originate from the same part on the backbone chain, as swing D, no difference will be seen in the colour flow between the backbone gluons.

In this way, not only exchange of individual soft gluons between the chains are simulated, but virtual chains of soft and hard gluons can carry colour flow between the chains, or between different parts of the same chain. The virtual cascade can thus give a very dynamic and detailed description on how the colour flow changes in saturated environments, which will be increasingly important at high energies, and can be an essential ingredient in heavy ion collisions.



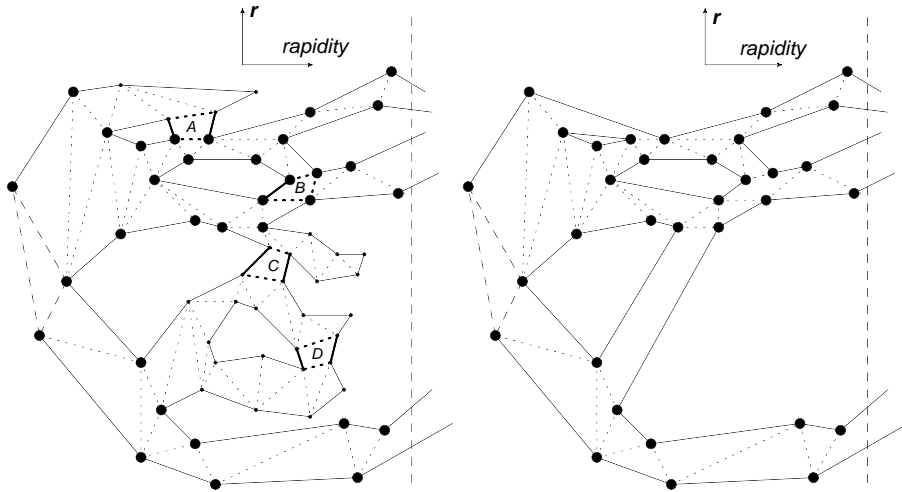
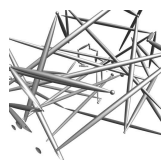


Figure IV.28: A cascade with swings and multiple interactions. The long dashed lines on the left side are the three valence dipoles of a proton. Full lines mark colour flow and dotted lines mark emissions. There are three interactions, which are the colour lines passing over the interaction rapidity marked by a vertical dashed line to the right. The big dots are the backbone gluons, selected through tracing each interaction back towards the valence partons, and the rest of the partons are virtual. The left figure is the virtual cascade, and four swings A to D are highlighted with thick lines. The right figure shows the backbone gluons after the virtual partons have been absorbed.



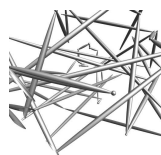
## IV References

- [1] E. A. Kuraev, L. N. Lipatov, and V. S. Fadin, “The Pomeranchuk Singularity in Nonabelian Gauge Theories,” *Sov. Phys. JETP* **45** (1977) 199–204.
- [2] I. I. Balitsky and L. N. Lipatov, “The Pomeranchuk Singularity in Quantum Chromodynamics,” *Sov. J. Nucl. Phys.* **28** (1978) 822–829.
- [3] E. Avsar, G. Gustafson, and L. Lönnblad, “Energy conservation and saturation in small- $x$  evolution,” *JHEP* **07** (2005) 062, arXiv:hep-ph/0503181.
- [4] E. Avsar, G. Gustafson, and L. Lönnblad, “Small- $x$  dipole evolution beyond the large- $N(c)$  limit,” *JHEP* **01** (2007) 012, arXiv:hep-ph/0610157.
- [5] E. Avsar, G. Gustafson, and L. Lönnblad, “Diffractive Excitation in DIS and pp Collisions,” *JHEP* **12** (2007) 012, arXiv:0709.1368 [hep-ph].
- [6] C. Flensburg, G. Gustafson, and L. Lonnblad, “Elastic and quasi-elastic  $pp$  and  $\gamma^*p$  scattering in the Dipole Model,” *Eur. Phys. J.* **C60** (2009) 233–247, arXiv:0807.0325 [hep-ph].
- [7] C. Flensburg and G. Gustafson, “Fluctuations, Saturation, and Diffractive Excitation in High Energy Collisions,” *JHEP* **10** (2010) 014, arXiv:1004.5502 [hep-ph].
- [8] A. H. Mueller, “Soft gluons in the infinite momentum wave function and the BFKL pomeron,” *Nucl. Phys.* **B415** (1994) 373–385.
- [9] A. H. Mueller and B. Patel, “Single and double BFKL pomeron exchange and a dipole picture of high-energy hard processes,” *Nucl. Phys.* **B425** (1994) 471–488, hep-ph/9403256.
- [10] A. H. Mueller, “Unitarity and the BFKL pomeron,” *Nucl. Phys.* **B437** (1995) 107–126, hep-ph/9408245.
- [11] E. Iancu, A. Leonidov, and L. McLerran, “The Color glass condensate: An Introduction,” arXiv:hep-ph/0202270 [hep-ph].
- [12] E. Iancu and R. Venugopalan, “The Color glass condensate and high-energy scattering in QCD,” arXiv:hep-ph/0303204



- [hep-ph]. To be published in QGP3, Eds. R.C. Hwa and X.N.Wang, World Scientific.
- [13] F. Gelis, E. Iancu, J. Jalilian-Marian, and R. Venugopalan, "The Color Glass Condensate," arXiv:1002.0333 [hep-ph]. \*  
Temporary entry \*.
- [14] E. Iancu, A. Leonidov, and L. D. McLerran, "Nonlinear gluon evolution in the color glass condensate. 1.," *Nucl.Phys.* **A692** (2001) 583–645, arXiv:hep-ph/0011241 [hep-ph].
- [15] J. Jalilian-Marian, A. Kovner, A. Leonidov, and H. Weigert, "The BFKL equation from the Wilson renormalization group," *Nucl.Phys.* **B504** (1997) 415–431, arXiv:hep-ph/9701284 [hep-ph].
- [16] S. Catani, F. Fiorani, and G. Marchesini, "Small  $x$  Behavior of Initial State Radiation in Perturbative QCD," *Nucl. Phys.* **B336** (1990) 18.
- [17] M. Ciafaloni, "Coherence Effects in Initial Jets at Small  $q^2 / s$ ," *Nucl. Phys.* **B296** (1988) 49.
- [18] B. Andersson, G. Gustafson, and J. Samuelsson, "The Linked dipole chain model for DIS," *Nucl. Phys.* **B467** (1996) 443–478.
- [19] G. P. Salam, "Soft emissions and the equivalence of BFKL and CCFM final states," *JHEP* **03** (1999) 009, hep-ph/9902324.
- [20] M. L. Good and W. D. Walker, "Diffraction dissociation of beam particles," *Phys. Rev.* **120** (1960) 1857–1860.
- [21] G. P. Salam, "An introduction to leading and next-to-leading BFKL," *Acta Phys. Polon.* **B30** (1999) 3679–3705, hep-ph/9910492.
- [22] A. H. Mueller and G. P. Salam, "Large multiplicity fluctuations and saturation effects in onium collisions," *Nucl. Phys.* **B475** (1996) 293–320, hep-ph/9605302.
- [23] J. Kwiecinski, A. D. Martin, and P. J. Sutton, "Constraints on gluon evolution at small  $x$ ," *Z. Phys.* **C71** (1996) 585–594, hep-ph/9602320.
- [24] I. Balitsky and G. A. Chirilli, "NLO evolution of color dipole," *Acta Phys. Polon.* **B39** (2008) 2561–2566.

- [25] E. Avsar, "On the High Energy Behaviour of The Total Cross Section in the QCD Dipole Model," *JHEP* **04** (2008) 033, arXiv:0803.0446 [hep-ph].
- [26] V. N. Gribov and L. N. Lipatov, "Deep inelastic e p scattering in perturbation theory," *Yad. Fiz.* **15** (1972) 781–807.
- [27] Y. L. Dokshitzer, "Calculation of the structure functions for deep inelastic scattering and  $e^+e^-$  annihilation by perturbation theory in quantum chromodynamics. (In Russian)," *Sov. Phys. JETP* **46** (1977) 641–653.
- [28] G. Altarelli and G. Parisi, "Asymptotic freedom in parton language," *Nucl. Phys.* **B126** (1977) 298.
- [29] H. Kharraziha and L. Lönnblad, "The linked dipole chain Monte Carlo," *JHEP* **03** (1998) 006, hep-ph/9709424.
- [30] H. Kharraziha and L. Lönnblad, "LDCMC version 1.0," *Comput. Phys. Commun.* **123** (1999) 153.
- [31] G. Gustafson, "Dual description of a confined color field," *Phys. Lett.* **B175** (1986) 453.
- [32] G. Gustafson and U. Pettersson, "Dipole Formulation of QCD Cascades," *Nucl. Phys.* **B306** (1988) 746.
- [33] L. Lönnblad, "ARIADNE version 4: A Program for simulation of QCD cascades implementing the color dipole model," *Comput. Phys. Commun.* **71** (1992) 15–31.
- [34] B. Andersson, G. Gustafson, and B. Soderberg, "A GENERAL MODEL FOR JET FRAGMENTATION," *Z. Phys.* **C20** (1983) 317.
- [35] B. Andersson, G. Gustafson, G. Ingelman, and T. Sjöstrand, "Parton fragmentation and string dyanmics," *Phys. Rept.* **97** (1983) 31.
- [36] T. Sjöstrand, S. Mrenna, and P. Z. Skands, "A Brief Introduction to PYTHIA 8.1," *Comput. Phys. Commun.* **178** (2008) 852–867, arXiv:0710.3820 [hep-ph].
- [37] T. Sjöstrand, S. Mrenna, and P. Z. Skands, "PYTHIA 6.4 Physics and Manual," *JHEP* **05** (2006) 026, arXiv:hep-ph/0603175.



- [38] UA4 Collaboration, D. Bernard *et al.*, "LARGE  $t$  ELASTIC SCATTERING AT THE CERN SPS COLLIDER AT  $S^{**}(1/2) = 630\text{-GeV}$ ," *Phys. Lett.* **B171** (1986) 142.
- [39] NA22 Collaboration, M. Adamus *et al.*, "STUDY OF ELASTIC  $\pi^+p$ ,  $K^+p$  AND  $p p$  SCATTERING AT  $250\text{-GeV}/c$ ," *Phys. Lett.* **B186** (1987) 223–226.
- [40] CDF Collaboration, F. Abe *et al.*, "Measurement of small angle  $\bar{p}p$  elastic scattering at  $\sqrt{s} = 546\text{ GeV}$  and  $1800\text{ GeV}$ ," *Phys. Rev.* **D50** (1994) 5518–5534.
- [41] CDF Collaboration, F. Abe *et al.*, "Measurement of the  $\bar{p}p$  total cross-section at  $\sqrt{s} = 546\text{ GeV}$  and  $1800\text{-GeV}$ ," *Phys. Rev.* **D50** (1994) 5550–5561.
- [42] E-710 Collaboration, N. A. Amos *et al.*, "A LUMINOSITY INDEPENDENT MEASUREMENT OF THE anti- $p p$  TOTAL CROSS-SECTION AT  $S^{**}(1/2) = 1.8\text{-TeV}$ ," *Phys. Lett.* **B243** (1990) 158–164.
- [43] E-710 Collaboration, N. A. Amos *et al.*, "Anti-proton - proton elastic scattering at  $s^{**}(1/2) = 1.8\text{-TeV}$  from  $|t| = 0.034\text{-GeV}/c^{*2}$  to  $0.65\text{-GeV}/c^{*2}$ ," *Phys. Lett.* **B247** (1990) 127–130.
- [44] E-811 Collaboration, C. Avila *et al.*, "The ratio,  $\rho$ , of the real to the imaginary part of the anti- $p p$  forward elastic scattering amplitude at  $s^{**}(1/2) = 1.8\text{-TeV}$ ," *Phys. Lett.* **B537** (2002) 41–44.
- [45] UA4/2 Collaboration, C. Augier *et al.*, "Measurement of the proton - anti-proton total cross- section at the S anti- $p p$  S collider by a luminosity dependent method," *Phys. Lett.* **B344** (1995) 451–454.
- [46] M. M. Block, F. Halzen, and T. Stanev, "Extending the frontiers: Reconciling accelerator and cosmic ray  $p p$  cross sections," *Phys. Rev.* **D62** (2000) 077501, [arXiv:hep-ph/0004232](https://arxiv.org/abs/hep-ph/0004232).
- [47] ZEUS Collaboration, S. Chekanov *et al.*, "Study of deep inelastic inclusive and diffractive scattering with the ZEUS forward plug calorimeter," *Nucl. Phys.* **B713** (2005) 3–80, [hep-ex/0501060](https://arxiv.org/abs/hep-ex/0501060).
- [48] H1 Collaboration, A. Aktas *et al.*, "Measurement of deeply virtual Compton scattering at HERA," *Eur. Phys. J.* **C44** (2005) 1–11, [arXiv:hep-ex/0505061](https://arxiv.org/abs/hep-ex/0505061).

- [49] **H1 Collaboration**, F. D. Aaron *et al.*, “Measurement of Deeply Virtual Compton Scattering and its  $t$ -dependence at HERA,” *Phys. Lett.* **B659** (2008) 796–806, arXiv:0709.4114 [hep-ex].
- [50] L. Lönnblad, “ThePEG, Pythia7, herwig++ and Ariadne,” *Nucl.Instrum.Meth.* **A559** (2006) 246–248.
- [51] M. Bähr *et al.*, “Herwig++ Physics and Manual,” *Eur. Phys. J.* **C58** (2008) 639–707, arXiv:0803.0883 [hep-ph].
- [52] A. Buckley *et al.*, “Rivet user manual,” arXiv:1003.0694 [hep-ph].
- [53] **Atlas Collaboration** Collaboration, G. Aad *et al.*, “Measurement of underlying event characteristics using charged particles in pp collisions at  $\sqrt{s} = 900\text{GeV}$  and 7 TeV with the ATLAS detector,” arXiv:1012.0791 [hep-ex]. \* Temporary entry \*.
- [54] **ATLAS Collaboration** Collaboration, G. Aad *et al.*, “Charged-particle multiplicities in pp interactions measured with the ATLAS detector at the LHC,” *New J.Phys.* (2010) , arXiv:1012.5104 [hep-ex]. Long author list - awaiting processing.
- [55] **CDF Collaboration**, A. A. Affolder *et al.*, “Charged jet evolution and the underlying event in  $p\bar{p}$  collisions at 1.8 TeV,” *Phys. Rev.* **D65** (2002) 092002.
- [56] A. Buckley, J. Butterworth, S. Gieseke, D. Grellscheid, S. Höche, *et al.*, “General-purpose event generators for LHC physics,” arXiv:1101.2599 [hep-ph].
- [57] R. Corke and T. Sjöstrand, “Interleaved Parton Showers and Tuning Prospects,” arXiv:1011.1759 [hep-ph].
- [58] **CDF Collaboration**, R. Field, “Min-bias and the underlying event in Run 2 at CDF,” *Acta Phys. Polon.* **B36** (2005) 167–178.
- [59] C. Flensburg, G. Gustafson, L. Lonnblad, and A. Ster, “Correlations in double parton distributions at small  $x$ ,” arXiv:1103.4320 [hep-ph].

